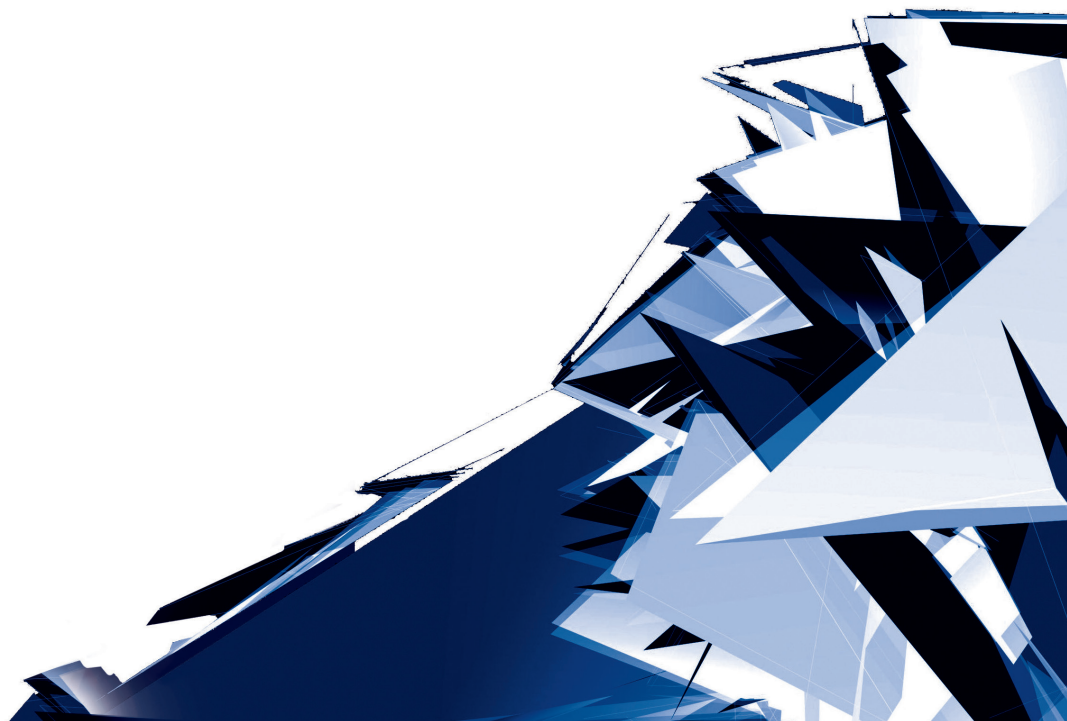


Technical Transactions

Czasopismo Techniczne

Issue 8

Volume 2018 (115)



Chairman of the Cracow University of Technology Press Editorial Board
Przewodniczący Kolegium Redakcyjnego Wydawnictwa Politechniki Krakowskiej

Tadeusz Tatara

Editor-in-chief
Redaktor naczelny

Józef Gawlik
(jgawlik@mech.pk.edu.pl)

Scientific Council
Rada Naukowa

Jan Blachut – University of Liverpool (UK)
Wojciech Bonenberg – Poznan University of Technology (Poland)
Tadeusz Burczyński – Silesian University of Technology (Poland)
Massimo Corcione – Sapienza University of Rome (Italy)
Leszek Demkowicz – The University of Texas at Austin (USA)
Joseph El Hayek – University of Applied Sciences (Switzerland)
Ameen Farooq – Technical University of Atlanta (USA)
Zbigniew Florjańczyk – Warsaw University of Technology (Poland)
Marian Gizejowski – Warsaw University of Technology (Poland)
Sławomir Gzell – Warsaw University of Technology (Poland)
Allan N. Hayhurst – University of Cambridge (UK)
Maria Kušnierova – Slovak Academy of Sciences (Slovakia)
Krzysztof Magnucki – Poznan University of Technology (Poland)
Herbert Mang – Vienna University of Technology (Austria)
Arthur E. McGarity – Swarthmore College (USA)
Antonio Monestiroli – Polytechnic of Milan (Italy)
Marek Pabich – Lodz University of Technology (Poland)
Ivor Samuels – University of Birmingham (UK)
Miroslaw J. Skibniewski – University of Maryland (USA)
Günter Wozny – Technical University in Berlin (Germany)
Roman Zarzycki – Lodz University of Technology (Poland)

Native Speakers

Weryfikacja językowa

Tim Churcher
Robin Gill
Mike Timberlike

Section Editor
Sekretarz Sekcji

Dorota Sapek
(dsapek@wydawnictwo.pk.edu.pl)

Editorial Compilation
Opracowanie redakcyjne

Aleksandra Urzędowska
(aurzedowska@pk.edu.pl)

Typesetting
Skład i lamanie

Małgorzata
Murat-Drożyńska

Design
Projekt graficzny

Michał Graffstein

Series Editors
Redaktorzy Serii

ARCHITECTURE AND URBAN PLANNING

Mateusz Gyurkovich
(mgyurkovich@pk.edu.pl)

CHEMISTRY

Radomir Jasiński
(radomir@chemia.pk.edu.pl)

CIVIL ENGINEERING

Marek Piekarczyk
(mpiekar@pk.edu.pl)

ELECTRICAL ENGINEERING

Piotr Drozdowski
(pdrozdow@usk.pk.edu.pl)

ENVIRONMENTAL ENGINEERING

Michał Zielina
(mziel@vistula.wis.pk.edu.pl)

**PHYSICS, MATHEMATICS
AND COMPUTER SCIENCES**

Włodzimierz Wójcik
(puwojcik@cyf-kt.edu.pl)

MECHANICS

Andrzej Sobczyk
(andrzej.sobczyk@mech.pk.edu.pl)

www.ejournals.eu/Czasopismo-Techniczne
www.technicaltransactions.com
www.czasopimotechniczne.pl

Contents

ARCHITECTURE AND URBAN PLANNING

Anna Staniewska

Sacred architecture and sacred areas in the designed space of mental health hospitals from the late 19th and early 20th centuries..... 5

Agnieszka Wójtowicz-Wróbel

Spatial significance of new municipal engineering structures – the case of Italian eco-incineration plants..... 21

CHEMISTRY

Izabela Czekaj, Natalia Sobuś

Concepts of modern technologies of obtaining valuable biomass-derived chemicals..... 35

Łukasz Majewski, Janusz W. Sikora

Mechanical properties of polyethylene filled with treated neuburg siliceous earth..... 59

Przemysław Migas, Jerzy Baron

The co-combustion of rubber waste with LPG fuel in a fluidised bed reactor..... 73

CIVIL ENGINEERING

Jolanta Dźwierzynska

Shaping curved steel rod structures..... 87

Agnieszka Chowaniec, Krzysztof Ostrowski

Epoxy resin coatings modified with waste glass powder for sustainable construction..... 99

Matthias Richter, Jan Paszkowski

Modelling driver behaviour in traffic-calmed areas..... 111

ELECTRICAL ENGINEERING

Marzena Hajduk-Stelmachowicz, Marek Gołębiowski, Marek Stelmachowicz

The use of preliminary hazard analysis to assess the risk of damage to the telecommunications wired access network..... 125

Kazimierz Kielkowicz

Unsupervised learning in latent space with a fuzzy logic guided modified BA..... 141

Ryszard Mielnik

The integration of an automatic reserve switching controller into a railway traffic control system power supply through the use of a Petri net and a graphical programming language..... 155

MECHANICS

Stanisław Kuciel, Karolina Mazur

The effect of long-term storage on the mechanical properties of composites based on polyamide 10.10 derived from renewable sources..... 167



Łukasz Ślusarczyk, Emilia Franczyk	
<i>Experimental determination of forces in a cutting zone during turning a stainless steel shaft....</i>	177
Łukasz Ślusarczyk, Emilia Franczyk	
<i>Experimental determination of the temperature in the cutting zone during turning of titanium alloy grade 2</i>	189
Krzysztof Wach	
<i>The influence of vehicle preparation on the results of suspension kinematics measurement ..</i>	199

Anna Staniewska  orcid.org/0000-0002-4003-8025

astaniewska@pk.edu.pl

Institute of Landscape Architecture, Faculty of Architecture, Cracow University
of Technology

SACRED ARCHITECTURE AND SACRED AREAS
IN THE DESIGNED SPACE OF MENTAL HEALTH HOSPITALS
FROM THE LATE 19th AND EARLY 20th CENTURIES

OBIEKTY SAKRALNE I OBSZARY SACRUM
W KOMPONOWANEJ PRZESTRZENI SZPITALI PSYCHIATRYCZNYCH
PRZEŁOMU XIX I XX WIEKU

Abstract

Mental hospitals from the late 19th and early 20th centuries resembled independent cities and were designed to fulfil all patients' needs, including spiritual. The idea of psychiatric care and healing also embraced the spiritual aspect of life. Churches, chapels and cemeteries were an indispensable part of many mental asylums of the time. The article explores the position of sites of worship in psychiatric hospitals and examines the place of sacred architecture and spaces in their layout and composition.

Keywords: sacred spaces, mental hospital in the past, landscape, composition

Streszczenie

Szpitaly psychiatryczne z przełomu XIX i XX wieku, które przypominały samodzielne miasteczka, miały zaspokajać wszelkie potrzeby pacjentów – w tym także i te duchowe. Duchowy wymiar troski o pacjentów oznaczał obecność w zakładach kościołów, kaplic i cmentarzy. Artykuł analizuje miejsce obiektów kultu w kompozycji krajobrazowej i rozplanowaniu historycznych szpitali psychiatrycznych.

Słowa kluczowe: przestrzeń sakralna, sacrum, szpital psychiatryczny, krajobraz, kompozycja

1. Introduction

Many of the pavilion system psychiatric hospitals built in the late 19th and early 20th centuries are designed to the like of self-sustainable districts, if not even independent little towns. It is hard to resist associations with the idea of garden-cities popular early in the 20th century, in Poland as a rule connected to the person of Ebenezer Howard [5]. Immersing the hospital buildings in greenery has earned them the colloquial label of “garden cities”. Analysing their functionalities and plans *ex post*, and later comparing them with Howard’s descriptions and ideograms of ideal cities, one can risk the statement that they embodied his idea. However, it is hard to find a clear substantiation of the argument that contemporary tendencies in designing hospital complexes resulted directly from his publication, yet it cannot be denied that the currents connected to the hygiene movement [24], the villa and cottage architecture [4], and the development of residential estates and industrial plants in the European urban tissue of the time, influenced their forms.

The functional programmes of psychiatric hospitals of the second half of the 19th century were predominantly designed by psychiatrists, who considered the organisation of space, both inside the pavilions and outdoors, a significant part of the therapy [8]. The time spent in the institution was to provide an opportunity to be isolated from the detrimental influence of civilisation, which, at the time, was considered one of the several mental disorders described as insanity. The space and environment of treatment designed in that way were to remind, as much as possible, of the regular world “beyond the walls”, which were often raised to isolate mental health institutions. A stay in such an institution was assumed to allow the return of patients to the society after a completed treatment, although, in fact, many patients remained in the institutions to the end of their lives.

Such an approach as well as the tradition of Christian care for the sick and service of the clergy in hospitals (both nuns serving as nurses and hospital chaplains) also implied the presence of sacred architecture and spaces, chapels, churches, and cemeteries, within the complexes. The article presents the results of studies of their place and role in the landscape of European psychiatric hospitals of the late 19th and early 20th centuries.

2. Purpose of the study

Reflections on the place of the sacred within the designs of hospitals for mental patients in the 19th/20th centuries belong to a more extensive scope of research of the history and therapeutic dimension of these complexes, which is of historical significance nowadays. The purpose of the research presented in the article is to describe how the care for the satisfaction of the patients’ spiritual needs was manifested in the design of the space, and how the visual connections and forms of expression applied influenced the shaping of the significative layer of the sacred realm.

3. State of the art

The development of psychiatry and its progressing deinstitutionalisation in the last four decades have caused numerous changes in healthcare management, and consequently in the management of mental health hospitals, many of which continued a tradition dating back to the 19th century. Some have been liquidated [3], and many others undergo various transformations [10]. In parallel came the awareness of historical heritage values of these sites and complexes built as modern institutions representing high functional, artistic, and aesthetic level, whether 100, 150 or 200 years ago. Former hospitals for psychiatric patients founded in the 19th and early 20th centuries are the objects of research of historians of art and architecture in the countries of Western Europe (the United Kingdom [21], Italy [18], Germany [11] and Austria [6]), and the United States [33], yet this research hardly ever crosses the borders of individual states. An exception in the field are the works of Leslie Topp, who in her latest book runs a comparative study of the architecture of hospitals in the Austro-Hungarian monarchy, namely Am Steinhof Hospital in Vienna, San Giovanni in Trieste, and Kromeriž, also mentioning the hospital in Kraków–Kobierzyn [31]. In her earlier studies, the researcher investigated the location and significance of mortuaries doubling for funerary chapels as a meaningful architectural framework for places of study and rituals of passage [30]. Claire Hickman analysed the history and therapeutic considerations of hospital gardens of bygone Great Britain from the point of view of landscape [9]. Sarah Rutherford presented the landscape architects and designers of Victorian gardens in lunatic asylums [22], and extensively described the origin and functioning of such institutions [23]. Extant publications about Poland concern the complex of the new institution in Lubiąż in the context of similar German projects [32], and an extensive review of the historical values of psychiatric hospitals in Poland against the background of contemporary threats facing historical gardens [25] and a study of forms commemorating the victims of the T 4 action in hospital and park compounds [26]. Some of the historical hospitals published monographic works and commemorative brochures to commemorate the anniversaries of their foundation.

4. Description of studies conducted

To study the place of the sacred within the complexes of historical psychiatric hospitals, available archive publications were accessed to determine the positioning of the churches, chapels, and cemeteries within the institutions. Digests with early 20th-century descriptions, plans and photographs provided precious information.

Later, study visits and examination of contemporary aerial photographs and maps made available on map portals made it possible to learn the terrain and degree of preservation of the designed landscape and links between the sacred and other elements of hospital complexes and their gardens.

Altogether over a dozen compounds representative for successive periods and representing the successive stages of development of the idea of a psychiatric hospital being a specialised treatment compound with a specified spatial and landscape form were analyzed.

The studies conducted made it possible to distinguish the fundamental types of sacred landscape present in the design of psychiatric hospital complexes in the late 19th and early 20th centuries.

5. Results

It happened in the first half of the 19th century that complexes of monastic orders, secularised *en masse* at the time [13], were adapted to the needs of psychiatric hospitals. Such cases were recorded in former Prussia, where the Prussian Finance Edict, signed by King Frederick William III, was announced on 27 October 1810 and quickly entered into force [27]. This is how the first hospital and alms-house for the disabled was set up in the former Bernardine monastery in Świecie (1822) before the construction of the West Prussian Institution for Mental Patients there. The new facility was raised on the premises of the former monastery gardens situated to the south of the Baroque church and monastery, and opened in 1855 after many years of problems, when the construction was repeatedly stalled [1]. The development of the first psychiatric hospital in Lubiąż followed similar tracks, as it opened in 1823 in the adapted premises of a monastery after the previous dissolution of one of the largest Cistercian abbeys in Europe.¹ Partitioning walls and wooden ceilings were installed to divide the spacious Baroque interiors, naturally at the cost of original stucco and painted decorations. Similarly, the former *Heil- und Pflegeanstalt Ravensburg-Weißenau*, today home to the *Zentrum für Psychiatrie Südwürttemberg*, was housed in the Baroque premises of the former Premonstratensian abbey and monastery since 1892 [15]. In these cases, the therapeutic and remedial functions replaced the original purpose of the monastic compounds, with the sacred function being only retained by the churches. It is best to bear in mind that such a succession of functions was justified to a degree, as monasteries and convents had run hospitals and alms-houses for the poor for centuries, with monks frequently being active herbalists, and *hortus medicus* a material element of the monastery's garden. The rationale for the placement of institutions for psychiatric patients in former monastic compounds early in the 19th century was, however, different. Neither the Lubiąż Cistercians nor the Weißenau Premonstratensians had hospitaller traditions, on the other hand, the prosperous abbeys thrived and had plenty of room available to be converted into patient wards. They were surrounded with gardens, farm buildings, factories, manor farms, as well as arables and pastures. When transformed into care centres, the towers flanking the façades of the Baroque monastery churches remained an ostensible sign of the sacred in the space. The gardens of the monasteries were not liquidated, as the medical personnel appreciated the significance of their patients' contact with nature. In Lubiąż they were replaced

¹ Other instances of hospitals organised in former monasteries include Zwiefalten in Württemberg and Marsberg in Westphalia; more extensive treatment of the subject and of the history of the Lubiąż facility is available in [14, p. 26–37].

with new designs. Separate sections were designed for a garden for the patients of the institution (wealthy individuals, also from beyond Silesia) and the director's garden. The garden of the public institution for the people of the Province of Silesia was to be an area where the convalescents could walk under strict supervision; the prints from the 1860s show the garden enclosed with a wooden gallery, and a tall fence with a guard tower [14, pp. 35–36]. The solution was known from the English asylums from the first years of the 19th century, which usually featured the so-called airing courts to be used by the patients to draw some fresh air and walk, thus ensuring the minimum of physical activity. Their placement between the wings of the building brought to mind the situation of the garth, although the greens were often freely designed and not limited to regular geometric designs only, even though they were popular. It is also probable that the patients fit for labour worked on hospital farms that, as previously monastery farms, provided the establishment with food. No traces of the original gardens have survived in these complexes besides individual specimens of ancient trees and the isolated spaces of the monastery cloister garths.

In the earliest years of the pavilion-based hospitals, greenfield hospital investments a restrained attitude toward the religion characteristic of the Enlightenment became visible, especially in Prussia. A chapel with a low ave-bell tower was but a part of the main administrative building, often situated by the entrance, on the axis of the whole complex. It was usually situated along the axis of the main building's projection, with the chancel pointing towards the centre of the hospital complex.² The new dominant features towering over the complexes were the huge accessory buildings: boiler houses with tall chimneys, kitchens and laundries, and water towers. In the gardens, the sacred was present on the fringes of the entire system, and assumed the form of the funerary chapel, often doubling for the mortuary, located in the direct vicinity of the institution's cemetery, which was usually designed as a simplest grid, resulting from the geometricised planting of trees and shade-tolerant plants (boxwood and yew hedgerows, and such groundcover as ivy).

The churches and chapels of the institutions became independent elements of spatial design at the time of heyday of pavilion system hospitals. Depending on the general principles, the organisation of the space designed by the architect and hospital management were situated in various, usually significant, locations.

The main axis of the complex was an important element in hospitals built on the orthogonal plan. It separated the pavilions for the patients (grouped by types of illnesses) deployed symmetrically on its sides. One side gathered the pavilions for the women, the other – for men. The main axis opened with the building of hospital administration, and was usually continued with the service buildings for the entire facility. These included both the back office (kitchens, bakeries, laundries, and boiler rooms) and buildings with special functions, including the facility's theatre and/or social building, and the church. Kocborów is an example of such a solution, with the axis terminating in a chapel adjacent to the wall separating the grounds of the hospital from the cemetery situated in the forest [20]. For

² This was the case i.a. in the institution in Świecie, developed outside the monastery, and in the Berlin hospitals designed by Hermann Blankenstein in late Classicist spirit, inspired by the works of Karl Friedrich Schinkel, in *Irrenanstalt Dalldorf* (once Karl-Bonhoeffer-Nervenlinik) opened in 1880 and in *Irrenanstalt Herzberge* (opened in 1893, currently Evangelisches Krankenhaus Königin Elisabeth Herzberge); more on the architect in [19].

major religious ceremonies, the function of the church was taken over by the social building situated on the main axis, immediately behind the building of administration.

Functions were combined in a similar manner also later in the institutions based on the multi-axis plans, which had the churches built in the central part of one of them. The design based on such a plan is found in Mauer-Öhling, opened in 1902, where the entire design, albeit with the outstanding main axis, was composed around a rhomboid system of internal roads. The hospital's chapel was built in the centre of the so-called *Mittelweg* (German for the central road) opening with the building of hospital administration. It combined two functions: the entrance to the social building, which could also double for the theatre, was situated on its other side [12]. When a large number of people participated in the religious functions, the large door between the two rooms) made it possible to extend the chapel by the space of the social building. Standing to its south-west, behind the four pavilions built by the side alleys for the patients, was the building of the administration overlooking a quartered garden on the side of the centre of the institution. The pavilions for patients with less serious ailments stood by the alleys arranged in fan-shape to the northeast, together with the pavilions of the "open doors" system clustered around round central round spaces. The facility's kitchen, laundry, and boiler house were situated at the end of the *Mittelweg*. The facility and the whole complex were designed by Carlo von Boog, who later drafted the preliminary plan for the Viennese hospital Am Steinhof. Not unlike in the pavilions, the façade of the chapel combines red brick with light detail, complemented with sculptures, Art Nouveaux ornaments wrought in metal, and beautiful stained glass with lavish floral motifs. In this case, it would be hard to discuss clear panoramic relations, as the facility is situated on a flat plot overgrown with pine forest. There were small squares in front of the building, and a pond on the side of the entrance to the theatre, while the nearest pavilions and administration buildings were hidden among the trees. Compared to other buildings of the hospital, the chapel stood out with its more lavish detail and decorations (partly lost by now), which added to its solemn character, especially as it was combined with spatial isolation. Thanks to such the above and to the connection of a sacred site with the of the social building used for entertainment, the buildings seem to belong to another, more beautiful world. In turn, the mortuary, the funerary chapel, and the cemetery were situated on the periphery of the institution, on its south-western edge, by the very road from Amstetten to Ulmerfeld. Such a location made it possible to transport quickly the bodies of deceased patients beyond the main area of the hospital, and at the same time keep participants in the funerary rites outside it [30, p.17]. The white façade turned towards them and towards the world outside was symmetrical and arranged with stucco panels and rustication. The flat-roofed chapel was built into the external perimeter wall of the hospital, and the highest, central projection was crowned with a simple cross, below which, over the entrance, a single word *FRIEDE*, that is "peace", was carved in a font used for the whole facility. It was the only building in the whole complex to be fully covered in plaster, and its whiteness could be considered symbolic in the context of its function. While the pavilions for the patients, with their red brick façades decorated with bright plaster and wrought iron elements painted light green, were hidden among the woods, the white solid stood against the dark green providing the symbolic gate to eternity.

The church of the San Giovanni Hospital in Trieste [2] is situated on a steep slope. It closes the main axis of the facility (Fig. 1) designed by Lodovico Braidotti, and opened in 1908. A

plantain-lined avenue leads uphill from the building of the administration, and closes in the impressive flights of stairs in the retaining wall clad with stone blocks, providing support to the terrace with the theatre and the hospital kitchen. Further, the road leads to the sacred building with its lofty tower, surrounded by a smallish, rectangular square, whose walls are formed by the arcaded buildings of the colony for the working patients. Such organisation of space reminds of the centres of little towns by the Adriatic and hamlets high in the Alps. The small funeral chapel with the ave bell is situated somewhat uphill, towards the north-west.

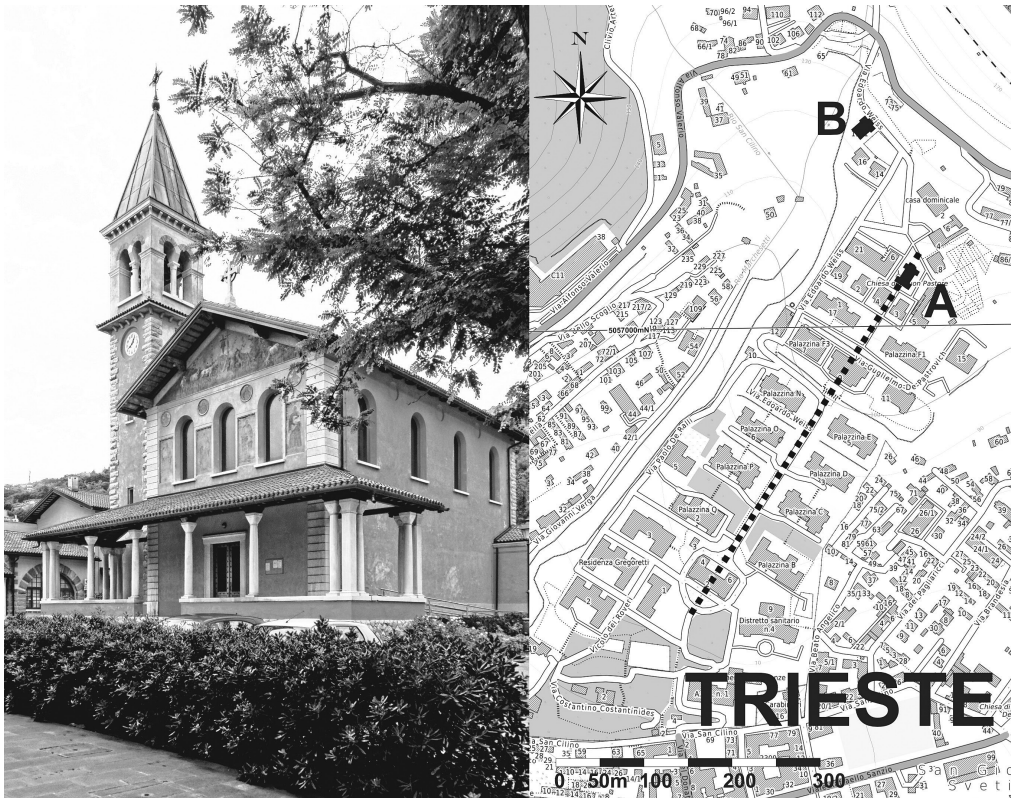


Fig. 1. The Church of the Good Shepherd at the San Giovanni Hospital in Trieste (photo by A. Staniewska, 2017) and the composition of the hospital, A – church, B – funeral chapel (drawing by A. Staniewska on Inkatlas.com map. Copyright OpenStreetMap contributors (openstreetmap.org), OpenTopoMap (CC-BY-SA)

When the main axis was clearly designed to be stately, the accessory buildings were situated on the periphery or behind the buildings that served the purposes of worship and entertainment. An example of such a grand principal axis, dominated by the church, is the Viennese hospital Am Steinhof (Fig. 2). The Church of St Leopold designed by Otto Wagner and crowned with its golden dome as the architect, who also designed the general plan of the institution, intended [29], is a symbolic building. This results from the combination of the impact of the architectural form and the skilful use of the terrain (the whole stands on a slope), which Wagner emphasised

by designing terraces connected with a system of gently winding paths. The compact, light solid on the plan of a Latin cross is covered with a glistening dome, visible from afar as it towers over the Hospital and the Provincial Sanatorium for paying patients at Steinhof in Vienna. The “white city” opened with a pomp in 1907³ to become the most modern, largest, model centre for care and treatment for psychological patients throughout the Austro-Hungarian Monarchy.

It was also the place where the state-of-the-art technologic solutions were applied: the plan of the church let the architect optimise the support of the steel construction of the double-layer dome. The lack of supports and spatial design make the interior clearly central. The architect’s powerful vision creates an entirely modern reference to the Absolute being the final destination

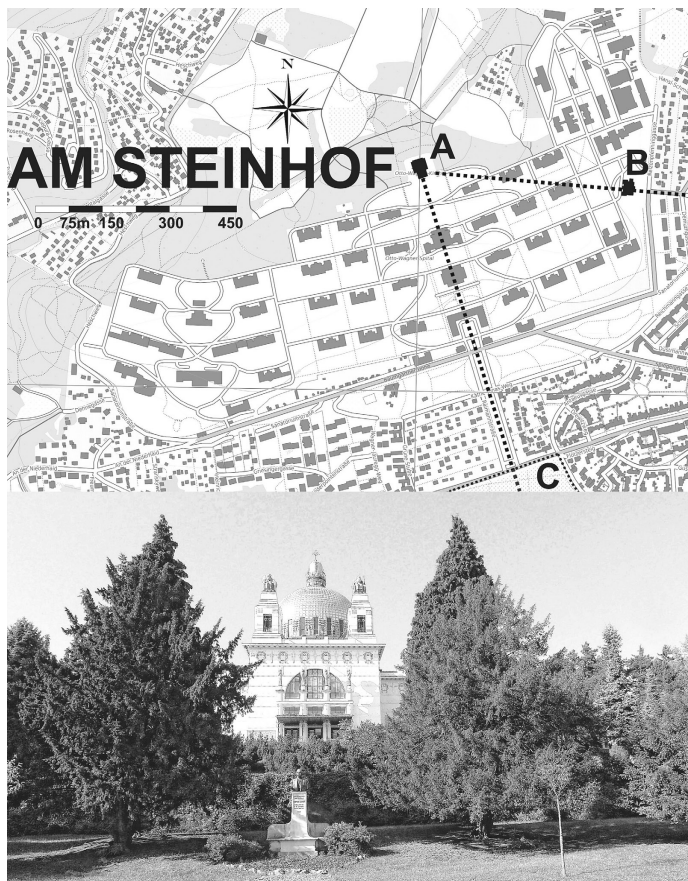


Fig. 2. Church of St. Leopold in the Hospital Am Steinhof in Vienna (photo by A. Staniewska, 2015) and the composition of the hospital, A – church, B – funeral chapel with mortuary, C – Baumgartner Friedhof cemetery, drawing by A. Staniewska on Inkatlas.com map. Copyright OpenStreetMap contributors (openstreetmap.org), OpenTopoMap (CC-BY-SA)

³ *Die weiße Stadt* is how Ludwig Hevesi, Viennese art critic and Secession movement advocate, described the view on the Lower Austrian Provincial Institution for the Cure and Care of the Mentally and Nervously Ill at Steinhof referring to the shining white marble walls of the church rather than the brick facades of the hospital pavilions [7, p. 249].

of the earthly pilgrimage, which at the same time encloses it in the unique entirely modern solid with individual Art Nouveau detail. The original watercolour Otto Wagner submitted to the competition includes the monumental central stairs leading to the square in front of the church, complemented with pergolas covered in creepers [17, the figure on page 104]. Finally, however, two narrower flights of stairs leading to the square were built. Moreover, the landscape that today frames the object results from the domination of nature: the backdrop is provided by the shrubbery covering the hill behind the church, while the lushly growing vegetation and the bushes framing the monument to Leopold Steiner cover the slope leading downhill towards the kitchens and the theatre. The funerary chapel shares its building with the mortuary and autopsy facilities. It is situated at the eastern end of the hospital grounds, at an angle to the design grid on which the remaining objects of the institution were deployed, as it stands on the axis of the street leading from the city towards *Baumgartner Höhe*.

The curved solid wall separating the driveway with the brick building with its arcaded decoration and central projection bearing the inscription *MEMENTO MORI* provides a distinctive border between the separate world of the hospital and those who arrive for funerary ceremonies.

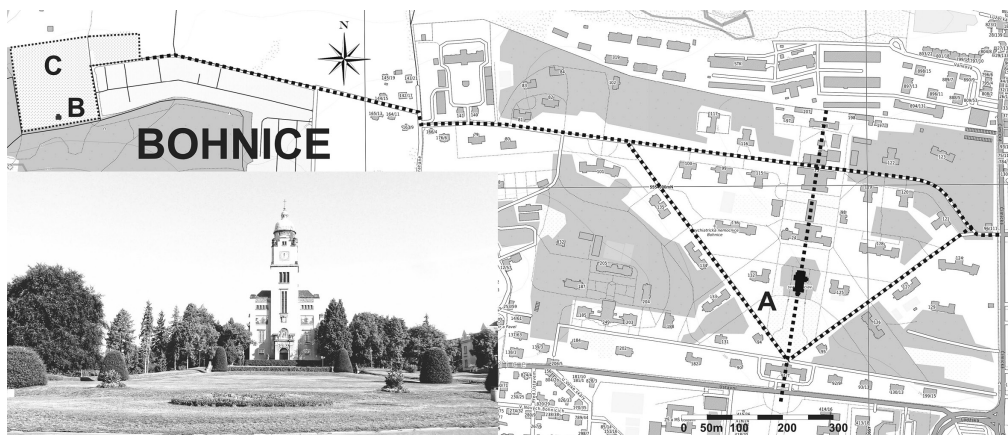


Fig. 3. Church of St Wenceslaus at the Bohnice Hospital in Prague (photo by A. Staniewska, 2016) and the composition of the hospital, A – church, B – cemetery chapel, C – cemetery, drawing by A. Staniewska on Inkatlas.com map. Copyright OpenStreetMap contributors (openstreetmap.org), OpenTopoMap (CC-BY-SA)

The church of the hospital in Prague-Bohnice is situated on the main axis of the composition, on a small knoll behind the building of the administration (Fig. 3). The lawn bears minimalist, geometrised forms of greenery and is framed by copper beaches, providing a broad first plane for the modernist façade of the church decorated symmetrically with mosaics, under a lofty tower designed by Václav Roštlapil. The mosaics made by Jindřich Hlavín in 1916–17 present scenes from the life of the patrons of Bohemia: St John the Baptist, St Ludmila, St Wenceslaus (the patron saint of the church), St Agnes, and St Norbert [28].

An unassuming façade with clear divisions and narrow geometric windows stands in contrast with the academic and horizontal building of the hospital administration, designed in

the spirit of Viennese historicism.⁴ The height of the tower (55 m) combined with its situation on a prominence⁵ let the silhouette of the church dominate the broad stately landscape framed on the sides with the villas of the doctors, and enclosed further away with the pavilions for the patients hidden among the greenery of the park, and hide the accessory buildings situated behind: the laundry, the kitchen, and the boiler house with its tall chimney. In this way, the church (with the space fronting it) becomes the semantic centre of the whole, as the other principal buildings, to mention the theatre situated in the sanatorium part, are situated in certainly far less exposed places. The smallish cemetery and its diminutive chapel are situated altogether beyond the precinct of the hospital, about 700 m to the west of the developments of the hospital farm as a crow flies.

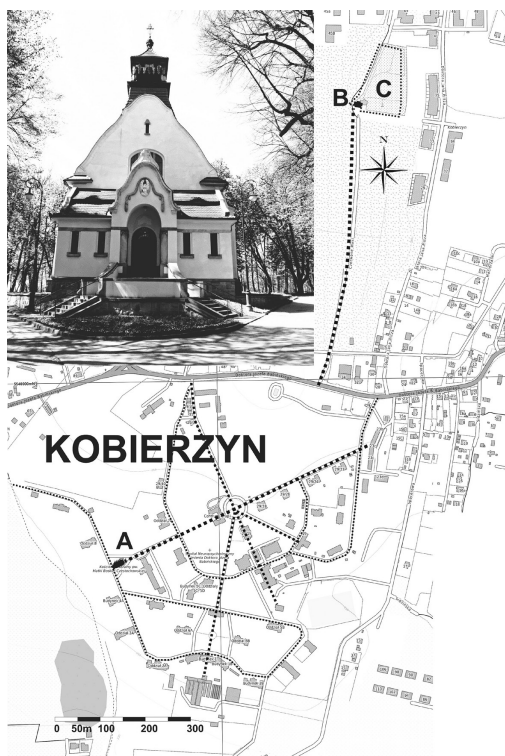


Fig. 4. Chapel dedicated to Our Lady of Częstochowa at the hospital in Kraków-Kobierzyn (photo A. Staniewska, 2016) and the composition of the hospital, A - church, B - cemetery chapel, C - cemetery, fig. A. Staniewska on the map Inkatlas.com. Copyright OpenStreetMap contributors (openstreetmap.org), OpenTopoMap (CC-BY-SA)

⁴ Born in Kostelec nad Orlicí, Roštlapil graduated from the University of Technology in Prague, studied architecture in Vienna in 1881–84 and remained under the influence of the Viennese artistic trends, which is visible in his designs (like Academy of Fine Arts, Akademia Straka: the current seat of the government of the Czech Republic in Prague).

⁵ Formerly a village of medieval origin, today's Bohnice is part of District 8 in the Northern part of Prague, on the high, right bank of the Vltava. Such a situation made the tower of the church of the institution a landmark and a point of bearing also for the Second World War aviation.

There is a concentric radiating composition in Kobierzyn near Kraków, with the hospital church designed by Antoni Budkowski standing at the end of the East-West line that becomes the main axis welcoming the visitors entering the premises of the hospital (Fig. 4), by which the most adorned buildings are gathered. The building of the management is situated on its left, and the building of the administration, bringing a hospitable Polish manor house to mind is situated by the central roundabout sporting plenty of flowers.

The bright façade of the church crowned with a small tower is first seen over its balcony flanked with twin columns. The church is reached by a slightly rising avenue lined with lime trees. It forks before the triangular terrace supported by retaining walls, on which the church was built. It is not a coincidence that its proportions and the neo-Baroque detail of the portico supported on two columns and the finishing of the portly ave bell tower bring to mind the smallish village churches. The legible reference to the manor house style made by the administration building combined with the church covered with steep roof build a sense of the local and create the “axis of hope” familiar to the patient.

A contemporary addition immediately behind the church is the Memorial devoted to hospital patients murdered during the Second World War. The hospital cemetery with its chapel is situated at a distance from the hospital complex [16, p. 137] – to the north of the road to Skawina (today’s Babińskiego Street), and has evolved into a municipal cemetery covering 1.27 ha (3.14 acres).

Similar references to the local small town landscape can be elicited from the design of the institutions built on organic plans, to mention Eglfing Haar near Munich (Fig. 5).

Haar I (formerly *Kreis-Heil- und Pflegeanstalt*, built in 1901–05) includes two sacred buildings: a small Evangelical-Lutheran chapel and a Roman Catholic Parish Church of St Raphael designed by Johann Schobloch⁶. The two are situated close by, with the Evangelical chapel standing to the right from the main road of the hospital leading from the entrance (with the administration building on its left side), and the Catholic Church being situated perpendicularly to it, on the only clear axis that can be found in the design. Its simple form boasting an appended tower and finished with neo-Romanesque detail in light stone, stands tall over the low pavilions surrounding it, and by all means is the key point of the design. The hospital complex Haar II built in 1910–12 (today are part of *Isar Amper Klinikum München Ost*, being partially liquidated) with its Catholic Church of the Seven Dolors of Mary (*Katholische Anstaltskirche Sieben Schmerzen Mariä*)⁷, designed with the participation of Georg Albertshofer, offers a similar case. This building is also situated perpendicularly to the main road, bisecting the entire design, yet it is surrounded by a low wall with horse chestnut trees planted nearby. The solid of a single-nave church with a tower over the western entrance received slightly more sculpted decorations. Despite the neo-Romanesque portal, it is decorated clearly in the Art Nouveau style. Standing in an angle of the wall surrounding

⁶ Data quoted from the *Bayerisches Landesamt für Denkmalpflege*, the complex was entered into the register at number D-1-84-123-9 (Bau R 34 and Bau R 35 respectively), online <http://geoportal.bayern.de> (access: 25.10. 2016).

⁷ Data quoted from the *Bayerisches Landesamt für Denkmalpflege*, the complex was entered into the register at number D-1-84-123–23D-1-84-123-9 (the church: Bau C 78), online <http://geoportal.bayern.de> (access: 25.10.2016).

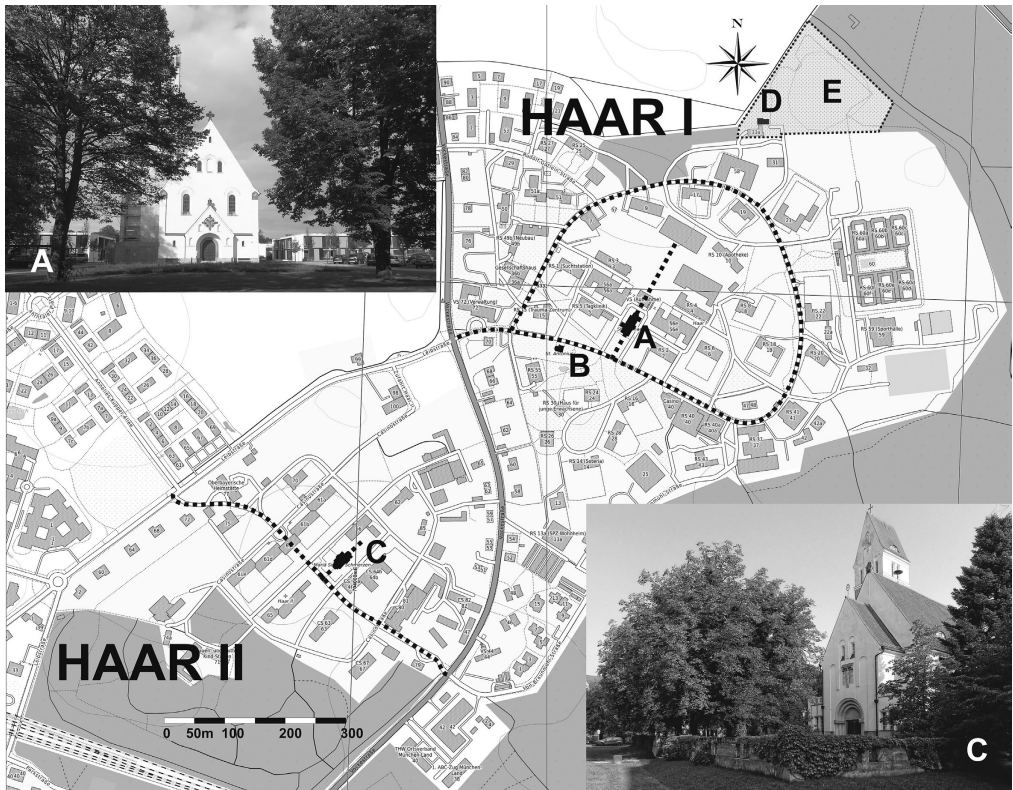


Fig. 5. Churches and sacred areas on the plan of the psychiatric hospitals in Eglfing-Haar near Munich, A – church of St Raphael (photo by A. Staniewska, 2017), B – Evangelical chapel, C – Church of the Seven Dolors of Mary (photo by A. Staniewska, 2017), D – cemetery chapel, E – the hospital cemetery, drawing by A. Staniewska on Inkatlas.com map. Copyright OpenStreetMap contributors (openstreetmap.org), OpenTopoMap (CC-BY-SA)

the church is a fountain-spring with modernist detail, complemented with benches. Such arrangements of the space clearly bring to the mind church squares in small towns, and encourage having a break by the church. The funerary chapel and cemetery of the institution were situated beyond the north-eastern perimeter of Haar I. The hospital necropolis melds smoothly into the natural woods surrounding the facility and is a typical *Waldfriedhof*, i.e. a forest cemetery with grave markers scattered among the trees and overgrown with a carpet of forest ground covering plants, still popular in Germany.

6. Summary: the place of the sacred in the design of the space and gardens of the historical mental hospitals

The sacred was present in multiple ways in the design of the space and gardens of the psychiatric hospitals of the late 19th and early 20th centuries. First and foremost, churches and chapels had their significant place in them. Characteristic sites included the funerary chapels

combined with mortuaries, where the rites of passage were held. Together with the chapels, the cemeteries of the institutions belong to the sacred landscape harmonised with nature, whose gentle wooded forms and simplest geometrical designs favour certain pensiveness accompanying passing away and bereavement.

The results presented above make it possible to discern a number of key types of landscape imbued with the spiritual dimension.

- ▶ The landscape of successors to the monastic properties was present in the hospitals opened in secularised monasteries, with examples including the first hospital in Lubiąż and the institution in Ravensburg-Weißenau, where the sacred pervades the hospital function, as it results directly from the initial architectural plan and spatial design that were originally driven by the needs of monastic life. In the case of new establishments, there are four main types of spatial relations that portray the significance of sacred places in the design of the psychiatric hospitals.

In the Prussian hospitals from the late 19th century, the sacred was subordinated to the lay function (with hospital chapels composed into administration buildings, as in Berlin-Dalldorf).

- ▶ At the time of pavilion hospitals, the monumental design of the Hospital Am Steinhof is a case of the dominance of the sacred landscape, with the church of the institution towering over the complex with its form and significance, crowning the whole composition and providing a legible reference to the beauty and omnipotence of the Creator;
- ▶ The sacred landscape provides the keystone for landscape design wherever the churches and/or chapels are designed in significant locations in the space, whether on the axes or in central areas, as is the case at Mauer-Öhling, which emphasises the significance of the sacred places in the spatial design of the hospitals;
- ▶ In turn, the churches in the hospitals in Kobierzyn and Eglfing Haar, whose location, architectural form, and the relevant symbolism and design of the environment provide an organic element that is appealingly designed into the space of the hospitals, make reference to the everyday local landscape thus providing examples of the familiar sacred.

References

- [1] Bręczewska-Kulesza D., *Zespół Wojewódzkiego Szpitala Psychiatrycznego dla Nerwowo i Psychicznie Chorych im. dr Józefa Bednarza w Świeciu*, inset into the fiche of a historic site, typescript in the collection of the Delegation of the Office for Heritage Protection of the Kujawsko-Pomorskie Region in Toruń.
- [2] Caltana D., *Psychiatrische Krankenanstalten in der Provinz der Monarchie: Görz und Triest*, [in:] *Psychopraxis* (Springer), No. 5, November 2008, 10–18.
- [3] Chaplin R., Peters S., *Executives have taken over the asylum: the fate of 71 psychiatric hospitals*, [in:] *Psychiatric Bulletin*, 2003, Vol. 27, 227–229.
- [4] Collins P., *Changing Ideals in Modern Architecture: 1750–1950*, McGill University Press, London and Montreal 1965, 42–43.



- [5] Czyżewski A., Howard E., *Trzewia Lewiatana. Miasta ogrody przyszłości*, Państwowe Muzeum Etnograficzne, Warszawa 2009.
- [6] *Die Stadt außerhalb: Zur Architektur der ehemaligen Niederösterreichischen Landes-Heil- und Pflgeanstalten für Geistes- und Nervenranke Am Steinhof in Wien*, eds. C. Jäger-Klein, S. Plakolm-Forsthuber, Birkhäuser, Wien 2015.
- [7] Hevesi L., *Altkunst - Neukunst: Wien 1894–1908*. Konegen, Wien 1909, Reprint: Wiederhrsg. u. eingeleitet von Otto Breicha. Ritter, Klagenfurt 1986
- [8] Hickman C., *Cheerful Prospects and Tranquil Restoration: The Visual Experience of Landscape as part of the Therapeutic Regime of the British Asylum, 1800–1860*, [in:] *History of Psychiatry*, Vol. 20 (4), December 2009, 425–441.
- [9] Hickman C., *Therapeutic landscapes. A history of English hospital gardens since 1800*, Manchester University Press, Manchester 2013.
- [10] Holborow W., Taylor S., *Reusing historic hospitals*, [in:] *CONTEXT 72 : DECEMBER 2001*, The Institute of Historic Building Conservation, also published online: http://www.ihbc.org.uk/context_archive/72/hospitals/reuse.html (access: 2.03.2015).
- [11] Jetter D., *Zur Typologie des Irrenhauses in Frankreich und Deutschland (1780–1840)*, F. Steiner Verlag, Wiesbaden 1971.
- [12] *Kaiser Franz-Josef- Landes-, Heil- und Pflgeanstalt Mauer-Öhling*, [in:] *Der Architekt. Wiener Monatshefte für Bauwesen und Dekorative Kunst*. IX. Jahrgang 1903, 39–42 and 95–98.
- [13] *Kasaty klasztorne na obszarze dawnej Rzeczypospolitej Obojga Narodów i na Śląsku na tle procesów sekularyzacyjnych w Europie (XVIII–XX wiek)*, ed. M. Derwich, Wrocławskie Towarzystwo Miłośników Historii, Wrocław 2012.
- [14] Kiejna A., Wójtowicz M., *Prowincjonalny Psychiatryczny Zakład Lecznico-Opiekuńczy w Lubiążu, 1830–1912/Provinzial Heil- und Pflgeirrenanstalt zu Leubus/Schlesien: 1830–1912*, Fundacja Ochrony Zdrowia Psychicznego, Wrocław 2002.
- [15] Kretschmer M., *Die Weissenau. Geschichte und Erinnerungen. Psychiatrisches Krankenhaus von 1945 bis 1990*, Verlag Psychiatrie und Geschichte, Zwiefalten 2002.
- [16] *Kraków – Kobierzyn, ul. Babińskiego 29, Zespół Szpitala Psychiatrycznego. Studium urbanistyczno-konserwatorskie*, L. Danilczyk et al., PKZ Oddział w Krakowie, Kraków 1988, typescript in hospital archive.
- [17] Kurdiovsky R., *Die Anstaltskirche Otto Wagners – Idealvorstellungen am Präsentierteller*, [in:] Jäger-Klein C., Plakolm-Forsthuber S. (ed.), *Die Stadt außerhalb...*, 95–106.
- [18] *L’Ospedale psichiatrico di San Giovanni a Trieste: storia e cambiamento 1908–2008*, ed. D. Barillari, Electa, Milan, Trieste 2008.
- [19] Michas U., *Hermann Blankenstein, der vergessene Baumeister*, [in:] *Die Mark Brandenburg*, Heft 76, Berlin 2010.
- [20] Milewski J., *Stulecie szpitala w Kocborowie*, Starogard Gdański 1995.
- [21] Rutherford S., *Landscapes for the mind and body*, [in:] *CONTEXT 72: DECEMBER 2001*, The Institute of Historic Building Conservation, also published online: http://ihbc.org.uk/context_archive/72/landscapes/hospital.html (access: 2.03.2015).

- [22] Rutherford S., *Landscapers for the Mind: English Asylum Designers, 1845–1914*, [in:] *Garden History*, Vol. 33, No. 1 (Summer, 2005), 61–86.
- [23] Rutherford S., *The Victorian Asylum*, Bloomsbury Publishing PLC, 2008.
- [24] Schrank S., Ekici D., *Healing spaces, modern architecture, and the body*, Routledge, Taylor & Francis Group, London–New York 2017.
- [25] Staniewska A., *Zagrożenia parków i ogrodów towarzyszących dawnym szpitalom psychiatrycznym w Polsce*, [in:] *Dziedzictwo zagrożone, ogrody historyczne w Polsce*, K. Hodor, K. Łakomy (ed.), Monografia, Architektura No. 491, Politechnika Krakowska, Kraków 2015, 102–120.
- [26] Staniewska A., *Miejsca upamiętnienia akcji T4 jako przykład współczesnej interwencji w historycznych założeniach parkowych szpitali psychiatrycznych przełomu XIX i XX wieku/ Akcja T4 memorials: one type of contemporary interventions in historical 19th/20th century psychiatric hospital parks*, [in:] *Teka Komisji Architektury i Urbanistyki, Oddział PAN w Krakowie, Tom XLV (2017)*, Kraków 2017, 217–232, online: http://teka.pk.edu.pl/wp-content/uploads/2017/12/Teka-2017_14_MIEJSCA-UPAMI%C4%99TNIENIA-AKCJI-t4.pdf (access: 12.02.2018)
- [27] *The Prussian Finance Edict of 1810, signed by State Chancellor Hardenberg and King Frederick William III* (October 27, 1810) (online: http://ghdi.ghi-dc.org/docpage.cfm?docpage_id=3799, access: 20.06.2018)
- [28] Tichy J., *Historie bohnické psychiatrie v letech 1903–2005*, Galén, Praga 2006.
- [29] Topp L., *Otto Wagner and the Steinhof Psychiatric Hospital: Architecture as Misunderstanding*, [in:] *The Art Bulletin*, Vol. 87, No. 1 (March 2005), 130–156.
- [30] Topp L., *Complexity and Coherence: The Challenge of the Asylum Mortuary in Central Europe, 1898–1908*, [in:] *Journal of the Society of Architectural Historians*, Vol. 71 No. 1, March 2012, 8–41, DOI: 10.1525/jsah.2012.71.1.8.
- [31] Topp L., *Freedom and the Cage. Modern Architecture and Psychiatry in Central Europe, 1890–1914*, PSU Press, University Park Pennsylvania, 2017.
- [32] Wójtowicz M., *Zakłady psychiatryczne w Langenhorn, Wiesloch i Lubiążu – komplementarne zespoły urbanistyczne*, [in:] *Architectus*, Nr 2(42), Oficyna Wydawnicza Politechniki Wrocławskiej, Wrocław 2015, 41–54.
- [33] Yanni C., *The Architecture of Madness: Insane Asylums in the United States*, University of Minnesota Press, Minneapolis 2007.

Agnieszka Wójtowicz-Wróbel  orcid.org/0000-0003-4087-395X

awojtowicz@pk.edu.pl

City Renewal Division, Institute of City and Regional Design, Faculty of Architecture,
Cracow University of Technology

SPATIAL SIGNIFICANCE OF NEW MUNICIPAL ENGINEERING STRUCTURES – THE CASE OF ITALIAN ECO-INCINERATION PLANTS

ZNACZENIE PRZESTRZENNE NOWYCH OBIEKTÓW TECHNICZNEGO ZAPLECZA MIAST – PRZYKŁAD WŁOSKICH EKOSPALARNI

Abstract

One of the indications of pro-environmental change is the construction of thermal waste processing plants, which occupy an excessive amount of space and are controversial structures in terms of public perception; however, they also create new potential possibilities for the areas in which they are placed. The objective of this study is to address the issue of the spatial significance of thermal waste processing plants from the points of view of accessibility, location and relations with the urban tissue; their architectural and visual significance within the environments they occupy is also considered. The study covered twelve Italian thermal waste processing plants located in varying spatial, economic and social conditions. The results of field analyses and the conclusions drawn from them can serve when conducting comparative studies of other structures of this type, both in Italy and further afield.

Keywords: thermal waste processing plants, industrial plants, pro-environmental structures, accessibility, industrial zones, metropolitan area, ecological city, eco-technology, circular economy

Streszczenie

Jednym ze znaków współczesnych proekologicznych przemian jest budowa zakładów termicznego przekształcania odpadów. Ekospalarnie, ze względu na swe gabaryty, mocno oddziałują na przestrzeń, są obiektami kontrowersyjnymi w odbiorze społecznym, lecz także stwarzają potencjalnie nowe możliwości dla stref, w których są lokalizowane. Celem niniejszego artykułu jest znalezienie odpowiedzi na pytanie, jakie znaczenie przestrzenne mają zakłady termicznego przekształcania odpadów w trzech ujęciach: dostępności, lokalizacji i relacji z miejską tkanką, a także jakie jest ich znaczenie architektoniczne i wizualne w przestrzeni. Badaniem objęto ekospalarnie znajdujące się w różnych uwarunkowaniach przestrzennych, gospodarczych czy społecznych. Otrzymane wyniki analiz terenowych i wyciągnięte na ich podstawie wnioski mogą posłużyć podczas prowadzenia badań porównawczych innych obiektów tego typu, zarówno na terenie Włoch, jak i poza granicami tego kraju.

Słowa kluczowe: zakłady termicznego przekształcania odpadów, obiekty przemysłowe, obiekty proekologiczne, dostępność komunikacyjna, strefy przemysłowe, obszar metropolitalny, miasto ekologiczne

1. Introduction

Increasing awareness of the necessity of protecting the natural environment sets new challenges before the residents of contemporary cities of the European Union, their authorities, as well as their designers. The necessity of protecting natural resources, ecosystems, as well as (or perhaps – from the point of view of the everyday life of a city resident – primarily) the necessity of reclaiming natural goods that have already been used by man is still a problem that becomes more and more topical. Awareness of increasing environmental pollution and of the exploitation of resources in a manner that is non-compliant with the precepts of sustainable development and the circulation economy generates two necessary actions that need to be taken in the public sphere:

- ▶ the ecological education of residents, right from the very start (pro-ecological kindergarten and primary-school-level education, etc.),

as well as:

- ▶ the adoption of pro-environmental stances on the matter of the protection of resources (e.g. raising the awareness of residents about the use of running water, etc.), as well as the reuse of resources (particularly focusing on the appropriate segregation of waste, so that only a very small amount will have to undergo thermal processing).

From the point of view of persons in charge of the management of cities, the rising problem of protecting natural heritage is also a manner of adapting municipal efforts to community policies which, on the one hand, introduce requirements concerning the adaptation of a city's economy, systems and legal documents, while on the other provide opportunities to benefit from European Union subsidies in terms of the protection of the environment and appropriate resource management. One of such possibilities is funding the construction of structures with new, pro-environmental functions from the European Union's budget. The construction of such structures is also a challenge to cities in social, economic and image-related (in the broader sense of the word) terms, as well as spatial ones. New possibilities of the development of pro-environmental technologies provide new opportunities, but also place new challenges before planners, urban designers and architects. Structures such as currently built thermal waste processing plants can and already are ecologically safe buildings. Following the examples set in other countries, municipal engineering structures do not need to focus solely on fulfilling a technical function, one that is associated with negative public reception. Currently built eco-incineration plants can be a challenge to an architect, urban designer and planner; in addition to constituting a social and spatial element, both from the architectural point of view, as well as in the field of spatial management.

This study is an extension of a research cycle of publications written by the author concerning structures with new pro-environmental functions within urban space. The author's research focuses on two groups of pro-environmental structures:

- ▶ thermal waste processing plants,
- ▶ wastewater treatment and water purification plants.

The research is being performed with a focus on a group of five types of problems:

- ▶ the social sphere, with a particular focus on influence on the space of cities,
- ▶ the architectural sphere and the broadly understood beauty of structures,
- ▶ the sphere of placement and accessibility,
- ▶ the sphere of spatial relations and significance within the urban tissue, in addition to –
- ▶ technical and technological matters that can directly affect the spatial sphere.

Furthermore, the cycle is being supplemented by examples of good practice, as well as analyses of cases of pro-environmental efforts. This article is one of the examples of such analyses in reference to the urban structure.

2. Thermal waste processing plants in Italy – an outline of the background and field of research

Italy is one of those European countries that have faced the challenge of searching for a fast and effective solution to the management of an increasing amount of municipal waste, and which also had to find the answer to the question concerning the manner of the adaptation of contemporary municipal waste management in such a manner so that it can be compliant with European Union regulations [1, 3]. The intensification of this problem was particularly observable in the first decade of the twenty-first century. At the time, the problem of the management of Italy's waste did not apply solely to municipal waste, but to – perhaps especially – industrial waste and its appropriate storage and neutralisation.

New forms of waste management started to be sought in the northern part of the country. This was a result of not only the necessity to process municipal waste, but primarily of the need to search for a solution to the problem of industrial waste with varying levels of threat to the environment. Simultaneously, in the southern and central parts, there arose the problem of depositing waste (including dangerous waste illegally buried as municipal waste) on landfills, as well as of the illegal depositing of waste on unauthorised waste dump sites, which were then being set aflame [2]. At the same time, the storage of dangerous materials in this manner caused a significant rise in soil, air and water pollution in agricultural areas, which constituted the basic source of income for many of the residents of those regions.

The lack of the possibility to deposit municipal waste in such cities like Naples (due to a lack of space in landfills), the aforementioned environmental pollution and failed attempts at solving this problem, like making decisions concerning the placement of new waste disposal sites in protected areas (e.g. in the national park at the foot of Mount Vesuvius), as well as the epidemiological threat associated with not removing waste from cities (e.g. from Naples) led to social and ecologically-based tensions [5]. One of the effects of the search for an effective solution to the problem of waste management was the construction of thermal waste processing plants. This was tied with both the redevelopment of existing incineration plants and the construction of new structures of this type in the spirit of environmentally-friendly solutions.

The redevelopment of existing plants was often a change focused not only on modernising their technology and adapting the architectural form of the structures themselves to new

installation solutions. It included and still includes much broader measures: their extension, the introduction of a greater number of technological lines, the implementation of new ways of processing municipal waste, but also the introduction of the possibility of incinerating waste of a different type (industrial, RDF and other types), in addition to a fuller utilisation of the energy that is produced (connecting the plants to the municipal power grid, etc.).

Italy is one of those European Union member states that solve the problem of municipal waste with great intensity and we can clearly see the effects of measures taken in terms of municipal and regional policy in this field. Currently, there are 59 thermal waste processing plants in Italy [5] that produce energy used in municipal power grids. These are both incineration plants that process municipal solid waste, as well as those that process other types of it (RDF, industrial waste, etc.). It is noteworthy that over 54% of the structures that have been mentioned began operating after the year 2000.

According to the concept of the circulation economy [7], thermal waste processing is the final element in this field, employed only when all other possibilities of reusing a resource have been exhausted. From a technological standpoint, these are mostly installation utilising movable grate technology, which is currently the most widely used, and is seen as the most proven and reliable in current conditions [4]. Apart from this method, Italian incineration plants also utilise the gasification method or a mixed technology, which features one technological line processing waste using a movable grate, while the other uses gasification or a different method. Of note is also the fact that even in the case of mixed technologies, one line always utilises the proven movable grate technology [6].

3. Scope and method of research

From the perspective of the shaping of the city, new technologies of waste management lead to the necessity of searching for new spatial solutions. At the same time, structures serving this purpose are buildings with technological lines that are safe to the natural environment, friendly to their surroundings and create new possibilities of using the structures themselves. For this reason, their significance in the space of cities over the period of the past couple of decades has been significantly altered. They are structures that, apart from their basic role of waste processing, can feature other, additional functions, improving the attractiveness of the place in which they are located. However, when searching for the answer to the question concerning which of these structures can play a significant role within the urban tissue, it is important to determine their location, accessibility, as well as their visual significance as works of architecture.

In order to answer this question, twelve thermal waste processing plants in Italy were analysed. They are located in the areas surrounding the following localities: Acerra (near Naples), Arezzo, Bergamo, Bolzano, Brescia, Forlì Casena, Gioia Tauro, Padua, Parma, Poggibonsi, Riccione near Rimini, as well as Trezzo sull'Adda. The group of structures that were analysed included both those that had been redeveloped (which in past decades had operated on the basis of environmentally unfriendly technologies, and that are currently adapted to

contemporary standards of environmental protection, often expanded and architecturally transformed), as well as those which have been built in recent years as pro-environmental plants from the ground up.

The group includes both structures located in the northern part of Italy, which features intensive industrial development (e.g. Bolzano or Bergamo), as well as those located in the south (e.g. Acerra, near Naples) – a much less developed region of the country, which has in recent decades been troubled by problems of an ecological, economic and social nature. Both thermal waste processing plants which provide services to agricultural areas and the small towns located within them (e.g. Gioia Tauro) and those which focus on the processing of municipal solid waste of large urban centres like Naples or Milan were chosen for analysis. An overview of the placement of the analysed structures within the country has been presented in Fig. 1.



Fig. 1. Placement of the analysed thermal waste processing plants in Italy (original work, 2018)

The research that was performed focused on three groups of problems: the accessibility of the plants, their architectural attractiveness and visual significance within their surroundings, as well as their placement in relation to broadly understood urbanisation units.

a) Accessibility

Although the purposefulness of studying the problems of the placement of thermal waste processing plants within urban structures or the architectural qualities and visual impact of these types of structures on space appears to be obvious, the study of accessibility can raise some doubt as to their purposefulness. Eco-incineration plants are not public or commercial service buildings, which is why studying their accessibility – in the current situation – can raise some doubt. Accessibility, however, is a key element that conditions the possibility of the development of new functions, and in many of the studied structures such functions are either



already present or are planned to be introduced in the immediate future. These are primarily functions associated with ecological education: from the organisation of educational paths to the planning of regular lectures, classes or courses, ranging from the level of primary education (classes for children promoting pro-environmental attitudes in everyday life) to specialist seminars or professional courses. In the case of such planned efforts accessibility or a lack thereof is a key element, significantly affecting the chances of the success of such endeavours.

The accessibility of the plants was measured in a number of ways: using an individual mode of transport (a car), public transport (which utilised various modes of transport depending on the city, in addition to using combined circulation), as well as the bicycle. The possibility of getting to the plants on foot was also investigated. A listing of the results of the research has been presented in table 1.

A five-point rating scale was adopted during the measuring of accessibility, on which “A” signified the highest accessibility, while “E” the lowest accessibility. An additional mark signifying a lack of accessibility using a given mode of transport (“-”) has also been introduced. The isochrone was adapted to the given mode of travel each time, as well as to the hours during which the measurements were taken. In the case of the car and public transport, accessibility was measured at different time intervals – during the periods of the lowest and the highest loads being placed on the transport network.

Table 1. Accessibility of thermal waste processing plants

Location of the thermal waste processing plant	Car		Public transport		Accessibility using a bicycle	Pedestrian accessibility
	Accessibility (min.) during the given traffic load on the transport network		Accessibility (min.) during the given traffic load on the transport network			
	Highest	Lowest	Highest	Lowest		
<i>Acerra (Naples)</i>	A	A	-	-	B	E
<i>Arezzo</i>	B	B	C	D	B	E
<i>Bergamo</i>	A	B	B	C	C	E
<i>Bolzano</i>	A	A	B	D	B	E
<i>Brescia</i>	A	A	B	C	B	E
<i>Forli Casena</i>	B	A	B	-	B	E
<i>Gioia Tauro</i>	A	A	-	-	B	E
<i>Padua</i>	B	B	B	C	B	E
<i>Parma</i>	B	A	D	-	A	E
<i>Poggibonsi</i>	A	A	A	-	B	E
<i>Riccione (Rimini)</i>	A	A	B	-	A	E
<i>Trezzo sull'Adda</i>	A	A	B	-	A	D

A/B/C/D/E – accessibility rating on a five-point scale, ranging from the highest (A), to the lowest (E)

Tab.1. Accessibility of selected thermal waste processing plants in Italy (original work, 2018)

In the first case, accessibility was measured in the morning (8:00–9:00) and afternoon (16:00–17:00) hours, during the time when commuting to and from work intensifies, while in the second case, the measurement was performed only once – between 24:00 and 01:00. The measurement was performed using the quickest possible route from a given plant to its city's main transfer node. This made it possible to compare the results of the analyses for numerous cities. For travel using a car during the greatest traffic load being placed on the circulation network, the following values for each isochrones were adopted, listed from the highest to the lowest accessibility: “A” (up to 15 minutes), “B” (15–30 minutes), “C” (30–45 minutes), “D” (45–60 minutes) and “E”, with a travel time exceeding one hour.

At the same time, for measurements taken outside of rush hour, the following values were adopted: “A” (up to 10 minutes), “B” (10–20 minutes), “C” (20–30 minutes), “D” (30–45 minutes) and “E”, above 45 minutes. As it has been mentioned earlier, accessibility using public transport was also measured in two extreme periods of temporal accessibility, and in this case, a five-point rating scale was adopted using the same principle. Accessibility using the bicycle or pedestrian accessibility was measured once throughout the day, because the load placed on the circulation network had no effect on the results, for obvious reasons. A five-point scale was also used. In the case of travelling by bicycle, the isochrones were adopted as follows: “A” (up to 10 minutes), “B” (10–20 minutes), “C” (20–30 minutes), “D” (30–45 minutes) and “E”, over 45 minutes. At the same time, pedestrian accessibility with a travel time of 5 minutes was considered the highest (A), within an interval of 5–10 minutes considered very good (B), 10–20 minutes was considered average (C), 20–30 was low (D), with very low being above 30 minutes (E).

b) Location

In order to determine the spatial relations that thermal waste processing plants either have or can have on the example of the analysed group of selected plants, an analysis of their surroundings was performed from an urban planning perspective. The research concerning the placement of the plants in relation to the more important elements of the urban tissue has been presented in table 2.

Twelve thermal waste processing plants were subjected to an evaluation in relation to four types of elements of an urban structure: residential buildings, industrial buildings, commercial service buildings and their accessibility, as well as open areas. The analysis of the spatial relations with residential buildings was important mainly due to social concerns, as the placement of thermal waste processing plants close to housing areas is the subject that generates the greatest amount of emotions in the public eye. In the residential buildings group, the analysis focused on the placement of dense multi-family residential complexes (M1) and dense complexes of single-family houses. Loosely placed single-family building complexes were also listed (M3)¹. Thermal waste processing plants located outside of housing areas were listed as well.

Eco-incineration plants were quite often placed in areas of an industrial character, which is why they were included in the analysis. The list includes placement inside an area (or directly

¹ Loosely placed multi-family residential buildings were not present in the vicinity of any of the plants, which is why they have not been included in table 2.

Table 2. Placement of thermal waste processing plants

Location of thermal municipal solid waste processing plants	Residential buildings	Industrial buildings	Commercial service buildings	Open areas
<i>Acerra (Naples)</i>	<i>M4</i>	<i>P1</i>	<i>U4</i>	<i>O4</i>
<i>Arezzo</i>	<i>M3</i>	<i>P1</i>	<i>U2</i>	<i>O1</i>
<i>Bergamo</i>	<i>M1,M2</i>	<i>P1</i>	<i>U2,U3</i>	<i>O3</i>
<i>Bolzano</i>	<i>M4</i>	<i>P2</i>	<i>U2</i>	<i>O1</i>
<i>Brescia</i>	<i>M1,M2,M3</i>	<i>P3</i>	<i>U3</i>	<i>O2</i>
<i>Forli Casena</i>	<i>M3</i>	<i>P1</i>	<i>U2</i>	<i>O3</i>
<i>Gioia Tauro</i>	<i>M3</i>	<i>P2</i>	<i>U4</i>	<i>O1</i>
<i>Padua</i>	<i>M1,M2</i>	<i>P1</i>	<i>U2</i>	<i>O3</i>
<i>Parma</i>	<i>M4</i>	<i>P1</i>	<i>U1</i>	<i>O4</i>
<i>Poggibonsi</i>	<i>M4</i>	<i>P1</i>	<i>U2,U3</i>	<i>O2</i>
<i>Riccione (Rimini)</i>	<i>M3</i>	<i>P1,P2</i>	<i>U1</i>	<i>O2</i>
<i>Trezzo sull'Adda</i>	<i>M1,M2</i>	<i>P1</i>	<i>U2</i>	<i>O2</i>

Due to the detailed description, the explanation of the individual symbols used in the table has been placed in the text.

Tab.2. Placement of selected thermal waste processing plants in Italy (original work, 2018)

adjacent to one) of an intensively developing industrial zone (P1), in areas featuring individual buildings that do not form an industrial zone in urban-planning-related terms (P2), as well as outside of areas of an industrial character (P3). Table 2 also lists the accessibility of varying types of commercial services as an element which improves the attractiveness of a space. This group lists both different types of commercial services, the intensity of their presence, as well as the intensity of the spatial relations themselves. The placement of eco-incineration plants directly inside areas with commercial services (H1), in the vicinity of such areas (H2), as well as in areas with a low presence of commercial buildings associated with industry (H3) or housing (H4) has been listed. The final group (H5) includes those eco-incineration plants that were located outside of areas with immediate access to services. During the development of the research method, a listing for public services located in the immediate vicinity of thermal waste processing plants was present in the analysis, however, no such relations were observed in any of the twelve cities that were analysed.

In the group of analyses referring to relations with open areas, five possible marks were listed: three concerning the direct placement of a thermal waste processing plant and two referring to access to open areas in areas without direct access to them. Concerning plants located in the immediate vicinity of such areas, the list includes eco-incineration plants located within open areas (agricultural, woodland, other - O1), structures located in the immediate vicinity of built-up areas (industrial, residential, etc. - O2), as well as structures placed in open areas that are assigned for intensive development and expansion (e.g. of an industrial area - O4). In addition,

the list also includes structures placed in places where open areas are located at a relatively close distance away (O3). Initially, the research was to take into account cases in which there were no open areas in the vicinity of the plants, however, the listing featured no such cases.

c) Architecture and visual impact within a space

Due to changes in technology and a greater awareness of the significance of pro-environmental structures, thermal waste processing plants are one of those sites, which have, over the past several decades, undergone considerable changes concerning their architectural form. This is particularly noticeable in the listing of buildings built over the last decade and of those buildings which were built in the second half of the previous century. The results of the research concerning aesthetic matters and the architectural evaluation of the buildings have been presented in table 3.

Table 3. Evaluation of the visual significance and architectural qualities of thermal waste processing plants.

Location of the thermal waste processing plants	Architectural qualities rating	Visual significance withiihn a space/ impact	Rating of the aesthetic and compositional qualities of the development of the site
<i>Acerra (Naples)</i>	<i>A</i>	<i>B</i>	<i>B</i>
<i>Arezzo</i>	<i>D</i>	<i>B</i>	<i>B</i>
<i>Bergamo</i>	<i>D</i>	<i>B</i>	<i>D</i>
<i>Bolzano</i>	<i>A</i>	<i>A</i>	<i>B</i>
<i>Brescia</i>	<i>B</i>	<i>A</i>	<i>A</i>
<i>Forli Casena</i>	<i>C</i>	<i>B</i>	<i>C</i>
<i>Gioia Tauro</i>	<i>E</i>	<i>C</i>	<i>E</i>
<i>Padua</i>	<i>A</i>	<i>A</i>	<i>C</i>
<i>Parma</i>	<i>A</i>	<i>A</i>	<i>A</i>
<i>Poggibonsi</i>	<i>C</i>	<i>E</i>	<i>D</i>
<i>Riccione (Rimini)</i>	<i>A</i>	<i>C</i>	<i>D</i>
<i>Trezzo sull'Adda</i>	<i>D</i>	<i>C</i>	<i>D</i>

A/B/C/D/E – visual significance and architectural qualities rating on a five-point scale, from the highest (A), to the lowest (E).

Tab. 3. Evaluation of the visual significance and architectural qualities of selected thermal waste processing plants in Italy (original work, 2018)

The analysis was conducted in three groups, referring to the different types of problems concerning the aesthetics of space. The architectural and compositional qualities of the plants' buildings were rated on a five-point scale, ranging from those of the highest quality (A), to those that featured a lack of aesthetic and compositional qualities (E). Due to the size of the thermal waste processing plants, an analysis of their visual significance in their surroundings, as well as of the impact of the buildings in both close and distant views was included as well.

A five-point scale was analogously used to rate architectural qualities. The final element of the analysis presented in table 3 was the evaluation of the aesthetic and compositional qualities of the plants' site development. Elements taken into consideration included both the composition of the entirety of a building's surroundings within the borders of its site, its structuring, elements of streets furniture or the composition of greenery.

4. Discussion and commentary on the results of the study

The analysis of twelve thermal waste processing plants located in Italy provided a basis for the formulation of initial conclusions concerning the accessibility of such structures to city residents and others, the relations between eco-incineration plants and their surroundings within the area of the influence of cities of varying size, as well as for the rating of these types of plants from an architectural perspective. Based on the results that have been listed in table 1, we can compare the accessibility of each structure while using various means of transport. Regardless of the amount of load placed on the transport network, accessibility by car was observed to be within the upper ratings. During the period of the highest load on the transport network, over 60% of the plants were observed to have the highest degree of accessibility (A), while the remaining had a very good degree (B). During the period of the lowest load being placed on the road network, the degree of accessibility was observed to increase and three-quarters of all of the analysed structures noted the highest degree of accessibility.

A slightly lower accessibility was noted only in the case of three plants, located in Padua, Bergamo and Arezzo, but they nevertheless did have a relatively short travel time (B rating). When analysing travel time using public transport, it was observed that during rush hour over half of the plants were still accessible to a satisfactory degree, while in two cases this accessibility dropped significantly (Parma and Arezzo), while two plants were not accessible by public transport at all. These were Gioia Tauro, which is located far away from large cities, as well as the eco-incineration plant in the locality of Acerra, which is tasked with the incineration of solid waste from Naples, and which is also located in an area that is outside of the reach of public transport. Accessibility through public transport during the period of the lowest traffic intensity was observed to be highly limited due to the fact that the measurements were performed during night time.

Over half of the structures were unreachable during that time, as the areas in which they are located did not have public transport provided during those hours. Such access was provided to the remaining five structures, however, it varied between low accessibility ("C" rating – 3 plants) and very low accessibility ("D" rating – 2 plants). Of note is the fact that there is no need for such plants to be accessible during night time, and the analysis of the travel time by car during nighttime hours (the same travel route) during the period of the lowest traffic intensity is proof enough of the potential that can be utilised in this regard. From among all of the categories of the analyses of the twelve thermal processing plants, pedestrian accessibility was rated the lowest. Only the eco-incineration plant located in Trezzo sull'Adda placed itself in the 20–30 minute isochrone ("D" rating). Travel on foot to all of the remaining plants took

more than 30 minutes (“E” rating), while only the eco-incineration plant in Brescia found itself in the timeframe of between 30 and 40 minutes, while all of the remaining plants can be reached after an hour or one and a half an hour of walking.

When analysing the types of residential buildings located in the vicinity of the selected thermal waste processing plants, it was observed that a comparable amount of plants was located in the vicinity of dense complexes of multi-family and single-family residential buildings, as well as among loosely placed buildings, in addition to being outside of any and all housing areas. Simultaneously, more than one type of buildings was possible to identify in the vicinity of four of the plants - these were most often dense complexes of single and multi-family residential buildings (Bergamo, Padua and Trezzo sull’Adda), while in one case, apart from dense complexes of buildings of various types, there were also complexes of loosely placed single-family residential buildings (Brescia). The eco-incineration plant in Brescia was also the only plant located far away from industrial buildings. Three quarters of the analysed thermal waste processing plants were located in intensively developing industrial zones, while only three were located in areas with loosely placed individual structures of this character, out of which the eco-incineration plant in Riccone near Rimini was located at the border of two of the abovementioned types of areas (P1 and P2). Analyses of accessibility to commercial services and their various types which can increase the attractiveness of the area in which a given eco-incineration plant is located showed that two structures were located in areas outside of the range of access to any services whatsoever.

These include Gioia Tauro, which is located in a seaside area, close to an industrial and cargo port, as well as the newly-built eco-incineration plant in Acerra, which provides services to Naples. Services were observed to be located in the vicinity of the remaining plants, however, most of them were individual buildings associated with providing services to the industrial sector or a residential area located nearby, while in only two cases were there any dense commercial service complexes to speak of. These included the eco-incineration plant in Parma, which was located near a complex of big box stores, as well as the incineration plant near Rimini (Riccone), which, apart from the close proximity of retail buildings (the Raibano zone, Raibano I and Raibano II) was located close to a recreational area (aquapark, theme park, etc.).

When analysing the accessibility of various types of open areas and their placement relative to thermal waste processing plants, it was observed that the accessibility of such areas was shaped in the following manner: the largest group was formed by those structures which were located at the border between open and built-up areas. A slightly smaller group was formed by eco-incineration plants placed in open areas (agricultural areas, meadows or woodland), or those in which open areas were located relatively close by. Another group that was of no smaller size were those plants which were located near intensively developing industrial zones and the physical changes of the development of these areas will probably take place in the next couple of years. However, when analysing the set of the plants being discussed, we can generally observe that quantitative differences between each of the types (O1, O2, O3 and O4) listed in table 2 are insignificant, so any advantage in numbers in terms of the occurrence of some areas in relation to others would probably change after taking into consideration a larger group of cases, or if a different selection of such were performed.



Aesthetic matters have been characterised in table 3 and were rated on a five-point scale in each of the groups. The evaluation of architectural qualities and values saw 50% of the plants rated either highly or very highly, while only one plant was rated as having no architectural values – being negative in its visual reception (Gioia Tauro – Fig.2).



Fig. 2. Eco incineration plant – Gioia Tauro (original work, 2017)

The highest rated plants were those that were built in recent years, in the case of which there was a visible tendency for the shaping of the massings of the eco-incineration plants to not only constitute a form of an envelope for their technological solutions, but also attractive architectural forms. The spatial composition of the site on which a thermal waste processing plant was located was also an essential element. In five cases aesthetic and compositional qualities were rated very highly or highly and there was a visible correlation between the attractiveness of a structure's massing and care for its surroundings, although the dependency was not present in one hundred percent of cases. In some cases, the attractiveness of a building obtained the highest rating, while its surroundings were rated much lower.

One example of this was the eco-incineration plant in Riccone (Rimini-fig.3), where the plant possessed an attractive massing, with some elements constituting references to Italian architectural traditions (the envelopes of the smokestacks resembled campanile), while the surroundings of the plant were sorely lacking not only in compositional terms, but also concerning their structure. Due to their size, thermal waste processing plants can significantly affect their surroundings. From among the twelve plants, eight were rated as having a visual impact that was either significant or highly significant. Only one structure was rated as having an

insignificant impact on its surroundings. It was the thermal waste processing plant in Poggibonsi, which was located in an area with terrain features and natural and landscape conditions that caused its visual significance to the surrounding space and its impact to be negligible.



Fig. 3. Eco incineration plant – Riccone, near Rimini (photo by A. Wójtowicz-Wróbel, 2017)

5. Summary and conclusions

Italy is one of those countries which are undergoing a rapid and necessary change of the manner in which they manage waste towards an approach that is friendlier to the environment and compliant with the requirements of the European Union. Due to this fact, a selected group of structures – located in different spatial conditions and that were built in different periods, yet due to the same need – can prove an interesting field of study for other structures of this type. The analyses of selected thermal waste processing plants in Italy have made it possible to draw the following conclusions concerning three groups of problems:

- ▶ **Accessibility:** Good accessibility using an individual mode of transport is one of the constituents that provide an actual opportunity for the utilisation of the extent potential of thermal waste processing plants. At the same time, the condition that is necessary for these plants to be used for purposes other than their basic, technological ones, is - primarily - good accessibility through public transport (e.g. the possibility for potential attendees to come to a workshop or to use an educational path, etc.). Such accessibility was present in the cases that were discussed. Of note is also good accessibility using a bicycle, which, when coupled with placement in attractive open spaces, creates the opportunity to, for instance, use the structure as an essential element

of urban or suburban bicycle trails (functionally - in the case of additional functions, or visually - as a landmark within the landscape).

- ▶ **Location:** A considerable majority of thermal waste processing plants is located either in or at the border of industrial areas. These are both dynamically developing and intensely built-up industrial areas, as well as those which are only starting to develop, resembling open areas with randomly placed buildings of an industrial character. At the same time, the vicinity of most eco-incineration plants includes residential buildings, ranging from dense multi-family residential complexes, complexes of row houses, etc. to individual houses either under construction or those that have already been built. It is most often the proximity of residential areas that causes the most controversy in the public eye and is the source of tensions of a social and ecological character.
- ▶ **Architecture and visual impact:** Due to their size, proportions and often also their location (e.g. near a bypass or a road entering the city) thermal waste processing plants are elements which have a strong spatial impact, which is why their architecture, as well as its appropriate highlighting (e.g. by nighttime illumination), is so essential. Placed in areas which are often lacking in terms of attractive architectural works, they can constitute the start of one of the variants of good patterns of designing industrial-type massings. Of note is the fact that structures designed after the start of the twenty-first century were much more often designed as works of architecture, instead of only constituting physical envelopes of technological installations.

References

- [1] Bukowski Z., *Prawo ochrony środowiska w Unii Europejskiej*, C.H.Beck, Warszawa 2007.
- [2] Greyl L., Vegni S., Natalischio M., Cure S., Ferretti J., *The Waste Crisis in Campania, Italy*, www.ceecec.net/case-atudies/waste-crisis-in-campania-italy retrieved on 2010 (access: 01.02.2018).
- [3] Gwiazdowicz M., Sobolewski M., *Ochrona środowiska w polityce UE*, www.orka.sejm.gov.pl (access: 01.04.2018).
- [4] Wielgosiński G., *Przegląd technologii termicznego przekształcania odpadów*, [in:] *Nowa Energia*, ISS 1/2011, 2011.
- [5] Wójtowicz-Wróbel A., *From a vision to a necessity – from a necessity to a vision. Thermal waste processing plants – case study: Italy* (article accepted for publication, [in:] *IOP Conference Series: Materials Science and Engineering*, (World Multidisciplinary Civil Engineering-Architecture-Urban Planning Symposium), Praha 2018.
- [6] *Waste – to – Energy. State of the Art. Report. Statistics, 6th edition*, International Solid Waste Association, 2012.
- [7] European Commission – Environment – Circular Economy Strategy, http://ec.europa.eu/environment/circular-economy/index_en.htm (access: 01.03.2018).

Izabela Czekaj  orcid.org/0000-0001-9322-940X

iczekaj@chemia.pk.edu.pl

Natalia Sobuś  orcid.org/0000-0002-5776-6934

Institute of Organic Chemistry and Technology, Faculty of Chemical Engineering
and Technology, Cracow University of Technology

CONCEPTS OF MODERN TECHNOLOGIES OF OBTAINING VALUABLE BIOMASS-DERIVED CHEMICALS

KONCEPCJE NOWOCZESNYCH TECHNOLOGII POZYSKIWANIA CENNYCH ZWIĄZKÓW CHEMICZNYCH Z BIOMASY

Abstract

In this paper, we present the review of modern technologies for obtaining valuable biomass-derived chemicals, such as furfural, levulinic acid, adipic acid, dihydroxyacetone, lactic acid and acrylic acid. We have included our own research approach using the nano-design of zeolites for the dehydration of lactic acid into acrylic acid.

Keywords: biomass, lignocellulose, zeolites, lactic acid, acrylic acid, adipic acid, furfural, levulinic acid

Streszczenie

W niniejszej pracy przedstawiono przegląd nowoczesnych technologii uzyskiwania cennych związków chemicznych pochodzących z biomasy, takich jak furfural, kwas lewulinowy, kwas adypinowy, dihydroksyacetone, kwas mlekowy i kwas akrylowy. Zaprezentowano również własne podejście badawcze obejmujące projektowanie w skali nanoskopowej zeolitów do odwadniania kwasu mlekowego do kwasu akrylowego.

Słowa kluczowe: biomasa, lignoceluloza, zeolity, kwas mlekowy, kwas akrylowy, kwas adypinowy, furfural, kwas lewulinowy

1. Introduction

Nowadays, crude oil and natural gas are the main sources for the production of fuels and feedstock chemicals. These resources are limited and the application of (renewable) alternatives will be needed in the future to sustain the progress of mankind. A major challenge of society research is to create fuels and chemical intermediates from available and renewable materials that do not compete with food crops for water or fertilizers [1].

Biomass is the one exceptional sustainable source for chemicals and fuels [2]. The U.S. Department of Energy has predicted that 25% of chemicals and 20% of transportation fuels will be prepared from biomass in the next two decades [3]. The main objective of the European Union, as well as other countries, is to make every effort to reduce global warming caused by the processing of fossil fuels. All attempts to protect the environment from the negative effect of economic development are included in the so-called climate packet, which describes the reduction of greenhouse gas emissions as well as developing and implementing efficient and modern technologies [4, 5]. In addition, quantitative targets have been introduced in EU countries until 2020, the so-called “3 x 20%”. It involves a reduction of greenhouse gases by 20% compared to 1990, a reduction of energy consumption by 20% by 2020 and an increase in the use of renewable energy resources to 20% [6]. Recently, technologies using organic waste as a raw material have been dynamically developing, as well as biomass for energy production, which constitutes 67% of primary energy, of which 48.1% is lignocellulosic biomass [7]. As a result of conducting research and creating technologies for receiving products from biomass, a new branch of industry was established – biorefinery [4, 5, 8, 9]. In this perspective, heterogeneous catalysis possesses a tremendous potential for overcoming scientific and engineering barriers, thus rendering feasible and economic bio-based conversion routes [10]. Biomass does not allow a direct extrapolation of petrochemical technologies. The abundant presence of oxygen makes biomass-derived molecules soluble in water, of low volatility, highly reactive, and prone to decomposition at high temperature. In the literature, numerous pathways (dehydrations, oxidations, hydrogenations, hydrogenolysis, isomerizations) are proposed to produce a large number of molecules [6,11]. Nevertheless, transforming these theoretical conversion routes into industrial reality is not straightforward.

2. Lignocellulosic biomass

Biomass from woody plant materials (e.g. corn and wood wastes, grass etc.) is a promising biorenewable feedstock [12]. However, the use of biomass for feedstock production requires a sequence of chemical conversions, which is blocked by the main building: carbohydrates. Recently, global efforts have been underway to convert plant cell walls (which are collectively called lignocellulosic biomass) to biofuels for transportation needs [13–15]. At first, this requires breaking down the lignocellulose nanostructure of biomass. Lignocellulose is built from cellulose crystals embedded in hemicellulose sugars and lignin polyphenols (Fig. 1) [16].

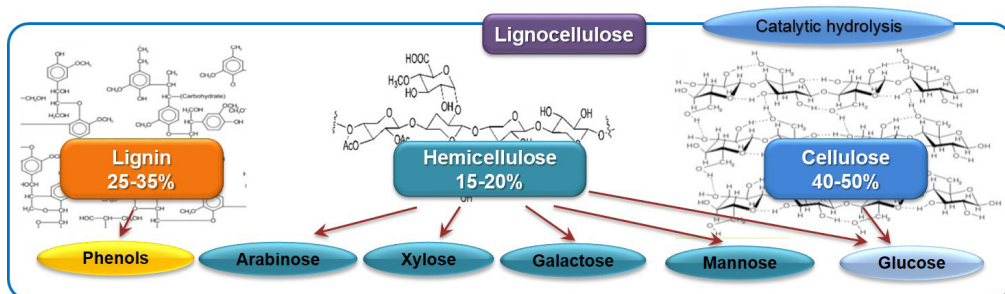


Fig. 1. The chemical composition of lignocellulose and the main products of catalytic hydrolysis [17]

Cellulose is the most abundant and important constituent in plant cell walls. Its crystal structure and complex network with other carbohydrate polymers are key factors determining the mechanical strength and degradability of plant cell walls [18, 19]. Another constituent is lignin, which is removed from wood meal by the paper industry. Lignin is one of the three main biopolymers, together with cellulose and hemicellulose, which builds the cell walls of plants. Lignin consists of aryl ethers, irregularly connected by a variety of linkages [20]. Lignin is taken as a base material to manufacture biopolymers by conventional polymer techniques. A further application field is agriculture; lignin products can be the basis for delayed-action fertilizers, which release nutrients slowly or serve as support for the production of humus in the soil. In view of its chemical composition, lignin is a rich raw material for aromatic (phenolic) compounds with a high added value. In 2004, the pulp and paper industry alone produced 50 million tons of extracted lignin, but only approximately 2% of the lignin available is used commercially, with the remainder used as a low-value fuel [21]. The extraction of lignin from wood is especially difficult.

There are a few explanations for the difficulty in extracting lignin [22]: (i) strong covalent bonds exist between lignin and carbohydrates, (ii) lignin has a high molecular weight and possibly forms a three-dimensional network [23], (iii) hydrogen bonds and physical phenomena, such as solid solution, may be involved in the retention of lignin in the wood-fiber wall. Pretreatment of lignocellulose requires extreme conditions (e.g. temperature, pressure, and reagent, which are toxic for environment). Cellulose is building up the structural substance of unignified cell walls and consists of fibrous macromolecules based on anhydrous *d*-glucose units. Single polysaccharide chains are hydrogen bonded and build microfibrils, which are resistant to hydrolysis. A high degree of polymerization causes orientation, elasticity and a large tensile strength of this carbohydrate. Hemicellulose is also a polysaccharide (such as arabinose, glucose, galactose, mannose and xylose) and consists of different monomers building a random, amorphous structure. Arabinose is aldopentose and mainly a component of hemicelluloses and pectins [17, 23, 24].

The general scheme (Fig. 2) illustrates the processes of fuels, chemicals and energy production from the biomass. The most crucial for the environment are three first steps (Fig. 2, dark blue color): (i) lignocellulose conversion (e.g. via dissolution by ionic liquids or hydrothermal gasification by Ru-catalysts), (ii) methanation by Ni-catalysts, (iii) selective conversion into chemicals (via isomerization, dehydration, oxidation etc. by e.g. zeolites).

All these three classes of processes require various types of catalysts, but they are connected and depend on each other, e.g. methanation and conversion into chemicals processes depend strongly on products mixture of lignocellulose conversion.

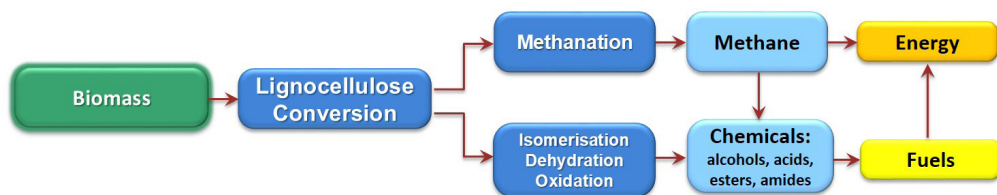


Fig. 2. Scheme illustrating the processes of biomass conversion

3. Zeolites in biomass conversion

Zeolites are very promising materials for biomass conversion into lactates, acrylates and may be valuable products derived from biomass. Zeolites, microporous and crystalline aluminosilicates, are effective catalysts in many applications [6]. The different zeolitic materials are characterized by a variety of micropore structures featuring specific sizes, shapes, and connectivity (Figure 3) as well as possibility to tune acid/base properties. Due to the ability to catalyze many types of hydrocarbon reactions zeolites are ideal candidates for the production of chemicals from biomass [25, 26]. Zeolites are effective three-dimensional supports for active nanoparticles. However, industrial performance and selectivity of microporous zeolites to the desired chemicals at the industrial scale is far from being optimal due to the limited access to the micropores with active basic/acid sites or nanoparticles and diffusion limitations. From the other hand ordered microporous metallosilicates containing auxiliary mesoporosity, have shown improved performance compared to purely microporous zeolites in a wide range of catalyzed reactions. The introduction of mesopores into the microporous zeolite network by selective demetallation has been shown to lead to strong variations in performance and changing the access to the active sites, enhancing catalyst selectivity and activity [27, 28]. Mesopores introduction is known to depend on internal properties of the zeolites (framework type and composition) resulting in a different distribution of mesopores. Structural origin increased mesopore surface area. However, up to now, knowledge about the demetallation process on the atomistic level is almost not existent. One of the major obstacles to unimproved understanding is the difficulty in modeling a complicated structure of zeolites mesopores.

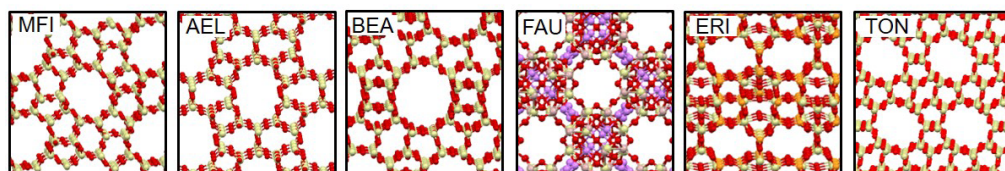


Fig. 3. Differences in natural micropores in various zeolite structures

The mesoporous structuring of conventional zeolites by post-synthetic modification is one of the most efficient means of enhancing their performance in diffusion-limited reactions [6]. The extent and distribution of the introduced mesopores have experimentally been observed to depend strongly on the intrinsic properties of the zeolite [29]. As the catalytic benefits of mesoporosity in zeolites primarily derive from an enhanced molecular transport, the extent and distribution of mesopores created within the zeolite crystals can be expected to have critical implications. Therefore, it is important to understand the structure of micro- and mesopores and their role in: (i) transport properties of adsorbates, (ii) distribution of metallic nanoparticles. Evidently, the molecular-level description of the synthesis and properties of mesoporous zeolites would be highly valuable to rationalize the demetallation behavior of zeolites. However, the complex structure of zeolites, particularly when integrating non-periodic mesopores, and the difficulty in accounting for their interaction with aqueous media, comprise major barriers to an improved theoretical understanding, which remains limited. The framework defects are expected to have an essential role in the mesopores formation process and give good perspectives to understand demetallation. One of the major obstacles to an improved understanding is the difficulty in modeling the complex and non-periodic structure of mesopores in zeolites. Several groups were tackled ZSM-5 crystal structure and model adsorption processes using both cluster and periodic DFT calculations [30–36].

The original acid/base properties can also be precisely modified to match the requirements of the target reaction. By depositing metal nanoparticles, additional functionalities can be integrated into one material. The use of a zeolite as a carrier for the metal phase is expected to be very favorable for obtaining a material with desirable properties. The mesopore zeolites have an even larger external surface into which the metal phase can be deposited, thus achieving higher dispersion, and the closer proximity of the metal and acid/base site in the solid with respect to the corresponding micropore zeolite. Zeolite-based catalysts have not been extensively applied in biomass conversion so far and never in mesoporous form, but the results are primarily promising [37]. Micro- and mesoporous zeolites are attractive and suitable catalysts for liquid-phase conversions taking into account their water compatibility and the benefits provided by a porous system for the transport to/from the active sites of typically highly viscous biomass-derived compounds. However, more detailed studies on the structure of active sites and metallic nanoparticles carried in zeolites, as well as the mechanism of biomass conversion into chemicals, are necessary.

4. Selected compounds from biomass

4.1. Fructose: aldo-keto isomerization of glucose

Acquiring fructose from biomass, due to low raw material costs, is an interesting pathway for obtaining a variety of useful monomers. One of the methods of fructose production is the aldol-keto isomerization from biomass-derived glucose. Figure 4 shows the reaction pathways of glucose and fructose [38]. Fructose may be an intermediate in subsequent



transformations to HMF or lactic acid. One of the concepts of performing fructose reactions is to obtain a catalyst with Lewis active centers. For this purpose, the Sn-Beta zeolite was designed, which has the ability to convert glucose to fructose. The presence of additional sodium cations in the structure enables the glucose reaction to mannose [38,39]. In order to confirm the effectiveness of the above catalyst, theoretical studies were carried out using the DFT method. Reaction barriers for partially hydrolyzed and fully coordinated tin at specific locations using energy distribution analysis were tested. In addition, Sn was replaced with other metals such as Ti, Zr, V, Nb, Si and Ge. It has been found that Sn and Zr are metals that have the lowest energy barrier for glucose isomerization. It also depends on the physical properties of metals and the basicity of the centers of active oxygen atoms associated with the metal atom [40]. Another example of the zeolite usage in the glucose isomerization reaction is Y, H-beta and H-USY zeolite. The reaction occurs in two stages in various solvents. The first step is the reaction of the isomerization of glucose in methanol to produce methyl-fructoside, followed by hydrolysis to fructose after the addition of water. The reaction takes place at 120°C for 1h involving the above-mentioned catalysts. As a result of the process, the product was obtained with the highest yield of 55% using H-USY. Conducting this process at higher temperatures leads to a product like methyl levulinate [41].

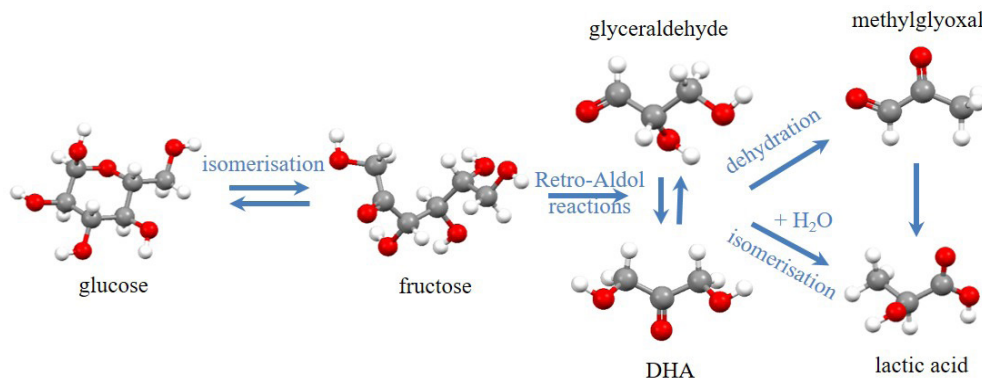


Fig. 4. Scheme of reaction pathways of glucose and fructose

The process of glucose isomerization to fructose was also carried out on NaY zeolite with magnesium cations incorporated into zeolite (0-15 wt.%). It was observed that the increase in magnesium content in the structure (10 and 15% by weight) significantly improves the degree of glucose conversion (6-49%). However, the yield of fructose was only about 32% [42]. Tests were also carried out with the zeolites A, X, Y and hydrotalcites. Alkaline cations: Na⁺, K⁺, Cs⁺, Ca²⁺, Ba²⁺ were introduced into the structure of these materials on the basis of ion exchange. The process was carried out in an aqueous environment at 95°C, at 8 bar. The best among the tested zeolites were NaX and KX zeolites with a selectivity into fructose of about 90% and a conversion of glucose of around 10-20% [43].

The further essential processes of fructose transformation into glyceraldehyde (GLA) and dihydroxyacetone (DHA) are retro-aldol reactions.

4.2. 5-hydroxymethylfurfural and furfural

The production of 5-hydroxymethylfurfural (HMF) and furfural should be essential for the industry since both compounds are used as a substrate in several syntheses. HMF is formed by the dehydration process of different aldoses from the hydrolysis of biomass [44]. HMF can be converted to a range of derivatives having potential applications in the biofuels, polymer, and solvent industries. There are several promising studies concerning catalytic processes of HMF production from biomass over a range of catalysts from hydroxyapatite supported chromium chloride, metal chlorides up to ZSM-5 [45–47].

Examples of reactions catalyzed with the corresponding zeolites are given in Figure 5. One of the zeolites used in the production of HMF is the dealuminated BEA zeolite, which has been formed by the calcination of the NH_4^+ BEA form at a temperature above 700°C or the treatment of this material with steam in 500°C . The Si-O-Al bonds inside the zeolite structure are broken, resulting in an increase of Lewis active centers. The calcinated BEA zeolite has been used in the reaction of the conversion of glucose to HMF with a selectivity of 55% at a 78% conversion [48]. Another possibility is to conduct the process of HMF production from glucose in a 1-butyl-3-methylimidazolium chloride solvent with BEA zeolite (Si / Al = 25) as a catalyst. The catalyst has the highest activity, resulting in HMF with a 50.3% yield at a 80.6% glucose conversion at 150°C for 50 minutes [49]. The HMF production process is also possible in the ionic liquid 1-butyl bromide-3-methylimidazolium solvent in MOR zeolite [50]. Also, the conversion of glucose to HMF takes place with the participation of catalysts such as SAPO-34 [51], H-, Fe-, Cu-ZSM-5 [52] or over the hierarchical Zr-Al-BEA [53].

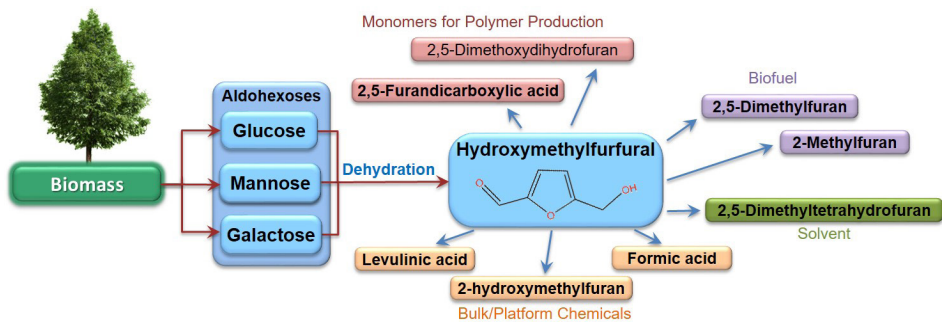


Fig. 5. Scheme illustrating the targeted product (HMF) from biomass-derived feedstocks and its usage as a substrate in further synthesis into valuable chemicals [44]

Additionally to the conversion of biomass to HMF, it is also important to obtain furfural. Furfural is one of the strategical and ultimate industrial intermediates [54]. Furfural is converted into furfuryl alcohol, methylfuran and furan via metal-catalyzed hydrogenation, reduction and decarbonylation, respectively (see Figure 6). Also, different valuable products are produced from furfural: α -furfuryl alcohol, tetrahydrofurfuryl alcohol, methylfurfuryl alcohol, 5-dimethylaminomethylfurfuryl alcohol, furoic acid, furfurylamine, methylfuran, 2-acetylfuran and 2,5-dimethoxydihydrofuran.

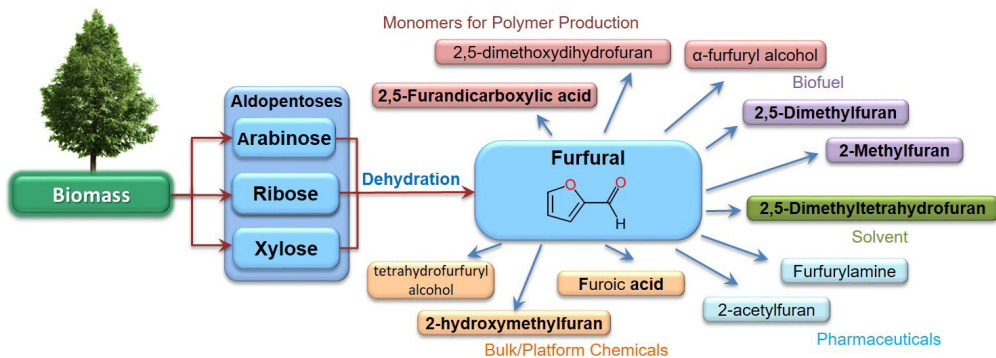


Fig. 6. Scheme illustrating the targeted product (furfural) from biomass-derived feedstocks and its usage as a substrate in further synthesis into valuable chemicals

The reaction of C5 monosaccharides (xylose, arabinose, ribose derived from corn fiber) to furfural using H-beta zeolites, sulfuric acid (VI) and H-mordenite has been carried out. The furfural has been obtained with yields of 62, 55 and 44% respectively, using H-beta, H-mordenite and sulfuric acid. The H-beta zeolite has been found to be the most active due to the presence of Brönsted and Lewis centers (respectively at a ratio of 1.66). The H-beta catalyst gives a bifunctional effect: isomerization (due to the presence of the Lewis center) and dehydration (presence of the Brönsted center) of monosaccharides into HMF [54]. Dumesic et al. developed a reaction to obtain HMF from xylose, fructose and glucose using various catalysts. Their process had been carried out in γ -valerolactone at 175°C. Catalysts that were used were γ -Al₂O₃, Sn-beta, Sn-SBA-15, H-ZSM-5, zirconium sulfate, 0.02M sulfuric acid (VI), Nafion-SAC-13, sulfonated carbon, H-beta, Amberlyst 70, SBA-15 functional with propylsulfonic acid. From all tested catalysts, H-mordenite has the highest activity: in the case of glucose conversion (97%), HMF has been obtained with a yield of 32% and 36% for fructose at a 100% conversion rate [55].

A process of hydrolytic hydrogenation of arabinogalactan from hemicellulose into 5-hydroxymethylfurfural and furfural in the presence of a modified Ru-USY zeolite (Si/Al = 15 and 30, 1-5% ruthenium) has also been developed [56]. Another example is the usage of H-ZSM-5 zeolite in the dehydration of xylose to furfural. The process was carried out in the temperature range of 140-220°C. The highest selectivity was obtained at 200°C [57]. The other zeolites, such as SAPO-34 zeolites [58] and K-BEA [59], have the ability to carry out this reaction. Zhang et al. conducted a process of glucose conversion on BEA zeolites (ion exchange Fe-BEA, Sn-BEA, Zr-BEA). A furfural and HMF were obtained as by-products. Sn-Beta zeolite showed the highest activity, giving a product with a yield of 69.2% [60].

4.3. Levulinic acid and γ -valerolactone

Levulinic acid is one of the platform molecules used as a precursor for pharmaceuticals, plasticizers, and various other additives. It can be obtained through hydrolysis/dehydration of aldohexoses such as glucose and fructose, or hexose-containing polymers like starch and cellulose.

Levulinic acid was obtained as a result of glucose, starch and cellulose conversion in a hydrothermal process using Ga-MOR zeolite [61]. The process lasted for 6 hours at 175°C with a yield of 59.9%. Amin et al. have developed a hybrid catalyst containing chromium chloride and an HY zeolite. As a result of the reaction at 145.2°C for 146.7 min., they obtained a product with a yield of 55.2% [62]. Another example is the dehydration of glucose using MFI zeolite with different silicon module (Si/Al = 25, 30, 80, 120, 260). This process was carried out at 180°C for 8 hours. The MFI zeolite with the silicon module 30 has been found the most active; the product obtained in this case had a yield of 35.8% [63]. They also developed a number of Fe-HY catalysts with various percentages of iron (5, 10, 15%). Among the above catalysts, the 10% Fe-HY catalyst showed the highest catalytic efficiency of around 62% [64,65]. Levulinic acid (LA) has also been obtained by the conversion of xylose in the presence of hot steam using alkaline zeolite catalysts. Zeolite Y was treated with a sodium base with various molar concentrations (0.05 M and 0.25 M). The dealuminated Y zeolite, 0.25 M NaOH proved to be the most effective catalyst. The product was obtained with a yield of 30.4% and a conversion of 84.3%. The process was carried out for 3 hours at 170°C [66]. Zeolite LZV has also found application in the catalytic dehydration of fructose. The process was carried out in a batch reactor at 140°C for 15 hours. From 1 g of fructose, 0.432 g of levulinic acid has been obtained [67].

The γ -valerolactone (GVL) is another biomass-derived chemical compound - a potential fuel and green solvent. The γ -valerolactone can be obtained from furfural by the hydrogenation process at 120°C in a 2-butanol solution on Zr-BEA and Al-MFI catalysts [39,68-70]. GVL is also produced via hydrogenation reaction from levulinic acid. Other important chemicals like 1,4-pentanediol or 2-methyltetrahydrofuran can be obtained by chemoselective hydrogenolysis of GVL.

4.4. Adipic acid

Adipic acid is used in the production of nylon, PVC and polyurethanes and its production is about 2.5 Mton/year. Adipic acid is produced from a mixture of cyclohexanol and cyclohexanone, oxidative cleavage of cyclohexene using hydrogen peroxide or by the hydrocarboxylation of butadiene [71]. Adipic acid has traditionally been produced from various petroleum-based feedstocks (e.g., phenol, benzene, and cyclohexane), but shifts in the hydrocarbon market have resulted in the virtual elimination of phenol as a feedstock. In recent years, cyclohexane-based processes have accounted for about 93% of the global production capacity. Two steps are involved in ADA production: 1) oxidation of cyclohexane to produce KA oil (cyclohexanone and cyclohexanol) and 2) nitric acid oxidation of KA oil to produce adipic acid.

Recently, start-up companies such as Rennovia, Verdezyne, BioAmber, Celexion, and Genomatica have developed bio-based routes to produce adipic acid. Rennovia's patented a two-step process for the production of bio-based adipic acid from glucose:

- (i) a selective catalytic oxidation of glucose to glucaric acid
- (ii) a selective catalytic hydrodeoxygenation of glucaric acid to adipic acid (see Figure 7).

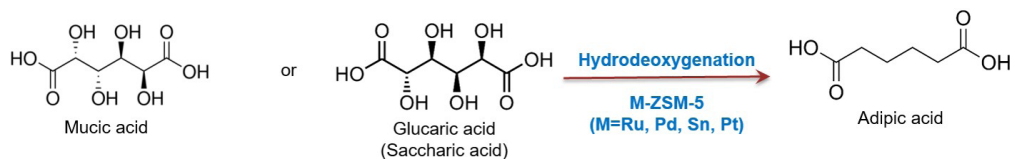


Fig. 7. Scheme illustrating the targeted product (adipic acid) from biomass-derived feedstocks (glucaric acid)

Two basic motivations for considering alternative biomass feedstock sources for the production of ADA are: 1) in the long term, they could be less expensive to produce than conventional methods using crude oil derivative cyclohexane and 2) societal demands for producing industrial chemicals via ‘sustainable’ methods or technology-specific market demand that results in requirements for producing ADA from bio-chemical resources. Potential catalysts for hydrodeoxygenation are metal (Ru, Pd, Sn, Pt) on ZSM-5.

4.5. Dihydroxyacetone

A new chemocatalytic technology for the continuous oxidation of glycerol (GLY) to dihydroxyacetone (DHA) in the gas phase has been developed. This process takes place over the Fe-MFI catalyst in the presence of molecular oxygen. The reaction was carried out in a fixed bed reactor. Activation of the steam generator at 600°C shows dispersed iron in the form of cations and FeOx clusters, which guarantee a product efficiency of 50% [72]. A method for converting dihydroxyacetone to C₁-C₄ alkyl lactate has also been developed. The process was carried out using MFI, MOR, FER, BEA zeolites with gallium particles. The Ga-FAU proved to be the most active, giving a product, such as n-propyl and n-butyl lactate and ethyl lactate [73]. Another possibility is the reaction of dihydroxyacetone into ethyl lactate in a Ga-USY catalyst [74].

4.6. Lactic acid / alkyl lactates

Developing efficient catalysts for the conversion of bio-renewable feedstocks to a selected key chemical, such as lactic and acrylic acid esters (see Figure 8), which would be alternative to the currently present in the industry technologies of obtaining them from non-renewable resources, is the main issue for scientists working in the field of catalysis.

Lactic acid is used in the food industry and for the production of other chemicals and polymers and its production is about 2.7 Mton/year. Lactic acid has three available atoms for adsorption: the oxygen atom of the alcohol group and the two oxygen atoms of the carboxyl group. Based on the literature [75], the lactic acid adsorption over metallic cations gives several possible binding modes at zirconia surfaces: monodentate, bidentate bridging and bidentate chelating, where a dissociative bidentate bridging mode is preferred. The classical pathway through a carbocation proceeds with a very high activation energy. Therefore, the authors suggested another mechanism through a carbanion and succeeded with the acrylic acid formation.

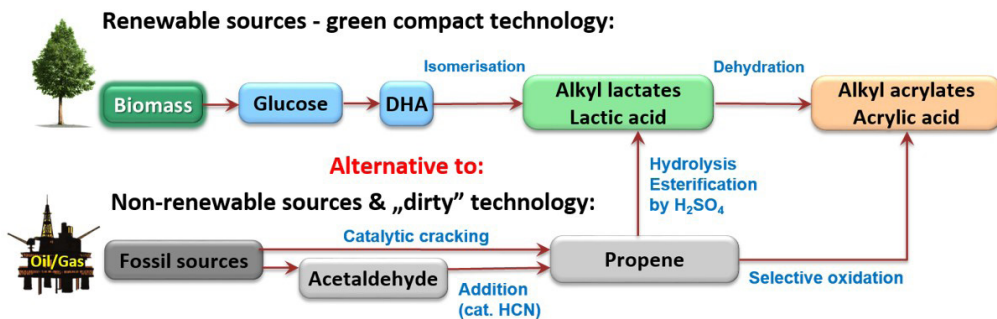


Fig. 8. Scheme illustrating the lactic acid and acrylic acid as well as their esters [44] (DHA=dihydroxyacetone)

From all family of biomass-derived compounds lactic acid is the most promising and can generate multiple final and intermediate chemicals, such as acrylic acid, pyruvic acid, 1,2-propanediol, 2,3-pentanedione or acetaldehyde (see Figure 9) [6, 26]. This compound can also be polymerized into biodegradable plastic, i.e. polylactide (PLA), or solvents.

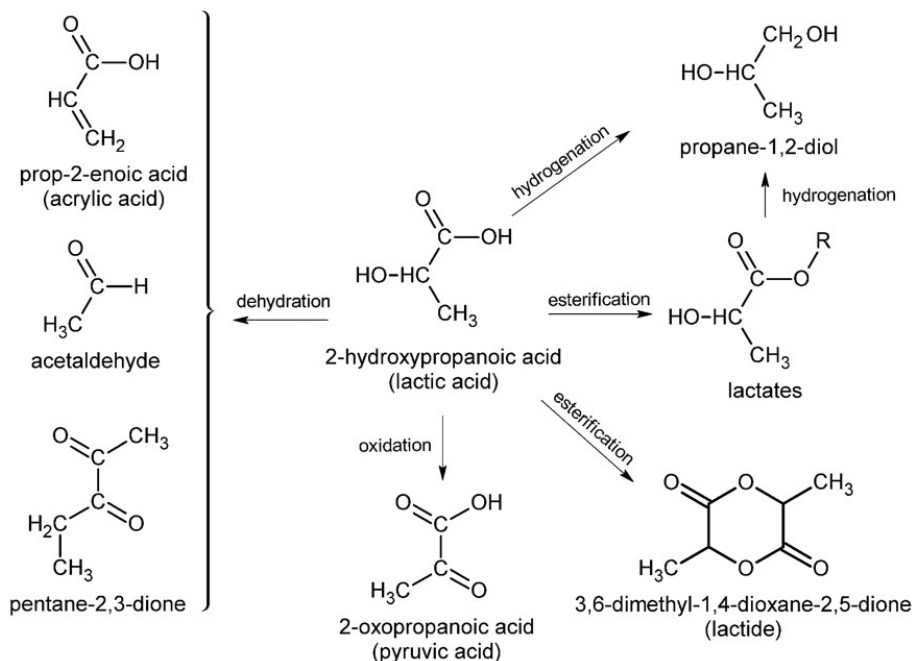


Fig. 9. Scheme illustrating the lactic acid reactions [6]

Dehydration of lactic acid provides the most promising and environmentally friendly way to produce for example acrylic acid. However, the dehydration of lactic acid may be accompanied by other competing reactions, such as hydrogenation, condensation, decarboxylation and esterification, where the decarboxylation to acetaldehyde is one of the

major side reactions and has a large effect on the low selectivity to acrylic acid. To inhibit the formation of acetaldehyde and improve the selectivity of the desired acrylic acid, the effects of many different catalysts are tested.

5. Catalytic dehydration of lactic acid/alkyl lactates to acrylic acid/alkyl acrylates

5.1. State-of-art of actual research of obtaining acrylic acid and alkyl acrylates

Acrylic acid is one of the most important compounds for the synthesis of organic. It is widely used for the preparation of a variety of materials. such as water absorbent polymers, adhesives, textile treating agents (see Figure 10).

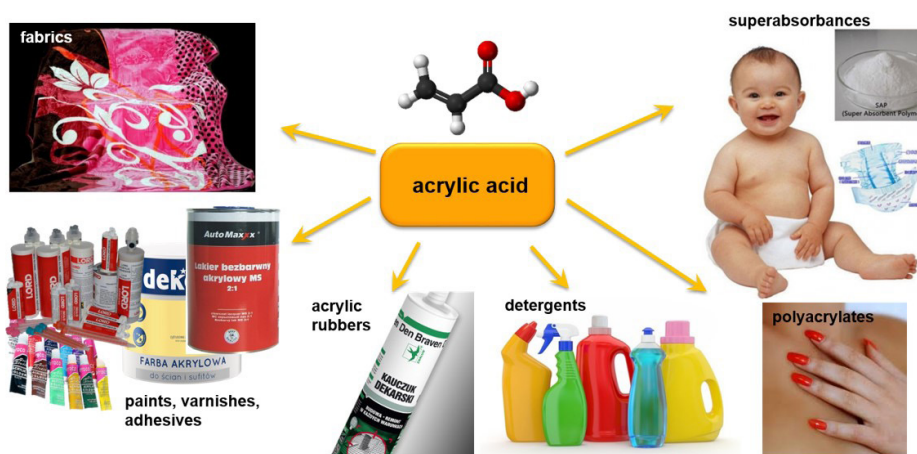


Fig. 10. Scheme illustrating the main directions of acrylic acid processing [76]

The most common industrial process for preparing acrylic acid is the selective oxidation of propylene. This is the basic method of obtaining the product in the fossil industry. Due to the high demand for fossil fuels and the relatively low stocks of crude oil, the price of propylene and its by-products grow, which leads to increased pressure on the production acrylic acid of the propylene.

Acrylic acid is a platform molecule used as a building block to produce acrylate polymers and plastics [77]. Its production had a grown of 4%/year between 2006 and 2011, reaching 4.2Mt in 2011 and was predicted to increase about 5% per year between 2012 and 2017, and recently, its production has been about 4.7 Mton/year. [78]. Acrylic acid is currently produced by the catalytic oxidation of propylene using a two-step process (Figure 2). However, it is widely affected by the propylene price, as it only represents 2% of its global consumption [77]. The value of the acrylic acid market in the 2013 year was equal to 11 billion \$ yearly and the forecast value before 2020 is around 18.8 billion \$. In the next 5 years, the global demand for acrylic acid will be around 8.169 billion tons/year.

An alternative route of producing acrylic acid is therefore required, especially in the context of the commitment to environment-friendly catalytic processes, for example, a single step dehydration of lactic acid. The catalytic dehydration of lactic acid to acrylic acid has received increasing attention in the last two decades, but high selectivity has proven elusive. Metal-exchanged zeolites are promising catalysts for further development for LA to AA dehydration. However, acrylic acid is rarely obtained selectively from lactic acid because of easy decarbonylation/decarboxylation leading to acetaldehyde and CO_x. High yields of acrylic acid were obtained using modified zeolites, but they suffered from coking and hydrothermal instability.

In 1958, Holmen was first to show that acrylic acid can be obtained in the dehydration of lactic acid using a mixture of sodium sulfate and calcium sulfate as a catalyst.

One of the methods could be the dehydration of lactic acid over hydroxyapatite (Ca-HAP) catalysts with different mole ratios of Ca/P and calcination temperatures described by Bo Yan *et al.* [79]. Hydroxyapatites (HAP) are known as important acid-based catalysts. According to the study, the HAP sample (with Ca/P = 1.62 and calcination temperature 360 °C) was identified as the most effective for the selective formation of acrylic acid from lactic acid, showing an acrylic acid selectivity within a range of 71–74 % and an acrylic acid yield of 50–62%. The gas-phase dehydration of lactic acid was conducted under atmospheric pressure in a vertical fixed-bed quartz reactor. The reaction feed, an aqueous solution containing 35.7 wt % or 10 mol % lactic acid with space velocity 2.1 h⁻¹ and in 360 °C.

Huang *et al.* [80–83] performed the LA dehydration process on NaY zeolites, modified by rare earth metals (lanthanum, cerium, samarium and europium) from which the La-NaY had the best selectivity. The catalysts were obtained by ion exchange of the corresponding cations (lanthanum, cerium, lanthanum and europium) in an aqueous nitrate solution. The modified zeolite was marked with the silicon module Si/Al = 4.5. Subsequent scientists have developed a catalyst by modifying NaY zeolite by potassium. The addition of potassium to NaY significantly improved its lifetime [84].

The other method of obtaining an acrylic acid, which was described by Xianghui Zhang *et al.* [85], involves ZSM-5 zeolite as a catalyst. It is well-known that ZSM-5 has strong acidic sites on the surface of H-ZSM-5, which gives a very low selectivity for acrylic acid. Fortunately, the surface acidity of H-ZSM-5 zeolite can be regulated in a wide range through alkaline treatment. At first, the H-ZSM-5 zeolite was treated with the NaOH aqueous solution. The dehydration reaction of lactic acid was carried out in a vertical fixed-bed steel reactor. Studies using 30 wt% lactic acid have shown that for differently modified ZSM-5 catalysts, lactic acid conversion changes little: it is only changing in the small range of 95.8–97.3% in the temperature range of 335–380°C. Although the selectivity for acrylic acid exhibits a volcano-type dependence on NaOH concentrations, the best acrylic acid selectivity with over 65% could be achieved when the concentration of NaOH is 0.3–0.5 mol/L. Increasing the NaOH concentration causes a decreased acrylic acid selectivity and appearance of other unknown products. The best catalytic performance, an achievement of lactic acid conversion of 96.9% and selectivity for acrylic acid accounting to 77.9%, were obtained over the resulted ZSM-5 catalyst treated by 0.5 mol/L NaOH and 0.5 mol/L Na₂HPO₄ under the optimized reaction conditions (350 °C,

LHSV = 4 h⁻¹). One of the main problems is the stability of catalysts for the dehydration reaction of lactic acid. Conversion of lactic acid in a reaction time of 52 hours is still 88% at a selectivity as high as 65% acrylic acid. A slight decrease in conversion and selectivity may be due to the inevitable deposition of coke, which is typical for acid-base catalysts.

Another way to modify ZSM-5 zeolites is by using ion exchange with alkali metals [86]. ZSM-5 zeolite (Si/Al molar ratio = 75) was preheated at 550 °C for 6 h and treated with an aqueous solution of MNO₃ (1 mol/L; M = NH₄, Li, Na, K, Rb, or Cs; 14 g of ZSM-5 zeolite in 140 mL of MNO₃) at 80 °C for 6 h to obtain ion-exchanged ZSM-5. The modified zeolites gave improved catalyst performance in lactic acid dehydration to acrylic acid. The conversion of lactic acid decreases in the following order: H > Li > Na > K > Rb > Cs modified ZSM-5. The highest selectivity of acrylic acid was prepared using a catalyst KZSM-5 (K_{0.84}Na_{0.16}ZSM-5). These results indicate that the introduction of the alkali metal effectively inhibited the decarbonylation and decarboxylation of lactic acid to acetaldehyde. It has been found that the introduction of alkali-metal cations decreased the total acid-base number, which improved acrylic acid selectivity.

A sequent article by Yan *et al.* discusses the dehydration of lactic acid carried by the Rb⁺- and Cs⁺-exchanged Beta zeolite catalysts [87]. In this case, raw powders of as-synthesized Beta zeolite (SiO₂/Al₂O₃ = ca. 40) were used and the Rb⁺- and Cs⁺-ions were added by ion-exchange with aqueous solutions of RbNO₃ and CsNO₃, respectively. The gas-phase dehydration of lactic acid was carried out under atmospheric pressure at 360 °C in a vertical down-flow, fixed-bed tubular quartz reactor. This study shows that the Rb⁺- and Cs⁺-exchanged Na zeolites with suitable exchange degrees could be highly efficient for catalyzing the gas-phase dehydration of bio-derivative LA for sustainable AA production. Samples of Rb_{0.95}Na_{0.05} and Cs_{0.81-0.90}Na_{0.19-0.10} were identified as the best performing catalysts for AA production by optimizing the exchange degrees for Rb⁺ and Cs⁺, respectively, to uncover the suitable acidity–basicity balance, offering the acrylic acid selectivity as high as 69–70 % and yields higher than 65 mol%.

The alkyl lactates are more promising for acrylic acid and its esters production. Alkyl lactates are easier to vaporize and less polymerizable than lactic acid. Their ester functions that are less reactive limit decarbonylation/decarboxylation reactions. The standard industrial reaction for producing, for example, methyl acrylate is esterification with methanol under acid catalysis (sulfuric acid, p-toluene sulfonic acid, acidic ion exchangers [76]). Ethyl acrylate is produced by acid-catalyzed esterification of acrylic acid, which in turn is produced by oxidation of propylene. It may also be prepared from acetylene, carbon monoxide and ethanol by a Reppe reaction. Biomass as a renewable resource for alkyl acrylate sounds to be more ecologically friendly, and much less robust technology is expected to be developed.

Interest in the use of alkyl lactate instead of lactic acid as a reactant to reach higher acrylic acid selectivity has been previously illustrated for Ca₃(PO₄)₂–Ca₂(P₂O₇) (50/50 wt%) mixture [88]. The highest acrylic acid molar selectivity was found for ethyl lactate (79%), followed by methyl lactate (75%) and lactic acid (54%). Moreover, the use of alkyl lactates could simplify the separation and purification process and reduce production costs [89] even if it would imply the recycling of co-produced alcohols. In that regard, additional molecules of

alkyl lactates could be produced. Alkyl lactates (AL) have been shown to be effective starting materials for the production of acetaldehyde, 2,3-pentanedione, lactide (a biopolymer starting material), and alkyl acrylates (AA) [90]. Growth in the demand for acrylic acid is forecasted at 4.5% per year during 2016-21, driven by the growth of acrylate esters at about 4%. After butyl acrylate and ethyl acrylate, methyl acrylate is the third most important acrylic ester with a worldwide annual production of about 200,000 tons per year [91]. The alkaline earth phosphates have been prepared and evaluated in the gas phase dehydration of ethyl lactate to acrylic acid and ethyl acrylate [92]. However, zeolites are much more promising materials for biomass conversion into lactates and acrylates. Zeolites, microporous and crystalline aluminosilicates, are effective catalysts in many applications [93].

5.2. Nanodesign of zeolites and the process of biomass transformation into acrylic acid

Taking into account all the previously reviewed state-of-art papers concerning biomass valorization into valuable chemicals in our study, we are interested in designing a new theoretical and experimental approach for the synthesis of acrylic acid from lactic acid over zeolite catalysts. The catalyst design of lactic acid dehydration, using both experimental and theoretical methods, helps in further development and synthesis of zeolite with a declared structure and obtaining a structure of substrates, products and intermediates. Actually, in our laboratory, the experimental and theoretical design of zeolite catalysts is performed.

In the theoretical part, the electronic structure of all clusters was calculated by *ab initio* density functional theory (DFT) methods (program StoBe) using the non-local generalized gradient corrected functionals according to Perdew, Burke, and Ernzerhof (RPBE), in order to account for electron exchange and correlation. The stabilization of monomeric and dimeric iron and tin complexes, such as M-OH, HO-M-O-M-OH and M-O-M (where M= Fe, Sn) in the zeolites pore and at the surface (MFI, BEA, FAU) has been investigated. The example is BEA structure (Figure 11), where M-O-M dimers stabilized in micro- and mesopores.

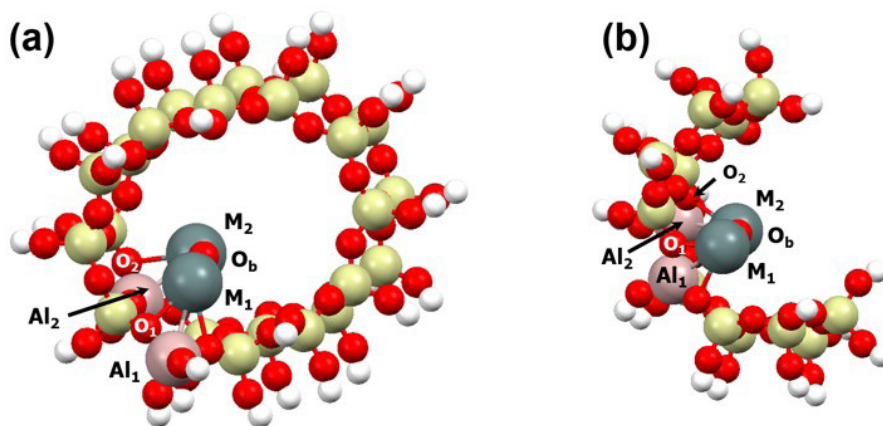


Fig. 11. Dimeric complex M-Ob-M in the BEA: (a) ideal inside pore, (b) after hierarchization

Experimentally, the dehydration reaction of lactic acid was carried out in a vertical fixed-bed quartz reactor (Figure 12) and operated under atmospheric pressure and with a temperature of 350 °C. The reaction feed, which was an aqueous solution containing 40 wt% lactic acid with 2cm³/h flow rates, was pumped into the reactor and driven by inert gas (50 mL/min).

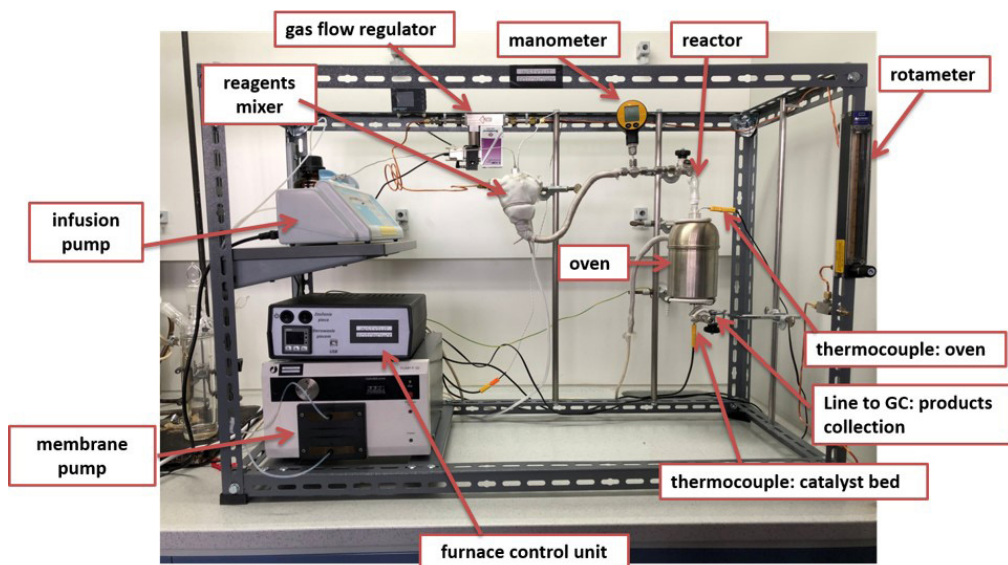


Fig. 12. Unit for catalytic tests in the gaseous phase

The metal M-O_p-M dimers have been found to be stable above oxygen bound with aluminum centers of MFI, BEA and FAU zeolites. The mechanism of direct lactic acid dehydration in Sn- and Fe- zeolites has been found. The geometric compatibility of the metallic dimers and lactic acid allows for the proposed direct dehydration mechanism (see Figure 13), where the oxygen center of the hydroxyl group of LA-a-carbon interacts with the metal center of dimer and hydrogen is subtracted from LA-b-carbon and bound with the bridge oxygen of the metal dimer.

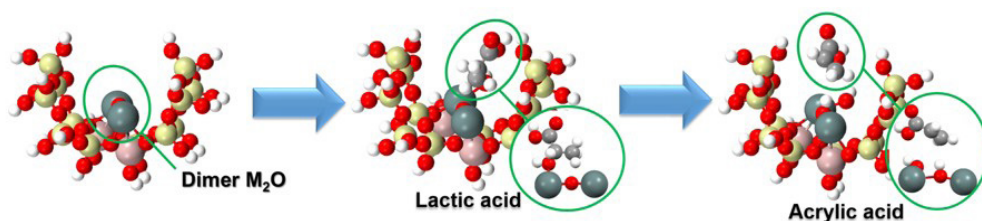


Fig. 13. Dimer M₂O, lactic and acrylic acid structures at the surface model of BEA zeolite

The results of our nano-design materials suggest that adsorption of lactic acid is endothermic in the case of Sn-BEA, slightly endothermic in ideal Fe-BEA and exothermic in the case of hierarchical Fe-BEA catalyst. The dehydration of lactic acid into acrylic acid

proceed with an energy barrier. However, the energy level of acrylic acid above Fe-BEA have been found to be lower than the energy level of lactic acid. The hierarchical metal modified BEA zeolite has been found theoretically to be the best catalyst for direct dehydration of lactic acid into acrylic acid. The hierarchization process increases the pore volume as well as increases the chance of adsorption of larger molecules at desired active sites. The theoretical results are confirmed experimentally. Besides acrylic acid, other products have been detected: pyruvic acid, 1,2-propanediol, 2,3-pentanedione, acetaldehyde and lactide. However, the process of lactic acid dehydration is very complex due to the fact of the formation of products in two liquid phases. Therefore, obtaining the full mass balance of reaction is very complicated and required further improvement.

6. Conclusions

The urgent needs for a more sustainable production of chemicals from renewable feedstock (e.g. biomass) have caused intensive research efforts in the search for novel porous nano-materials, such as zeolites. Important properties of zeolites, which make them ideal candidates for the transformation of biomass into high-value chemicals, are their high hydrothermal stabilities. The problematic in using zeolites in biomass conversion is the production of a large number of products. The catalysts are still discovered through a combination of trial-and-error and serendipity due to a limited understanding of the molecular structure and the complexity of active centers. The main goal of the research should be zeolite design in a nano-scale with an improved catalytic performance, optimized for biomass transformation to dedicated chemicals. The research is focused on zeolites with different pore sizes. Another problem is the existence of many phases during processes, e.g. water and organic phases, which makes the process very difficult for industrial scale. Additionally, the products have a tendency to polymerize.

We present here a comprehensive literature study on valuable biomass-derived chemicals and technologies connected with extraction and processing of: aldo-keto isomerization of glucose, 5-hydroxymethylfurfural and furfural, levulinic acid and γ -valerolactone, adipic acid, dihydroxyacetone, lactic acid and acrylic acid. From all the families of such biomass-derived compounds, lactic acid and its alkyl lactates are the most promising and can generate multiple final and intermediate chemicals, such as acrylic acid, alkyl acrylates, pyruvic acid, 1,2-propanediol, 2,3-pentanedione or acetaldehyde. This compound can also be polymerized into biodegradable plastic, i.e. polylactide (PLA), or solvents. Therefore, the development of biomass-derived processes requires a lot of multidisciplinary research before it would be finally applied in industrial practice. However, it is worth considering, especially by using zeolites with a more declare structure and design properties. Therefore, the methodology of designing simultaneously zeolites theoretically and experimentally that we have used gives an exceptional chance to obtain knowledge about the process and simultaneously modify its parameters.



This article is the effect of the realization of a project entitled, "Nano-design of zeolite-based catalysts for selective conversion of biomass into chemicals", sponsored by the National Science Centre, Poland, under Polonez-1 grant no. 2015/19/P/ST4/02482. This project has received funding from the European Union's Horizon 2020 research and innovation program under the Marie Skłodowska-Curie grant agreement No. 665778. This work was supported in part by the PL-Grid Infrastructure.



References

- [1] Pacala S., Socolow R., *Stabilization wedges: solving the climate problem for the next 50 years with current technologies*, Science 305/2004, 968–972.
- [2] Werpy T., Petersen G., *Top Value Added Chemicals from Biomass: Vol. I-Results of Screening for Potential Candidates from Sugars and Synthesis Gas*, Report No. NREL/TP-510-35523; National Renewable Energy Laboratory, Golden, CO, 2004.
- [3] *The roadmap for biomass technologies in the U.S.*, Biomass R&D Technical Advisory Committee, US Department of Energy, Accession No. ADA 436527, 2002.
- [4] Lalak J., Kasprzycka A., Murat A., Paprota E.M., Tys J., *Obróbka wstępna biomasy bogatej w lignocelulozę w celu zwiększenia wydajności fermentacyjnej metanowej*, Acta Agrophysica 21/2014, 51–62.
- [5] Burczyk B., *Biorafinerie: Ile w nich chemii ?*, Wiadomości chemiczne, 63/2009, 9–10.
- [6] Corma A., Iborra S., Velty A., *Chemical Routes for the Transformation of Biomass into Chemicals*, Chemical Reviews 107/2007, 2411–2502.
- [7] Tan K.T., Lee K.T., Mohamed A.R., *Role of energy policy in renewable energy accomplishment: the case of second-generation bioethanol*, Energy Policy, 36/2008, 3360–3365.
- [8] Clark J., Deswarte F., *Introduction to Chemicals from Biomass, Second Edition*, John Wiley & Sons, Ltd. Published by John Wiley & Sons, Ltd., 2015.
- [9] Balat M., Balat H., Oz C., *Progress in bioethanol processing*, Progress in Energy and Combustion Science 34/2008, 551–573.
- [10] Lin Y.-C., Huber G.W., *The critical role of heterogeneous catalysis in lignocellulosic biomass conversion*, Energy Environmental Science 2/2009, 68–80.
- [11] Gandini A., *The irruption of polymers from renewable resources on the scene of macromolecular science and technology*, Green Chemistry 13/2011, 1061–1083.
- [12] Huber W., Iborra S. and Corma A., *Synthesis of Transportation Fuels from Biomass: Chemistry, Catalysts, and Engineering*, Chemical Reviews 106/2006, 4044–4098.
- [13] Langan P., Gnanakaran S., Rector K. D., Pawley N., Fox D. T., Cho D. W., Hammel K. E., *Exploring new strategies for cellulosic biofuels production*, Energy Environmental Science 4/2011, 3820–3833.
- [14] da Costa Sousa L., Chundawat S. P. S., Balan V., Dale B. E., *'Cradle-to-grave' assessment of existing lignocellulose pretreatment technologies*, Current Opinions Biotechnology 20/2009, 339–347.

- [15] Himmel M. E., Ding S. Y., Johnson D. K., Adney W. S., Nimlos M. R., Brady J. W., Foust T. D., *Science* 315/2007, 804.
- [16] Ragauskas A. J., Williams C. K., Davison B. H., Britovsek G., Cairney J., Eckert C. A., Frederick, Jr W. J., Hallett J. P. and Leak D. J., et al., *Science* 311/2006, 484.
- [17] Wiercigroch E., Szafraniec E., Czamara K., Pacia M. Z., Majzner K., Kochan K., Kaczor A., Baranska M., Malek K., *Raman and infrared spectroscopy of carbohydrates: A review*, *Spectrochimica Acta Part A: Molecular and Biomolecular Spectroscopy* 196/2018, 413–417.
- [18] Jarvis M.C., McCann M.C., *Macromolecular biophysics of the plant cell wall: concepts and methodology*. *Plant Physiol Biochem*, 38/2000, 1–13.
- [19] Ding S.-Y., Liu Y.-S., Zeng Y., Himmel M. E., Baker J. O., Bayer E. A., *How Does Plant Cell Wall Nanoscale Architecture Correlate with Enzymatic Digestibility?*, *Science* 338/ 2012, 1055–1060.
- [20] Dorrestijn E., Laarhoven L. J.J., Arends I. W.c.E., Mulder P., *The occurrence and reactivity of phenoxyl linkages in lignin and low rank coal*, *Journal of Analysis and Applied Pyrolysis* 54/2000, 153–192.
- [21] Gosselink R.J.A., de Jong E., Guran B., Abächerli A., *Co-ordination network for lignin—standardisation, production and applications adapted to market requirements (EUROLIGNIN)*, *Industrial Crops and Products* 20/2004 121–129.
- [22] Björkman A., *Isolation of Lignin from Finely Divided Wood with Neutral Solvents*, *Nature* 174/1954, 1057–1058.
- [23] Zheng, R., Wei, W., Shi Q., *Density Functional Theory Study on Sum-Frequency Vibrational Spectroscopy of Arabinose Chiral Solutions*, *Journal of Physical Chemistry A* 113/2009, 157–164.
- [24] Brauer B., Pincu M., Buch V., Bar I., Simons J. P., Gerber R. B., *Vibrational Spectra of α -Glucose, β -Glucose, and Sucrose: Anharmonic Calculations and Experiment*, *Journal Physical Chemistry A* 115/2011, 5859–5872.
- [25] Rinaldi R., Schüth F., *Design of solid catalysts for the conversion of biomass*, *Energy Environmental Science* 2/2009, 610–626.
- [26] Stöcker M., *Biofuels and biomass-to-liquid fuels in the biorefinery: catalytic conversion of lignocellulosic biomass using porous materials*, *Angewandte Chemistry Int Ed Engl.* 47/2008, 9200–9211.
- [27] Pérez-Ramírez J., Christensen C.H., Egeblad K., Christensen C.H., Groen J.C., *Hierarchical zeolites: enhanced utilisation of microporous crystals in catalysis by advances in materials design*, *Chemical Society Reviews* 37/2008, 2530–2542.
- [28] Verboekend D. , Pérez-Ramírez J., *Design of hierarchical zeolite catalysts by desilication*, *Catalysis Science and Technology* 1/2011, 879–890.
- [29] Milina M., Mitchell S., Crivelli P., Cooke D., Pérez-Ramírez J., *Mesopore quality determines the lifetime of hierarchically-structured zeolite catalysts*, *Nature Communication* 5/2014, 4922.
- [30] Zhang X.Q., Trinh T.T., van Santen R.A., Jansen A.P.J., *Mechanism of the Initial Stage of Silicate Oligomerization*, *Journal of American Chemical Society* 133/2011, 6613–6625.

- [31] Szyja B.M., Hensen E. J. M., van Santen, R.A., *Retro-analysis of silicate aggregation in pentasil zeolite formation*, *Catalysis Today* 169/2011, 156–166.
- [32] Yang G., Pidko E., Hensen, E. J. M., *Structure, Stability, and Lewis Acidity of Mono and Double Ti, Zr, and Sn Framework Substitutions in BEA Zeolites: A Periodic Density Functional Theory Study*, *Journal of Physical Chemistry C* 117/2013, 3976–3986.
- [33] Lisboa O., Sanchez M., Ruetter F., *Modeling extra framework aluminum (EFAL) formation in the zeolite ZSM-5 using parametric quantum and DFT methods*, *Journal of Molecular Catalysis A: Chemistry* 294/2008, 93–101.
- [34] Malola S., Svelle S., Bleken F. L., Swang O., *Detailed Reaction Paths for Zeolite Dealumination and Desilication From Density Functional Calculations*, *Angewandte Chemistry Int. Ed.* 51/2012, 652–655.
- [35] Fjermestad, T.; Svelle, S.; Swang, O. *Detailed Reaction Paths for Zeolite Dealumination and Desilication From Density Functional Calculations*, *J. Phys. Chem. C* 117/2013, 13442–13451.
- [36] Silaghi M.C., Chizallet C., Raybaud P., *Challenges on molecular aspects of dealumination and desilication of zeolites*, *Micro. Mesop. Materials* 191/2014, 82–96.
- [37] Dhainaut J., Dacquin J.-P., Lee A.F., Wilson K., *Hierarchical macroporous–mesoporous SBA-15 sulfonic acid catalysts for biodiesel synthesis*, *Green Chemistry* 12/2010, 296–303.
- [38] Davis M.E., *Heterogeneous Catalysis for the Conversion of Sugars into Polymers*, *Topics in Catalysis* 58/2015, 405–409.
- [39] Cejka J., Corma A., Zones S., *Zeolites and Catalysis: Synthesis, Reactions and Applications*, Vol. 1, 2010 WILEY-VCH.
- [40] Li Y.P., Head-Gordon M., Bell A.T., *Analysis of the Reaction Mechanism and Catalytic Activity of Metal-Substituted Beta Zeolite for the Isomerization of Glucose to Fructose*, *ACS Catal.* 4/2014, 1537–1545.
- [41] Saravanamurugan S., Paniagua M., Melero J.A., Riisager A., *Efficient Isomerization of Glucose to Fructose over Zeolites in Consecutive Reactions in Alcohol and Aqueous Media*, *Journal of American Chemical Society* 135/2013, 5246–5249.
- [42] Graca I., Iruretagoyena D., Chadwick D., *Glucose isomerisation into fructose over magnesium-impregnated NaY zeolite catalysts*, *Applied Catalysis B: Environmental* 206/2017, 434–443.
- [43] Moreau C., Durand R., Roux A., Tichit D., *Isomerization of glucose into fructose in the presence of cation-exchanged zeolites and hydrotalcites*, *Applied Catalysis A: General* 193/2000, 257–264.
- [44] Alonso D.M., Bond J.Q., Dumesic J.A., *Catalytic conversion of biomass to biofuels*, *Green Chemistry* 12/2010, 1493–1513.
- [45] Nandiwale K.Y., Galande N.D., Thakur P., Sawant S. D., Zambre V. P., and Bokade V.V., *One-Pot Synthesis of 5-Hydroxymethylfurfural by Cellulose Hydrolysis over Highly Active Bimodal Micro/Mesoporous H-ZSM-5 Catalyst*, *ACS Sustainable Chemical Engineering* 2/2014, 1928–1932.

- [46] Zhang Z., Zhao Z., *Production of 5-hydroxymethylfurfural from glucose catalyzed by hydroxyapatite supported chromium chloride*, *Bioresource Technology* 102/2011, 3970–3972.
- [47] Guan J., Cao Q., Guo X., Mu X., *The mechanism of glucose conversion to 5-hydroxymethylfurfural catalyzed by metal chlorides in ionic liquid: A theoretical study*, *Computational and Theoretical Chemistry* 963/2011, 453–462.
- [48] Otomo R., Yokoi T., Kondo J.N., Tatsumi T., *Dealuminated Beta zeolite as effective bifunctional catalyst for direct transformation of glucose to 5-hydroxymethylfurfural*, *Applied Catalysis A: General* 470/2014, 318–326.
- [49] Hu L., Wu Z., Xu J., Sun Y., Lin L., Liu S., *Zeolite-promoted transformation of glucose into 5-hydroxymethylfurfural in ionic liquid*, *Chemical Engineering Journal* 244/2014, 137–144.
- [50] Chanie Y., Diaz I., Perez E., *Kinetics and mechanisms of adsorption/desorption of the ionic liquid 1-butyl-3-methylimidazolium bromide into mordenite*, *Journal of Chemical Technology and Biotechnology* 91/2016, 705–710.
- [51] Zhang L., Xi G., Chen Z., Qi Z., Wang X., *Enhanced formation of 5-HMF from glucose using a highly selective and stable SAPO-34 catalyst*, *Chemical Engineering Journal* 307/2017, 877–883.
- [52] Moreno-Recio M., Santamaria-Gonzalez J., Maireles-Torres P., *Brønsted and Lewis acid ZSM-5 zeolites for the catalytic dehydration of glucose into 5-hydroxymethylfurfural*, *Chemical Engineering Journal* 303/2016, 22–30.
- [53] Song S., Di L., Wu G., Dai W., Guan N., Li L., *Meso-Zr-Al-beta zeolite as a robust catalyst for cascade reactions in biomass valorization*, *Applied Catalysis B: Environmental* 205/2017, 393–403.
- [54] Gallo J.M.R., Alonso D.M., Mellmer M.A., Yeap J.H., Wong H.C., Dumesic J.A., *Production of Furfural from Lignocellulosic Biomass Using Beta Zeolite and Biomass-Derived Solvent*, *Topics in Catalysis* 56/2013, 1775–1781.
- [55] Gürbüz E.I., Gallo J.M.R., Alonso D.M., Wettstein S.G., Lim W.Y., Dumesic J.A., *Conversion of Hemicellulose into Furfural Using Solid Acid Catalysts in γ -Valerolactone*, *Angewandte Chemistry Int. Ed.* 52/2013, 1270–1274.
- [56] Murzin D.Y., Kusema B., E. Murzina E.V., Aho A., Tokarev A., Boymirzaev A.S., Wärnl J., Dapsens P.Y., Mondelli C., Pérez-Ramírez J., Salmi T., *Hemicellulose arabinogalactan hydrolytic hydrogenation over Ru-modified H-USY zeolites*, *Journal of Catalysis* 330/2015, 93–105.
- [57] O’Neill R., Ahmad M.N., Vanoye L., Aiouache F., *Kinetics of Aqueous Phase Dehydration of Xylose into Furfural Catalyzed by ZSM-5 Zeolite*, *Engineering and Chemistry Resources* 48/2009, 4300–4306.
- [58] Bruce S.M., Zong Z., Chatzidimitriou A., Avci L.E., Bond J.Q., Carreon M.A., Wettstein S.G., *Small pore zeolite catalysts for furfural synthesis from xylose and switchgrass in a γ -valerolactone/water solvent*, *Journal of Molecular Catalysis A: Chemical* 422/2016, 18–22.

- [59] Kikhtyanin O., Bulanek R., Frolich K., Cejka J., Kubicka D., *Aldol condensation of furfural with acetone over ion-exchanged and impregnated potassium BEA zeolites*, Journal of Molecular Catalysis A: Chemical 424/ 2016, 358–368.
- [60] Zhang L., Xi G., Chen Z., Jiang D., Yu H., Wang X., *Highly selective conversion of glucose into furfural over modified zeolites*, Chemical Engineering Journal 307/2017, 868–876.
- [61] Kumar V.B., Pulidindi I.N., Mishra R.K., Gedanken A., *Ga Modified Zeolite Based Solid Acid Catalyst for Levulinic Acid Production*, Chemistry Select 1/2016, S952–S960.
- [62] Ya'aini N., Amin N.A.S., Asmadi M., *Optimization of levulinic acid from lignocellulosic biomass using a new hybrid catalyst*, Bioresource Technology 116/2012, 58–65.
- [63] Zeng W., Cheng D., Zhang H., Chen F., Zhan X., *Dehydration of glucose to levulinic acid over MFI-type zeolite in subcritical water at moderate conditions*, Reaction Kinetics and Mechanisms of Catalyts 100/2010, 377–384.
- [64] Ramli N.A.S., Amin N.A.S., *Fe/HY zeolite as an effective catalyst for levulinic acid production from glucose: Characterization and catalytic performance*, Applied Catalysis B: Environmental 163/2015, 487–498.
- [65] Ramli N.A.S., Amin N.A.S., *Kinetic study of glucose conversion to levulinic acid over Fe/HY zeolite catalyst*, Chemical Engineering Journal 283/2016, 150–159.
- [66] Chamnankid B., Ratanatawanate C., Faungnawakij K., *Conversion of xylose to levulinic acid over modified acid functions of alkaline-treated zeolite Y in hot-compressed water*, Chemical Engineering Journal 258/2014, 341–347.
- [67] Jow J., Rorrer G.L., Hawley M.C., *Dehydration of d-fructose to levulinic acid over LZV zeolite catalyst*, Biomass 14/1987, 185–194.
- [68] Antunes M.M., Lima S., Neves P., Magalhaes A.L., Fazio E., Fernandes A., Neri F., Silva C.M., Rocha S.M., Ribeiro M.F., Pillinger M., Urakawa A., Valente A.A., *One-pot conversion of furfural to useful bio-products in the presence of a Sn,Al-containing zeolite beta catalyst prepared via post-synthesis router*, Journal of Catalysis 329/2015, 522–537.
- [69] Bui L., Luo H., Gunther W.R., Roman-Leshkov Y., *Domino Reaction Catalyzed by Zeolites with Brønsted and Lewis Acid Sites for the Production of γ -Valerolactone from Furfural*, Angewandte Chemistry Int. Ed. 52/2013, 8022 –8025.
- [70] Wang J., Jaenicke S., Chuah G.K., *Zirconium–Beta zeolite as a robust catalyst for the transformation of levulinic acid to γ -valerolactone via Meerwein–Ponndorf–Verley reduction*, RSC Advances 4/2014, 13481–13489.
- [71] Pavone A., *Bio-based adipic acid*, A private report by the Process Economics Program Report 284, Santa Clara, California 2012.
- [72] Lari G.M., Mondelli C., Perez-Ramirez J., *Gas-Phase Oxidation of Glycerol to Dihydroxyacetone over Tailored Iron Zeolites*, ACS Catalysis 5/2015, 1453–1461.
- [73] Dapsens P.Y., Kusema B.T., Mondelli C., Pérez-Ramírez J., *Gallium-modified zeolites for the selective conversion of bio-based dihydroxyacetone into C1–C4 alkyl lactates*, Journal of Molecular Catalysis A: Chemical 388–389/2014, 141–147.
- [74] Dapsens P.Y., Menart M.J., Mondelli C., Pérez-Ramírez J., *Production of bio-derived ethyl lactate on GaUSY zeolites prepared by post-synthetic galliation*, Green Chemistry 16/2014, 589–593.

- [75] Hammaecher, C., Paul, J.-F. *Density functional theory study of lactic acid adsorption and dehydration reaction on monoclinic 011, 101, and 111 zirconia surfaces*, *Journal of Catalysis* 300/2013, 174–182.
- [76] Ohara T., Sato T., Shimizu N., Prescher G., Schwind H., Weiberg O., Marten K., Greim H., *Acrylic Acid and Derivatives in Ullmann's Encyclopedia of Industrial Chemistry* Wiley-VCH, Weinheim 2003.
- [77] Mäki-Arvela, P., Simakova, I., Salmi, T., Murzin, D. Yu., *Production of Lactic Acid/Lactates from Biomass and Their Catalytic Transformations to Commodities – A Review*, *Chemical Reviews* 114/2014, 1909–1971.
- [78] <https://mcgroup.co.uk/news/20140508/china-leads-acrylic-acid-market-terms-production-consumption.html> (access: 15.04.2018).
- [79] Yan B., Li-Zhi Tao, Liang Y., Bo-Qing Xu, *Sustainable Production of Acrylic Acid: Catalytic Performance of Hydroxyapatites for Gas-Phase Dehydration of Lactic Acid*, *ACS Catalysis* 4/2014, 1931–1943.
- [80] Wang H., Yu D., Sun P., Yan J., Wang Y., Huang H., *Rare earth metal modified NaY: Structure and catalytic performance for lactic acid dehydration to acrylic acid*, *Catalysis Communications* 9/2008, 1799–1803.
- [81] Sun P., Yu D., Fu K., Gu M., Wang Y., Huang H., Ying H., *Potassium modified NaY: A selective and durable catalyst for dehydration of lactic acid to acrylic acid*, *Catalysis Communications* 10/2009, 1345–1349.
- [82] Yan J., Yu D., Heng H.L., Sun P., Huang H., *NaY zeolites modified by La³⁺ and Ba²⁺: the effect of synthesis details on surface structure and catalytic performance for lactic acid to acrylic acid*, *Journal of Rare Earths*. 28/2010, 803.
- [83] Sun P., Yu D., Tang Z., Li H., Huang H., *NaY Zeolites Catalyze Dehydration of Lactic Acid to Acrylic Acid: Studies on the Effects of Anions in Potassium Salts*, *Industrial Engineering and Chemical Resources* 49/2010, 9082–9087.
- [84] Sun P., Yu D., Fu K., Gu M., Wang Y., Huang H., Ying H., *Potassium modified NaY: A selective and durable catalyst for dehydration of lactic acid to acrylic acid*, *Catalysis Communications* 10/2009, 1345–1349.
- [85] Zhang X., Lin L., Zhang T., Liu H., Zhang X., *Catalytic dehydration of lactic acid to acrylic acid over modified ZSM-5 catalysts*, *Chemical Engineering Journal* 284/2016, 934–941.
- [86] Yuan C., Liu H., Zhang Z., Lu H., Zhu Q., Chen Y., *Alkali-metal-modified ZSM-5 zeolites for improvement of catalytic dehydration of lactic acid to acrylic acid*, *Chinese Journal of Catalysis* 36/2015, 1861–1866.
- [87] Yan B., Mahmood A., Liang Y., Xu B.Q., *Sustainable production of acrylic acid: Rb⁺- and Cs⁺-exchanged Beta zeolite catalysts for catalytic gas-phase dehydration of lactic acid*, *Catalysis Today* 269/2016, 65–73.
- [88] Hong J.H., Lee J.-M., Kim H., Hwang Y.K., Chang J.-S., Halligudi S.B., Han Y.-H., *Efficient and selective conversion of methyl lactate to acrylic acid using Ca₃(PO₄)₂-Ca₂(P₂O₇) composite catalysts*, *Applied Catalysis A* 396/2011, 194–200.

- [89] Zhang Z., Qu Y., Wang S., Wang J., *Effect of Municipal Sewage Treatment Plant Effluent on Bioaccumulation of Polychlorinated Biphenyls and Polybrominated Diphenyl Ethers in the Recipient Water*, *Environmental Science Technology* 41/2007, 6026–6032.
- [90] Murphy B.M., Letterio, M.P. and Xu B., *Catalyst Deactivation in Pyridine-Assisted Selective Dehydration of Methyl Lactate on NaY*, *ACS Catalysis* 7/2017, 1912–1930.
- [91] *CEH Marketing Research Report Acrylic Acid and Esters*, SRI Consulting, <https://chemstore.ihsmarket.com/products/ceh-acrylic-acid-and-esters> (access: 15.04.2018).
- [92] Blanco E., Lorentz C., Delichere P., Burel L., Vrinat M., Millet J.M.M., Loridant S., *Dehydration of ethyl lactate over alkaline earth phosphates: Performances, effect of water on reaction pathways and active sites*, *Applied Catalysis B: Environmental* 180/2016, 596–606.
- [93] Corma, A., *Inorganic Solid Acids and Their Use in Acid-Catalyzed Hydrocarbon Reactions*, *Chem. Rev.* 95/1995, 559–614.

Łukasz Majewski  orcid.org/0000-0002-9766-2064

l.majewski@pollub.pl

Janusz W. Sikora  orcid.org/0000-0002-2790-8823

Department of Technology and Polymer Processing, Mechanical Engineering Faculty,
Lublin University of Technology

MECHANICAL PROPERTIES OF POLYETHYLENE FILLED WITH TREATED NEUBURG SILICEOUS EARTH

WŁAŚCIWOŚCI MECHANICZNE POLIETYLENU NAPEŁNIONEGO MODYFIKOWANĄ NEUBURSKĄ GLINKĄ KRZEMIANOWĄ

Abstract

This paper reports the results of research on the mechanical properties of HDPE-matrix composite filled with three types of Neuburg Siliceous Earth (NSE). The HDPE/NSE composites are prepared by twin-screw direct extrusion, with the filler content ranging between 0wt% and 60wt%. Thereby, the prepared molded pieces are subjected to tests in order to determine Young's modulus and tensile strength, impact strength and hardness. The results are thoroughly examined based on the morphological and geometrical features of the applied fillers, such as particle size (2–10 μm) and specific surface (7–9 m^2/g). The effect of the chemical properties of the filler surface on its interaction with the matrix and strength is determined. The effects of the chemical activation of the filler surface by vinyl-functional silanes on their strength properties is described, and the variations in interactions on the matrix-filler interface are explained.

Keywords: mineral filler, polyolefins, coupling agent, high density polyethylene, HDPE

Streszczenie

W poniższej pracy przedstawiono wyniki badań właściwości mechanicznych kompozytów na osnowie HDPE napełnionych trzema różnymi rodzajami modyfikowanej Neuburskiej Glinki Krzemianowej. Kompozyty HDPE/NGK przygotowano w procesie dwuślimakowego wytłaczania współbieżnego zmieniając zawartość napełniacza w przedziale 0–60% mas. Gotowe wypraski wtryskowe poddano próbie zrywania, w celu wyznaczenia m.in. modułu Younga i wytrzymałości na rozciąganie oraz badaniom udarności i twardości. Dokonano szczegółowej analizy otrzymanych wyników w oparciu o cechy morfologiczne i geometryczne napełniaczy, takie jak wielkość ziarna (2–10 μm) i powierzchnia właściwa (7–9 m^2/g). Określono wpływ chemicznych właściwości powierzchni napełniacza na jego interakcje z osnową i właściwości wytrzymałościowe. Opisano efekty chemicznej aktywacji powierzchni napełniaczy środkami sprzęgającymi w postaci winylo-funkcyjnych silanów na właściwości wytrzymałościowe oraz wyjaśniono, w jaki sposób zmieniają oddziaływania na granicy fazowej osnowa-napełniacz.

Słowa kluczowe: napełniacz mineralny, poliolefiny, środek sprzęgający, polietylen dużej gęstości, PE-HD

1. Introduction

Injection molding is currently the most popular polymer processing method, mainly because of its short duration, a wide range of operational opportunities it offers, and high precision of produced molded pieces regardless of the material used. This process is employed to manufacture a vast majority of complex-shaped parts, which must meet high dimensional accuracy requirements [1]. Currently, about a third of thermoplastics used in the polymer processing industry are subjected to injection molding, and a half of manufactured machines and devices are used for injection molding [1]. The application of untreated polymers does not, however, meet today's design and economic requirements. Given the emphasis on reducing production costs along with a growing demand for materials with specified new properties, polymers are more and more often subjected to modification [2, 3]. Polymers with varying properties are produced by physical or chemical modification, reactive processing, the addition of fillers or auxiliary agents [2, 4–6]. For this reason, the composite injection molding process is preceded by extrusion to produce extrudate made of primary polymers and composite granulated products, which are then used to manufacture composite molded pieces [7].

The making of polymer compounds is an interdisciplinary problem. When selecting a filler and its content, one must take into account various factors and parameters from the field of chemistry, physical chemistry of polymers, mechanical engineering, rheology, materials engineering, and even the design of processing machines [2, 3, 8]. The selection of a suitable filler and its content enables shaping properties of composite materials as desired. Polymer compounds are usually used in order to improve properties, such as impact strength, hardness, grindability, tensile or bending strength, chemical resistance, temperature stability, flammability, thermal and electrical conductivity, etc. [2–4, 9]. Besides the filler's type and content, the properties of produced composites are also significantly affected by the degree of polymer dispersion together with the polymer's structure, characteristics of adhesion phenomena, the applied processing technology, etc. [4, 10, 11]. It is a more and more common practice to modify filler surface in order to intensify surface interactions by increasing the specific surface area of the particles or by coating the particles with an active compound to increase interfacial compatibility [2, 3, 5]. This leads to higher cohesion and uniformity of the composite [4, 9, 12].

The objective of this study is to describe the variations in selected mechanical properties of a high-density polyethylene-matrix composite versus the content of treated Neuburg Siliceous Earth (NSE), and to explain the effect of NSE modifications on the observed variations in the examined properties of the produced composite. Another goal of this paper is also to determine the suitability of NSE for thermoplastics processing applications, a problem which has not yet received adequate attention.

2. Experimental

2.1. Material

The tests were conducted using high-density polyethylene, Hostalen GD 7255, manufactured by Orlen Polyolefines (Plock, Poland) and mainly used for the production of details and thin-walled parts. Basic properties of the tested polymer provided by the manufacturer are listed in Table 1.

Table 1. Basic properties of high-density polyethylene Hostalen GD 7255

Property	Unit	Value
Density	kg/m ³	955
Melt flow rate (190°C/2.16kg)	g/10 min	4
Melt flow rate (190°C/5.0kg)	g/10 min	11
Tensile modulus	MPa	1180
Tensile Stress at Yield	MPa	27
Tensile Strain at Yield	%	8
Charpy notched impact strength (23°C, Type 1, Notch A)	kJ/m ²	10
Charpy notched impact strength (-30°C, Type 1, Notch A)	kJ/m ²	5
Shore hardness (Shore D)	°ShD	60
Ball indentation hardness (H 132/30)	MPa	52
Vicat softening temperature (B50, 50°/h, 50N)	°C	70

The applied fillers were different types of treated siliceous earth manufactured in the vicinity of Neuburg, Germany. Neuburg siliceous earth is a natural mixture of silica and lamellar kaolinite impossible to separate by physical methods. The two minerals form a loose structure the silica has the form of aggregated spherical cryptocrystalline particles covered by its amorphous variety due to natural forming processes. Given such a structure, the silica has an extensive specific surface, which has a positive effect on its mechanical properties [13, 14].

Currently, there are two groups of fillers containing Neuburg Siliceous Earth manufactured by Hoffman Mineral (Neuburg, Germany). The first group includes natural siliceous earth, Silitin, the types of which differ with respect to particle size distribution and color neutrality. The other group includes siliceous earth treated with silanes; these fillers have varying properties.

Table 2 lists a selection of properties describing the three NSE types examined in this study.

Table 2. Selected properties of treated types of NSE [15]

Property	Unit	Silfit Z91	Aktifit VM	Aktisil VM56
Base material	–	Sillitin Z86	Silfit Z91	Sillitin Z86
Particle size	µm	2–10	2–10	2.2–10
Density	kg/m ³	2600	2600	2600
Bulk density	kg/m ³	330	420	320
Specific surface area	m ² /g	8	7	9
Oil absorption	g/100g	55	55	45
Treatment	–	Thermal treatment – calcination	Addition of vinyl–functional silane	Addition of vinyl–functional silane
Mineral composition:				
Cryptocrystalline silica		60	60	60
Amorphous silica	%	0	0	10
Kaolinite		0	0	25
Calcinated kaolinite		30	30	0
Other		10	10	5

Silfit Z91 is a natural mixture of amorphous and cryptocrystalline silica and lamellar kaolinite subjected to calcination [13, 15], hence it can be used as a functional filler [13]. The fillers Aktifit VM and Aktisil VM56 were treated by the addition of vinyl-functional silane, an adhesion promoter used for the modification of the surface of mineral materials joined with polyolefines [4, 13, 15].

2.2. Test stand

The preparation of test specimens and determination of their mechanical properties were made possible using the equipment available at the Institut für Produktionstechnik which is part of Westsächsische Hochschule in Zwickau, Germany. The composite granulate was prepared using a ZSK18 MEGAlab twin-screw direct extruder manufactured by Coperion Werner and Pfeleiderer GmbH (Stuttgart, Germany). At its end, the extrusion line had an SP 30 Pure pelletizer from Pell-Tec GmbH (Stuttgart, Germany), used for pelletizing cooled plastic strands. Composite specimens were produced using a Krauss Maffei KM 50-55 CX injection molding machine (Munich, Germany). The tensile testing of the obtained molded pieces was performed using a Z010 Zwick/Roell testing machine (Ulm, Germany). Hardness measurements were made with a Shore hardness tester from Heinrich Bareiss Prüfgerätebau GmbH (Oberdisingen, Germany). Impact strength measurements were made using a QC-639 F impact tester manufactured by Comotech (Taizhong, Taiwan).

2.3. Investigated parameters

Given the objective of the study, we devised a set of key parameters describing the two investigated processes, i.e. extrusion with pelletizing and injection molding, as well as individual test stands. The parameters were divided into five groups.

Direct factors:

- ▶ molded piece width a , mm,
- ▶ molded piece thickness b , mm.

Indirect factors:

- ▶ the cross-sectional area of the molded piece s , mm²,
- ▶ the energy required to break the test piece L , kJ,
- ▶ Young's modulus E , MPa,
- ▶ tensile strength σ_m , MPa,
- ▶ strain at maximum tensile stress, %,
- ▶ tensile strain at break A , %,
- ▶ tensile stress at break σ_u , MPa,
- ▶ Shore hardness H , °ShD,
- ▶ impact strength U , kJ/m².

Variables:

- ▶ filler type (Silfit Z91, Aktifit VM, Aktisil VM56),
- ▶ filler content (10 wt%, 20 wt%, 30 wt%, 40 wt%, 50 wt%, 60 wt%).

Constant parameters:

- ▶ polymer (HDPE),
- ▶ geometrical dimensions of the extruder head nozzle and injection mold cavity,
- ▶ the pressure in the extruder head 8 bar,
- ▶ technological parameters of the extrusion process: screw rotational speed in the plasticizing unit: 120 rev/min, the temperature in individual zones of the plasticizing unit: 130°C, 140°C, 150°C, 160°C, 170°C and 180°C,
- ▶ the temperature of the injection mold: 19°C,
- ▶ technological parameters of the injection molding process: temperature in the plasticizing unit - 180, 200 and 220°C, injection pressure - 1050 bar, holding pressure - 600 bar, holding time - 6 s, cooling time - 20 s, injection cycle time - 35 s.
- ▶ Charpy pendulum machine energy - 5 J.

Disturbing factors:

- ▶ electric voltage: from 219 V to 241 V,
- ▶ relative air humidity: from 55% to 65%,
- ▶ ambient temperature: from 20°C to 24°C.

The above disturbing factors had a negligible effect on the obtained measurement results.

2.4. Experimental details

For the experiments, we prepared three batches of injection molded pieces filled with three types of treated Neuburg Siliceous Earth. The polymer granulate was coated with a surface modifying agent, i.e. carbofunctional silane with the trade name aminopropyltriethoxysilane, and then mechanically mixed with the filler. The modifying agent was 0.4 wt% of the prepared polymeric compound. The composite granulate was prepared by twin-screw direct extrusion with cold pelletizing. The granulates containing 40%-60 wt% of the filler were prepared by the



mechanical mixing of the composite granulate with 30 wt% of NSE containing between 10% and 30% of the filler. As a result, we obtained 18 groups of granulated products with different filler types and contents, which were then used to make tensile test pieces. The injection mold cavities had the dimensions complying with ISO 294-1:2002. The tensile tests of composite molded pieces and the determination of their strength parameters were conducted in compliance with ISO 527-1:2012. The Charpy impact tests were run in compliance with ISO 179-1:2010. The Shore hardness measurements were made in compliance with ISO 868:2005.

3. Results and discussion

Based on the results, we devised charts illustrating the relationships between Young's modulus, tensile strength, tensile strain at break, strain at maximum tensile stress, tensile strength at break, hardness, as well as the type and content of Neuburg Siliceous Earth. In addition, the results of impact strength tests are discussed.

3.1. Tensile strength

The relationship between Young's modulus and the content and type of treated Neuburg Siliceous Earth is illustrated in Fig. 1. The addition of the lowest investigated content of NSE leads to a decrease in Young's modulus of all three types of the filler compared to untreated polyethylene; however, a further increase in the NSE content leads to a gradual increase in Young's modulus for all types of NSE. The decrease in Young's modulus in the entire investigated range for Silfit Z91 is 33 MPa, which is 4.6% of the initial value. Young's modulus of Aktifit VM-filled specimens increases to 844 MPa for 60 wt% of the filler, which is 117.2% of the initial value, and for Aktisil VM56 – the parameter is 817 MPa (60 wt% filler), which means an increase by 13.4%.

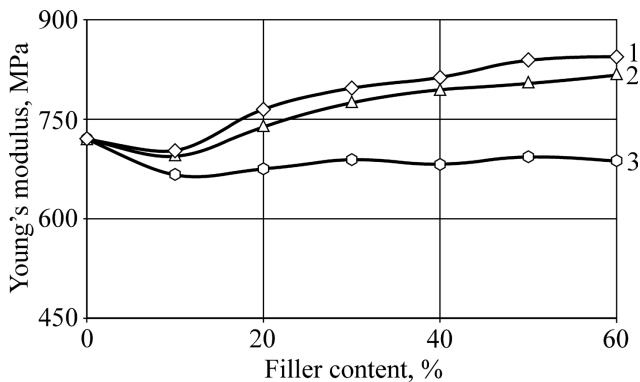


Fig. 1. Young's modulus versus filler content: 1 – Aktifit VM, 2 – Aktisil VM56, 3 – Silfit Z91

Young's modulus describes the elasticity of a given material, and its increase means that rigidity has increased while strain has decreased due to stress. The addition of mineral

microfillers leads to an increase in rigidity by increasing the crystallization degree of the polymer matrix in the immediate vicinity of the filler [4, 12, 16, 17]. To improve composite rigidity, it is necessary to obtain an adequate degree of dispersion of the filler in the die impression [4]. The coating of Aktisil VM56 and Aktifit VM particle surfaces with a compatibilizer (vinyl-functional silane) to facilitate particles dispersion [18] led to a higher rigidity and Young's modulus. Silfit Z91 was not treated with any coupling agent. It was subjected to calcination, a process which leads to the degradation of surface hydroxyl groups and assigning filler particles with hydrophobic properties [19, 20]. This operation should improve the dispersion of filler particles in the matrix with hydrophobic polymer chains. Nonetheless, the study [20] reports that calcinated kaolinite bonds steam from the air, and hence spontaneously produces polar hydroxyl groups on the filler surface, thereby providing this surface with hydrophilic properties, which can decrease the dispersion of filler particles in the non-polar matrix due to the incompatibility of the filler surface and the polymer matrix [18]. This is a probable cause of the decrease in Young's modulus.

The results demonstrate that tensile strength changes in a similar way to Young's modulus. Following the addition of the filler, the tensile strength suddenly decreases; then, it begins to gradually increase with increasing the NSE content (Fig. 2). The tensile strength of the investigated composites obtained at 60 wt% of the filler is lower than the tensile strength of the original polyethylene (21 MPa), and the measured percentage differences are: 0.5% for Aktifit VM, 1.9% for Aktisil VM56 and 6.7% for Silfit Z91.

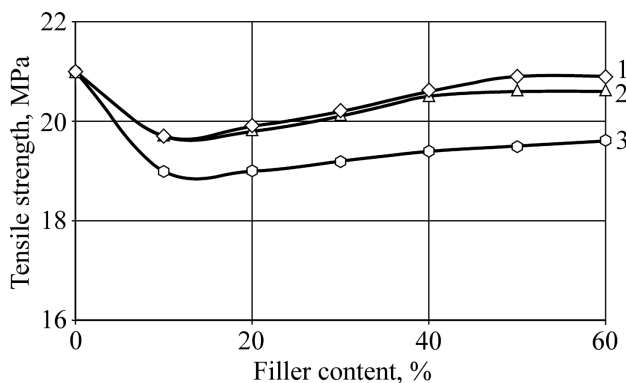


Fig. 2. Tensile strength versus filler content: 1 – Aktifit VM, 2 – Aktisil VM56, 3 – Silfit Z91

The consolidation mechanisms of composites with powder fillers are strictly connected with such properties as particle size, specific surface and the degree of particle dispersion in the matrix, as well as the properties of adhesion promoters which cause the coupling of filler particles and matrix material due to chemical bonds [4]. The observed drop in the tensile strength of the three filler types can result from a wide range of particle sizes (Table 2). The mechanism of consolidating polymers with particles is connected with cavitation and the tension of spaces formed in a direction of the acting force [16, 18]. A detailed description of this mechanism is given by Kim and Michler [21]. It is taken that the promoter effect occurs

for particle size lower than 5 μm ; otherwise, the formed pockets will be too large, and can hence be the place promoting crack initiation [15]. Composite strength can be reduced even due to a small amount of oversized particles [3, 4]. A large specific surface of particles will not produce the desired consolidation effect without a suitable distribution of particles in the matrix [16]. Despite the larger specific surface of particles, the composite specimens filled with Silfit Z91, reveal a significantly higher decrease in their tensile strength than the specimens filled with Aktifit VM. Besides mechanical adhesion, Silfit Z91 does not reveal the presence of any additional fiber-matrix bonding mechanisms, which – combined with lower dispersion – leads to a higher drop in tensile strength. The smaller specific surface of Aktifit VM, when compared to Silfit Z91, results from the nature of the coupling agent. Vinyl-functional silanes can undergo condensation and form complex compounds on the surface, with two alkoxy groups forming a long chain, while the third one forms a bond with the filler's surface [22]. The particle size prevents them from penetrating all surface irregularities, which results in a reduction of the specific surface [4]. The main promoter effect is therefore based on chemical interactions [12], with the surface modifier acting as an intermediary between the mineral filler and the polymeric matrix due to the alkoxy group and the carbon-carbon double bond in the vinyl group [22]. The same relationships can be observed for composites filled with Aktisil VM56, which means that the coupling agent increases the interactions between the polymeric phase and the filler surface [23]. The observed small differences regarding the silane-treated fillers (with the best results observed for Aktifit VM) can stem from the difference in particle size (Table 2).

Minimal tensile strengths at break are shown in Fig. 3. The increase in the content of Aktifit VM causes a decrease in tensile strength at break in the entire investigated range of its content. The tensile strength at break decrease from 11.5 MPa for untreated PE to 7.79 MPa for 60 wt% of Aktifit VM, i.e. by 32.3%. The charts illustrating the variations in tensile strengths at break versus filler content for Aktisil VM56 and Silfit Z91 differ from those for Aktifit VM. The tensile strength at break initially decreases, and after reaching a certain critical filler content it begins to increase rapidly.

The curve illustrating the relationship between tensile strength at break and filler content for Aktisil VM56 has two characteristic points: the first point marks the moment when the tensile strength at break suddenly increases and can be observed at 40 wt% of the filler, while the other point marks the beginning of plateau and can be observed at 50 wt% of the filler. The measured change in the tensile strength at break is 71.3%, from 11.5 MPa for the unfilled polymer to 19.7 MPa for 60 wt% of the filler. The minimal tensile strength at break for 40 wt% filler is 4.98 MPa. The curve for Silfit Z91 would probably have the same pattern, but the filler contents applied in accordance with the research program did not enable us to indicate on the diagram the point which marks the beginning of the upper plateau. The tensile strength at break at the maximum filler content is 18.9 MPa, which indicates an increase of 64.3%, while the minimal value for the 50 wt% content would amount to 6.46 MPa.

The relationship between the strain at maximum tensile stress and the filler type and content is shown in Fig. 4. Compared to the original HDPE, one can observe that the strain at maximum tensile stress decreases from 9% to 8.7% for the test specimens containing Aktisil

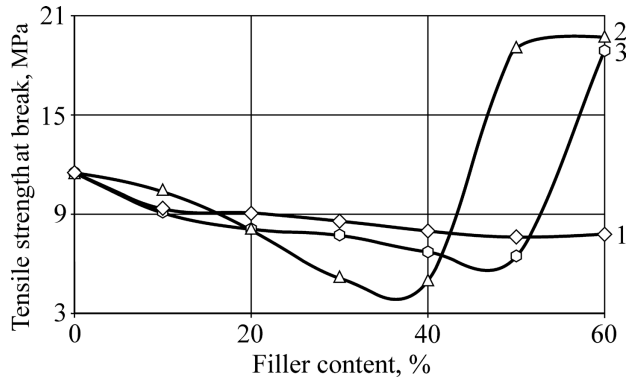


Fig. 3. Tensile strength at break versus filler content: 1 – Aktifit VM, 2 – Aktisil VM56, 3 – Silfit Z91

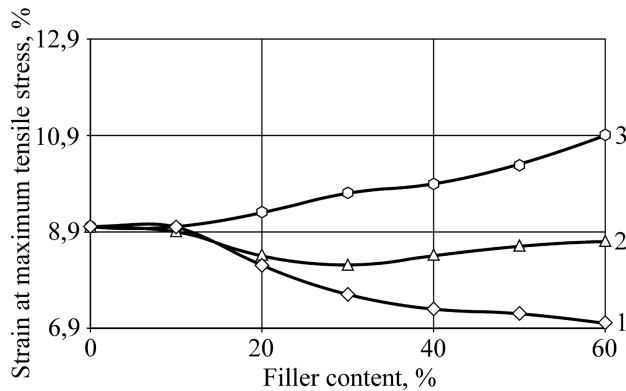


Fig. 4. Strain at maximum tensile stress versus filler content: 1 – Aktifit VM, 2 – Aktisil VM56, 3 – Silfit Z91

VM56. With increasing the content of Aktifit VM in a range from 0 wt% to 60 wt%, the strain at maximum tensile stress drops to 7%. On increasing the content of Silfit Z91, the strain at maximum tensile stress increases steadily, irrespective of the applied filler content.

The pattern of curve 3 (Fig. 4) probably results from the distribution of filler particles. The filler without a coupling agent can form agglomerates with scarce interactions between the particles [12]. The loose agglomerations of filler particles easily decompose due to tensile stress. As a result, the composite has a lower tensile strength. The study [17] demonstrates that in the composites containing over 5 wt% of silica, silica tends to form agglomerates and hence its strength decreases, which proves the above considerations. Therefore, an increase in the content of Silfit Z91 leads to a slight yet continuous increase in the tensile strain. The interaction between Aktifit VM and Aktisil VM56 particles and the matrix is much stronger than that observed for Silfit Z91 particles. Modified with silane, the filler surface has acquired organophilic properties, and hence increased its interfacial compatibility enabling their dispersion in the polymeric matrix [23, 24, 25]. The formation of suspended fine particles chemically bonded with the matrix leads to a higher rigidity and lower strain by constraining the movement of polymer chains. The energy of particles dispersion in the matrix decreases with an increase in particle size [4]; therefore, given the presence of aggregated spherical

silica particles in NSE, the addition of the coupling agent can have a crucial effect on both the filler's dispersion in the matrix and the mechanical properties of the composite.

The diagrams illustrating the relationship between tensile strain at break and filler content and type shown in Fig. 5 reveal a tendency for the tensile strain at the break to decrease with an increase in the content of the three types of NSE. The highest variation in the tensile strain at break in the entire range of the investigated variable is observed for the specimens containing Aktifit VM, where the tensile strain at break decreases from 590% (PE) to 16% at the highest filler content. Following the application of Aktisil VM56, the strains in the polyethylene composite decrease to 8.4%, and after the addition of Silfit Z91 – they decrease to 44% for the same range of the investigated variable.

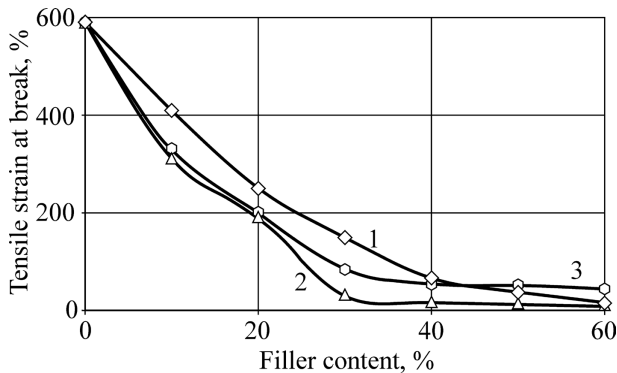


Fig. 5. Tensile strain at break versus filler content: 1 – Aktifit VM, 2 – Aktisil VM56, 3 – Silfit Z91

The addition of high contents of the mineral fillers leads to reduced composite elasticity described by tensile strain at break. Despite the modification of filler surface by vinyl-functional silane, the test specimens containing Aktifit VM exhibit only slightly higher strength properties compared to those filled with Aktisil VM56. This can probably result from a slight difference in the particle size of the two fillers (Table 2). The effect of modifying the filler with the coupling agent is that long polymer chains become stable in the structure of the matrix while the energy required for the initiation of polymer chain motion increases [12]. High contents of Silfit Z91, despite no applied chemical modification of particle surface, also lead to a rapid drop in the maximum strains, which can result from the accumulation of large amounts of imprecisely mixed mineral particles on the section of the specimen and low interaction between the filler particles and the polymer matrix, as well as the nature of polymer reinforcement with dispersed particles [16, 21].

3.2. Impact strength

Analyzing the results for all tested specimen batches, i.e. three types of Neuburg Siliceous Earth and all filler contents, we can observe that there occurs no single case of complete specimen fracture. Given the lack of complete fracture, it must, therefore, be stated that based on ISO 179-1:2010 the impact strength of all tested specimens is 0 kJ/m². Examples

of specimens after the impact strength tests are shown in Fig. 6. Based on the experimental results and the behavior of the specimens during the impact test, we can, however, draw some conclusions about the strength of the tested specimens. Due to the impact, the specimens made of Silfit Z91-filled PE undergo deformation and then they fall out of the holder. Using a comparative method it has been found that the deflection angle increases with increasing the filler content. A different observation was made for the specimens containing Aktiftit VM – they undergo slight deformation but do not fall out of the holder, while the drop weight rebounds. It has been estimated by a comparative method that the deflection angle of the specimens decreases after the impact with increasing the content of Aktiftit VM. In the tests of Aktisil VM56-filled specimens, the drop weight also rebounds during the impact. The angle of deflection slightly increases with changing the filler content in a range between 10 wt% and 40 wt%. It is however difficult to estimate the deflection at higher contents of Aktisil VM56 due to the occurrence of partial cracking. The observed phenomena confirm the previously reported relationships between rigidity and strain versus applied filler contents.

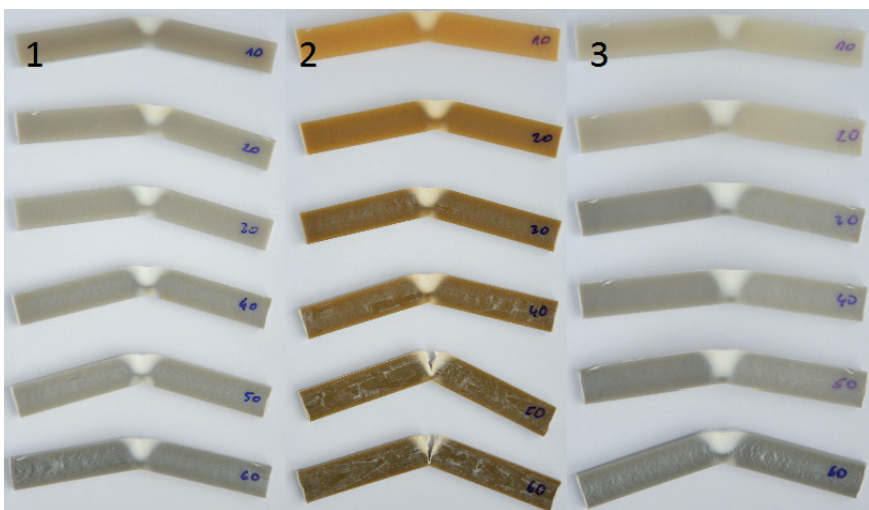


Fig. 6. Specimens after impact strength tests: 1 – Aktiftit VM, 2 – Aktisil VM56, 3 – Silfit Z91

3.3. Hardness

The chart given in Fig. 6 illustrates the hardness of injection molded pieces versus the type and content of the filler. The results are similar for the three investigated types of Neuburg Siliceous Earth.

Initially, the hardness increases to the maximum value for 30% content of the filler; a further increase in the filler content causes a slight decrease in hardness. The measured values of the maximum harness are respectively: 66.1°ShD for Aktisil VM56, 66.5°ShD for Aktiftit VM and 64.7°ShD for Silfit Z91. The differences between the hardness of the original PE (60°ShD) and that of the composite with 60 wt% of the filler are: 10.2% for Aktisil VM56, 10.8% for Aktiftit VM, and 7.8% for Silfit Z91, respectively.

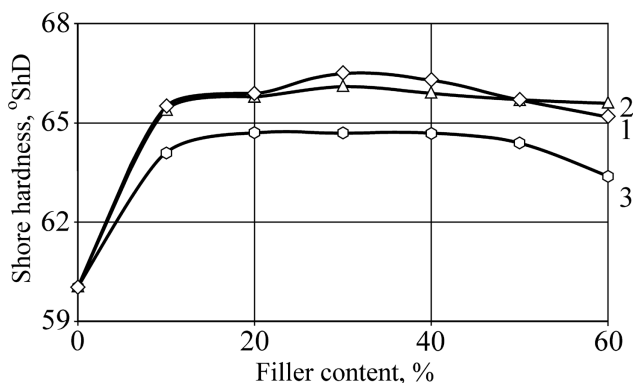


Fig. 7. Shore hardness versus filler content: 1 – Aktifit VM, 2 – Aktisil VM56, 3 – Silfit Z91

The addition of the mineral filler leads to a higher degree of crystallinity of the polymer matrix in the immediate vicinity of the filler [4, 12, 16, 17]. The increase in hardness of the composites containing silane can result from the fact that the addition of silica-organic compounds causes an additional increase in the degree of crystallinity of the polymer matrix [3]. It is, however, difficult to explain the drop in hardness at the maximum filler contents based on the test results.

4. Conclusions

The effect of the filler on the polymer matrix depends on a number of factors, the most important of these being the size and shape of particles as well as the type of adhesive interactions. The above factors have a decisive effect on the impact between the matrix polymer and the disperse phase. The strength of the tested mineral fillers predominantly depends on their chemical properties which are, in turn, affected by modification via the addition of adhesion promoters. The highest strength has been observed for the fillers treated with vinyl-functional silanes.

Comparing the results of the composites filled with Silfit Z91 and Aktifit VM, it can be observed that the addition of the fillers containing silane-based adhesion promoters leads to higher mechanical properties of the composites than is the case with the fillers which do not contain any coupling agent. The chemical modification of the mineral fillers can lead to producing composites with the desired physical and mechanical properties at relatively low costs.

The results of the specimens filled with Silfit Z91 demonstrate that the filler has a negative influence on their strength properties which, in many cases, are lower than the properties of the original PE. In addition, the results for the composites containing Silfit Z91 significantly differ from those obtained for the specimens filled with vinyl-functional silane.

The results demonstrate that the mechanical properties of the tested composite materials can be shaped as desired via the addition of a suitable content of silane-treated NSE. Given the observed improvement in the mechanical properties of the tested NSE-filled specimens, it can be concluded that this type of filler is suitable for polyethylene injection molding.

The authors would like to thank the German Academic Exchange Service (DAAD) and Prof. Dr. Ing. Torsten Merkel, head of the Institut für Produktionstechnik of Westsächsische Hochschule in Zwickau, for financial and organizational support of the research.

References

- [1] Osswald T., Turng L., Gramann P., *Injection molding handbook*, Hanser Publishers, Munich 2001.
- [2] Katz H., Milewski J., *Handbook of fillers for plastics*, Van Nostrand Reinhold, New York 1987.
- [3] Rotheron R., *Particulate-filled polymer composites*, Second Edition, Rapra Technology Limited, Shawbury 2003.
- [4] Rotheron R., *Mineral fillers in thermoplastics, filler manufacture and characterisation*, Advances in Polymer Science, 139, 1999, 67–107.
- [5] Xiang B., Jiang G., Zhang J., *Surface modification of TiO₂ nanoparticles with silane coupling agent for nanocomposite with poly(butyl acrylate)*, *Plastics, Rubber and Composites*, 44, 2015, 148–154.
- [6] Hidayah N., Mariatti M., Ismail H., Kamarol M., *Evaluation of PP/EPDM nanocomposites filled with SiO₂, TiO₂ and ZnO nanofillers as thermoplastic elastomeric insulators*, *Plastics, Rubber and Composites*, 44, 2015, 259–264.
- [7] Samujlo B., Sikora J. W., *The impact of selected granulometric properties of poly(vinyl chloride) on the effectiveness of the extrusion process*, *Journal of Polymer Engineering*, 28, 2013, 77–85.
- [8] Sikora J. W., Sasimowski E., *Influence of the length of the plasticating system on selected characteristics of an autothermal extrusion process*, *Advances in Polymer Technology*, 24, 2005, 21–28.
- [9] Chou T., *Structure and properties of composites. Materials science and technology*, Volume 13, Structure and properties of composites, VCH Verlagsgesellschaft, Weinheim 1993.
- [10] Mareri P., Bastide S., Binda N., Crespy A., *Mechanical behaviour of polypropylene composites containing fine mineral filler, Effect of filler surface treatment*, *Composite Science and Technology*, 58, 1998, 747–752.
- [11] Głogowska K., Sikora J. W., Duleba B., *Effect of mechanical properties of metal powder-filled hybrid moulded products*, *Journal of Polymer Engineering*, 7, 36, 2016, 705–712.
- [12] Pukanszky B., Fekete E., *Adhesion and surface modification*, *Advances in Polymer Science*, 139, 1999, 109–217.
- [13] Heckl S., Oggermüller H., Zehnder M., *Neuburg Siliceous Earth in MS-polymer based Sealants*, Hoffman Mineral GmbH, www.hoffman-mineral.com, access 15.11.2017.
- [14] Göske J., Kachler W., *Morphology, physicochemistry and phase analysis of Neuburg Siliceous Earth*, *Microscopy and Analysis*, 22, 2008, 23–24.
- [15] *Functional fillers for coatings*, Hoffman Mineral GmbH, www.hoffman-mineral.com (access 15.11.2017).

- [16] Zuiderduin W., Westzaan C., Huetink J., Gaymans R. J., *Toughening of polypropylene with calcium carbonate particles*, *Polymer*, 44, 2003, 261–275.
- [17] Fu S., Feng X., Lauke B., Mai Y., *Effects of particle size, particle/matrix interface adhesion and particle loading on mechanical properties of particulate-polymer composites*, *Composites, Part B*, 39, 2008, 933–961.
- [18] Tjong S., *Structural and mechanical properties of polymer nanocomposites*, *Materials Science and Engineering, R. Reports*, 53, 2006, 73–197.
- [19] Liu Q., Spears D., Liu Q., *MAS NMR study of surface-modified calcined kaolin*, *Applied Clay Science*, 19, 2001, 89–94.
- [20] Zuhua Z., Xiao Y., Huajun Z., Yue C., *Role of water in the synthesis of calcined kaolin-based geopolymer*, *Applied Clay Science*, 43, 2009, 218–223.
- [21] Kim G., Michler G., *Micromechanical deformation processes in toughened and particle filled semicrystalline polymers, Part 2, Model representation for micromechanical deformation processes*, *Polymer*, 39, 1998, 5699–5703.
- [22] Liu P., *Polymer modified clay minerals, A review*, *Applied Clay Science*, 38, 2007, 64–76.
- [23] Fischer H., *Polymer nanocomposites, from fundamental research to specific applications*, *Materials Science and Engineering C*, 23, 2003, 763–772.
- [24] Alexandre M., Dubois P., *Polymer-layered silicate nanocomposites, preparation, properties and uses of a new class of materials*, *Materials Science and Engineering*, 28, 2000, 1–63.
- [25] Suberlyak O.V., Krasins'kyi V.V., Moravs'kyi V.V., Gerlach H., Jachowicz T., *Influence of aluminosilicate filler on the physico-mechanical properties of polypropylene-polycapramide composites*, *Materials Science*, 50, 2014, 296–302.
- [26] PN-EN ISO 294-1, 2002 Tworzywa sztuczne – Wtryskiwanie kształtek do badań z tworzyw termoplastycznych – Część 1, Zasady ogólne, formowanie uniwersalnych kształtek do badań i kształtek w postaci beleczek.
- [27] PN-EN ISO 527-1, 2012 Tworzywa sztuczne – Oznaczanie właściwości mechanicznych przy statycznym rozciąganiu – Część 1, Zasady ogólne.
- [28] PN-EN ISO 179-1, 2010 Tworzywa sztuczne – Oznaczanie udarności metodą Charpy'ego – Część 1, Nieinstrumentalne badanie udarności.
- [29] PN-EN ISO 868, 2005, Tworzywa sztuczne i ebonit – Oznaczanie twardości metodą wciskania z zastosowaniem twardościomierza (twardość metodą Shore'a).

Przemysław Migas  orcid.org/0000-0003-4940-0999

przemyslaw.migas@pk.edu.pl

Jerzy Baron  orcid.org/0000-0002-6512-8983

Faculty of Chemical Engineering and Technology, Cracow University of Technology

THE CO-COMBUSTION OF RUBBER WASTE WITH LPG FUEL IN A FLUIDISED BED REACTOR

WSPÓLSPALANIE ODPADÓW GUMOWYCH Z PALIWEM LPG W PĘCHERZOWYM ZŁOŻU FLUIDALNYM

Abstract

This paper presents experimental results relevant to the thermal utilisation of rubber wastes. The investigation employed a laboratory-scale bubbling fluidised bed combustor, (BFBC) running on liquefied petroleum gas with quartz sand as the inert bed material. When rubber samples (tyre fragments) were added, the reactor temperature and flue gas concentrations of CO, VOC, SO₂, NO_x and HCl were monitored. Tests were performed with bed temperatures of 800-1000°C and two different masses of the bed. It has been found that the emitted quantities of NO_x and CO were dependent not only on the sample mass but also on the mass (depth) and temperature of the fluidised bed and dropped whilst the bed depth was increased and its temperature was raised.

Keywords: rubber composite materials, combustion, fluidisation, LPG fuel

Streszczenie

W artykule przedstawiono rezultaty eksperymentu termicznej utylizacji odpadów gumowo-kompozytowych w pęcherzowym złożu fluidalnym zasilanym paliwem gazowym LPG. Podczas procesu dokonywano pomiaru temperatury złoża oraz analizy składu spalin jak CO, VOC, SO₂, NO_x oraz HCl. Proces współspalania materiałów gumowych prowadzony był przy zmiennej masie (250 i 500g) i temperaturze złoża 800–1000°C. Bazując na bilansie masowym węgla, przeprowadzono obliczenia kinetyczne termicznej utylizacji próbki. Stwierdzono, że ilości emitowanych NO_x oraz CO zależą nie tylko od masy próbki, ale również od masy i temperatury złoża fluidalnego, i zmniejszają się one wraz ze wzrostem wartości wspomnianych zmiennych.

Słowa kluczowe: materiały gumowo-kompozytowe, spalanie fluidyzacja, paliwo LPG

1. Introduction

The mass consumption of industrial goods is the main cause of municipal waste. Furthermore, there is a growing demand for both heat and electric power. Burning waste such as rubber or plastic, with very high fuel values, can combine waste disposal with energy production. Rubber waste consists of old vehicle tyres, transmission belts, rubber hoses, inner tubes, gaskets, etc. Therefore, by far the main source of rubber waste is the motor industry.

A vehicle tyre is a complex product containing, in addition to very durable rubber, strengthening components such as synthetic fibres and steel cords [1]. The construction of a tyre, from the point of view of the vehicle user, gives an ideal result with respect to its mechanical properties, but creates environmental problems. In Europe, around 3 million tons of old tyres (used tyre – UT) have to be disposed of annually. In 2013, around 3.6 million tons [2] had to be dealt with. Some (around 0.9 million tons) could still be used after re-trading [5]; the remainder were classified as ‘end of life’ ELT. In 2013, 2.7 million tons were recycled as materials or through energy recovery, which accounts for 96% of the total ELT [4]. In 2010, waste tips contained about 0.15 million tons of tyres [5]. This naturally had adverse effects on the environment, created a fire hazard and a health hazard as old tyres can serve as a breeding ground for rodents and insects [3]

A number of methods for utilising this waste have been developed, ranging from simple solutions like using whole tyres in various constructions to more advanced technologies of recycling and energy recovery [1]. As a fuel, the rubber from vehicle tyres is more homogeneous than coal. Its heat of combustion is high ($31.438.8 \text{ MJ kg}^{-1}$) and the content of mineral matter does not usually exceed 3.3% [6]. The efficiency of the combustion of a fuel normally depends on many factors such as its type and form, the concentration of the oxidiser and the temperature of the process. Parameters such as the size of the surface for heat and mass exchange or the degree of homogeneity of the fuel-oxidiser mixture depend on the combustion technology and the type of furnace employed.

Usually, the co-combustion of rubber waste takes place during the production of cement and this accounts for 91% of the tyres utilised during energy recovery[4]. Using tyres as an alternative to coal makes it possible to lower the costs of cement production. One of the advantages is that rubber provides the necessary sulphur as well as, for example, certain non-combustible components, such as metal oxides, the presence of which improves the quality of the clinker obtained.

The tyres are fed to the furnace either whole or fragmented as tyre derived fuel (TDF). Since the residence time of tyres or TDF in an environment is short where the prevailing temperature is significantly higher than $1,500^\circ\text{C}$ it is completely consumed[7], while the emissions of dioxins and the products of incomplete combustion remain very low. However, cement kilns are few and far between which increases the costs of transportation. Furthermore, tyres are completely consumed in a cement kiln, so that even partial recovery of the steel elements present in the tyres is impossible. In addition to utilisation in rotary cement kilns, TDF can be used in heat and power plants, e.g. in moving grate furnaces. This makes it possible to utilise tyres of various sizes, with relatively low operational costs. Complications

arising during the process are usually associated with the limited availability of the oxidiser necessary to assure the complete combustion of the waste[8].

Installations employing fluidised beds are free from this problem and their use in the thermal utilisation of rubber wastes has been discussed in many publications. For example, Chyang et al. used a rotating bed to burn tyres and other forms of rubber waste[9, 10] They found that if the combustor is supplied with rubber fragments that are uniform in size, the increased frequency with which the fuel is fed in leads to lower CO emissions and a higher mean bed temperature. In addition, they noted that if an additional stream of air was directed to the freeboard, this improved the conversion of the volatile products of the incomplete decomposition of hydrocarbons and its suitable method of introduction and feed rate can help in the formation of horizontal eddies, facilitating the efficient removal of small dust particles. Another example of the use of FBC technology is the co-combustion of rubber waste with coal. Alvarez et al. [6] and Calle 'n et al. [11] found that an increased rubber content in a solid fuel mixture leads to higher emissions of aromatic compounds and an increased zinc content in the solid products from the process, particularly in the form of volatile ash. Fluidised bed combustors, FBCs, should be suitable for burning tyre wastes. The disadvantages are the costs, both operational and those associated with fragmenting the material. In this respect, the effectiveness could be improved by, for example, burning larger batches of the waste. However, the main advantage of the method is its flexibility, since it offers the possibility of utilising not only combustible solids, but also liquids or gases. Another factor is the possibility of limiting noxious emissions. Thus, FBC installations can be used to burn various other forms of waste[12], such as polymers[13, 15] biomass, [16], [18] and electronic waste[23] in addition to rubber.

The literature suggests that the problems associated with the batch method of burning rubber can be avoided if the fragmented waste is continuously supplied to a FBC running on gaseous fuel. This stabilises the temperature and the continuous combustion of the gas and ensures the presence of sufficient concentrations of free radicals, which play a crucial role in the attack on the volatile products of the thermal decomposition of both rubber volatiles and solids. However, basic information relevant to this type of approach to burning rubber waste appears to be absent. The present work was undertaken to elucidate the thermal decomposition of rubber during combustion, to study the composition of the flue gases and its dependence on the type of rubber waste burned and on the temperature and the effective height of the fluidised bed.

2. Materials, Apparatus, Methods

The experiments were carried out using a laboratory-scale bubbling fluidised bed reactor described in detail elsewhere[24]. It consisted of a cylindrical quartz glass tube, 98 mm in diameter and 500 mm long, resting on a distributor plate made of Cr-Ni steel, with approximately 433 uniformly distributed holes (diameter = 0.6 mm; free area = 1.6%). The bed material used was quartz sand, 250 or 500 g, particle size 300-385 μm , giving a stationary bed depth of 2.2 or 4.5 cm, depending upon the experimental condition. At 20°C, the air supply rate was $1.92 \cdot 10^{-3} \text{ m}^3 \text{ s}^{-1}$, and the supply rate of LPG was $3.42 \cdot 10^{-4} \text{ m}^3 \text{ s}^{-1}$. The two



streams were mixed with before entering the reactor (air excess was 40%). The temperature inside the reactor was monitored using two shielded Ni-NiCr thermocouples, mounted at 20 and 50 mm above the distributor. Readings from these were registered at a frequency of 10 Hz. The flue gases were analysed using a FTIR Gasmet™ DX-4000 analyser, the time of analysis was approximately 8 s. A schematic diagram of the apparatus is shown in Fig. 1.

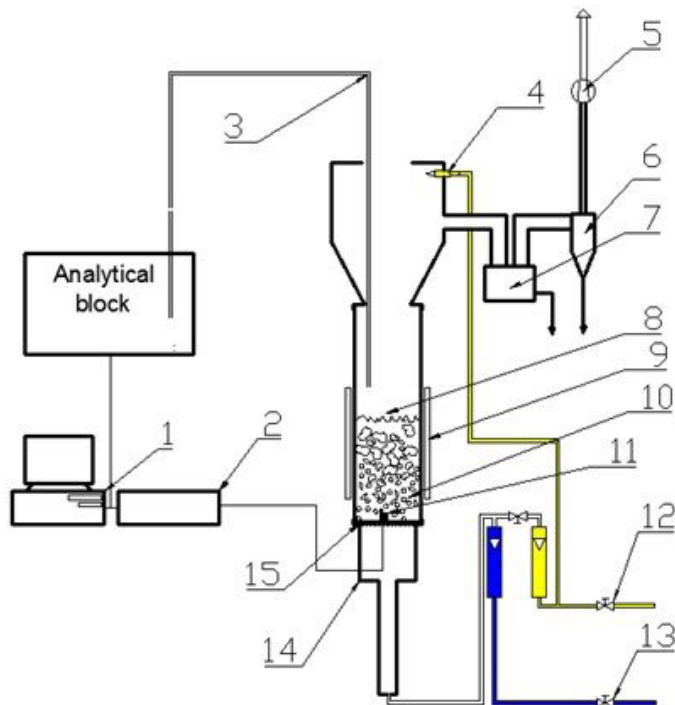


Fig. 1. Experimental arrangement – schematic representation

- 1 – computer storing chemical analysis quantities and temperature signals, 2 – A/D convertor for thermocouple signals, 3 – heated probe for sampling the flue gases, 4 – pilot flame, 5 – exhaust fan, 6 – cyclone, 7 – ash trap for coarser particles, 8 – freeboard space, 9 – movable radiation shield, 10 – bubbling bed, 11 – thermocouples, 12 – fuel supply valve, 13 – air supply valve, 14 – plenum chamber, 15 – flat, perforated metal plate

In the course of the experiments, three types of tyre rubber were tested: samples with synthetic fibres (with a polyester coating) taken from the sides of tyres, fragments with steel reinforcement and fragments with chlorinated copolymers. The sample mass used was up to 4 g. Table 1 shows the three types of sample and gives their C, H and N contents, determined by the combustion method, using a Perkin Elmer 2400 instrument (detection is conducted using an IR detector).

The results obtained for the C, H and N content of the samples investigated were comparable with the analytical results provided by other investigators [8, 19, 20, 21, 22]. The carbon in the copolymer was lower and amounted to 70-75% of that in the rubber samples while the nitrogen content was 3-4 times higher.

Table 1. Samples of the wastes investigated and their analytical content of C, H and N, mass %



Tyre fragments containing synthetic fibre		Material from a tyre with steel reinforcement		Copolymer	
C	85.1	C	78.2	C	60.2
H	7.8	H	6.9	H	5.1
N	0.3	N	0.44	N	1.3

3. Results and discussion

a) Visual observations

Single Samples of car tyre material were added to a fluidised bed combustor operating at a stable temperature. Rapid fragmentation of the sample started immediately and blue flames appeared inside the bed (Fig. 2).

Because of the rapid formation of combustible volatiles, they may remain unburned inside the bed. Since the position of the sample and later the positions of its fragments in the bed were constantly changing, the residence time of the volatile pyrolysis products inside the bed was not always sufficient for the reaction to finish. This led to transient diffusion flames also appearing above the bed surface, a typical flame lasted for around 0.1s [13]. It was also noted that not all gas bubbles ignited on reaching the bed surface. This was probably because the time spent by the gases inside the bubbles that failed to ignite was less than the induction period for ignition [25]. It was also possible that the composition of the gases inside some bubbles was outside the ignition limits for the mixture (i.e. insufficient combustibles or lack of oxidant). The flames above the bed gradually died out whilst inside the bed, the remaining carbonaceous solid particles were slowly consumed in a heterogeneous combustion process. The bright burning particles could be clearly seen moving inside the bed in a similar manner as during the combustion of coal (Fig. 2). The VOC formation and their combustion had a stochastic character, consistent with the intensive movement of fuel particles inside the bed. The sinking down of a sample inside the bed and its remaining there would be possible if its density is greater than the local mean density of its surroundings [14]. This might occur with sand grains sticking to the sample, increasing its effective size and thus the apparent mean density.

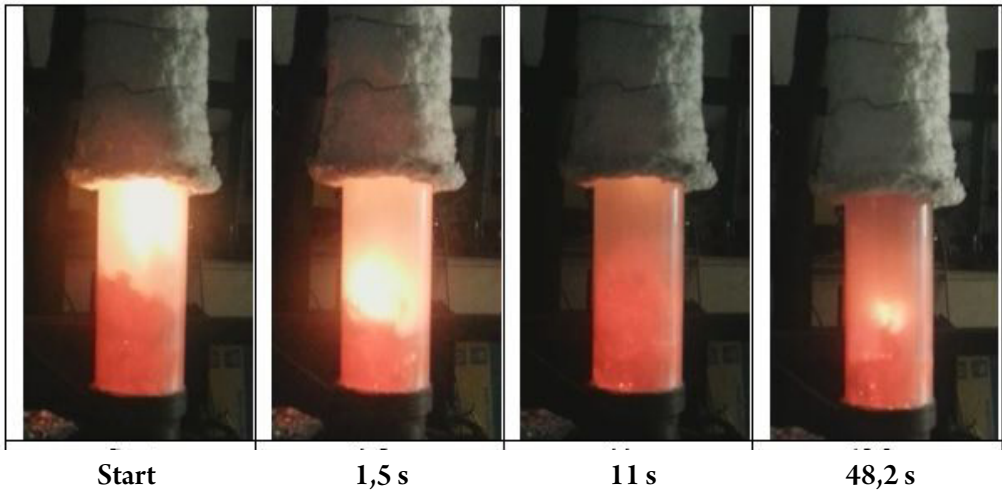


Fig. 2. Selected frames from a film documenting selected stages of the experiment of copolymer combustion

b) Chemical Analysis of the flue gases

When a sample of tyre material was dropped on the surface of the hot fluidised bed, there was always a sharp decrease in the O_2 concentration in the off gases and peaks appeared in the concentrations of the reaction products, including VOC and CO (Fig. 3), resulting from the pyrolysis of the sample and the combustion process.

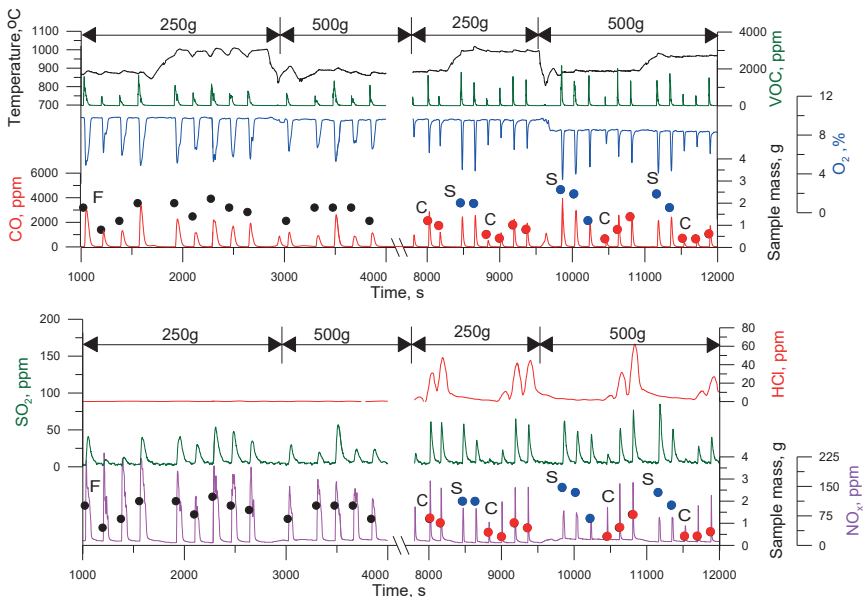


Fig. 3. Selected experimental results (sample F – with synthetic fibre, S – with steel reinforcement, C – the copolymer; dots show the sample mass)

Changes in the concentrations of CO and VOC were linked and the width of the VOC peaks was less than that of the other products. This indicates that the VOC emission drops in the further stages of sample decomposition e.g., after the burning of solid residues (char particles). HCl and SO₂ emission depends on the mass and sample type, whereas for the VOC and NO_x depends also on the height and temperature bed. The maximum values of nitrogen oxide varied within the range of 50–250 ppm, and they did not exceed 400 ppm for sulphur dioxide. HCl was detected only during copolymer combustion, and the concentration changed within the range of 5–80 ppm.

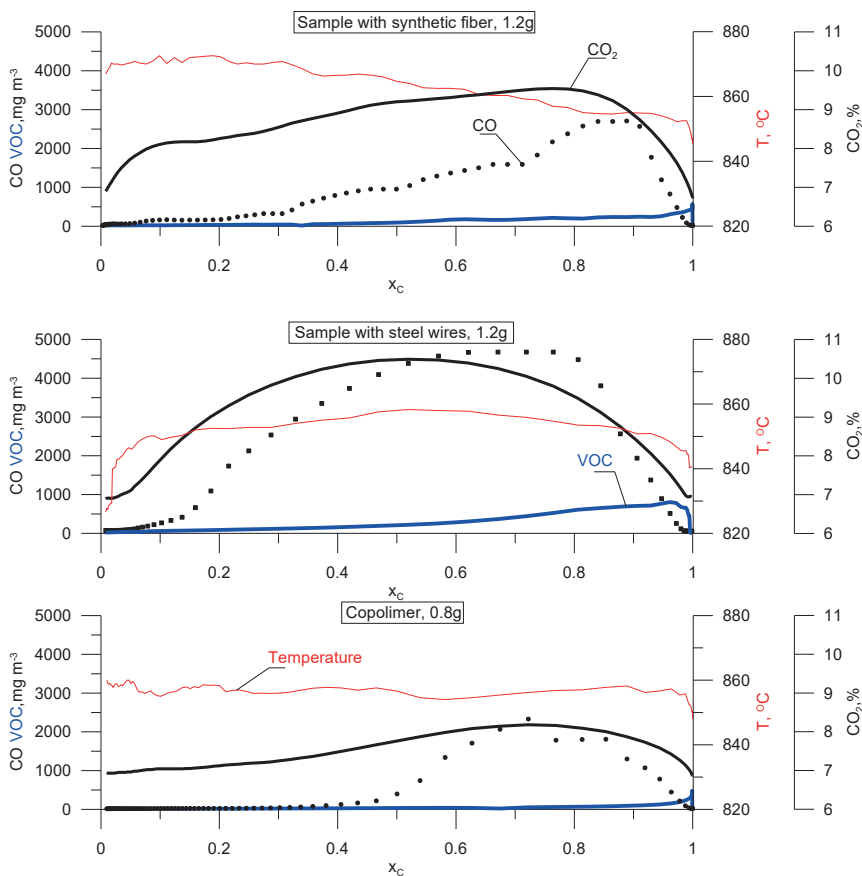


Fig. 4. Selected experimental results as a function of a carbon mass fraction (remaining in the combustion zone)

Rapid emissions of VOC may be recorded immediately samples are introduced to the hot bed. The peak level of VOC is twice as high for the sample with steel reinforcement than for the other samples. During the latter stages of VOC decomposition VOC concentration drops, which may indicate that the thermal decomposition of the samples is slower than the VOC oxidation process.

CO concentration (Fig. 5) decreases with increases in temperature; this is certainly attributed to the oxidation rate. The ignition of combustible gas products (in the gas-air bubble) of rubber degradation is possible at a certain bed height only if the flammability limit and proper temperature is maintained inside the bubble. If the VOC emission (caused by the rubber sample devolatilisation) is located near the bottom of the FBC while the bed temperature and air velocity remain constant, a higher bed enables a longer VOC residence time in the reaction zone. Therefore, if the bed porosity is similar, CO concentration decreases with increases to the bed mass. It was also observed that the presence of chlorine in the incinerated sample increases CO emission. Chlorine may behave like a flame retardant – gaseous HCl (a product of combustion) reacts with H· and OH· radicals which play an important role in hydrocarbon chain decomposition.

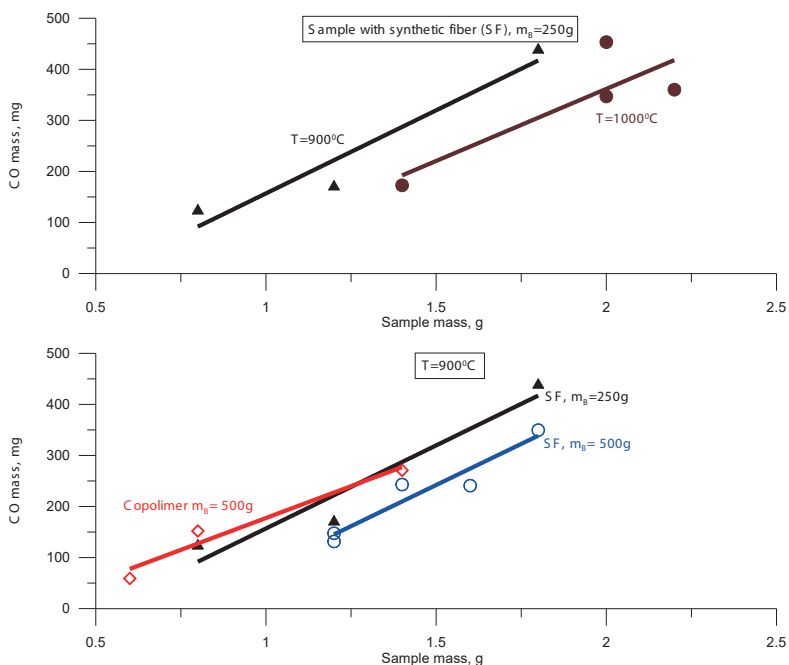
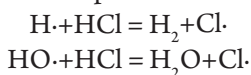


Fig. 5. Selected parameters influence on CO emission

NO_x emission (Fig. 6) decreases as the bed temperature increases. It is possible that two parallel processes occur. The first is that the pyrolysis rate rises as the bed temperature increases, which causes more intensive VOC emissions. As a consequence, NO_x reduction may occur in the gas layer surrounding the rubber sample (in processes such as re-burning) [27] [28]. An increasing rising bed temperature also causes the VOC and CO oxidation rate to increase resulting in a lack of oxygen in the reaction environment. NO_x emission (similar to CO) decreases with a higher bed mass. This phenomenon is connected with an increasing gas

residence time, which causes higher CO and VOC conversion. It may also be observed that the smallest NO_x concentration is measured during copolymer combustion, which can also be explained by the CO, and VOC reductive effect.

Comparison between CO and NO_x concentration didn't prove the diverse proportionality between concentrations of those two gases, as suggested by Duan's study [26]. Duan used rubber balls during the combustion process. During our research, additional effects may occur, such as the influence of synthetic fibre combustion, which may disturb the CO and NO_x concentration relationship.

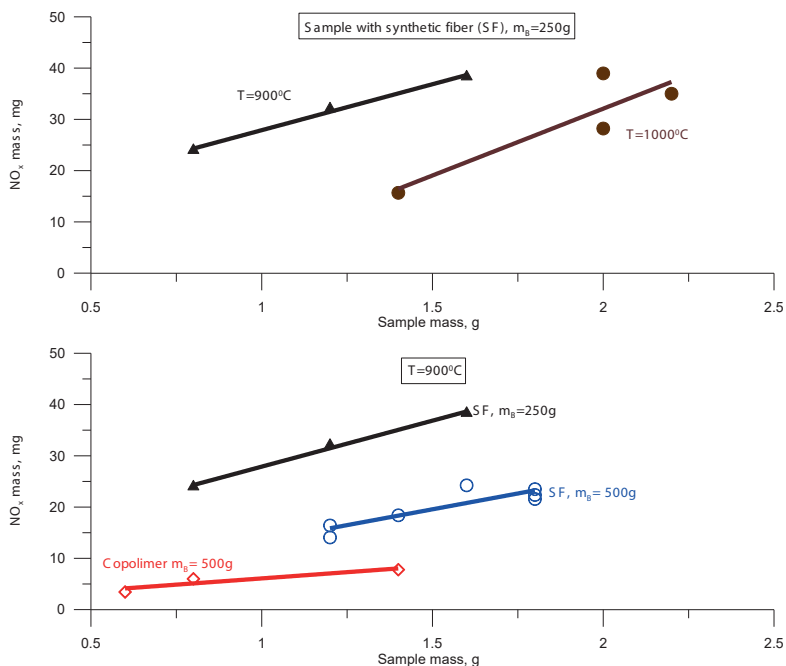


Fig. 6. The influence of selected parameters on NO_x emission

In Fig. 7, the comparison that was made between the co-incineration and incineration processes (with and without additional LPG fuel) is presented for the 0.4 g rubber sample with synthetic fibres. Changes in the NO_x and CO concentrations in the two processes are presented in Fig. 7 (oxygen concentration during co-combustion was around 10%). When additional fuel wasn't supplied, CO concentration was around 50 ppm whilst during co-combustion, it reached around 2,500 ppm.

Drops in the level of CO concentration are certainly linked with a higher rates of burning with O_2 concentration. Nitrogen oxide synthesis is possible not only from the fuel's nitrogen but also from the air if the temperature is high enough. Thus, NO_x emission during co-incineration is higher than it is from combustion. Which is attributed to the presence of CHi radicals that are formed during the combustion of hydrocarbons [29]

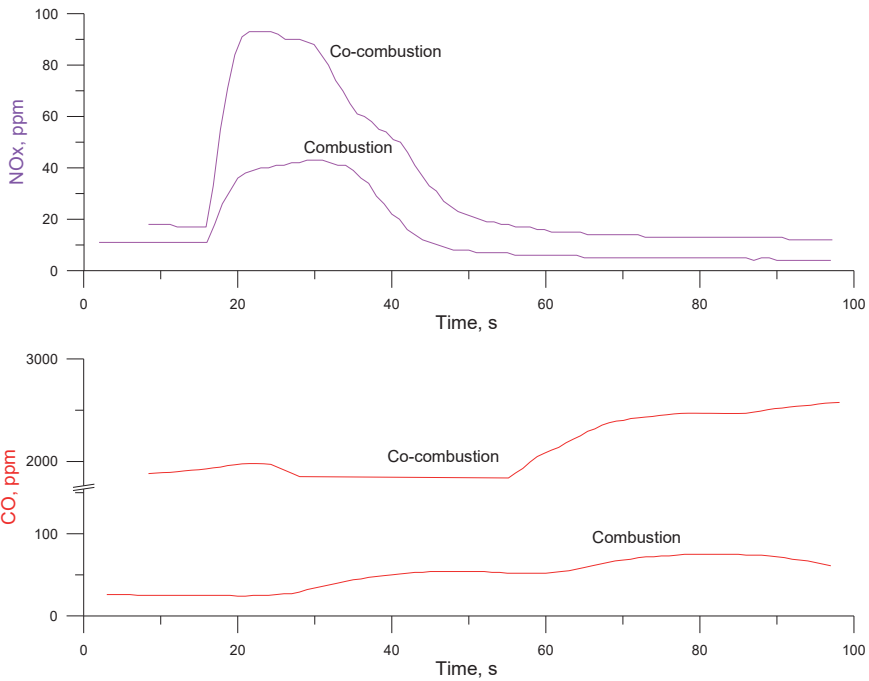


Fig. 7. Comparison between CO and NO_x concentration during combustion and co-combustion processes (sample with synthetic fibre)

The recovery of steel elements may be important from the economic point of view due to this being a special steel of high quality. The long residence time of steel elements at high temperature and the very corrosive environment of HCl, and SO₂ gases causes huge deterioration of its surface and internal structure (Fig. 8). From the material recovery point of view, it's important to limit the steel element residence time to the necessary minimum.

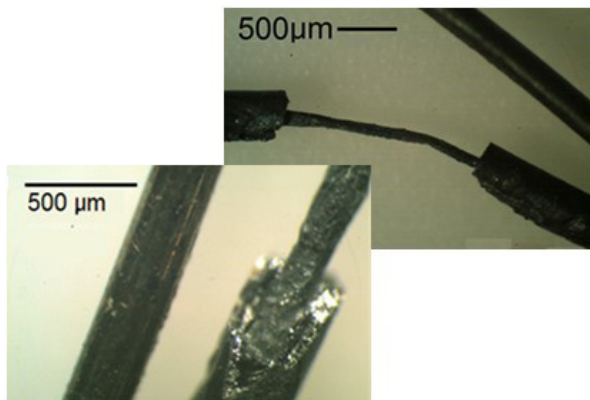


Fig. 8. Steel elements before and after being introduced to the reactor ~1h residence time in the reaction zone

4. Conclusions

During the incipient stage of rubber composite material combustion (intensive rubber devolatilization), high emission of VOC and flame above the bed is observed. Next, the residual char particles are after-burned. Flame occurrence was very irregular; this may be linked to the inflammable character of the gas inside the bubble, the stochastic rubber sample movement, and the subsequent changeable residence time of gaseous products and the time of bubble heating (time ignition initiation must be exceeded in order for combustion to occur in the bed).

During the combustion of the copolymer and the sample with steel elements, the VOC emission is higher than from the sample with synthetic fibres. In the copolymer, this is attributed to the presence of chlorine, while in the sample with steel elements, it may be caused by the thermal degradation rate growth (the presence of steel elements causes an intensification of the heat transfer to the interior of the sample).

The recovery of steel elements may be important from the economic point of view due to this being a special steel of high quality. However, due to high temperature corrosion and the presence of HCl and SO₂ in the reaction zone, it is necessary to limit the steel elements residence time to the minimum that is necessary.

References

- [1] Erich F., Erman B., Mark J., *The science and technology of rubber*, Elsevier, 2005.
- [2] The Waste & Resources Action Programme – The Composition of a Tyre: Typical Components Project code: TYR0009-02,
- [3] <http://www.wrap.org.uk/sites/files/wrap/2%20-%20Composition%20of%20a%20Tyre%20-%20May%202006.pdf> (access: 08.03.18).
- [4] UNEP/CHW.10/6/Add.1/Rev.1 Technical guidelines on the environmentally sound
- [5] co-processing of hazardous wastes in cement kilns, <http://www.basel.int/Portals/4/Basel%20Convention/docs/pub/techguid/cement/tg-cement-e.pdf> (access: 12.03.18).
- [6] ETRMA, End-of-life Tyre Report 2015,
- [7] <http://www.etrma.org/uploads/Modules/Documentsmanager/elt-report-v9a---final.pdf> (access: 08.03.18).
- [8] End of life tyres. A valuable resource with growing potential 2011 edition, <http://www.etrma.org/uploads/Modules/Documentsmanager/brochure-elt-2011-final.pdf> (access: 12.03.18).
- [9] Bautista D., Carmen M., Jul C., Jul R., Mastral A.M., Rodríguez A., Rodríguez M.A., *AFBC of coal with tyre rubber Influence of the co-combustion variables on the mineral matter of solid by-products and on Zn lixiviation*, "Fuel", 106/2013, 10–20.
- [10] Scrap Tire Management Council, The Use of Scrap Tires in Rotary Cement Kilns, https://rma.org/wp-content/uploads/cement_kiln_report.pdf (access: 12.03.18).
- [11] Annus J., Jelemenský L., Juma M., Koreňová Z., Markoš J., *Pyrolysis and combustion of scrap tyre*, "Petroleum & Coal" 48/2006, 15–26.

- [12] Chyang C., Ho J.A., Shang S., Teng H., *Characterization of Waste Tire Incineration in a Prototype Vortexing Fluidized Bed Combustor*, "Journal of the Air & Waste Management Association", 47/1997, 49–57.
- [13] Duan F., Chyang C., Hsu S., Tso J., *Combustion behavior and pollutant emissions of batch fluidized bed combustion*, "Journal of the Taiwan Institute of Chemical Engineers" 44/2013, 1034 – 1038.
- [14] Calle'n, M.S. Mastralm A.M., Garcí'a T., *Fluidized Bed Combustion (FBC) of Fossil and Nonfossil Fuels. A Comparative Study*, "Energy & Fuels" 14/000, 275–281.
- [15] Chirone R., Scala F., *Fluidized bed combustion of alternative solid fuels*, "Experimental Thermal and Fluid Science" 28/2004, 691–699.
- [16] Baron J., Bulewicz E.M., Kandeferski S., Pilawska M., Żukowski W., Hayhurst A.N., *The combustion of polymer pellets in a bubbling fluidised bed*, "Fuel", 85/2006, 2494–2508
- [17] Davidson J.F., Dennis J.S., Hayhurst A.N., Rees A.C., *The rise of a buoyant sphere in a gas-fluidized bed*, "Chemical Engineering Science" 60/2005, 1143–1153.
- [18] Burgess F., Lloyd P.D.W., Fennell P.S., Hayhurst A.N., *Combustion of polymer pellets in a bubbling fluidised bed*, "Combustion and Flame", 158/2011, 1638–1645
- [19] Khan A., Jong W., Jansens P.J., Spliethoff H., *Biomass combustion in fluidized bed boilers: Potential problems and remedies*, "Fuel processing technology", 90/2009, 21–50.
- [20] Fyttili D., Zabaniotou A., 4, "Renewable and Sustainable Energy Reviews", 12/2008, 116–140.
- [21] Okasha F., Zaater G., El-Emam, S., Awad M., Zeidan E., *Co-combustion of biomass and gaseous fuel in a novel configuration of fluidized bed: Combustion characteristics*, "Fuel", 133/2014, 143–152.
- [22] Cabrero M.A., Caballero B., Chomon M.J., Laresgoiti M.F., Rodriguez I., Torres A., *Pyrolysis of scrap tyres*, "Fuel Processing Technology" 72/2001, 9–22.
- [23] Kim D., Kim J., Lee J., Lee J., *Pyrolysis of waste tires with partial oxidation in a fluidized-bed reactor*, "Energy", 20/1995, 969–976.
- [24] Chirone R., Salatino P., Senneca O., *A fast heating-rate thermogravimetric study of the pyrolysis of scrap tyres*, "Fuel", 78/1999, 1575–1581.
- [25] Canito J., Encinar J., González J., Rodríguez J., *Pyrolysis of automobile tyre waste. Influence of operating variables and kinetics study*, "Journal of Analytical and Applied Pyrolysis", 58/2001, 667–683.
- [26] Woynarowska A., Witold Żukowski W., Żelazny S., *Thermal treatment of electronic waste in a fluidised bed and chemical digestion of solid products*, "Waste Management & Research", 34/2016, 605–618.
- [27] Baron J., Bulewicz E.M., Zabagło J., Żukowski W., *Propagation of Reaction Between Bubbles with a Gas Burning in a Fluidised Bed*, "Flow, Turbulence and Combustion" 88/2012, 479–502.
- [28] Żukowski W., *A simple model for explosive combustion of premixed natural gas with air in a bubbling fluidized bed of inert sand*, "Combustion and Flame" 134/2003, 399–409.

- [29] Chyang C.S., Duan F., Hsu S.H., Tso, J., *Combustion behavior and pollutant emissions of batch fluidized bed combustion*, "Journal of the Taiwan Institute of Chemical Engineers", 44/2013, 1034–1038.
- [30] Ho L., Maly P., Payne R., Zamansky V., *Alternative fuel reburning*, "Fuel" 78/1999, 327–334.
- [31] Smoot L.D., Hill S.C., Xu H., *NO_x Control Through Reburning*, "Progress in Energy and Combustion Science", 24/1998, 385–408.
- [32] Fenimore C.P., 13th Symposium (Int.) on Combustion, 13/1971, 373–380.

Jolanta Dźwierzynska

joladz@prz.edu.pl

Faculty of Civil and Environmental Engineering and Architecture, Rzeszow University
of Technology

SHAPING CURVED STEEL ROD STRUCTURES

KSZTAŁTOWANIE KRZYWOLINIOWYCH, STALOWYCH KONSTRUKCJI PRĘTOWYCH

Abstract

The paper addresses the problem of the efficient shaping of curved steel rod structures conducted based on the Enneper surface. The proposed parametric design process consists in linking the geometric shaping of grid models with their structural analysis and optimization, which is realized through the application of design tools working in the Rhinoceros 3D software. The mechanical performance of lattices covered with glass panels is evaluated and the structures are pre-dimensioned. The presented aesthetic grid shells with good structural characteristics may constitute original coverings. However, the analysis, which targets an early stage of the design, aims at providing design guidelines to facilitate communication between architects and civil engineers.

Keywords: parametric modeling, structural analysis, rod structures, Rhinoceros 3D, Grasshopper, Karamba 3D

Streszczenie

W artykule podejmuje się problem efektywnego kształtowania krzywoliniowych, stalowych konstrukcji prętowych utworzonych na bazie powierzchni Ennepera. Zaproponowany parametryczny proces kształtowania polega na powiązaniu geometrycznego kształtowania siatkowych modeli z ich analizą strukturalną i optymalizacją, realizowanymi za pomocą narzędzi projektowych pracujących w środowisku Rhinoceros 3D. Oceniono mechaniczne właściwości kratownic pokrytych taflami szklanymi, a struktury wstępnie zwymiarowano. Zaprezentowane powłoki kratowe o dobrych właściwościach strukturalnych mogą stanowić oryginalne przekrycia, natomiast analiza strukturalna ukierunkowana na wczesny etap projektowania ma na celu dostarczenie wytycznych projektowych ułatwiających komunikację między architektami i inżynierami.

Słowa kluczowe: parametryczne modelowanie, analiza strukturalna, struktury prętowe, Rhinoceros 3D, Grasshopper, Karamba 3D

1. Introduction

Architectural and civil engineering design during the last decade was inspired not only by various possibilities offered by digital technology, but also by other disciplines, such as mathematics and physics. The so-called “parametric design thinking” has been introduced, which stands for the ability to understand and construct complex and parametrized operations, which make a designed form respond and evolve [1–4].

Along this line of thought, the paper discusses a novel parametric approach to the conceptual design of steel grid structures. Grid shells are usually long span structures composed of a lattice of a single layer or multilayer members, which form a curved surface. The application of grid shell structures increased in the past decade, as they are an effective means of covering space. Grid structures can be used in various vertical and overhead applications, as well as in order to form complete building enclosures. They have a great potential to be applied both in readapting existing spaces and creating new aesthetically interesting and pleasing structures. Grid shell structures can be made of a wide range of materials, from wood to steel. The most popular are layered geodesic domes, which are shaped using the procedures of sphere division into triangles elaborated by Fuller [5]. However, the parametric study in this paper is conducted on the example of spatial lattice created basing on an Enneper surface. Recently, optimization in the parametric environment has been a subject of interest to many researchers [6,7]. Most contributions in this field are concerned with the optimization of geometric properties of meshes approximating free-form structures. Many works address the problem of the planarity of grid faces. However, we have not found research works considering the Enneper surface as a base for grid structure modeling. Our approach to grid shell design is to link geometric shaping of grid spatial forms with their structural analysis and optimization. A similar approach was applied in the case of designing roof shells composed of repetitive concrete modules of Catalan surfaces presented in [8]. The goal of our research is to elaborate universal scripts in order to create digital grid structure models of various shapes and various grid patterns, as well as to develop a methodology to calculate the change of the load-bearing capacity of grid structures depending on their curvature, the number of supports and topology. The geometric shaping of grid shells embraces the following phrases: parametric description of the models, assigning values to parameters in accordance with given requirements and constraints, generating alternatives as well as evaluating them.

2. Materials and methods

2.1. Characteristics of the applied software

Digital architecture has profoundly changed the processes of design and construction. Thanks to the application of new digital design tools, new forms can be examined much more comprehensively. The design approach to parametric modeling of grid structures proposed in this research is realized by the application of versatile tools: Grasshopper, and Karamba

3D, working in the same modeling software- Rhinoceros 3D. Grasshopper is generally used to algorithmically generate the desired framework and form the model, modify it, visualize and finally analyze it. However, the structural analysis is carried out using Karamba 3D. This plugin makes it extremely simple to combine parameterized complex geometric forms, load calculations and finite element analysis. Rhino/Grasshopper gives plenty of flexibility for design exploration. Due to this fact, it is very convenient during the initial design process. Grasshopper is one of the most commonly used generative design editors. It allows designers to build both simple and complicated complex forms. Moreover, during the generation of models, their geometric shapes are presented, whereas the mathematical description is hidden. Parametric design refers to the use of parameters, which are various constraints and dependencies. However, they are substantially responsible for determining the relationship between design intentions and design possibilities.

2.2. Geometric properties of the Enneper surface

Analytical definition of the geometric characteristics of the designed forms is becoming of more and more increasing interest and importance today. It concerns both the visual representation focused on the aesthetic appearance of structures and the analytical representation relating to the analysis of their geometric properties. The Enneper surface is a minimal and self-intersecting surface [9, 10]. However, it can take different shapes depending on the choice of parameters that define it. It also displays intrinsic curvature, so it should be resistant to certain deformations. Due to this fact, it is worth considering as a base surface for grid structures.

Enneper surfaces as three-dimensional objects in three-dimensional space can be described mathematically by simple equations with three space variables (x, y, z) . However, for the need of the creation of Grasshopper's algorithms, the surfaces should be described by two parameters (u, v) , which determine their shapes. The Grasshopper's toolbox provides components, which allowed us to analyze and evaluate various Enneper surface shapes. As the base surface for the generation of spatial lattices, we have chosen a regular, non-intersecting shape of the Enneper's surface, of which the horizontal projection is a circle (Fig. 1).

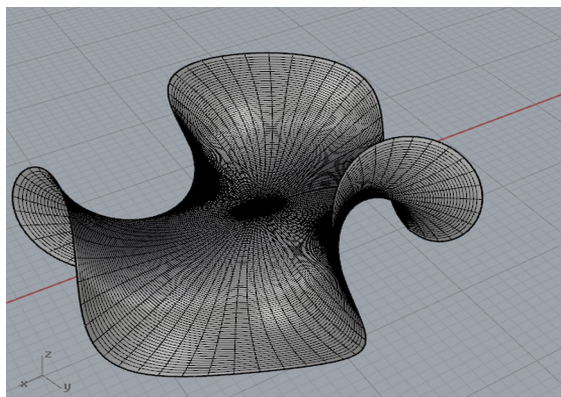


Fig. 1. The Enneper surface's shape used for formation of lattices (by J. Dźwierzyńska)

A lot of works analyze the geometric properties of Enneper surfaces, but little is known about the application of these surfaces in the construction industry. However, tensioned fabric structures in the form of an Enneper surface are studied in [11].

2.3. Grid shell structures

The term “grid shell” is used in the paper alternatively with the term “lattice shell”. It is defined as a structure composed of a network of straight members, creating a single layer, which forms a shell surface. It is a type of structural discrete system in which the axes of bars form a specific spatial geometric grid [12]. Covering panels, if applied, act only as a load. There are both aesthetical and structural benefits of the application of grid shells. They not only create beautiful spaces by segmenting the existing space by their discretized topology, but also exhibit additional stiffness due to their curvature. Moreover, the grid structural system constitutes a means to minimize the visual mass of the structure. The load bearing capacity of the grid shell is directly related to its corresponding mesh topology. In general, triangular meshes are more rigid and stronger than the meshes of other types. However, polygonal meshes also have some structural advantages, as they are torsion-free structures [13]. Due to the fact that triangulated grid structures can easily approximate free-form shapes, we have chosen this kind of structures for further considerations.

3. Results

3.1. Assumption of the grid topology

In general, the robustness of the grid shell structure is strictly related to the distribution of load along its beams. The more uniform the distribution, the stronger the structure. Due to this fact, the grid pattern should affect the load-bearing capacity of the structure. In our research, several representative grid shells, formed on the base of the same Enneper surface, have been subjected to structural analysis. In order to conduct further calculations, we assumed that each

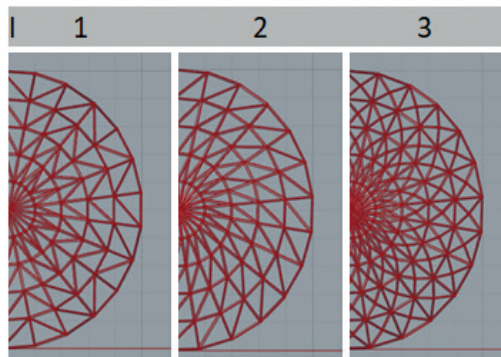


Fig. 2. Considered types of grid patterns (by J. Dźwierzyńska)

grid shell covered a round place whose radius was equal to 5.0 m. Moreover, each grid shell was of the same height of 4.5 m or 2.0 m. The considered grid shells differed due to various grid patterns applied. The rectangular projection of half of all the grid coverings is shown in Fig. 2.

Each of the patterns constitutes a triangular mesh with the same division into $u=5$ segments along the radius and a division into $v=25$ segments along the boundary circle. Due to this fact, each grid shell is composed of 126 nodes included in the Enneper surface and 350 faces being triangles.

3.2. Analysis of the static behavior of the grid structures

3.2.1. Characteristics of the structural models

In order to perform the structural analysis by means of Karamba 3D, first, we created parametric geometric models of each grid structure by means of Grasshopper's form generative algorithmic modeling tools. Next, these geometric models were converted into structural models.

Due to the fact that the FEM simulation represents physical objects as a collection of discrete components or elements, the geometry of grid shells was presented by meshes. In order to study the structural behavior, the following characteristics have been considered:

- ▶ the way of supporting the structure,
- ▶ material – steel resistant against stress and external actions,
- ▶ cross sections,
- ▶ assembly,
- ▶ load properties [14].

Depending on the value of the parameter applied during the generation of the Enneper surface, we could achieve various shapes of this surface. However, we have analyzed only those surfaces, which could constitute coverings of a round place. For each of the shapes, we applied various ways of supporting (three-, four- or five-point supports located in the grids' boundary nodes) Fig. 3–5.

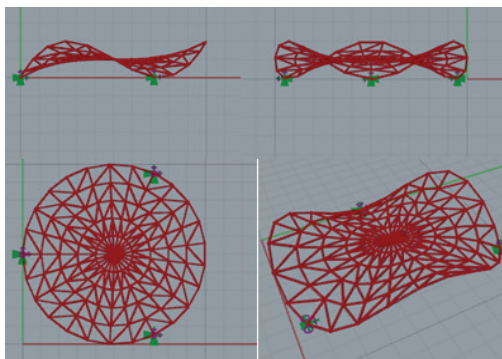


Fig. 3. Representation of a grid shell with three supports (by J. Dźwierzynska)

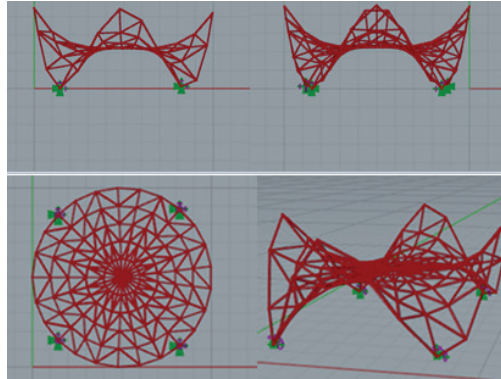


Fig. 4. Representation of a grid shell with four supports (by J. Dźwierzynska)

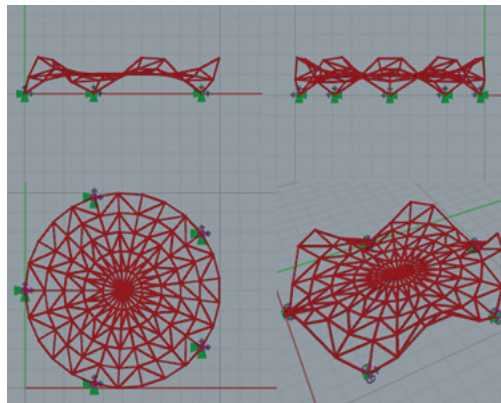


Fig. 5. Representation of a grid shell with five supports (by J. Dźwierzynska)

Due to this fact, for further consideration, we have taken three different grid shapes. However, each of these shapes could be characterized by three various topologies: 1, 2, 3 (Fig. 2). Additionally, in order to perform further calculations, we have assumed two possible heights of the structures: 2.0 m and 4.5 m.

Preliminary, the cross sections of all pipes were assumed to be 10.16 cm, whereas the thickness – 0.36 cm. All pipes were rigidly joined by welded joints. The structure was subjected to a combination of dead loads and live loads.

3.2.2. Performance of the first simulation

The first simulation by means of Karamba 3D was performed for all kinds of steel grids (of various patterns and various supporting systems). The grids were subjected to a dead load, which was a self-weight of the spatial steel grid structure. The dead load acted on the structure in the negative z direction (Fig. 6).

The structural behavior was analyzed both for the steel grid of 2.0 m in height and of 4.5 m in height. We have taken into account the minimal mass of the structure and the maximum

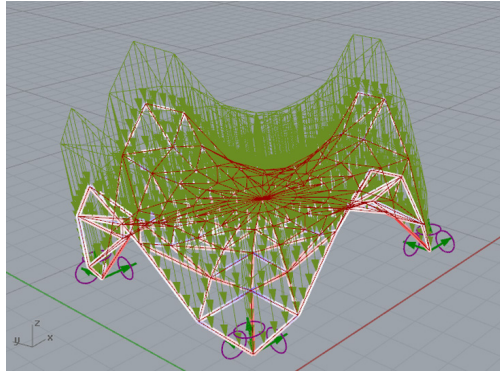


Fig. 6. Dead load acting on the structure (by J. Dźwierzynska)

displacement, both at end-points and mid-points of the mesh elements. The achieved results of the performed analysis are presented in Table 1 and Table 2.

Table 1. Results of the structural analyses for the spatial grid of pattern 1 and of a height equal to 2.0 m

Number of supports	Radius/ Thickness [mm]	Mass [kg]	Maximum displacement [mm]
3	101.6/3.6	3061.20	23
4	101.6/3.6	3081.91	27
5	101.6/3.6	3102.01	31

Table 2. Results of the structural analyses for the spatial grid of pattern 1 and of a height equal to 4.5 m

Number of supports	Radius/ Thickness [mm]	Mass [kg]	Maximum displacement [mm]
3	101.6/3.6	3269.32	16
4	101.6/3.6	3345.67	17
5	101.6/3.6	3412.84	21

Based on the above results, the structure of topology 1 has been chosen as the structure with the smallest node deformations and the smallest mass.

In the case of grid structures of topology 2 and 3, the assumed radii of 10.16 cm for the beams' circular cross sections were not sufficient to carry their own weights. In order to increase the load-bearing capacity of these structures, it was necessary to compact the meshes or increase the cross-sections of beams. However, both actions significantly increased the mass of the structures. Due to this fact, the structure with the grid pattern of type 1 has been chosen as the most effective.

3.2.3. Performance of the second simulation

Next, the first order static analysis was performed for the chosen structure taking into account permanent and variable loads. Permanent loads constituted an own load, which was the sum of the weight of the lattice structure and the weight of the covering glass panels. However, the variable loads were loads from snow and wind. Both snow and wind loads can have a considerable effect on grid shell structures. These loads are calculated in the form of pressure coefficients acting over the surface of the shell. We assumed a snow pressure of 1,3 KN/m² and a wind pressure of 1 KN/m², and applied different possible load combinations. The most unfavorable combination of loads turned out to be a combination taking into account permanent loads and variable loads of snow and wind. It was possible to predict the behavior of the shell grid structures under loads and calculate deflections. This was thanks to the application of Karamba 3D components, which enabled to create static models based on parametric geometric models of grid structures prepared before. In order to specify various types and different load combinations for the models, we have oriented self-loads and snow loads globally to the system of axes x, y, z , whereas wind loads locally to the mesh. The procedure for calculating nodal forces from surface loads in Karamba 3D consisted of a calculation of the resultant load on each face of the given mesh and the distribution of loads among nodes. The achieved results of the performed analysis are presented in Table 3 and Table 4.

Table 3. Results of the structural analyses for the grid shell of pattern 1 and of a height equal to 2.0 m

Number of supports	Radius/ Thickness [mm]	Mass [kg]	Maximum displacement [mm]
3	101.6/3.6	3061.20	33
4	101.6/3.6	3081.91	38
5	101.6/3.6	3102.01	44

Table 4. Results of the structural analyses for the grid shell of pattern 1 and of a height equal to 4.5 m

Number of supports	Radius/ Thickness [mm]	Mass [kg]	Maximum displacement [mm]
3	101.6/3.6	3269.32	27
4	101.6/3.6	3345.67	24
5	101.6/3.6	341.841	29

Analyzing the obtained results, we can state that, in the case of grid shells of a height equal to 2.0 m, the increase in mass causes a slight increase in deformation. There is no such regularity for structures of a height equal to 4.5 m. In this case, an increase in the mass of the structure with four supports does not cause an increase in deformation. The results of Karamba's analysis for this case are presented in Fig. 7.

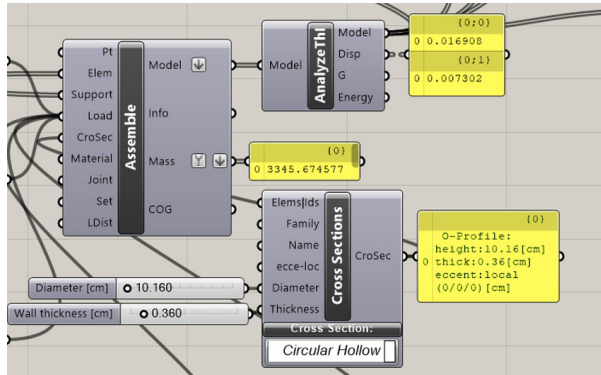


Fig. 7. Calculations of the mass and maximum displacement for the grid shell of 4.5 m in height and with four supports (by J. Dźwierzyńska)

Maximum utilization of beams was achieved in the case of the structure with four supports and it was equal to 93%. However, the minimum utilization for the same structure was equal to 12 %. Due to the big difference between these values, it was recommended to increase the beams' cross-sections at supports as well as slightly reduce the cross sections of other beams, followed by recalculating the new model. Another solution to cause the loads to be distributed more evenly throughout the structure was increasing the density of the grid pattern at supports or increasing the number of supports. That is due to the fact that the greatest axial stress for each structure occurred in the beams located at supports, which is presented in Fig. 8.

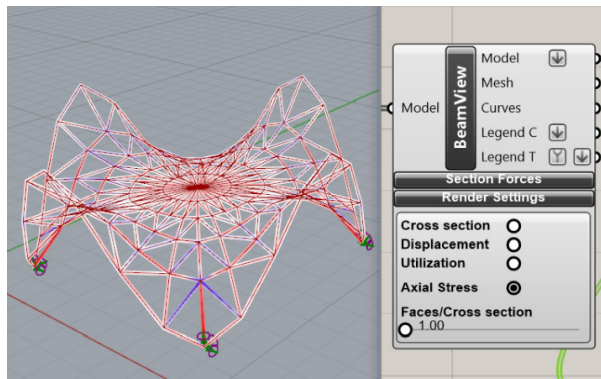


Fig. 8. The distribution of axial stresses in the grid shell with four supports (by J. Dźwierzyńska)

3.2.4. Static behavior of spherical cap grid shells

In order to evaluate the performance of grid structures based on the Enneper surface in comparison to the performance of other structures, we have created Grasshopper models of spherical cap grid shells. We have applied the same grid pattern in the models as the pattern 1 of the Enneper grid structures, as well as the same cross-sections (Fig. 9). Next, the model was converted into a structural model and a structural analysis assuming the most unfavorable combination of loads was performed.

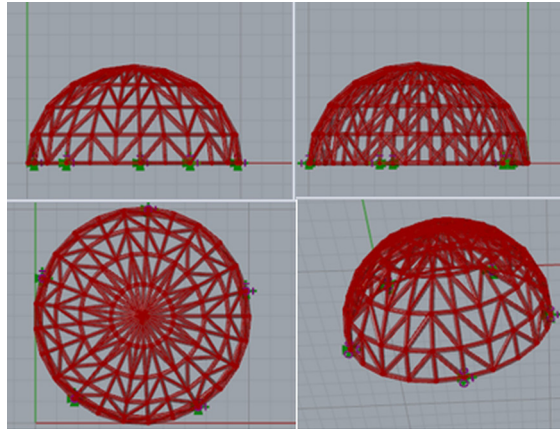


Fig. 9. Representation of a spherical cap grid shell with five supports (by J. Dźwierzynska)

In fact, the shape of the above grid structure was not spherical, but ellipsoidal, owing to the height of the structure. The grid's height was equal to 2.0 m or 4.5 m, whereas the radius of the covered round place was equal to 5.0 m. We have calculated both the mass and the maximum deflection for the structure being supported by five supports. The results are presented in Table 5.

Table 5. Results of the structural analyses for the grid structure based on a spherical shape with pattern 1 applied

Number of supports	Height of the structure [m]	Mass [kg]	Maximum displacement [mm]
5	2.0 m	3519.7	5
5	4.5 m	4155.46	2

Comparing the obtained results for the grid structure created based on a spherical surface with the results achieved for the grid structure created based on the Enneper surface, we can state that both structures are stable with the assumed load; however, the latter structure is lighter.

4. Conclusions

The elaborated scripts for the parametric shaping of grid shells created based on the Enneper surface work well. They seem to be especially useful as they allowed us to create various geometric models of grids and analyze their structural performance using various boundary conditions. An implementation of structural analysis at the early stage of design is very beneficial. The conducted analysis showed that the load-bearing capacity of the grid shell is directly related to its corresponding mesh topology and enables one to choose the grid pattern with the best structural characteristics. In all cases of the analyzed forms, decreasing the span-to-height ratio (becoming steeper) improves the load-bearing capacity of the grid structure.

However, our intention was not to design a specific structure, but to show a practical framework of a parametric design approach, which consists in testing the mechanical performance of the designed forms at the initial stage of design. Our method is fairly general, and it can be applied for generating various grid structures. However, the results of the analysis concerning grid shells created based on the Enneper surface showed that they are structures with good static properties and may be an interesting proposal when it comes to covering large areas.

References

- [1] Bhooshan S., *Parametric design thinking: A case study of practice-embedded architectural research*, Design Studies, Vol. 52/ 2017, 115-143, 10.1016/j.destud.2017.05.003.
- [2] Bródka J., *Przekrycia strukturalne*, Arkady, Warszawa 1985.
- [3] Bródka J., Kozłowski A. (ed.), *Projektowanie i obliczanie połączeń i węzłów konstrukcji stalowych*, Polskie Wydawnictwo Techniczne, Warszawa 2015.
- [4] Dźwierzynska J., Prokopska A., *Pre-rationalized parametric designing of roof shells formed by repetitive modules of Catalan surfaces*, Symmetry, Vol.10/2018, 1–16, doi.org/10.3390/sym10040105.
- [5] Kolarevic B., *Architecture in the Digital Age: Design and Manufacturing*, 1st ed., Publisher: Spon Press, London 2003, 20–98.
- [6] Krivoshapko S., Ivanov V.N., *Encyclopedia of Analytical Surfaces*, Springer International Publishing, Switzerland 2015, 60–77.
- [7] Oxman R., *Thinking difference: Theories and models of parametric design thinking*, Design Studies, Vol. 52/2017, 52, 4–39, doi.org/10.1016/j.destud.2017.06.001.
- [8] Pottman H., Asperl A., Hofer M., Kilian A., *Architectural Geometry*, 1st ed., Bentley Institute Press: Exton, PA 2007, 35–194.
- [9] Tarnai T., *Spherical Grids of triangular network*, Acta Technica. Academiae. Scientiarum. Hungaricae, Vol. 76/1974, 307–338
- [10] Turrin M., von Buelow P., Stouffs R. *Design explorations of performance driven geometry in architectural design using parametric modeling and genetic algorithms*, Advanced Engineering Informatics, Vol.25/2011, 656–675.



- [11] Woodburg R., Mohiuddin A., *Interactive design galleries: A general approach to interacting with design alternatives*, Design Studies, 52/2017, 40–72, doi.org/10.1016/j.destud.2017.06.001.
- [12] Wortmann T., Tuncer B., *Differentiating parametric design: Digital Workflows in Contemporary Architecture and Construction*, Design Studies, Vol.52/2017, 173–197, doi.org/10.1016/j.destud.2017.05.004.
- [13] Yee H. M., Hadi N.N.A., *Tensioned Fabric Structures with Surface in the Form of Chen-Gackstatter and Monkey Saddle*, International Journal of Structural and Civil Engineering Research, Vol. 4/2015, 331–335.

Agnieszka Chowaniec

agnieszka.chowaniec@pwr.edu.pl

Faculty of Civil Engineering, Wrocław University of Science and Technology

Krzysztof Ostrowski  orcid.org/0000-0001-5047-5862

kostrow@agh.edu.pl

Faculty of Mining and Geoengineering, AGH University of Science and Technology

EPOXY RESIN COATINGS MODIFIED WITH WASTE GLASS POWDER FOR SUSTAINABLE CONSTRUCTION

POWŁOKI Z ŻYWIC EPOKSYDOWYCH MODYFIKOWANE ODPADOWĄ MĄCZKĄ SZKLANĄ DLA ZRÓWNOWAŻONEGO BUDOWNICTWA

Abstract

Due to their numerous advantages, epoxy resin coatings are a common way to finish industrial floors. Obtaining coating strength at the level declared by the manufacturer requires preparation of the cement substrate through mechanical treatment, for example, in the form of sandblasting. The next step is the thorough cleaning and vacuuming of the surface and the application of the adhesives. The aim of this research was to improve the strength parameters of a coating in which no adhesive were used. Materials which have a potentially positive effect on epoxy resins are mineral additives. This paper presents the results of tests aimed at improving the adhesion between a concrete foundation and an epoxy resin coating modified with waste glass powder obtained from the production of glass microspheres.

Keywords: epoxy resin coating, glass powder

Streszczenie

Powłoki na bazie żywicy epoksydowej ze względu na liczne zalety są częstym sposobem wykończenia posadzek przemysłowych. Uzyskanie wytrzymałości powłoki na poziomie deklarowanym przez producenta wymaga przygotowania podłoża cementowego poprzez jego mechaniczną obróbkę w postaci np. piaskowania. Następnym krokiem jest dokładne oczyszczenie i odkurzenie powierzchni oraz naniesienie środka szepnego. Celem badań było polepszenie parametrów wytrzymałościowych powłoki, w której nie zastosowano środka szepnego. Materiałem mającym potencjalnie pozytywny wpływ na żywice epoksydowe są dodatki mineralne. W pracy przedstawiono wyniki badań mających na celu poprawę przyczepności pomiędzy podkładem betonowym a powłoką na bazie żywicy epoksydowej modyfikowaną odpadową mączką szklaną pochodzącą z produkcji mikrokulek szklanych.

Słowa kluczowe: powłoka z żywicy epoksydowej, mączka szklana

1. Introduction

Industrial floors are crucial elements of buildings because they constitute a significant part of the investment budget [1]. Improper design or manufacture of these floors can result in the requirement for costly repairs. Therefore, industrial floors should primarily be functional and economical [2]. One of the most important aspects during the design and manufacture of the floors is to obtain properties that will ensure their trouble-free operation for a long time [17]. The durability of industrial floors is influenced by technologies and materials which are mainly intended to finish their surfaces [4].

One of the common ways to finish the floor slab, especially in the pharmaceutical, chemical and food industries, is the application of a resin coating. The main advantage of resin floors is their high resistance to aggressive chemicals and the sealing of the top layer of concrete, reducing the penetration of unfavorable media. The resin coating prohibits concrete to dust contact. An additional advantage is the fact that they are easy to clean and have a very aesthetic appearance [3].

This paper presents the results of research conducted on a floor coating based on epoxy resin modified with waste glass powder. This kind of industrial waste is a popular additive in concrete manufacturing [10]. The waste glass powder has been recently proposed to make overlays in the construction industry [14]. The aim of the research was to improve the mechanical properties of the coating, including its adhesion to the substrate, through the application of waste glass powder.

2. Literature survey

In recent years, numerous studies have been carried out in the construction industry to improve the recipes of building materials used. The aim of the research is not only to improve the strength parameters, but also economic aspects, and to facilitate and speed up the process of their incorporation.

The researchers analyzed the ways of modification of industrial floors, which play a very important role in industrial construction. It is particularly important to ensure continuous use of the floor, because any functional defect and subsequent damage to the structure can cause difficult repairs [12]. An important aspect in floors design is the use of a suitable coating to finish their top layer. These coatings have a decisive influence in ensuring adequate durability of floors. The expected load capacity, durability and individual aesthetic considerations determine the trend in the search for the optimal way to make floors. Only the appropriate materials, the proportion of ingredients together with carefully developed production technology will allow investors and users to meet the requirements [7].

The floors can be modified: plastics, i.e. polymers [18], natural materials such as glass or glass powder [13] or waste materials [5]. One of the first materials used to modify the floors were polymers. These contributions added to the mortar allowed to obtain a very thin (from 5–15 mm) and also very durable coating that is the top layer of the floor [6]. Industrial floors

can also be modified by adding rinsed sand to epoxy resins. This component is usually used as a filler for floors and mortars based on epoxy resin. As pointed in [19], the appropriate weight ratio of resin components and rinsed sand additive allow for better mechanical properties of mortars. Another way to modify the properties of the floors is by coating the surface with an epoxy solution with a carbonyl solvent. The application of such a solution on the surface of a concrete floor increases its strength by closing the pores and sealing small cracks [20].

3. Materials

3.1. Basic material – epoxy coating

An industrial coating formed from epoxy resin was chosen for the tests. Epoxy resin consists of two components; the first is base 'A', an epoxy resin based on bisphenol A, and the other is component 'B', which acts as a hardener based on aliphatic polyamines (Fig. 1) [16]. The combined ingredients are easy to apply and are characterised by very good flow and self-venting.

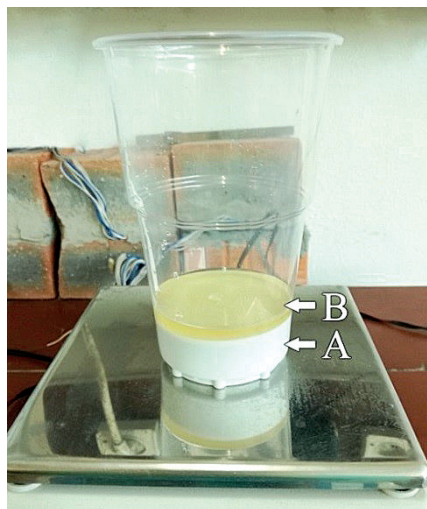


Fig. 1. Coating ingredients – components A and B

This coating is intended for use as a top finishing layer for internal industrial floors subjected to medium and high mechanical loads, e.g. in the automotive industry. This coating makes it possible to finish the floor in a non-slip and smooth form. Its main aesthetic advantage is the possibility of obtaining jointless decorative surfaces with high gloss and different colors.

The epoxy coating is characterised by its high chemical resistance. After hardening, it has high tightness for CO₂ diffusion and creates a surface resistant to impact and damage caused by:

- ▶ mineral oils,
- ▶ lubricants,
- ▶ fuels,

- ▶ diluted acids and lyes,
- ▶ sea water,
- ▶ sewage.

Another advantage is that after curing, the coating becomes neutral to the environment and is very easy to clean. For these reasons, it is recommended for use in rooms with high requirements for cleanliness.

3.2. Additive material – glass powder

The addition of glass powder, silicon dioxide SiO_2 , was chosen as a positive contribution to the properties of the epoxy-based coating. It is a waste material from the production of glass microspheres. SiO_2 is chemically inert; it is stable in water and at elevated temperatures. The SiO_2 compound is widely used in industry and is low cost, and glass powder as an additional waste material, the more it generates low costs. Due to its chemical composition, as well as fine graining, silica is typically economical, aesthetic and provides adhesion between the epoxy coating and the concrete substrate.



Fig. 2. Glass powder used in the research

4. Specimen preparation

4.1. Concrete substrate

The tests were performed using concrete foundations taken from existing screed floors. They were previously tested for compressive strength and bending strength [11]. The obtained strength parameters are summarised in Table 1. Eleven foundations were selected and prepared in accordance with the recommendations of the resin coating manufacturer (Fig. 3). In the first step, the top layers of the concrete substrates were mechanically prepared. For this purpose, the surface of the samples was ground using a disc grinder and was then

thoroughly cleaned of dust. The surface of the concrete was required to be plain, but at the same time rough, which would guarantee the absorbency of the resin (Figs. 3 and 4). A graft layer was not applied.

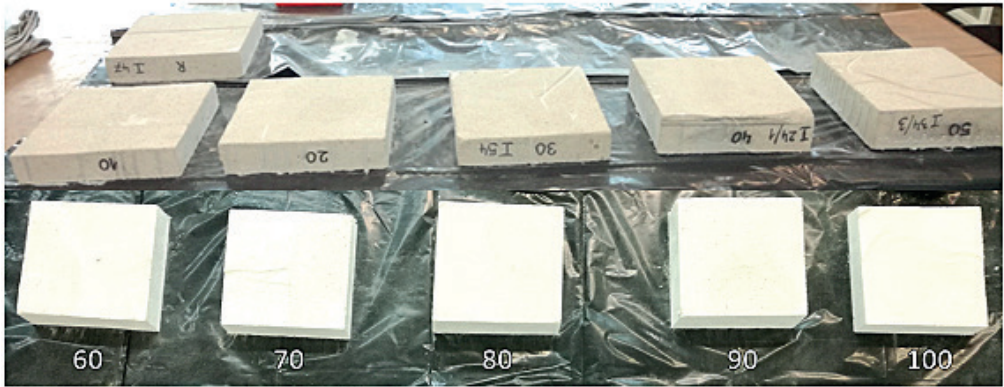


Fig. 3. Concrete substrates used in the research



Fig. 4. Concrete substrate after the grinding process

4.2. Preparation and application modified epoxy coating

The components used to make the resin coating have a liquid consistency and a different colour at first. Hardener 'B' was added to the base 'A', then thoroughly mixed until a homogeneous consistency and colour was obtained throughout the entire mass. Mixing the ingredients took three minutes and was performed using a plastic spoon. The ratio (by weight) of component 'A' to component 'B' was 4:1. The glass powder was added in a fixed amount to each sample and mixed again until a homogeneous mixture was obtained (Figs. 5 and 6).



Fig. 5. The stages of preparation of the resin coating (1 – resin, 2 – addition of hardener, 3 – mixing of components, 4 – addition of glass powder)



Fig. 6. Epoxy coating mixed with glass powder

The letter ‘R’ denotes the control sample (Fig. 3 and Table 1), which was coated with an epoxy coating without the addition of glass powder; numbers 10-100 indicate the weight proportions of the glass powder X content by weight to the coating components (A: B: X). The finished mixture was spread on the surface of the foundations by means of a serrated trowel (Fig. 7a). The coating was then thoroughly vented with a paint roller (Fig 7b). The prepared

coating is presented in Fig. 7c. Both activities were performed on the cross, in perpendicular directions. The sample preparation and curing of the resin coating was performed at an air temperature of $21\pm 2^\circ\text{C}$ and a humidity of $50\pm 5\%$.

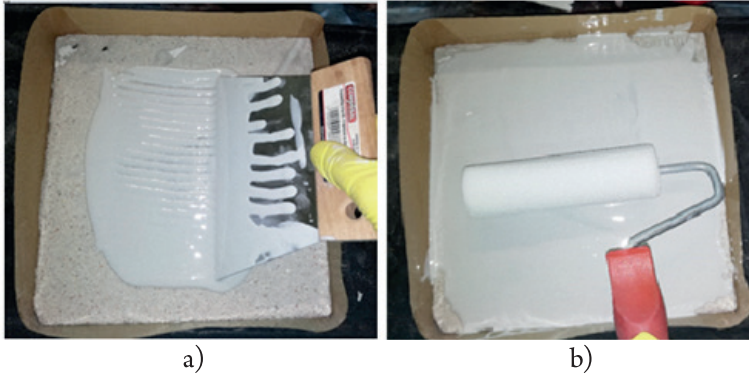


Fig. 7. Coating application

5. Bond strength tests

Bond strength tests were performed after seven days, in order to obtain the full mechanical load capacity of the epoxy coating used. The test of the adhesion of the coating to the concrete substrate was performed using the pull-off method at three points for each sample (Fig. 8) [15].

The pull-off test is a semi-destructive method and is performed by slight destruction of the top layer of the material. Proper preparation of the concrete surface has a very significant effect on the properties of the coating [8, 9]. A steel disc is glued to the surface to be tested by means of epoxy glue, then an incision is made around the disc to a depth greater than the thickness of the coating. After hardening of the adhesive, the disc is pulled off using a measuring device that displays the measured readings. In this study, detachment of the measuring disc always occurred at a shallow depth in concrete (Fig. 10).



Fig. 8. A view of the test bench for pull-off testing

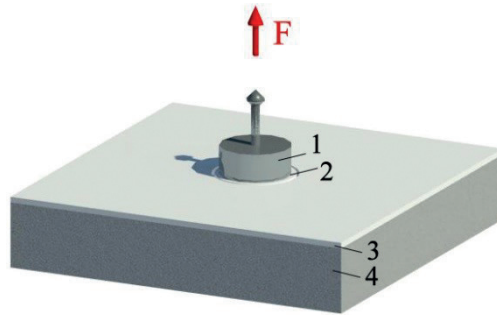


Fig. 9. Peeling off the disc (1 – steel disc, 2 – epoxy adhesive, 3 – epoxy resin coating, 4 – concrete substrate)



Fig. 10. View of the sample before (left) and after (right) detachment of the steel discs

6. Results

Table 1 presents the results and the average pull-off strengths for individual concrete substrates.

During the sample preparation, it was observed that by increasing the amount of added glass powder, the density of the mixture, the mixing time, and the precision of mixing process was increased. The mixing force needed to be increased, especially for samples 80, 90 and 100. For samples from 10 to 40, the resin spread very well over the surface of the concrete substrates and self-levelled. Further increases in the content of the glass powder caused a gradual decrease in the self-levelling ability of the coating and the formation of small irregularities. Coverage of the concrete substrates with 80, 90 and 100 coatings was not feasible.

During coating the control sample 'R' with an epoxy resin layer, without the addition of glass powder, the roller absorbed the largest amount of the mixture in comparison to the other samples. According to the manufacturer's recommendations, the average peel strength, tested by the pull-off method, should be min. 1.5 MPa. However, individual results should not be less than 1.0 MPa. All samples obtained results in line with the above requirements.

Table 1. Experimental results

Designation of concrete substrate	Compressive strength of concrete substrate	Bending strength of concrete substrate	The proportions by weight of glass powder content X	Measurement from the pull-off method [MPa]			Average pull-off strength	Standard deviation
	[MPa]	[MPa]		A	B	C	[MPa]	[MPa]
I 47	14.2	1.7	R-0	2.59	2.70	2.83	2.71	0.120
I 50	12.5	1.8	10	2.30	2.40	2.24	2.31	0.081
I 53	16.5	1.4	20	2.25	2.54	2.51	2.43	0.160
I 54	10.3	1.4	30	1.82	1.87	1.64	1.78	0.121
I 24/1	14.0	1.5	40	3.38	3.05	2.77	3.07	0.305
I 34/3	15.7	1.6	50	2.69	2.81	2.86	2.79	0.087
II 122a	15.5	3.0	60	2.12	2.18	2.30	2.20	0.092
II 1.25b	14.9	2.3	70	2.33	2.27	3.00	2.53	0.405
II 107	8.7	2.1	80	2.17	2.07	3.08	2.44	0.557
II 121/2	10.9	3.0	90	2.76	2.79	2.27	2.61	0.292
II 121/3	13.0	2.9	100	2.13	2.37	1.87	2.12	0.250

7. Conclusions

This work presents an experimental investigation of coatings from epoxy resin modified with waste glass powder. The main conclusions of the tests are as follows:

- ▶ The preliminary tests have indicated that glass powder is a material that affects the adhesion between the coating and the substrate. An additional advantage is the increase in the efficiency of the coating caused by a decrease in the absorptiveness of the roller;
- ▶ For some samples, the addition of glass powder improved the adhesion between the epoxy resin coating and the concrete substrate. The highest average peel strength of 3.07 MPa was obtained for sample 40. Values lower than the reference sample (<2.71 MPa) result from inferior strength parameters of the concrete substrates. Therefore, the increase in adhesion is visible only in the graphs of functions of three variables, which also take into account the strength of the underlay concrete;
- ▶ Based on the results, it was found that the optimal weight ratio between the epoxy coating components 'A' and 'B', and the content of glass powder 'X' is (A: B: X = 100: 25: 40).

References

- [1] Chandler J.W.E., *Design of floors on ground*, Slough: Cement and Concrete Association, 1982.
- [2] Chmielewska B.G., Czarnecki L.E., *Wymagania norm dotyczące posadzek przemysłowych*, *Materiały Budowlane*, 2, 2012, 5–9.
- [3] Chowaniec A., *W kierunku modyfikacji posadzek żywicznych nanododatkiem*, *Nowoczesne Hale*, 2, 2018.
- [4] Czarnecki S., Sadowski Ł., Hoła J., *Evaluation of the height 3D roughness parameters of concrete substrate and the adhesion to epoxy resin*, *International Journal of Adhesion and Adhesives*, 67, 2016, 3–13.
- [5] Dachowski R., Kostrzewa P., *The Use of Waste Materials in the Construction Industry*, *Procedia Engineering*, 161, 2016, 754–758.
- [6] Do J., Soh Y., *Performance of polymer-modified self-leveling mortars with high polymer-cement ratio for floor finishing*, *Cement and Concrete Research*, 33, 2003, 1497–1505.
- [7] Drozd W., Kowalik M., *Współczesne posadzki przemysłowe*, *Przegląd budowlany*, 7–8, 2014, 34–39.
- [8] Figueira D., Sousa C., Calçada R., Neves S.A., *Design recommendations for reinforced concrete interfaces based on statistical and probabilistic methods*, *Structural Concrete* 17(5), 2016, 811–823.
- [9] Figueira D., Sousa C., Calçada R., Neves A.S., *Push-Off Tests in the Study of Cyclic Behavior of Interfaces between Concretes Cast at Different Times*, *Journal of Structural Engineering*, 142(1), 2015, 04015101.
- [10] Galińska A., Czarnecki S., October, *The Effect of Mineral Powders Derived From Industrial Wastes on Selected Mechanical Properties of Concrete*, *IOP Conference Series: Materials Science and Engineering*, Vol. 245, No. 3, 2017, p. 032039, IOP Publishing.
- [11] Hoła J., Sadowski Ł., *Badania wytrzymałościowe na zginanie i na ściskanie próbek pobranych z posadzek jastrychowych w budynku Szpitalnego Oddziału Ratunkowego w Lubinie*, Wrocław 2017.
- [12] Mynarčík P., *Technology and Trends of Concrete Industrial Floors*, *Procedia Engineering*, 65, 2013, 107–112.
- [13] Raju S., Kumar P.R., *Effect of Using Glass Powder in Concrete*, *IJIRSET*, 3, 2014, 421–427.
- [14] Sadowski Ł., *Towards the utilization of waste glass powder in sustainable cement based overlays*, *MATEC Web of Conferences*, Vol. 163, 2018, p. 03001, EDP Sciences.
- [15] Sadowski Ł., *Multi-Scale Evaluation of the Interphase Zone between the Overlay and Concrete Substrate: Methods and Descriptors*, *Applied Sciences*, 7(9), 2017, 893.
- [16] Sadowski Ł., Chowaniec A., *Środek do wykonywania powłok na bazie żywicy epoksydowej oraz jego zastosowanie*, *Zgłoszenie patentowe nr PL.425183 z dnia 11.04.2018*
- [17] Szymanowski J., Sadowski Ł., *Ultrasonic Pulse Velocity Evaluation of the Pull-Off Adhesion between Epoxy Resin and Concrete Substrate*, *Key Engineering Materials*, Vol. 728, 2017, Trans Tech Publications, 390–395.

- [18] Wang H., Chen J., *Polyurethane–modified epoxy resin and their polymer particle filled epoxies*, *Journal of Polymer Research*, 3, 1996, 133–138.
- [19] Yemam D.M., Kim B., Moon J., and Yi Ch., *Mechanical Properties of Epoxy Resin Mortar with Sand Washing Waste as Filler*, *Materials*, 10, 246, 2017, 1–11.
- [20] Zhang G., Xie Q., Ma Ch., Zhang G., *Permeable epoxy coating with reactive solvent for anticorrosion of concrete*, *Progress in Organic Coatings*, 117, 2018, 29–34.

Matthias Richter

Jan Paszkowski

jan.paszkowski@fh-zwickau.de

Fakultät Wirtschaftswissenschaften, Westsächsische Hochschule Zwickau

MODELLING DRIVER BEHAVIOUR IN TRAFFIC-CALMED AREAS

MODELOWANIE ZACHOWAŃ KIEROWCÓW W OBSZARACH O RUCHU USPOKOJONYM

Abstract

The aim of this paper is to investigate driver behaviour in order to develop a method for improving micro- and macrosimulation traffic models with a particular focus on traffic calming solutions. Therefore, speed profiles were calculated, a PTV Vissim model was created, and an attempt to estimate volume-delay functions was made. Driver behaviour was modelled on the basis of video recordings of traffic in traffic-calmed links. Speed profiles were divided into parts where the speed is influenced with the traffic calming and not, and speed distributions were calculated in order to be used in Vissim. Vissim microsimulation was tested on various traffic volumes, with various traffic compositions, in order to identify the relationship between traffic flow and travel time.

Keywords: traffic calming, modelling, volume-delay function

Streszczenie

Celem niniejszego artykułu jest zbadanie zachowań kierowców na ulicach o ruchu uspokojonym, w celu stworzenia metody modelowania mikro- i makrosymulacyjnego ulic tego typu. Za pomocą nagrań wideo ruchu odtworzono trajektorie pojazdów w celu ustalenia wyglądu funkcji oporu odcinka. Prędkości zostały podzielone na te występujące w miejscach, gdzie ruch jest spowolniony z powodu urządzeń uspokojenia ruchu, oraz te, w których ruch odbywa się bez zakłóceń, w celu stworzenia modelu w programie PTV Vissim. Model ten został przetestowany dla różnych natężeń ruchu, tak aby odkryć relację między natężeniem ruchu a zwiększeniem czasu przejazdu.

Słowa kluczowe: uspokojenie ruchu, modelowanie, funkcja oporu odcinka

1. Introduction

Cities nowadays cope with increasing amount of cars, which, together with high urban density, can lead to a decrease in the attractiveness of the affected area. Over the years, urban planners and scientists have discovered that costly expansion of the road infrastructure does not give the desired results. One of the first discoveries was Braess's paradox (1968), which identified the mathematical chance of time loss caused by enlarging the road network [1]. Induced and latent demand [2] were discovered in 1969. Finally, the Downs-Thomson paradox [3] of risks of congestion in the case of unsustainable transport development and the Lewis-Mogridge position [4] proved that the bigger the car network, the greater the level of traffic and the more congestion will occur. Therefore, cities promote public transport, which is more flexible with a big demand than car transport. In order to encourage people to reduce car usage, the most radical idea is to completely close the most vulnerable zones to car traffic. However, to meet the needs of the inhabitants of these zones and those whose places of work lie within these areas, car traffic must be maintained. Therefore, a solution which redirects transit traffic from the vulnerable areas to the transit roads, is needed – one such solution is traffic calming. Traffic calming devices are often applied in zones with a large amount of pedestrians, for example, in residential areas or city centres.

1.1. Traffic calming

Traffic calming is a set of measures, the purposes of which are to reduce the negative effects of motor vehicle use, alter driver behaviour and improve conditions for non-motorised street users. [5] That includes reduction of traffic volume, thus noise and air pollution, improvement of road safety level, and the quality of life. Another aim of traffic calming is to change travel behaviour, such as by reducing the share of car travel in the modal split in favour of public transport, and changes to the traffic assignment, especially with regard to reducing transit traffic in the problem area. The traffic calming measures can be divided in two groups: area and point traffic calming. Area traffic calming is, for 30 km/h speed limit zones, reduced access zone, residents only zone, and shared Point traffic calming refers to measures that are placed at specific points on the road, for example: speed humps, speed cushions, elevated street at pedestrian crossing areas, narrowing of the street, chicanes.

2. Area

The area examined in this paper is Stachiewicza Street in Kraków. It is located in the Prądnik Biały district, in the Azory residential area. This street runs from north to south in the central area of this district. It is one of the main routes connecting the north-western outskirts and suburbs of Kraków with the western part of the city centre, as well as the main north-south transit avenue – Aleja Trzech Wieszców. Public transport buses operate on those street, creating a connection between stated above areas and the city centre. On the

southern end of Stachiewicza street is the railway underpass and the Kraków Łobzów station. There are two other streets parallel to Stachiewicza street, one on each side, but with level railway crossings instead of an underpass. During the measurements, one of the level railway crossings was closed due to reconstruction of the railway.

A primary school is located on the analysed Stachiewicza street. One of the main routes between the Azory area and the school crosses Stachiewicza street. On both sides of the crossing, in both directions, there are traffic calming devices installed – speed cushions to slow down car traffic without lowering the comfort level for bus passengers.

3. Measurement methods

To reproduce driver behaviour to a high level of precision, it was necessary to have precise vehicle motion recorded including data relating to speed, acceleration and braking. Moreover, for further investigation of the problem, it was important to note interactions between vehicles; these interactions between vehicles include the distances between successive vehicles, braking forces when noticing the approach to the car in front, and the speed and distance fluctuations when following. These parameters can be adopted in the Wiedemann model, used in PTV Vissim software.

The measurement types can be divided into two categories: inside and outside the vehicle. Measurements inside the vehicle, known also as floating car, stands, that there is a measurement car, equipped with movement tracking device, such as car computer, recording distance travelled and speed of the car, or additional values, such as acceleration and braking pedal press. Another solution for floating car motion recording is the use of GPS devices, which record not only the speeds of the vehicle, but also its trajectory; this means that in every time stamp (for example one second), the position of the vehicle is recorded. When using this method, it should be noted that GPS has an accuracy of 2-5 meters [6], which can have a negative influence on the results. Measurements outside the vehicle, unlike the methods above, are able to record the behaviour of more than one vehicle. These methods include strategies such as pneumatic tubes for speed measurement. or radar control [7], can be connected to speed control, photographing or video recording facilities. Unfortunately, most of these methods are only working in one specific point of the measured road or area; therefore, it is needed to provide measurements in more points. However, gaps between measurement points still exist.

In order to ensure continuity in the recording of every vehicle in the traffic flow, video recording can be used. Previously, analysis of the video and identification of the vehicles trajectories were performed manually and this was a very time-consuming task. Nowadays, with the use of deep machine learning through creating classifiers, it is possible do detect vehicles automatically, trace them, and produce trajectories.

The area which can be recorded depends on the angle of the camera and the obstacles which covers the traffic, as well as the shape of the road, which can limit the size of the area that can be recorded. The optimal solution is to position the camera in such a manner that it



is recording from above in order to minimize the amount of obstacles, as well as to simplify the trajectory calculations. This would mean installing the camera at a point high above the street or to record from the air. To provide coverage of a great area, when only low buildings are present, an unmanned quadcopter was used, hovering 80 meters above ground level, and recording the traffic along an approximate length of 110 meters of road. The quadcopter used is able to fly for around 25 minutes, which, taking into account a safe reserve of battery time, take off, positioning above the street and landing, leaves around 15-20 minutes of traffic recording at any one time. Recordings were made at a high definition of 1920*1080 pixels resolution, and 40 frames per second.

The trajectories from the video were processed by the company DatafromSky [8]. The result of processing is delivered in two files – one of these is the file for the DatafromSky viewer software which is used to visualise the results, and the other is the csv file with all the data, containing timestamp, coordinates, object ID, and object type (car, heavy vehicle, bus, bicycle, pedestrian). The screenshot of the DatafromSky viewer software is presented in Fig. 1.



Fig. 1. DatafromSky viewer software screenshot with car detection and trajectory data displayed (source: own work)

4. Measurement results

The data acquired from recordings was processed. The street visible in Fig. 1 was divided into 10 cm sections and for each section instantaneous velocities were identified for every vehicle, divided to vehicle classes, such as cars (standard and van), busses and heavy vehicles. From these speeds, charts showing the speed profiles have been for different points along the analysed road, including the installed speed cushions. The following measurement results are based on approx. 20 minutes recording and contain trajectories of a total of 192 vehicles: 165

cars, 18 vans, 3 heavy vehicles, and 6 buses. There were also 90 pedestrians detected, but for the purposes of the model, only vehicles have been taken into the consideration. Charts of speed profiles are presented below in Figs. 2 and 3.

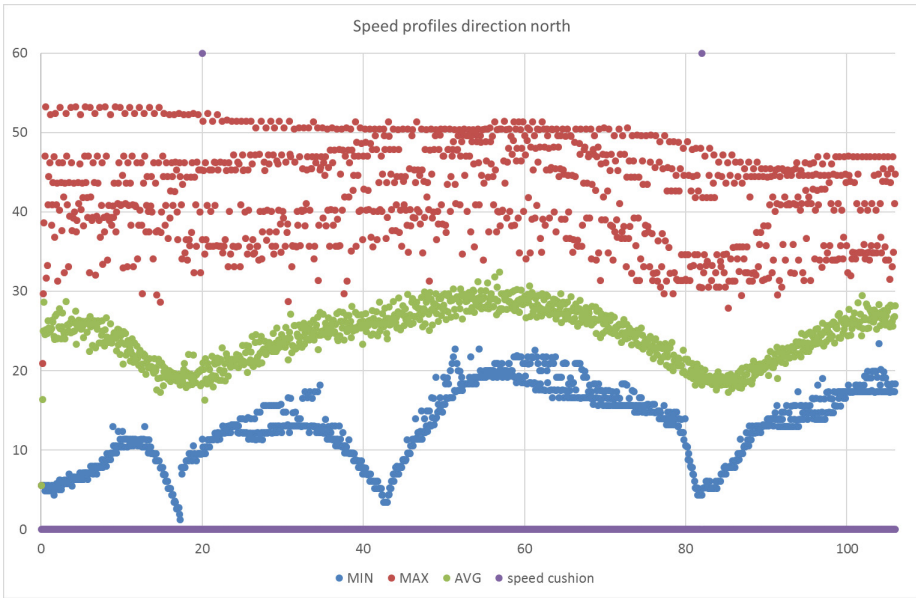


Fig. 2. Speed profile for Stachiewicza street, direction north *consider changing to 'northbound'* (source: own work)



Fig. 3. Speed profile for Stachiewicza street, direction south *consider changing to 'southbound'* (source: own work)



On the charts, the studied 107-metre length of Stachiewicza Street can be seen. Speed cushions, as indicated by the violet line, are located at 20 and 82 metres along this section northbound, whereas southbound – on 26th and 88th meter. The blue points indicate the minimum speed. The decrease of the minimal speed between the speed cushions (between 40 and 60 metres) depicts the car stopping on the pedestrian crossing. The green points show average speeds – slowing down in the area of speed cushions are clearly visible. Maximal speeds, marked with red points, show that not every vehicle is decelerating on speed cushions, especially, on the first device in the northbound? direction. possibly because some of the vehicles avoid speed cushions by driving between them.

5. Microsimulation – PTV Vissim

5.1. Preparation

A microsimulation model was created on the basis of the measurements. The model was prepared using the PTV Vissim software. Vissim’s traffic flow model is a stochastic, time-step based, microscopic model that treats driver-vehicle units as the basic entities. The car following model is based on the Wiedemann model. Driving behaviour in this model is divided to four states: free driving, approaching, following, braking. Driving behaviour in detail is described with Wiedemann model parameters: Wiedemann 74, such as safety distances, lack of attention duration or lack of attention probability and Wiedemann 99: time distribution of the speed-dependent part of the desired safety distance, time of deceleration before reaching safe distance, influence of distance on speed oscillation, desired acceleration

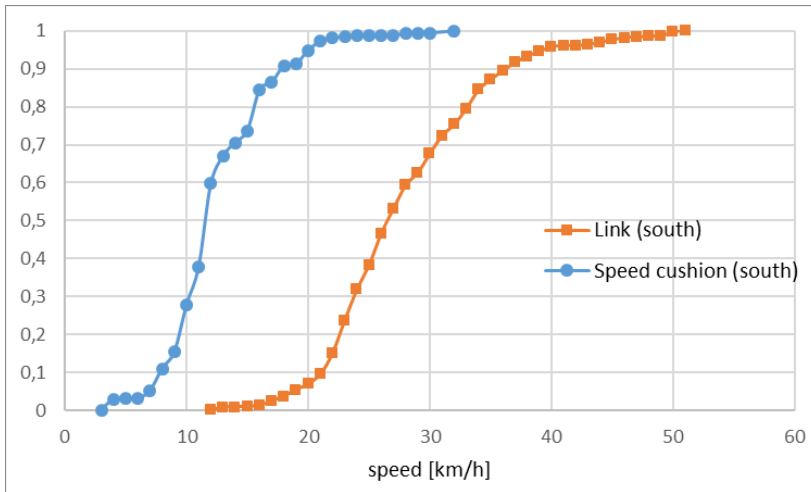


Fig. 4. Car speed distributions for the link, direction south (orange) ‘southbound link’? (although, see above note re use of ‘link’) and its second speed cushion (blue) (source: own work)

when starting from standstill. Initially in this paper, the basic parameters of the model, such as speeds and accelerations, were taken into consideration without modifying the Wiedemann parameters describing interactions between vehicles [9].

For the each vehicle type, speed distributions have been created according to measured cumulated frequencies, for two kinds: near or away the speed cushions. On the slowing down and speeding up areas around the speed cushions, the accelerations and decelerations were identified. The model consists of two links, representing two directions of the road and four reduced speed areas, one for each speed cushions. Speed distributions parameters for both links and all four reduced speed zones were inputted. Two examples of speed distributions are presented in Fig. 4.

5.2. Comparison and calibration

After inputting all of the speed distributions to the Vissim model, the simulation was started for the same traffic flow as was observed during the measurement. The results of the simulation were exported and extracted as average speed profiles of all vehicles in order to compare them with the measurements. Calibration of the model required using only the speed distributions of unimpeded vehicles – otherwise, the simulated speeds were higher than measured. The shape of the speed profile was calibrated by estimating the acceleration and the braking characteristics of the vehicles. For the first direction (northbound), the correlation between the model and the measurement is 0.79. The compared speed profiles are presented in Fig. 5.

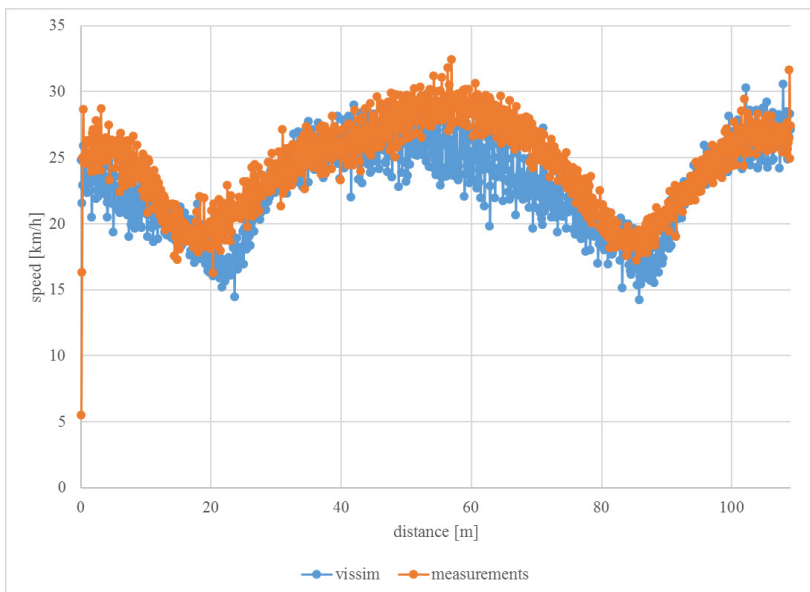


Fig. 5. Comparison of speed profiles on the measured street section, heading north 'northbound'? (source: own work)

For the second direction (south 'southbound') along Stachiewicza street, the correlation between the measured and modelled speed profiles is 0.71. Fig. 6 shows this comparison.

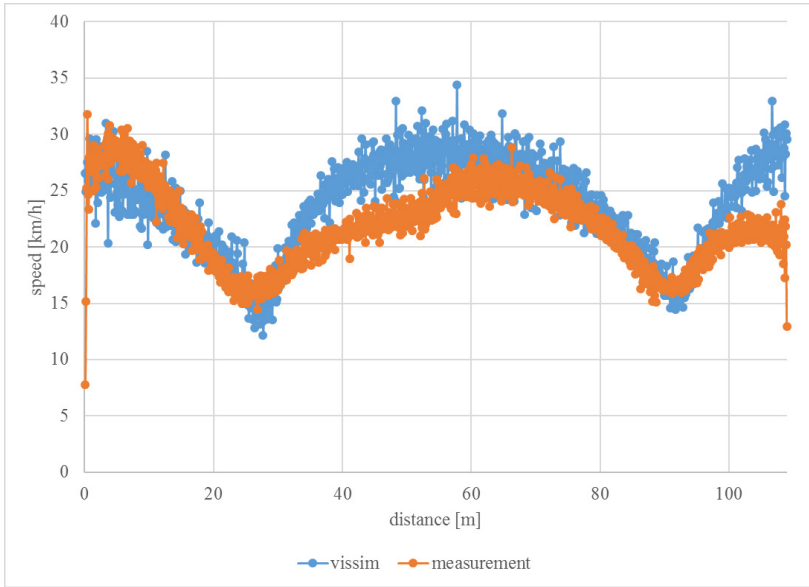


Fig. 6. Comparison of speed profiles on the measured street section, heading southbound (source: own work)

Comparing the measured and simulated speed profiles, a strong correlation between the speeds both in and out of the area of the traffic calming device can be observed. However, there is a difference in the shape of the speed profiles between the speed cushions. To minimise this difference, further activities should be undertaken, such as adaptation of the Wiedemann model parameters, acceleration and braking, or dividing the link into speed zones.

6. Use of the volume-delay functions in the macrosimulation model

Results of microscopic link model, done in PTV Vissim lead to estimating suitable network link characteristics of PTV Visum. This kind of model consists of two main parts: demand and supply. Demand is represented by an origin-destination matrix between the traffic areas, with homogenous urban and transport functions. Supply is the transport network, set for various transport modes, both private and public. The aim of the model is to assign the trips from origin to destination to the road network. Traffic assignment is calculated by setting a path with the lowest cost (for example, travel time) for every network user. In this project, demand remains unchanged, although link parameters regarding traffic were modified. Traffic on the link is described in terms of three basic variables: traffic flow q – amount of vehicles passing one point in a given period of traffic density – amount of vehicles on the link and their velocities. In the PTV Visum model, the relationship between the amount of traffic flow

and the link travel time is described by volume-delay functions, which is one of the Visum link type parameters. Their shape can be chosen from default function formulas, and their parameters can be freely changed.

7. Experiment and results

Measuring, modelling and simulating driver behaviour under varying flow conditions and creating a microsimulation model will facilitate understanding of the relationship between traffic flow and travel time and allows formulating the volume-delay functions for traffic-calmed roads. To reach this aim, Various traffic flows were tested and compared for traffic-calmed and not traffic-calmed links. In the simulation, the links were lengthened beyond the limits of the drone camera coverage, reaching the nearest intersections without right-of-way: Wybickiego and Radzikowskiego street on the southern end, and Makowskiego on the northern end. The length of the simulated link is 568 meters. In the simulation, the vehicle composition stays the same as during the measurements for both directions; for direction 1 (northbound) these are: cars, 82%; HGVs, 16%; buses, 2%. For direction 2 (southbound), the proportions are: cars, 84%; HGVs, 14%; buses, 2%.

7.1. Capacity

As mentioned above, the Vissim microsimulation model was tested for the whole range of traffic flows. The minimal traffic flow simulated was around 100 vehicles per hour. The capacity of the link was estimated in Vissim through increasing the traffic flow until the message about achieving maximum traffic flow was displayed. Maximum traffic flows were estimated in Vissim by increasing traffic flow until no more vehicles were able to pass the link in the simulated period of time. A comparison of maximal traffic flow, counted as vehicles per hour, for traffic-calmed and non-traffic-calmed (standard) streets is presented in Table 1.

Table 1. Comparison of maximal traffic flow for both directions with and without traffic calming

Direction	1 (north)	2 (south)
Traffic calmed [veh/hour]	1068	1044
Standard [veh/hour]	1308	1158

7.2. Speed

The relation between amount of traffic flow and the traffic speed was calculated by analysing the results of the simulation. In both directions, the speed functions for with and without traffic calming are parallel to each other, with a difference of speed equal to 2.5 km/h for direction 1 and 2 km/h for direction 2. The speed with traffic calming decreases from 41 km/h to 24 km/h for direction 1, and from 35km/h to 18 km/h for direction 2. Speed charts are presented in Fig. 7.

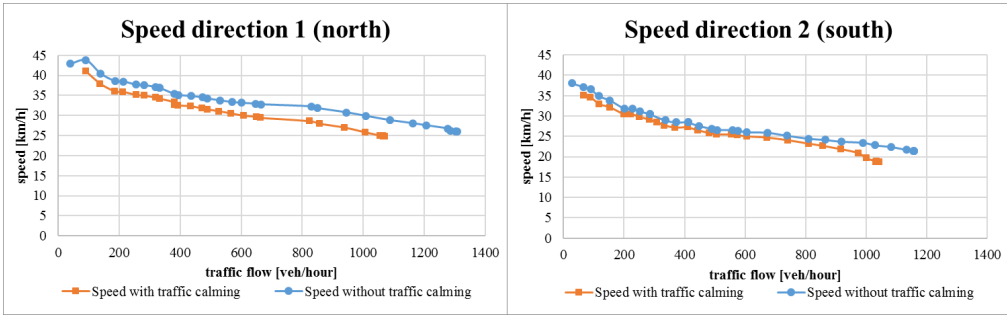


Fig. 7. Relationship between speed and traffic flow (source: own work)

7.3. Travel time

The next chart shows the growth of the travel time in the link. For direction 1, the shortest travel time for the lightest traffic flow is 50 seconds, and increasing linearly to around 80 seconds for the heaviest traffic flow. For direction 2, the minimal travel time amounts around 60 seconds, and grows to around 100 seconds for the non-traffic-calmed street, and 110 seconds for the road with traffic calming. Both travel times increase similarly in lower traffic flows; however, with the traffic flow above around 900 vehicles per hour, the traffic-calmed street travel time starts to increase sharply.

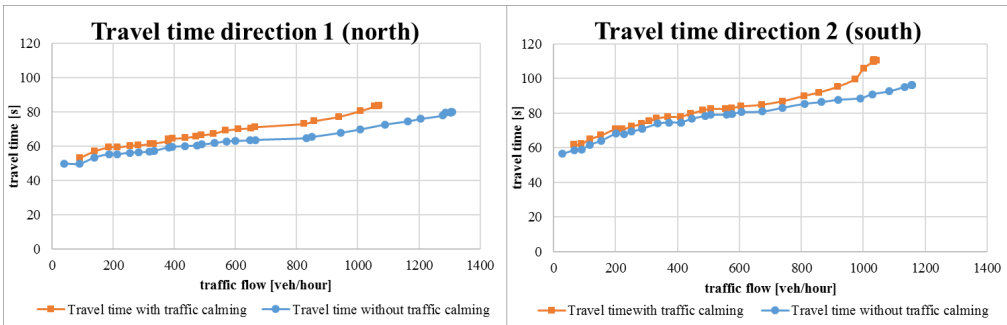


Fig. 8. Relationship between travel time and traffic flow (source: own work)

7.4. Delay

In PTV Vissim, delay is defined as the difference between the shortest, ideal travel time and the actual travel time for each vehicle. As expected, in the minimal traffic flows, delay amounts to zero. For direction 1, delay times are similar for both link types until the traffic flow is around 500 veh/hour, then the delay for the traffic-calmed roads starts to increase more sharply. At the maximal traffic flow, the delay is 26 seconds for both link types. For the opposite direction, delay amounts are the same until the traffic flow is around 800 vehicles per hour, then the delay on the traffic calmed road increases sharply to reach a maximum delay of 45 seconds, whereas the non-traffic-calmed street reaches 32 seconds of delay.

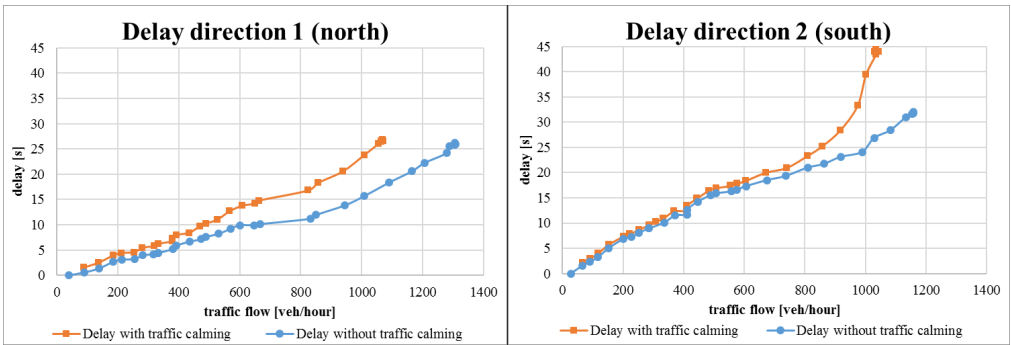


Fig. 9. Relationship between delay and traffic flow (source: own work)

8. Visum volume-delay function

Travel times were calculated in such a manner, to correspond with the form of volume-delay function available in PTV Vissim, thus showing the relationship between saturation grade (traffic flow divided by maximum traffic flow) and the travel time gain compared to $x \cdot t_0$ (t_0 - free flow travel time). In the Kraków transport model, volume-delay function were estimated based on BPR2 volume-delay function shape, with five sets of parameters. The formula of the volume-delay function is:

$$t_{\text{cur}} = \begin{cases} t_0 \cdot (1 + a \cdot \text{sat}^b), & \text{sat} \leq \text{sat}_{\text{crit}} \\ t_0 \cdot (1 + a \cdot \text{sat}^{b'}), & \text{sat} > \text{sat}_{\text{crit}} \end{cases}$$

where:

- t_0 – free flow travel time
- a, b, b' – shape parameters
- sat – saturation grade

In the Kraków transport model, the following parameters of volume-delay functions are given:

Table 2. Comparison of BPR function parameters

Number of function	01	02	03	04	05
a=	1.00	0.91	1.71	1.15	1.32
for sat < 1 b1=	2	6	4	3	3
for sat >= 1 b2=	2	6	6	6	6

8.1. Comparison with estimated BPR function parameters

For the analyzed Stachiewicza street, in Kraków model, none of the functions were used – instead, constant function of travel time was implemented. According to the simulation results, the parameters of the BPR function were estimated. In order to obtain better function fitting, the BPR function was divided into two sections:

$$t_{\text{cur}} = \begin{cases} t_0 \cdot (1 + a \cdot \text{sat}^b), & 0 < \frac{\text{sat}}{\text{sat}_{\text{crit}}} < x \\ t_0 \cdot (1 + a \cdot \text{sat}^{b'}), & x < \frac{\text{sat}}{\text{sat}_{\text{crit}}} < 1 \\ \dots & \dots \end{cases}$$

where: x is the border value of saturation grade between two sections

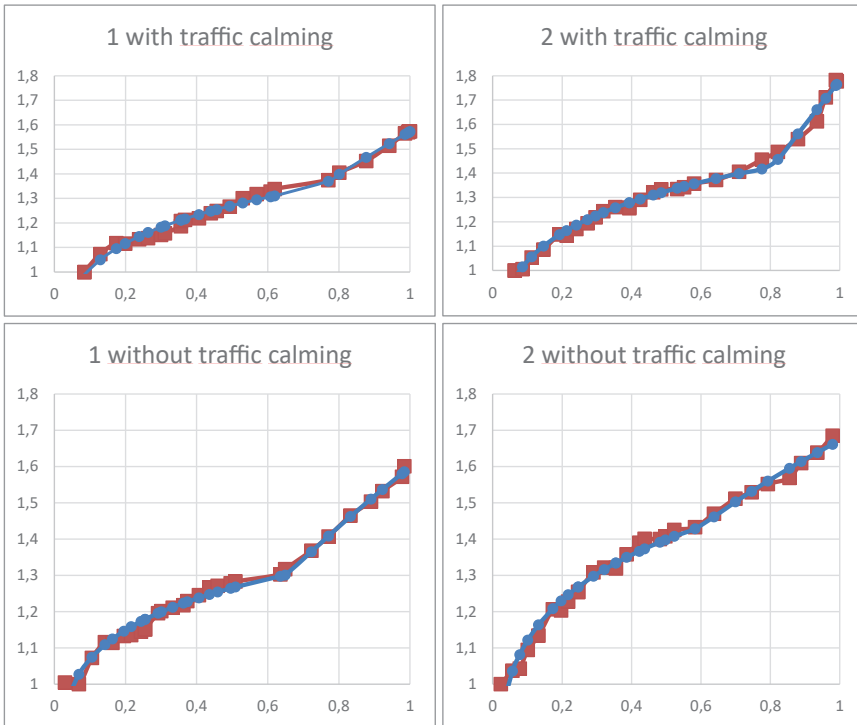


Fig. 10. Comparison of results and BPR function fitting (source: own work)

The parameters of the BPR function were estimated using squared difference minimization method. On the table below, the result of estimation is showed in Table 3.

Table 3. Estimated BPR function parameters

Number of function	Direction 1 with traffic calming	Direction 2 with traffic calming	Direction 1 without traffic calming	Direction 2 without traffic calming
a=	sat<0.7satcrit a=1.40	sat<0.8satcrit a=1.47	sat<0.7satcrit a=1.36	sat<0.6satcrit a=1.54
a=	sat>0.7satcrit a=1.57	sat>0.8satcrit a=1.78	sat>0.7satcrit a=1.6	sat>0.6satcrit a=1.67
b=	sat<0.7satcrit b=0.14	sat<0.8satcrit b=0.15	sat<0.7satcrit b=0.11	sat<0.6satcrit b=0.14
b=	sat>0.7satcrit b=0.52	sat>0.8satcrit b=1.02	sat>0.7satcrit b=0.48	sat>0.6satcrit b=0.30

The fitting of functions, compared to empirical results, were presented in ill. 10. Correlation factor for the functions is between 0.9 and 0.95.

On the chart (Fig. 11) used shapes of BPR functions and measured volume – delay relations.

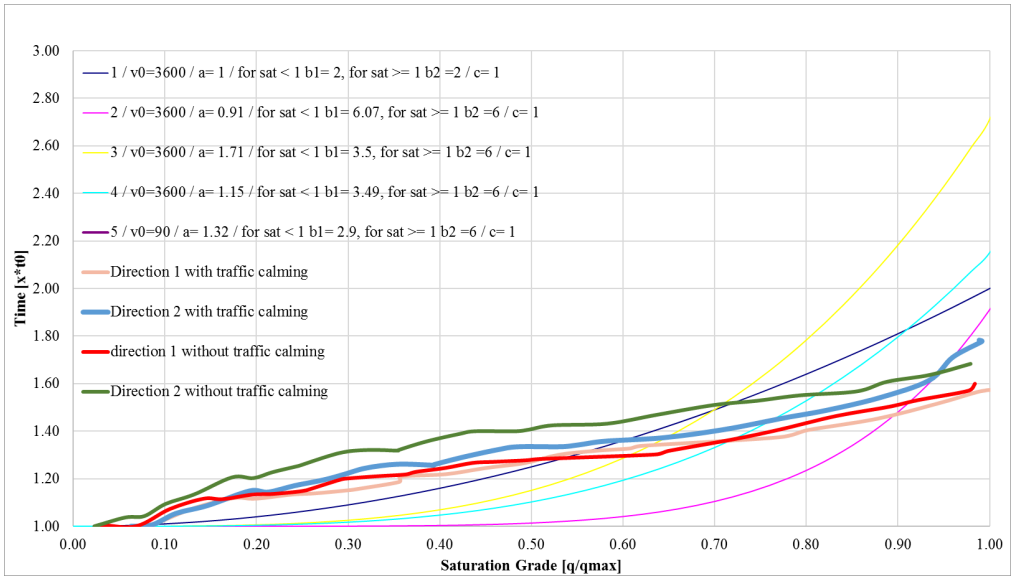


Fig. 11. Comparison of measured volume-delay functions and volume-delay functions used in the Kraków model, and on the analyzed street (source: own work)

9. Summary and possible further research

This paper uses video recordings and trajectory extraction software to create a microsimulation model of the traffic-calmed street. From the data, only dynamic behaviour of drivers was extracted, this included speed distributions, together with braking and acceleration when entering and leaving the reduced speed area. For further research, in order to improve the precision of the model, an attempt to estimate Wiedemann model parameters will be made. Moreover, the transfer of the simulation from a micro- to a macroscopic model must be made in order to estimate travel times in the situation, when the traffic flow is greater than capacity. Ultimately, a larger driving behaviour database and more types of traffic calming measures should be studied. This would be likely to deliver more precise forecasts of the impact of traffic calming than could be achieved using traditional methods.

References

- [1] A1 Braess D., *On a Paradox of Traffic Planning*, “Transportation Science”, 39, 2005, 446–450.
- [2] Leeming J.J., *Road Accidents: Prevent or Punish?*, 1969.
- [3] Downs A., *Still Stuck in Traffic: Coping With Peak-Hour Traffic Congestion*, 2004.
- [4] J H Mogridge M., *Travel in towns: jam yesterday, jam today and jam tomorrow?*, 1990.
- [5] Traffic Calming: State of the Practice ITE/FHWA, August 1999.
- [6] <https://www.gps.gov/systems/gps/performance/accuracy> (access: 5.07.2018).
- [7] Barbosa H.M., *Impacts of traffic calming measures on speeds on urban roads*, Diss. University of Leeds, 1995.
- [8] <http://datafromsky.com> (access: 5.07.2018).
- [9] A7 PTV-Ag, PTV VISSIM 9 User Manual, Karlsruhe 2017.
- [10] Bliemer M.C.J. et al., *Genetics of traffic assignment models for strategic transport planning*, Transport Reviews 37.1, 2017, 56–78.
- [11] Kucharski R., Drabicki A., *Estimating Macroscopic Volume Delay Functions with the Traffic Density Derived from Measured Speeds and Flows*, Journal of Advanced Transportation 2017.

Marzena Hajduk-Stelmachowicz  orcid.org/0000-0003-4945-7207

marzenah@prz.edu.pl

Department of Management, Faculty of Economics, Rzeszów University of Technology

Marek Gołębiowski

Department of Electrical Engineering and Information Technology, Faculty of Electrical Engineering and IT Basics, Rzeszów University of Technology

Marek Stelmachowicz  orcid.org/0000-0001-5134-6077

Ph.D. Student, Rzeszów University of Technology

THE USE OF PRELIMINARY HAZARD ANALYSIS TO ASSESS THE RISK OF DAMAGE TO THE TELECOMMUNICATIONS WIRED ACCESS NETWORK

ZASTOSOWANIE METODY PHA DO OCENY RYZYKA USZKODZEŃ SIECI NA PRZYKŁADZIE MIEDZIANEJ DOSTĘPOWEJ SIECI TELEKOMUNIKACYJNEJ

Abstract

This article presents the results of studies relating to the possibility of the practical use of the preliminary hazard analysis method to assess the risk of damage to the telecommunications copper access network. Use of the PHA method allows the identification and evaluation of risk factors; it enables the comparison of the risk of damage to components of the telecommunications copper access network located in different geographical areas. This generates the possibility of the effective application of a comparative analysis (including the service quality) by the operator for different network areas. The method also allows the setting of benchmarks for improving the effectiveness of the technical services of the operator.

Keywords: overhead and cable lines, copper access network, telecommunications wired access network, preliminary hazard analysis (PHA), damage risk assessment, risk management.

Streszczenie

W artykule przedstawiono wyniki badań własnych dotyczących możliwości praktycznego wykorzystania metody Preliminary Hazard Analysis (PHA) do oceny ryzyka wystąpienia uszkodzeń miedzianej dostępowej sieci telekomunikacyjnej. Zastosowanie metody PHA pozwala na identyfikację i ocenę czynników ryzyka. Umożliwia porównywanie ryzyka uszkodzeń komponentów miedzianej dostępowej sieci telekomunikacyjnej zlokalizowanej na różnych obszarach geograficznych. Generuje to możliwość skutecznego stosowania analizy porównawczej (m.in. jakości obsługi) przez operatora dla różnych obszarów sieci. Pozwala także na benchmarking w zakresie poprawy efektywności m.in. pracy służb technicznych operatora.

Słowa kluczowe: Preliminary Hazard Analysis, (PHA), miedziana dostępowa sieć telekomunikacyjna, ocena ryzyka uszkodzeń, zarządzanie ryzykiem.

1. Introduction

In the 21st century, effective electricity supply systems and efficient IT systems are strategic areas of activity undertaken to guarantee the proper functioning of states, societies and economies based on knowledge. This is an important issue in the following areas:

- ▶ in crisis management, where the key roles of electricity supply systems, communication systems and IT networks within the critical infrastructure are emphasised [41 – art. 3] – special attention is paid to making sure that such attributes of critical infrastructure remain available;
- ▶ in the context of ensuring broadly understood security [44] and effectiveness [13] at the micro-, meso- and macroeconomic level (in connection with the implementation of the Europe 2020 strategy for smart and balanced development [11]);
- ▶ in connection with the necessity of undertaking technical activities aimed at diagnosis and forecasting adverse events (damage) within a specific ICT network (particularly the identification and assessment of risk related to this damage in the context of the effective preparation of specialist engineering teams for technical performance of activities as part of interdisciplinary risk management.

The aim of this paper is to assess the options for use of the preliminary hazard analysis (PHA) method in order to evaluate the risk of damage to the telecommunications copper access network operating in the area of a selected district. In consideration of the above, the following objectives were attempted:

- ▶ defining the important terms related to the subject of this analysis,
- ▶ identifying and shortlisting the risk factors,
- ▶ using PHA for the assessment of the risk of damage to components of the telecommunications copper access network.

A description of the research methods used to accomplish the objectives of this study is provided later in this paper.

2. The risk of damage to the telecommunications copper access network – terminological issues

Definitions related to risk differ from each other as their range (broad or narrow) refers to different contexts, approaches and meanings [30]. These have been created to satisfy the requirements of various groups of interested parties (risk is defined differently by engineers [34], management specialists [31], lawyers, doctors [27] and physicians). Thus, depending on whether the author of the given definition creates it within the framework of a specific scientific discipline or for the needs of specific practical issues, not only is it possible to define risk differently, it is also possible to measure it differently [38]. However, emphasis is placed on the fact that ‘risk’ is an interdisciplinary term [23]. The common feature of the definitions proposed in the literature is that risk refers to many different things [8]. It is the type of the hazard (e.g.

for the management board, employees, investors, natural environment), the likelihood of an adverse event and the ‘severity’ of its effects, etc. which are of importance here [21].

Analysis of scientific publications allows the drawing of the conclusion that the issue of risk refers to the broadly understood security and technical aspects [2]. The authors emphasise that an unambiguous definition of risk is a very complex process as, depending on the given situation, the risk may well be in the form of damage, a hazard, or an adverse event [36]. It must be emphasised – although some authors overlook this – that risk is also the impact of uncertainty on a given objective [28 – section 3.48]. The impact may generate a negative or positive deviation from expectations (in the latter case, it generates chances) [12].

In technical sciences, it is particularly important to differentiate between risk and reliability. In practice, these terms are misused [32]. Reliability means the property that the system is able to fulfil its functions under specific conditions of existence and operation and during an assumed period of time [16]. In the context of this paper, the measure of network reliability is failure rate.

We encounter the risk when it is possible to indicate the actual hazard and estimate the likelihood of its occurrence. In situations characterised by uncertainty, it is not possible to unambiguously indicate the existing hazard and/or estimate its likelihood [33]. Uncertainty is the state of a lack or partial lack of understanding or knowledge of an event, its consequences or likelihood [29 – section 3.48].

Telecommunications law defines the telecommunications network as transmission systems and switching or routing devices as well as other resources including inactive network components, which enable the broadcasting, reception and transmission of signals by means of wires, radio and optical waves or other means that use electromagnetic energy irrespective of their type [40]. For the purposes of this ‘paper’ the main focus is on the access network and subscriber network built using copper cable technology.

An access network (within the meaning of the factory standard ZN-02/TD S.A.- 05 Construction of Copper Access Networks) is a network that covers a set of access lines in a given area [9] from the main distribution frame to the access point.

In contrast to an access network, a subscriber network is comprised of a network from the access point to a port at the customer’s premises. Analysis of the report of the Office of Electronic Communications from the year 2016 allows the drawing of the conclusion that copper routes account for 95% of wired access networks (Fig. 2). Thus, it is important to identify the risk of damage to services based on the copper transmission medium.

A wired access network can be built using underground and/or overhead cables. The choice of the technology depends on many factors analysed at the design stage of the network. The network analysed in this paper uses xDSL (digital subscriber line) and LAN-Ethernet (ethernet-based local area network) technologies for the provision of services ordered by customers.

A hazard is an event which has an adverse effect on the proper functioning of the telecommunications service. In the context of this study, hazards may relate to deliberate or accidental events which disrupt transmission. Accidental events include weather anomalies, equipment and/or system failures, and natural disasters [3]. Thus, a hazard is the potential

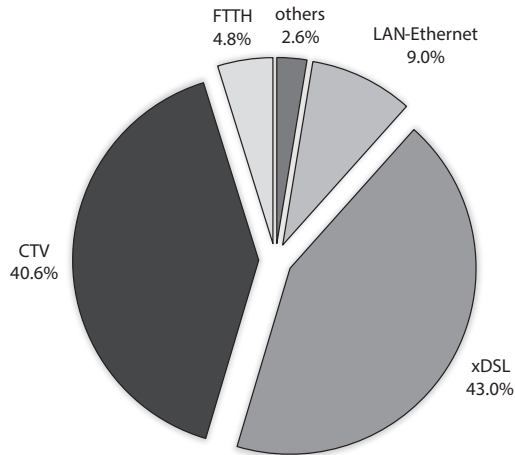


Fig. 1. Structure of the subscribers according to the used wired access technology
 Note: The FTTH category uses fibre-optic cables and not copper cables. The 'other' category cannot be classified precisely. Cable television, xDSL and LAN-Ethernet use copper lines.
 (Source: Compiled on the basis of data gathered by the Office of Electronic Communications for the year 2015 [35])

cause of an incident, which may result¹ in damage to the system/service recipient. In this paper, the risk of damage to the telecommunications network is considered from the point of view of an operator.

In this context of this study, damage is understood as interruption to or interference of the operation of the telecommunications service, which is reported by the customer to the relevant operator.

Risk of damage to the telecommunications network is considered unacceptable in instances where either or both of the following situations apply: there is a substantial likelihood of damage to the continuity and effectiveness of the services; the costs of restoring the required level of service following such damage are likely to be at a level that results in repair being deemed to be unprofitable by the operator.

3. Assessments of the risk of damage to a telecommunications wired access network using preliminary hazard analysis

In connection with the necessity to accomplish the objective of this study and also because of the subject of this study, a decision was taken to perform an overview of the available literature on the subject and to present the gist of the PHA (Preliminary Hazard Analysis) method.

¹ An effect is the result of an adverse event.

A case study was applied in the course of the research work. During the first quarter of 2016, as part of the scientific research, the author participated in field operations of a representative of one of the local telecommunications operators within the district² located in the area of the podkarpackie province and obtained empirical data. The researcher had access to important information included in the technical documentation of the network³. Additionally, detailed interviews were conducted with specialists who performed work on the copper network and with their managers.

A model of the analysed telecommunications network⁴ is presented in Fig. 2.

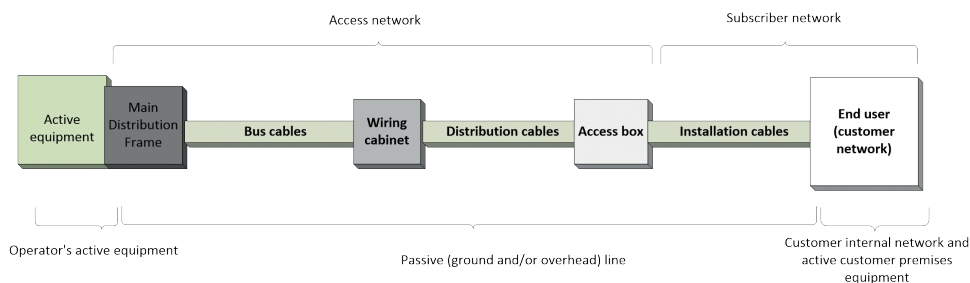


Fig. 2. Model of the analysed telecommunications network
(Source: Own study)

Broadly speaking, it can be assumed that the analysed telecommunications network consists of active devices operated by the operator, underground and overhead passive lines and customers' internal networks including the active devices that are in their possession.

During the conducted analysis, the reliability of the analysed network was established at a level of 97%. This means that 3% of customers reported an issue regarding the faults that interfered with the proper functioning of the provided services during the analysed quarter.

The conducted studies allowed for the performance of typologisation based on the location of disruption in the provision of telecommunication services. The locations of the faults reported by customers which were identified during the 3-month period, referred to:

- ▶ active devices owned by the operator
- ▶ the telecommunications line for connecting operator's devices to the customer's port? (overhead lines were dominant)

² Disclosure of more detailed characteristics of the area covered by the analysis was not allowed.

³ Because of security issues relating to users and the necessity to protect the competitive advantage of the company, no consent was given for the detailed publication of data, which would enable the identification of the operator and the analysed network.

⁴ In the analysed case, the access network covers active equipment of the operator and the local loop (the circuit that connects the network termination with the access point to the fixed-line public telephone network, in particular, the main distribution frame).

- ▶ the customer's own network (defined as the line section starting from the customer's port, including active devices)
- ▶ the 'other' category, which covers events in which no damage was found and/or intervention was not justified, etc.

The presented typologisation became the basis for the identification of risk factors.

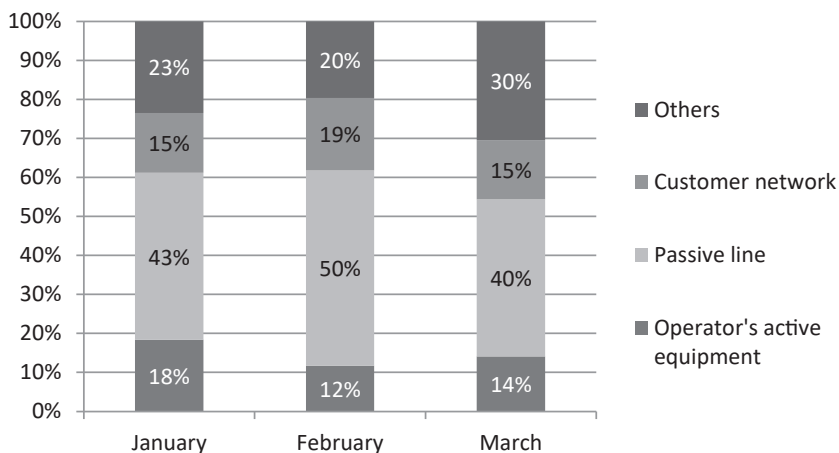


Fig. 3. Typologisation of faults which occurred during the period from January to March 2016 in the analysed geographical area (expressed in percentages)
N = 292 (covers all the interventions of employees of the analysed telecommunications network operator) (Source: Own work based on the studies)

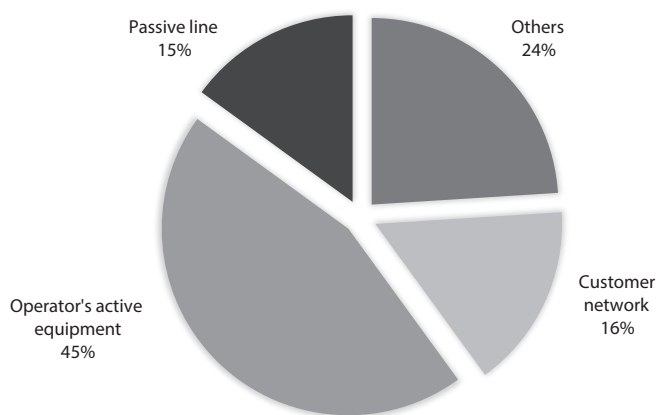


Fig. 4. Division of faults in terms of the location of adverse events (average values for the 3-month period, expressed in percentages); *N* = 292 (covers all the interventions of employees of the telecommunications network operator in the analysed geographical area)
 (Source: Compiled on the basis of results of own studies)

Analysis of the data presented in Chart 2 allows drawing the conclusion that the percentage distribution of faults in the analysed area was similar in each month of the first quarter of 2016. Therefore, based on the data obtained during the study, the results were averaged in order to standardise the data and estimate the likelihood of damage in the given network element (Fig. 4).

It can be seen in Fig. 4' that 45% of faults were found in the passive line. During the analysed period, damage to the operator's equipment accounted for barely 15% of the analysed cases. The causes of 16% of the irregularities related to service functioning issues diagnosed in the internal network and/or devices owned by customers. The remaining 24% of cases mainly covered so-called alleged faults, in which issues reported to the operator by the customers were not confirmed by service technicians (e.g. the customer had managed to fix the issue before the arrival of the technical services).

In this paper, the author uses the term 'repair time required'; this refers to important cost-generating factors [10]. It represents the use of work time measured by the number of man-hours spent on the completion of activities/interventions on network components and provides a parameter for the allocation of resource costs to activities in the activity based costing⁵ [19]. In accordance with the TDABC (time-driven activity-based costing) concept⁶ [17], the time-driven use of resources allows the cost pools involved in the performance of activities to be easily allocated, especially in the case of the service companies with a high share of human resources⁷ [37], [39]. Because of the editing limitations and the objectives set for this paper, analysis of costs was not a subject of this study.

An additional element of our studies included attempts to determine the average time required to repair damaged network elements. Based on analyses of documentation, the results of measurements and information obtained during in-depth interviews conducted with service technicians and managers, it was possible to average the time required to carry out an intervention. The data presented in Table 1 refers to the period from the moment of dispatching a service technician to determine the cause and solve the reported issue to the moment of reporting effect of the intervention upon completion.

⁵ The literature on the subject indicates the use of the concept of the resource cost driver in economic practice. This driver is described as the time-driven use of the resource which allows for the allocation of the costs of difficult resources to activity based costing, using information about the working times of the respective employees. Activity-based costing (as one of the calculation methods) enables the best possible allocation of the overall costs incurred during a given period of time to the given elements responsible for the occurrence of these costs. In the case of the ABC method, costs are assigned to activities and cost objects (e.g. materials).

⁶ Time-driven activity-based costing.

⁷ In the case of the TDABC approach, the calculation of the costs of each service/repair requires: 1) the calculation of the costs of all resources allocated to the given type of activity; 2) the division of all the costs by the number of work hours of employees to obtain the cost per unit of available time; 3) the multiplication of the cost of the time unit by the number of units related to each cost object.

Table 1. Average time required to repair the telecommunications copper access network depending on the location of the fault within the analysed geographical area in the first quarter of 2016

Location of damage	Operator's equipment	Line	Customer's equipment and or network	Other
Required repair time	1 hour	2 hour	1.3 hour	0.5 hour

(Source: Compiled on the basis of results of own studies)

While analysing the time required to identify and/or repair an instance of damage, it is necessary to take into account the fact that it was determined from the point of view of specialist crews responding to requests made by customers. In the case of the defectiveness of customer's equipment and/or the network, the time required for damage repair was out of the operator's control. Pursuant to the agreement, the operator is not held liable for the customer network and/or equipment failures which interfere with the proper functioning of the service. The operator, when precluding the necessity of his intervention, may identify the problematic area to be on the side of the customer's network (e.g. related to the necessity to replace equipment). In such cases, the intervention time (limited to the identification of the cause of a fault on the subscriber's side) was specified to be an average of 1.3 h.

As a result of the abovementioned data, it is possible to proceed with the assessment of the risk of adverse events (faults) in the analysed telecommunications copper access network. Risk assessment is important as it allows the proper treatment of the risk, which can cover; the risk avoidance, the risk reduction, the risk transfer or the risk acceptance [29]. The risk handling involves a risk modification process by, among others, removal of the source of risk, change in consequences, the risk sharing and the risk retention [16– def. 3.8.1].

In literature regarding the issue of risk, authors indicate various methods for its assessment. The majority of the described methods are based on a similar operating scheme which is essentially the ranking in seriousness of adverse events, the determination of the likelihood of a given risk type and the estimation of the potential adverse effects/losses related to its occurrence again, [4, 15].

In order to achieve the objectives of this paper, a decision was taken to use the matrix method, which is referred to as preliminary hazard analysis (PHA). The PHA method is a universal method, which is characterised by a broad spectrum of options for its use in different areas⁸ [45, 43, 46]. It is classified among the induction, qualitative, two-parameter, four-phase methods. Its use is recommended in the developmental phase of work (studies), design (modification) and construction (building). It is applied in the estimation of risk related to hazardous events which occur with regard to devices, machines and their systems [14, 24].

The use of this method requires making preliminary arrangements⁹ [5]. Specifically, these activities include:

⁸ The literature indicates that it is often used to assess industrial risk at a given workplace.

⁹ The determination of the aim and scope, the selection of the team, the collection of information, etc.

- a) The identification of the risk – this includes the ongoing process of search, recognition and description of the risk (what may happen, where and why) [16 - def. 3.5.1, 25].
- b) The assignment of the likelihood¹⁰ of an event (P) occurring to a given network element. For the purposes of this paper, a five-stage division of the likelihood has been adopted. During the creation of the abovementioned divisions, reference has been made to the results obtained during our own studies (Chart 3). Variant ‘1’ refers to a highly unlikely occurrence of an event/fault. The likelihood of occurrence ranges between 0% and 20% in this case. Variant ‘S’ refers to the occurrence of a very likely event/fault (from 81% to 100%).
- c) The assignment of a rating which refers to the time spent on interventions by the operator’s repair services to a given network element, which result in the fault being identified and, if possible, proper service being restored. A scale between 1 and 5 was adopted, where 1 refers to an intervention time up to 30 min, and 5 is an intervention time exceeding 2 hours.
- d) The determination of the risk level using the matrix (Fig. 5)

In accordance with ISO Guide 73, a risk includes both the combination of the likelihood of an event and its effects. In order to calculate the risk level based on the PHA method, the required formula is modified as follows:

$$R = S * P \quad (\text{formula 1})$$

where:

R – the risk level

S – the degree which refers to the time required for the intervention of the operator’s services,

P – the likelihood of a fault of a given network element.

		Likelihood of a fault in reference to a given network element [P]				
		1 0–20%	2 21–40%	3 41–60%	4 61–80%	5 81–100%
Degree referring to the time required for the intervention of the operator’s repair services [S]	1 0–30 min.	1	2	3	4	5
	2 31–60 min.	2	4	6	8	10
	3 61–90 min.	3	6	9	12	15
	4 91–120 min.	4	8	12	16	20
	5 >120 min.	5	10	15	20	25

Fig. 5. Risk level determination matrix

¹⁰ Likelihood must be understood as the degree of certainty that a given incident will happen.

Compiled on the basis of the guidelines of the Polish standard - PN-N-18002:2011 [26]).

The quantitative risk analysis consisted of the determination of the likelihood of a fault on a given network element and an indication of the consequences of such an adverse event taking place. The adverse effects were expressed in degrees from 1 to 5. The degrees refer to the time required by the operator's repair services to intervene (Table 1).

		Likelihood of a fault on a given network element [P]				
		1 0–20%	2 21–40%	3 41–60%	4 61–80%	5 81–100%
Degree which refers to the time required for the intervention of the operator's repair services [S]	Level					
	1 0–30 min	1	2	3	4	5
	2 31–60 min	2 Operator's equipment	4	6	8	10
	3 61–90 min.	3 Customer's equipment and/or network	6	9	12	15
	4 91–120 min.	4	8	12 Line	16	20
	5 >120 min.	5	10	15	20	25

Fig. 6. Specific levels of the risk of damage according to the respective locations.

If the calculated risk level ranges between 1 and 2, the risk is minimal – it is tolerated at the current level and no specific action is required

If the calculated risk level ranges between 3 and 9, the risk is average and must be managed [16 – def. 2.1, 22]. The area must be monitored in order to guarantee supervision of the costs and of whether the hazard moves to a different risk level range over time. The implementation of new solutions or improvements is justified if they do not result in any additional costs.

If the calculated risk level ranges between 10 and 25, the risk for the operator is high and significant. Despite the fact that it is within the tolerance limits, it may escalate to reach the intolerance limit¹¹ [47]. Because this is a risk, which requires particular attention, specific and comprehensive actions must be taken both in the short-term and in the long-term. In order to reduce the risk, it is necessary to strive for a reduction in the levels of some risk factors. The likelihood of a fault may be decreased by, for example, a change in the used technology or as a result of improvement in the process of identification of the cause of faults, which will significantly reduce repair times.

¹¹ The higher the risk level, the more attention is required. Tolerance with regards to risk does not mean acceptance of the given status quo and requires a response.

Analysis of the data presented in Fig. 6 allows the drawing of the conclusion that the most sensitive part of the analysed network was the passive line. Repairs of damage to components of this line required a comprehensive technical diagnosis; this included several specialist measurements, which often required service engineers to relocate and work at height as a result of the nature of the passive line. Such activities extended the time of restoration of the service; the average intervention time of the operator during completion of a repair order was estimated to be in the range of 1.5 to 2 hours and thus generated significant costs. It must be emphasised that the likelihood of damage in the area of the abovementioned network was very high. In order to ensure the usefulness and reliability of the network, which translates to a reduction in the likelihood of damage, it is necessary to apply the technologies and tools that allow for the shortening of the repair time. The diagnosis and improvement of the quality parameters of the copper network existing in a given area is absolutely vital as the highest risk of damage was actually observed in relation to the functioning of the network. In the context of technological changes, the rapid, gradual replacement of the copper access network with the fibre-optic network may turn out to be necessary [1, 6].

As a result of the conducted assessment of the risk of damage to the telecommunications copper access network, it was found that the second important reason for a lack of availability of the services was the customer's equipment and/or network; faults in this area accounted for 16% of the diagnosed causes of interventions carried out by the operator's employees. In order to minimise the risk of damage perceived by the service recipient, the customers may be offered professional installation of the internal network and lease of the customer premises equipment (CPE). If the services are unavailable, the entire responsibility for the restoration of the operation of the system lies with the operator, including the replacement of the equipment; this applies throughout the term of the agreement. This will undoubtedly shorten the time required to eliminate faults in the customer's network, contributing to a faster return of a properly functioning service.

4. Conclusions/Summary

The PHA method is a relatively cheap tool, which can be used to assess the risk of damage to the components of a telecommunications copper access network. It can be recommended as a useful diagnostic solution. Preliminary hazard analysis constitutes a useful tool from the point of view of both its technical and investment purposes. The use of the PHA method allows the identification and assessment of risk factors; it enables comparison of the risk of damage to the components of the telecommunications copper access network located in different geographical areas. This generates the possibility of using comparative analysis, i.e. benchmarking for the different network areas handled by the operator, or for the network performance. From a technical point of view, the location of the site where the number of faults is the largest is of key importance for the optimisation of technological solutions. The use of the PHA method in the analysed case allowed drawing the conclusion that the majority of faults in the telecommunications network were detected in the area of the passive line. This

is a very important finding for further considerations regarding the factors which determine the reliability of the ground and overhead passive line in a given geographical area during different seasons of the year. It is important to be aware that telecommunications networks are characterised by the variability of technical standards; this means that the replacement of their components is not essentially a consequence of wear and tear but rather their age. The gradual replacement of the permanent access networks is necessary; these networks are built mainly of cables with pairs of copper wires designed for analogue voice services with a frequency band of 3.4 kHz, at a length of the subscriber connection up to about 10 km. For the HDTV services, it is necessary to introduce subscriber access with the bit rate of around 50 Mbit/s and the construction of a new generation network (NGN) [7].

Pursuant to the recommendations of the European Commission described in the Digital Agenda for Europe [12], comprehensive and multi-dimensional measures must be undertaken so as to make sure that all Europeans will have a common and fast access to the Internet at competitive prices. Telecommunication network planning and maintenance involves complex issues that are in constant demand for better solutions [1]. By the year 2020, the European Union intends to guarantee access to lines with a capacity exceeding 30 Mbps. Additionally, the aim is to also provide at least half of the European households with access to connections with a capacity exceeding 100 Mbps [18]. While analysing the degree of accomplishment of the objectives mentioned above, it is clear that there is still a lot that needs to be done. In the year 2016, the capacity of 61% of lines was above 10 Mbps and almost 11% of users of these lines had access to the network with a capacity exceeding 100 Mbps [35].

On 20 September 2010, the European Commission adopted a recommendation on regulated access to next generation access networks (NGA). NGA was defined as wired access networks which consist of fibre-optic cables, either entirely or partially. Currently, copper networks are becoming more and more expensive to maintain; this is partly due to the cost of electrical power. Furthermore, the required capacities (above 30 Mbps), as a consequence of the parameters of copper cables, are available only at small distances (up to 1.5 km) from the telephone exchange [42]. Pursuant to article 16, section 4 of Directive 2002/21/EC, the national regulatory bodies are obliged to prepare regulations for the transition of copper networks to fibre-optic networks [48]. The Office of Electronic Communications (the national regulator) imposes an obligation on operators with significant market power (SMP) to provide access to fibre loops for alternative operators.

References

- [1] Alarcón M.J., Zorzano F.J., Jevtić A., Andina D., *Telecommunications Network Planning and Maintenance*, WMSCI 2008, 2th World Multi-Conference on Systemics, Cybernetics and Informatics, Vol. 8, 2008, 64–68.
- [2] Arunraj N.S., Maiti J., *Risk-based maintenance-Techniques and applications*, Journal of Hazardous Materials, Vol. 142, Issue 3, 11 April 2007, 653–661.
- [3] Baniak K., *Analiza zagrożeń telekomunikacyjnych sektora publicznego, Bezpieczeństwo w telekomunikacji i teleinformatyce*, Biblioteka „Bezpieczeństwa Narodowego”, kwartalnika wydawanego przez Biuro Bezpieczeństwa Narodowego, tom 3, 2007, 38, <https://www.bbn.gov.pl/download/1/1000/analizazagrozen.pdf> (access: 03.07.2018)
- [4] Baybutt, P., *Analytical Methods in Process Safety Management and System Safety Engineering-Process Hazard Analysis*, Handbook of Loss Prevention Engineering, Volume 1&2, J.M. Haight (red.), Wiley-VCH Verlag GmbH & Co. KGaA, Weinheim, Germany 2013.
- [5] Baybutt, P., *Requirements for improved process hazard analysis (PHA) methods*, Journal of Loss Prevention in the Process Industries, Vol. 32, November 2014, 182–191.
- [6] Begović A., Škaljo N., Behlilović N., *A Methodology of Modern Copper Access Network Design and Redesign*, International Journal of Research in Wireless Systems (IJRWS), Vol. 2, Issue 2, June 2013, 40–49.
- [7] Borzycki K., *Światłowodowe sieci dostępne*, Telekomunikacja i Techniki Informacyjne, nr 1–2/2008, 1.
- [8] Clifton A. Ericson II, *Hazard Analysis Techniques for System Safety*, 2nd Edition, John Wiley & Sons, 2015, 125.
- [9] Departament Planowania i Modelowania Sieci, Telefonii Dialog S. A. *Projektowanie i Budowa Sieci Telekomunikacyjnej ZN-02/TD S.A., 05 Budowa Sieci Dostępowych Miedzianych*, norma branżowa wersja 2, Wrocław 2002, 4.
- [10] Dyhdalewicz A., *Próba identyfikacji czynników kosztotwórczych w przedsiębiorstwach handlowych branż informatycznej na podstawie raportów rocznych*, Economics and Management, nr 2, 2014, 198–200.
- [11] *Europa 2020 – Strategia na rzecz inteligentnego i zrównoważonego rozwoju sprzyjającego włączeniu społecznemu*, KOM(2010) 2020, <http://uniaeuropa.org/strategia-europ-2020/> (access: 03.07.2018).
- [12] Hajduk-Stelmachowicz M., *System zarządzania środowiskowego jako część systemu zarządzania ryzykiem*, [in:] E. Urbanowska-Sojkin, M. Brzozowski (ed.), Wydawnictwo Uniwersytetu Ekonomicznego w Poznaniu, Poznań 2013, 84–87.
- [13] Hajduk-Stelmachowicz M., Stelmachowicz M., *Efektywność energetyczna jako atrybut bezpieczeństwa energetycznego*, [in:] *Bezpieczeństwo energetyczne na wspólnym rynku energii UE*, S. Gędek, M. Ruszel (ed.), Wydawnictwo Rambler, Warszawa 2015, 139–154.
- [14] Hajduk-Stelmachowicz M., Buczek I., *Ocena ryzyka zawodowego na stanowisku operatora wtryskarki*, [in:] *Praktyczne aspekty bezpieczeństwa i ergonomii*, Monografie 2017, G. Dahlke (ed.), Wydawnictwo Politechniki Poznańskiej, Poznań 2017.

- [15] Huang, Hui-Wen, et al., *System-level hazard analysis using the sequence-tree method*, *Annals of Nuclear Energy*, 35.3 (2008), 353–362.
- [16] *ISO Guide 73:2009*, definicja 3.5.1.
- [17] Kapłan R.S., Anderson S.R., *Rachunek kosztów działań sterowany czasem-TDABC Time-Driven Activity Based Costing*, Wydawnictwo Naukowe PWN, Warszawa 2008.
- [18] Komisja Europejska, *Europejska Agenda Cyfrowa: kluczowe inicjatywy*, Memo 2010, Bruksela 19 maja 2010, http://europa.eu/rapid/press-release_MEMO-10-200_pl.htm (access: 03.07.2018).
- [19] Kowalski M., Kuchta D., *Wykorzystanie czasu pracy jako parametru rozliczania kosztów zużycia zasobów*, *Badania Operacyjne i Decyzje*, nr 2, 2006, 64–71.
- [20] Kwietniewski M., *Awaryjność infrastruktury wodociągowej i kanalizacyjnej w Polsce w świetle badań eksploatacyjnych*, XXV Konferencja Naukowo-Techniczna Awarie Budowlane 2011, Międzyzdroje 24–27 maja 2011, 130, http://www.awarie.zut.edu.pl/files/ab2011/referaty/T1_01_Referaty_plenarne/07_Kwietniewski_M_Awaryjnosc_infrastruktury_wodociagowej_i_kanalizacyjnej_w_Polsce_w_swietle_badan_eksploatacyjnych.pdf (access: 03.07.2018).
- [21] Kubińska-Kaleta E., *Zarządzanie ryzykiem w przedsiębiorstwach przemysłowych na przykładzie huty stali*, Akademia Górniczo-Hutnicza, Wydział Zarządzania, Kraków 2008, <http://winntbg.bg.agh.edu.pl/rozprawy/9919/full9919.pdf> (access: 03.07.2018)
- [22] Kulawik D., *Bezpieczeństwo w telekomunikacji i teleinformatyce z punktu widzenia operatora telekomunikacyjnego*, 109–141, <https://www.bbn.gov.pl/download/1/1006/bezpieczenstwotelekomunikacji.pdf> (access: 03.07.2018).
- [23] Hua-wei L., Zhong-yuan S., *Application of Preliminary Hazard Analysis in the Accident Analysis of Fire and Explosion of Oil Depots*, *Forestry Labour Safety*, 2008, Issue 2.
- [24] Mauborgne P., Deniaud S., Levrat E., Bonjour E., Micaëlli JP., Loise D., *Preliminary Hazard Analysis Generation Integrated with Operational Architecture – Application to Automobile*, [in:] Boulanger F., Krob D., Morel G., Roussel JC. (ed.), *Complex Systems Design & Management*. Springer 2015, Cham, 298.
- [25] Nakayama J., Sakamoto J., Kasai N., Shibutani T., Miyake A., *Preliminary hazard identification for qualitative risk assessment on a hybrid gasoline – hydrogen fueling station with an on – site hydrogen production system using organic chemical hydride*, *International Journal of Hydrogen Energy*, Vol. 41, Issue 18, 2016, 7518–7525.
- [26] Norma PN-N-18002:2011 *Systemy zarządzania bezpieczeństwem i higieną pracy – Ogólne wytyczne do oceny ryzyka zawodowego*, PKN, Warszawa 2011, 13.
- [27] Niel-Lainé, J., et al. *Interest of the preliminary risk analysis method in a central sterile supply department*. *Quality and Safety in Health Care*, Vol. 20, Issue 8, *BMJ Qual Saf* 2011, 698–703.
- [28] Norma BS ISO 22301:2012, *Zabezpieczenie społeczne – system zarządzania ciągłością działania – Wymagania*. Warszawa 2015, Pkt 3.48.
- [29] Norma PN-ISO 31000:2012, wersja polska, *Zarządzanie ryzykiem – Zasady i wytyczne*, Warszawa 2012.
- [30] Pinto A., Nunes I.L., Ribeiro R.A., *Occupational risk assessment in construction industry – Overview and reflection*, *Safety Science*, Volume 49, Issue 5, June 2011, 616–624.

- [31] Pisarewicz P., Galiński P. (red.), *Zarządzanie ryzykiem i wartością organizacji współczesne wyzwania*, Wydział Zarządzania Uniwersytetu Gdańskiego, Sopot 2016.
- [32] Połoński M., *Rozkład czasu trwania czynności a termin zakończenia przedsięwzięcia z uwzględnieniem elementów analizy ryzyka*, ACTA Scientiarum Polonorum 4(2)2005, Wyd. SGGW, 95–106.
- [33] Połoński M., Pruszyński K., *Interdyscyplinarny charakter nauki o ryzyku*, Materiały konferencyjne, „Zarządzanie ryzykiem w przedsiębiorstwie”, Ciechocinek 2006, 1–5; http://mieczyslaw_polonski.users.sggw.pl/Ryzyko2006b.pdf (access: 03.07.2018).
- [34] Połoński M., Pruszyński K., *Ryzyko projektowania przedsięwzięć inżynierskich*, Wiadomości Projektanta Budownictwa, nr 1, 2008, 23–27.
- [35] Prezes Urzędu Komunikacji Elektronicznej, *Raport o stanie rynku telekomunikacyjnego w Polsce w 2015 roku*, Warszawa czerwiec 2016, 5–11, https://uke.gov.pl/files/?id_plik=23480 (access: 03.07.2018)
- [36] Radkowski S., *Podstawy bezpiecznej techniki*, Wyd. PW, Warszawa, 2003.
- [37] Raulinajtys-Grzybek M., *Wycena kosztu godziny pracy lekarza weterynarii w Polsce wykonującego czynności lekarsko-weterynaryjne w ramach zakładu leczniczego dla zwierząt*, SGH, Warszawa 2014, 2–19, http://webcache.googleusercontent.com/search?q=cache:tjHWuX-Mh3wJ:www.vetpol.org.pl/prawo-projekty-legislacja/doc_download/2785-wycena-kosztu-godziny-pracy-lekarza-weterynarii+%&cd=7&hl=pl&ct=clnk&gl=pl (access: 03.07.2018)
- [38] Rausand M., *Risk Assessment Theory, Methods, and Applications*, Wiley, 2011.
- [39] Świdarska G.K., Raulinajtys M., *Rachunek kosztów działań jako podstawa wyceny usług*, Zeszyty Teoretyczne Rachunkowości, tom 49, nr 105, 2009, 255–267.
- [40] Ustawa z dnia 16 lipca 2004 r. Prawo telekomunikacyjne (Dz.U. z 2016 r. poz. 1489).
- [41] Ustawa o zarządzaniu kryzysowym, Dz.U. z 2007 r., nr 89, poz. 590 z późniejszymi zmianami.
- [42] Wach M., *Kierunki rozwoju technologii: FTTH, VULA, vectoring, unbundling – wobec priorytetów Europejskiej agendy cyfrowej*, Prawo i Regulacje Świata Telekomunikacji i Mediów, Warszawa, Październik 2011, 70–71; https://www.dzp.pl/files/Art/PiR_Marlena_Wach.pdf (access: 03.07.2015).
- [43] Ward J., Clarkson J., Buckle P., Berman J., Lim R., Thomas J., *Prospective Hazard Analysis: Tailoring Prospective Methods To A Healthcare Context*, Final Report 6 July 2010, V1.1, University of Cambridge, University of Surrey, Greenstreet Berman Ltd., Research Project PS/035, Engineering Design Centre, University of Cambridge, 2010, <https://www.birmingham.ac.uk/Documents/college-mds/haps/projects/cfhcp/psrp/finalreports/PS035-RevisedPHAFinalReportv11withToolkitJuly2010.pdf> (access: 03.07.2018).
- [44] Witkowski M., *Bezpieczeństwo systemów teleinformatycznych w zarządzaniu kryzysowym*, ZESZYTY Naukowe WSOWL, Nr 4 (162) 2011, 82.
- [45] Woźny A., Pacana A., *Ocena ryzyka zawodowego. Teoria i przykłady*, OWPRz, Rzeszów 2013.
- [46] Valis D., Koucky M., *Selected overview of risk assessment techniques*, Problemy Eksploatacji, 2–2009, 19–32.

- [47] *Przegląd wybranych metodyk*, Wróblewski D. (ed.), Wydawnictwo CNBOP-PIB, Józefów 2015, 47.
- [48] Zalecenie Komisji z 20 września 2010 roku w sprawie regulowanego dostępu do sieci nowej generacji (2010/572/UE), <http://eur-lex.europa.eu/legal-content/PL/TXT/?uri=celex:32010H0572> (access: 03.07.2018).

Kazimierz Kielkowicz  orcid.org/0000-0001-5791-6069

kkielkowicz@pk.edu.pl

Department of Computer Science, Faculty of Electrical and Computer Engineering,
Cracow University of Technology

UNSUPERVISED LEARNING IN LATENT SPACE WITH A FUZZY LOGIC GUIDED MODIFIED BA

UCZENIE NIENADZOROWANE W PRZESTRZENI UTAJONEJ Z WYKORZYSTANIEM ZMODYFIKOWANEGO ALGORYTMU NIETOPERZOWEGO STEROWANIA ROZMYTEGO

Abstract

In this paper, a modified bat algorithm with fuzzy inference Mamdani-type system is applied to the problem of document clustering in a semantic features space induced by SVD decomposition. The algorithm learns the optimal clustering of the documents as well as the optimal number of clusters in a concept space; thus, making it suitable for a large and sparse dataset which occur in information retrieval system. A centroid-based solution in multidimensional space is evaluated with a silhouette index. A TF-IDF method is used to represent documents in vector space. The presented algorithm is tested on the 20 Newsgroup dataset.

Keywords: document clustering, unsupervised machine learning, BA, fuzzy logic

Streszczenie

W publikacji zmodyfikowany algorytm nietoperzowy z rozmytym kontrolerem typu Mamdaniego został zastosowany do problemu analizy skupisk dla danych tekstowych. Proces uczenia odbywa się w przestrzeni skompresowanej, otrzymanej z dekompozycji SVD zbioru uczącego. Prezentowany algorytm uczy się jednocześnie optymalnego pokrycia klastrami przestrzeni oraz liczebności klastrów. Do oceny jakości rozwiązania zastosowano wskaźnik Silhouette. Dane w reprezentacji wektorowej otrzymano z wykorzystaniem transformacji TF-IDF. Prezentowany algorytm przetestowana na zbiorze „20 Newsgroup”.

Słowa kluczowe: klasteryzacja dokumentów, uczenie nienadzorowane, BA, logika rozmyta

1. Introduction

Unsupervised learning, also known as cluster analysis or classification, is a process of exploring the unknown structure of the data by separating a finite data set into clusters. Partitional unsupervised learning in particular divides the data object into a predefined number of clusters. Formally, in mathematical terms partitional unsupervised learning can be stated as follows [11]: given a set of m objects $X=\{x_1, \dots, x_j, \dots, x_m\}$, where $x_j=(x_{j1}, x_{j2}, \dots, x_{jn}) \in R^n$, find a K -partition of X , $C=\{C_1, \dots, C_K\}$ ($K \leq m$) such that $C_i \neq \emptyset$ for ($i=1, \dots, K$) and $\bigcup_{i=1}^K C_i = X$ and $C_i \cap C_j = \emptyset$ for $i, j=1, \dots, K$ and $i \neq j$. The problem of unsupervised learning can be stated as the optimisation of a predefined criterion function so that data objects belonging to cluster C_i are more similar to each other than objects belonging to cluster C_j . In principal, such optimisation can be performed by a 'brute force' methods; however, in practice this is often unfeasible. An alternative approach is to use a heuristic algorithm like K -means. However, such a hill-climbing-like algorithm suffers from being sensitive to the initial starting point and is likely to get stuck in local minima. To overcome these limitations, it is advisable to use a more sophisticated metaheuristic algorithm.

In principal, metaheuristics algorithms can be divided into a few groups, e.g. algorithms based on an evolutionary approach that model evolutionary processes and algorithms exploring the phenomenon of swarm intelligence [6].

Another approach, such as algorithms for modelling the response of a human immune system (e.g. artificial immune system algorithms) might be considered as a separate category due to the multiplicity of these proposed solutions.

Metaheuristics methods which are focused on exploring models of natural evolution generally, although not exclusively, take the following forms: genetic algorithms (GA) [10], genetic programming (GP) and differential evolution (DE) [20, 21]. Algorithms based on swarm intelligence are broadly presented by particle swarm optimisation (PSO) [13], ant colony optimisation (ACO) [4] or some of its modifications.

In recent years, unsupervised learning based on natural inspired metaheuristic algorithms, including PSO [7, 14, 22] and ant algorithms [5] has attracted attention as a result of its demonstrated effectiveness in solving complicated optimisation problems.

The recently introduced method, based on the group of solutions which explore the phenomenon of swarm intelligence was presented by Yang [22] in 2010 and is called the bat algorithm (BA). In [22], by modelling the behaviour of bats hunting for prey and by exploring phenomena of their echolocation capabilities, the author managed to incorporate methods for balancing the exploration phase, as well as the exploitation phase of modern swarm based algorithms.

The BA have already been applied to solve numerous hard optimisation problems such as multi-criteria optimisation [23] or optimisation of the topology of microelectronic circuits [9]. The growing popularity of the BA has encouraged researchers to focus their work on its further improvement. Most work was done regarding the hybridisation of BA with other metaheuristics or local search methods [8]. Some other solutions were involved in the context of adding self-adaptability capabilities to algorithm [1]. Some work has also been done in the

area of the adaptation of the standard BA to binary problems [19] and in modifying scheme of acceptance of a new solution [16].

Unfortunately, most of these modifications not only improve the quality of the obtained solutions, but also increase the number of control parameters that need to be set to obtain solutions of an expected quality. This makes such solutions quite impractical. More recent work [15] introduces a fuzzy logic control system built on a Mamdani-type inference method to control the exploration and exploitation phases of an evolutionary system based on a modified BA [15]. The application of fuzzy logic to control the exploration and exploitation phases frees the user from explicit specifying control parameters and only requires the defining of expected behaviour in a knowledge-based form of *if-then* sentences that is readable for humans.

Section 2 describes a modified BA (MBA) used as an optimisation algorithm. Section 3 provides information about incorporating a fuzzy logic controller to dynamically adjust the behaviour of a MBA and define linguistic variables used in *if-then* sentences in the knowledge base. Section 4 describes used solution encoding as a Bat positing in the search space. Section 5 describes the used cost functions (Silhouette Coefficient index) that are used to evaluate a given solution. Section 6 provides information about inducing semantic feature space from raw data point space using singular value decomposition (SVD). Section 7 discusses methods to transform the raw text-based representation of documents to vector space used by the unsupervised learning algorithm. Section 8 provides experimental results conducted on subsets of the well-known 20 Newsgroup. Section 9 concludes this paper.

2. Modified Bat Algorithm (MBA)

The BA has been recently proposed as a bio-inspired metaheuristics method for solving hard real-valued optimisation tasks. It tries to mimic the behaviour of bats hunting for their prey. The algorithm was introduced by Yang in 2010 [22]. BA is based on a population of bats, which fly through and explore the solution search space in order to find interesting areas. Each single bat represents one solution in multi-dimensional search space. Solutions are evaluated in terms of their fit value by provided a fit function. The full discussion of BA, its shortcomings, and some proposed modifications to form a modified bat algorithm (MBA) can be found in [16]. A MBA is presented as pseudocode in algorithm 1:

- 1: Randomly initialise position x_i and velocity v_i of i -th bat in the population. A bat is an encoded solution as described in section 4.
- 2: Initialise pulsation frequency $Q_i \in [Q_{min}, Q_{max}]$, pulsation r_i and loudness A_i of i -th bat in the population.



- 3: **while not** termination conditions are satisfied:
 $Q =$ fuzzy inference system (diversity, error, iteration) Q adaptation using FLC
- 4: **for** **_each** bat in population:
- 5: $v_i(t) = \alpha_i v_i(t-1) + Q_i(x^* - x_i(t-1)) + Q_i(x_{ever}^* - x_i(t-1))$
 $x_i(t) = x_i(t-1) + v_i(t)$
- 6: **if** **randn(0,1)** $> r_i^t$:
 $x_i^t \leftarrow$ generate new solution around current bat x_i
- 7: **if** $f(x_i^t) < f(x_i)$ **or** **randn(0,1)** $< A_i^t$:
 $x_i \leftarrow x_i^t$
Update values of pulsation and loudness, r_i^t and A_i^t , respectively, as:
 $A_i^{t+1} \leftarrow \alpha A_i^t$; $r_i^{t+1} \leftarrow r_i^t (1 - \exp(-\gamma t))$
- 8: Evaluate bat population using the fit function f described in section 5.
- 9: Find the best bat in the population and mark it as x^*
- 10: **if** $f(x^*) < f(x_{ever}^*)$:
- 11: $x_{ever}^* \leftarrow x^*$

Algorithm 1. Modification of bat algorithm to form MBA

where:

- $v_i(t)$ – real-valued velocity vector of i -th bat,
- $x_i(t)$ – real-valued position vector of i -th bat,
- Q_i – pulsation frequency of i -th bat,
- $\alpha, \gamma, Q_{min}, Q_{max}$ – constant.

The equations used for the bat position and the velocity update used in algorithm 1, step 5, were introduced in [22].

The modifications to BA introduced by Kiełkiewicz and Grela in [16] are twofold: the scheme of acceptance of a new solution; a modified velocity equation to overcome some limitations of the original BA introduced in [22] and a memory of the best solution found during the process of optimisation by the algorithm is also introduced.

Modifications introduced in [16] also change the bat position and the velocity update equations. In comparison to equations presented in [22], the use of an archive component to help direct the bats towards the area where good solutions have previously been found and the concept of cognition coefficients instead of using upper bounds limits are used in [16]. Finally, equations (1) and (2) show the introduced modification:

$$v_i(t) = \alpha_i v_i(t-1) + Q_i (x_i^* - x_i(t-1)) + Q_i (x_{ever}^* - x_i(t-1)), \quad (1)$$

$$x_i(t) = x_i(t-1) + v_i(t). \quad (2)$$

where:

α_i – cognition coefficient of i -th bat,

$x_i^* - x_i(t-1)$ – social component,

$x_{ever}^* - x_i(t-1)$ – archive component,

Q_i – pulsation frequency of i -th bat.

In contrast to equations proposed by Yang in [22], modified velocity equation (1) uses cognition coefficients to limit the influence of past direction (taken at time $t - 1$) in the decision taken at current t iteration. There is also an archive component that helps bats build social knowledge of the previously found globally best solution.

The proposed modifications to the scheme of acceptance of new solutions tend to limit the probability of acceptance of the worse solution. Comparing the original BA with the modification in [16], the worse solution is accepted with probability A_i , where in the modified algorithm, the worse solution is accepted only with probability $(1 - r_i)A_i$. There is an obvious relation, that given $r_i > 0$ and $A_i > 0$, the following is true $(1 - r_i)A_i < A_i$. Moreover, modifications introduced in [16] also include the form of memory x_{ever}^* which represents the best solution ever found.

It is important that the introduced modifications do not change the computation complexity of the algorithm in the context of the big O notation since these modifications are linear in nature and are not based on additional computation or the evaluation of a fitness function.

3. Parameter auto-adaptation using fuzzy logic controller

The dynamic of the MBA is defined by the position and velocity update equations (1) and (2). Pulsation frequency Q_i was chosen to be dynamically adjusted using a fuzzy logic Mamdani-type inference system since this parameter has the most influence on the movement of bats in the colony. Dynamic changes of this parameter can improve the overall performance of the algorithm. However, it is not always possible to derive clear mathematical formula describing how parameters should be adopted during the optimisation process. It is easier to describe an expected behaviour of an algorithm in the form of an *if-then* human-readable sentence describing the situation and expected behaviour, e.g. “If the iteration is small, then exploration is intensive” or “if diversity is small and iteration is big, then exploration is less”.

In the paper, a fuzzy logic Mamdani-type inference system is used to control the exploration/exploitation phase of a MBA through dynamic modification of the pulsation frequency Q_i , as it was introduced and analysed in the author’s other publication [16].

To build a Mamdani-type inference system, it is required to define the input value range, the linguistic variable and the knowledge base in the form of an *if-then* sentence and define the output value range (and their defuzzification method). In the paper, as introduced in

[17], we also use diversity of the colony, the error of the flock and the number of iterations as the input parameters. As our output parameter, we choose Q_{max} . We expect all our input and output parameters to be in the range of

The diversity (dispersion) of the flock is defined by the following equation (3):

$$diversity(t) = \frac{1}{n} \sum_{i=1}^n \sqrt{\sum_{j=1}^D (x_{ij}(t) - x_j^*(t))^2} \quad (3)$$

It can be considered as the average Euclidean distance between each bat and the bat representing the best solution at the i -th iteration. Diversity measures the degree of dispersion in the flock. When bats are close to each other, the diversity is small. Diversity needs to be normalised before it can be considered as input to a fuzzy inference system, since input must be in Equation (4) was used to normalise diversity:

$$normalizedDiversity(t) = \begin{cases} \text{if } minDiversity = maxDiversity, 0 \\ \text{if } minDiversity \neq maxDiversity, \frac{diversity(t) - minDiversity}{maxDiversity - minDiversity} \end{cases} \quad (4)$$

For iteration to be considered as input to a fuzzy logic inference system it needs to be normalised, we used formula (5):

$$Iteration = \frac{currentIteration}{maximumNumberOfIteration} \quad (5)$$

From now on, *normalised Diversity*(t) will be referred to simply as *diversity*(t) and Q_{max} as Q . Membership functions defining input and output linguistic variables over crisp $[0, 1]$ interval are the triangular functions shown in Figs. 1 and 2.

The knowledge base for Mamdani-type inference is in the form of a set of *if-then* sentences, where the *if* part is a premise and the *then* part is the conclusion. Each sentence is constructed using linguistic variables and (possibly) 'and/or' connectors and hedges. In the paper, the author considers two linguistic variables (diversity and iteration) as inputs to the inference system and one output linguistic variable (Q). Each variable can take linguistic values from the set {small, big}. Input and output linguistic values are fuzzy sets defined on interval. Thus, we expect crisp input values and output to be in interval. The used knowledge base is as follow:

KnowledgeBase:

$$= \left\{ \begin{array}{l} \text{"If diversity is } small \text{ and iteration is very } small, \text{ then } Q \text{ is very } big \\ \text{If diversity is } small, \text{ then } Q \text{ is } big \\ \text{If iteration is } big, \text{ then } Q \text{ is } small \\ \text{If iteration is very } big, \text{ then } Q \text{ is very } small \end{array} \right.$$

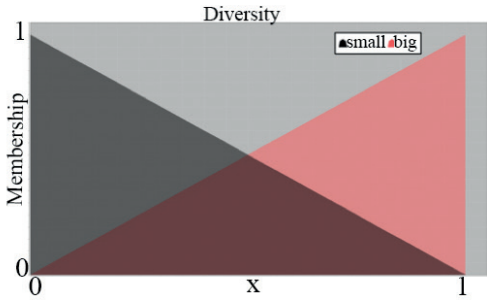


Fig. 1. Diversity linguistic variable and terms {small, big}

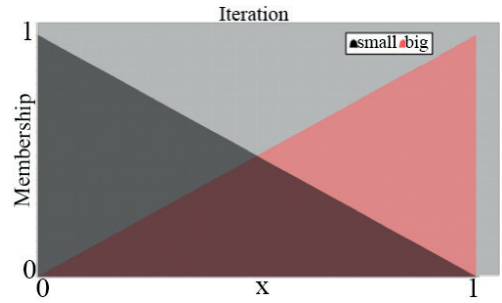


Fig. 2. Diversity linguistic variable and terms {small, big}

4. Solution encoding as bat position in dimensional space

One of the major design considerations in developing unsupervised learning algorithms based on the bat optimisation metaheuristic is encoding the solution as bat position in search space. In the context of clustering N data points into K clusters with cluster centroids $M = \{m_i\}$ $i = 1, \dots, K$ ($m_i \in \mathbb{R}^n$ for learning in n -dimensional space), one way is for the bat position to directly encode the centroid positions as $bat_i := (m_1, \dots, m_K)$ and assign a data point to the cluster based on similarity measures, e.g. the Euclidean distance. Which is known in literature, for other types of population-based metaheuristics, as centroid-based representation [18]. However, in this paper the author augments bat representation with thresholds and encodes the *maximum* numbers of centroids (given as inputs for the algorithm) in the bat position. This way, the optimisation process searches for both the optimum number of centroids and the optimal centroids position in the search space regarding the given cluster index (in this paper, the silhouette coefficient is used). The solution encoded as the bat position in the search space is given as $bat_i := (t_1, \dots, t_K, m_1, \dots, m_K)$, where threshold $t_i \in [-1, 1]$, $m_i \in \mathbb{R}^n$. If t_i satisfied $t_i > 0$ the corresponding centroid is considered active. All active centroids form a valid solution which is evaluated under the given clustering index (discussed in section 5).

5. Cost function

In literature, there are few cluster indices that can be used to evaluate clustering obtained by the optimisation algorithm, for example CH-index [2] or DB-index [3]. However, in this work, the silhouette coefficient [24] index is used as a cost function to evaluate a given solution found by the MBA. Since it evaluates how a given object (here a document) is similar to other objects (documents) in a cluster, it seems reasonable to use it in a document clustering problem where we are interested in having similar documents within a cluster.

In order to construct silhouettes, one needs two things: the partition obtained by the MBA and collections of all proximities between data objects. For each data object i within the data, we calculate the value $s(i)$. The mean value of all data objects is then calculated. Let us define $s(i)$ in terms of dissimilarities. Consider data object i in the data set and corresponding

cluster A to which data point i belongs. When cluster A contains other object that we define $a(i)$ as the average distance to all other data points in A.

Let us define $d(i,C)$ as the average dissimilarity from data point to all data points in the other cluster C ($A \neq C$). After obtaining all $d(i,C)$ for all other clusters in the solution, we can define $b(i)$ as:

$$b(i) = \min_{\text{for every } C \neq A} d(i,C) \quad (6)$$

$$s(i) = \frac{b(i) - a(i)}{\max\{a(i), b(i)\}} \quad (7)$$

Using silhouette coefficients is useful when seeking compact and clearly separated clusters.

6. Latent semantic analysis using SVD

Before unsupervised learning can take place, the learning dataset must be transformed to a vector space of reduced dimensionality – the latent space. The transformation is linear and is based on singular value decomposition [12]. SVD factorises the given learning data (in the form of a matrix X_{mn} with m learning data points $x_i \in R^n$, $X_{mn} = [x_1; \dots; x_m]$) to three matrices $X_{mn} = U_{mr} \Sigma_{rr} V_m^T$, where U and V are orthogonal matrices $U^T U = V^T V = I$ and the diagonal matrix Σ contains r singular values of X_{mn} . The approximation of X is computed by setting all by the largest k singular values in Σ to zero ($= \tilde{\Sigma}$), which is rank k optimal in the sense of L_2 -matrix norm. Once the approximation $\tilde{X} = U \tilde{\Sigma} V^T \approx U \Sigma V^T = X$ is obtained, notice that the data-to-data inner products based in this approximation are given by $X \tilde{X}^T = U \tilde{\Sigma}^2 V^T$ and thus the rows of $U \tilde{\Sigma}$ are defining coordinates for data points in latent space. Once latent representation of a training data set is induced, unsupervised learning can take place.

7. Term frequency-inverse document frequency

In order to perform machine learning on text documents, we first need to convert text-based represented documents into numerical feature vector-space representation. There are numerous transformation methods known in the machine-learning community to perform such transformations of raw dataset text representation to vector representation. For example, ‘bag of words’ methods, which can be summarised as follows: first assign an integer number to each word occurring in any document in a training dataset, for example, by building a dictionary from words to integer indices. Then, for each document, count the number of occurrences of each word from the dictionary and store it in the matrices’ representation as the number of appearances of each word from the dictionary in the document. However, dictionary representation has severe limitations. Consider the space requirements for storing matrices that were built using a dictionary with 100,000 different words on 10,000 documents in 32-bit float data type; this would require more than 4GB of RAM.

Transformation methods based on occurrence count have other severe limitations: longer documents have, by their nature, a larger average count than shorter documents, even though they might talk about exactly the same topics. To avoid these potential pitfalls, it suffices to divide the number of occurrences of each word in a document by the total number of words in the document: these new features are called term frequencies or tf for short.

Another refinement in addition to term frequencies is to weight the words that occur in many documents in the corpus and are therefore less informative than those that occur only in a smaller portion of the corpus. This weighting is called term frequency-inverse document frequency or tf-idf method for short. Words that are common in a single or a small group of documents tend to have higher tf-idf numbers than common words such as articles and prepositions. Search engines and modern information retrieval systems widely use tf-idf methods. Equation (8) represents the classical formula for tf-idf used for term weighting.

$$w_{i,j} = tf_{i,j} \log \left(\frac{N}{df_i} \right) \quad (8)$$

Where: $w_{i,j}$ is the weight for term i in the documents j , N is the number of documents in collections, $tf_{i,j}$ is the term frequency of term i in document j and df_i is the document frequency of term i in the collections.

The tf-idf method evolved from IDF which was proposed by [25] and [26] with intuition that a term which occurs in many documents is not as good a discriminator as a term occurring in fewer documents and should have lower weight than the second.

8. Experimental results

The dataset used for simulation experiments is the 20 Newsgroup. This is a collection of approximately 20,000 newsgroup documents, partitioned across 20 different newsgroups. It is a popular collation, widely used in text application experiments of machine learning techniques, such as text clustering. The data is organised into 20 different newsgroups, each corresponding to a different topic. Some of these topics are highly related, for example ‘comp.sys.ibm.pc.hardware’ and ‘comp.sys.mac.hardware’, while others are highly unrelated like ‘talk.politics.mideast’ and ‘sci.crypt’.

For simulation experiments, a few datasets were constructed. The first dataset consists of documents from three different topics: ‘soc.religion.christian’, ‘comp.graphics’, ‘rec.motorcycles’ – this is referred to as DS1. The second dataset consists of dataset from four topics: ‘soc.religion.christian’, ‘comp.graphics’, ‘rec.motorcycles’ and ‘rec.sport.hockey’ and is referred to as DS2. The third dataset consists of five topics: ‘soc.religion.christian’, ‘comp.graphics’, ‘rec.motorcycles’, ‘rec.sport.hockey’ and ‘comp.sys.ibm.pc.hardware’ and is DS3. The fourth dataset consists of six topics: ‘soc.religion.christian’, ‘comp.graphics’, ‘rec.motorcycles’, ‘rec.sport.hockey’, ‘comp.sys.ibm.pc.hardware’ and ‘sci.crypt’ and is DS4.

After being loaded into memory, the datasets were transformed from text-based representation into vector-space representation of documents with the aforementioned tf-idf

method. Latent concept space was induced with SVD decomposition. The data was then normalised. On the normalised dataset, the modified BA was used to perform unsupervised machine learning. The algorithm not only returns the optimal partitioning of the given dataset, but also the optimum number of clusters given used clustering index silhouettes coefficient. The obtained solutions were compared with the kMeans algorithm for which the silhouettes coefficient was also calculated. Firstly, we performed experiments to see how the dimensionality of the concept space influenced the quality of the solutions; we then compare the proposed method with the kMeans algorithm.

During the simulation experiments, we used the knowledge base for dynamic parameter adjustments based on the current state of the colony for example, during the optimisation process using a Mamdani-type fuzzy inference system, the diversity and iteration number were as follows:

KnowledgeBase:

= {

 "If diversity is *small* and iteration is very *small*, then Q is very *big*

 If diversity is *small*, then Q is *big*

 If iteration is *big*, then Q is *small*

 If iteration is very *big*, then Q is very *small*

For all experiments, the algorithm was set to stop after 5000 iteration steps; the number of bats was set to $1000 \times \text{dimensions}$; and maximum number of cluster to discover was set to 6; $\alpha = 0.1, \gamma = 0.85$. Each test was re-run 50 times.

Figures 3 shows the mean solution found after 50 re-runs against a concept space dimensionality for a dataset containing three topics: ‘soc.religion.christian’, ‘comp.graphics’, ‘rec.motorcycles’ DS1.

Figures 4 shows mean solution found after 50 re-run against a concept space dimensionality for dataset containing four topics: “soc.religion.christian”, “comp.graphics”, “rec.motorcycles” and “rec.sport.hockey” DS2.

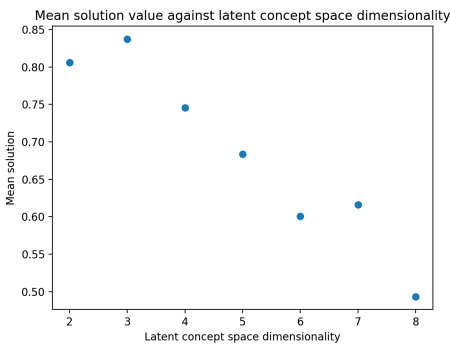


Fig. 3. Mean solution found for dataset DS1

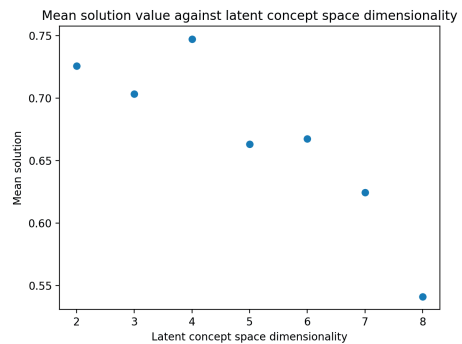


Fig. 4. Mean solution found for dataset DS2

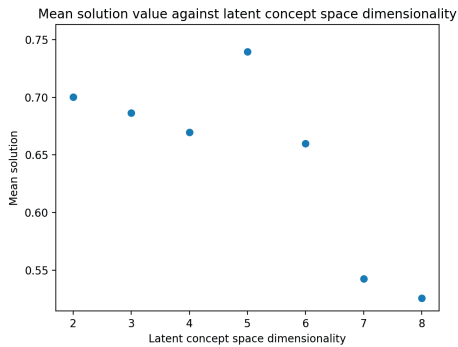


Fig. 5. Mean solution found for dataset DS3

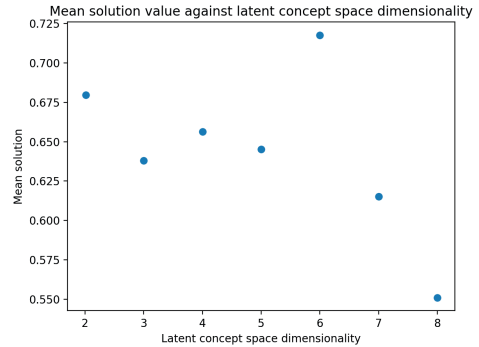


Fig. 6. Mean solution found for dataset DS4

Figure 5 shows the mean solution found after 50 re-runs against a concept space dimensionality for a dataset containing five topics: ‘soc.religion.christian’, ‘comp.graphics’, ‘rec.motorcycles’, ‘rec.sport.hockey’ and ‘comp.sys.ibm.pc.hardware’ DS3. Figure 6 shows the mean solution found after 50 re-runs against a concept space dimensionality for a dataset containing six topics: ‘soc.religion.christian’, ‘comp.graphics’, ‘rec.motorcycles’, ‘rec.sport.hockey’, ‘comp.sys.ibm.pc.hardware’ and ‘sci.crypt’ DS4.

The results presented in Table 1 show how the proposed algorithm performs on used test datasets and it is compared to the classic kMeans algorithm, for which the silhouette coefficient was calculated.

Table 1. Mean solution and standard deviation of the proposed algorithm compared to the kMeans algorithm

Dataset	Mean solution	Standard deviation	kMeans
DS1	0.849	0.096	0.755
DS2	0.751	0.145	0.714
DS3	0.745	0.163	0.656
DS4	0.715	0.193	0.516

9. Summary

The first modification to the BA are briefly discussed, then Mamdani-type inference system is shortly introduced and used linguistic variable and linguistic values have been defined. A full discussion of this modification and simulation experiments using different Mamdani-type inference systems for the dynamic modification of behaviour of a flock of bats in the BA can be found in the author’s other publications [15] and [16]. This paper focused on the application of the proposed methods *in the document clustering problem of information retrieval systems*. An appropriate solution encoding the bat position in the search space is introduced which allows for both optimisation of cluster as well as their number.

Simulation experiments were conducted on the well-known 20 Newsgroup datasets. Since datasets, in their raw form, are word-based representations, they need to be transformed to vector-space representation before unsupervised machine learning can take place. The tf-idf transformation method was used for that transformation. Since the tf-idf method produces a sparse matrix, the concept space is induced using SVD decomposition.

A few tests were designed and conducted on different subsets of 20 Newsgroup original datasets. The first dataset (DS1) consists of documents from three different topics: 'soc.religion.christian', 'comp.graphics', 'rec.motorcycles'. The second dataset (DS2) consists of dataset from four topics: 'soc.religion.christian', 'comp.graphics', 'rec.motorcycles' and 'rec.sport.hockey'. The third dataset (DS3) consists of five topics: 'soc.religion.christian', 'comp.graphics', 'rec.motorcycles', 'rec.sport.hockey' and 'comp.sys.ibm.pc.hardware'. The fourth dataset (DS4) consists of six topics: 'soc.religion.christian', 'comp.graphics', 'rec.motorcycles', 'rec.sport.hockey', 'comp.sys.ibm.pc.hardware' and 'sci.crypt'.

The obtained results are reported, as well as their mean value and standard deviation for 50 re-runs of the proposed algorithm. The results obtained by the proposed method (MBA) were compared with the kMeans algorithms, which are well-known in literature. The mean solution found in terms of dimensionality of latent space is also considered.

The obtained results show that the proposed method is capable of finding a higher quality solution (in terms of the used clustering index silhouette coefficient) than the traditional method; therefore, it is better suited for the document clustering of information retrieval systems.

References

- [1] Baziar A., Kavosi-Fard A.A., Zare J., *A Novel Self Adoptive Modification Approach Based on Bat Algorithm for Optimal Management of Renewable MG*, Journal of Intelligent Learning System and Application, Vol. 5, Issue 1, 2013, 11–18.
- [2] Caliński R., Harabasz J., *A dendrite method for cluster analysis*, Commun. Stat., Vol. 3, No. 1, 1–27, 197.
- [3] Davies D., Bouldin D., *A cluster separation measure*, IEEE Trans. Pattern Anal. Mach. Intell., Vol. PAMI-1, No. 2, 224–227.
- [4] Dorigo M., Maziezzo V., Colorni A., *The ant system: optimization by a colony of cooperating ants*, IEEE Trans. on Systems, Man and Cybernetics B, Vol. 26, No. 1, 1996, 29–41.
- [5] Dorigo M., Stützle T., *Ant Colony Optimization*, MIT Press, 2004
- [6] Eberhart R. C., Shi Y., *Empirical Study of Particle Swarm Optimization*, 1999
- [7] Eberhart R., Shi Y., *Particle swarm optimization: Developments, applications, and recourses*, Proc. Congr. EVol. Comput., 2001, 81–86.
- [8] Fister I. Jr, Fister D., Yang X.S., *A Hybrid Bat Algorithm*, Elektrotehniski Vestnik, 2013, 1–7.
- [9] Fong S., Yang X.S., Karamanglu M., *Bat Algorithm for Topology Optimization in Microelectronic Application*, International Conference on Future Generation Communication Technology (FGCT), IEEE, 2012, 150–155.

- [10] Goldberg D.E., *Genetic Algorithms in Search, Optimization and Machine Learning*, Kluwer Academic Publishers, 1989.
- [11] Hansen P., Jaumard B., *Cluster analysis and mathematical programming*, Math. Program., Vol. 79, 1997, 191–215.
- [12] Hofmann T., *Probabilistic Latent Semantic Analysis*, Proc of the Fifteenth conference on Uncertainty in artificial intelligence, UAI'99, 289–296.
- [13] Kennedy J., Eberhart R.C., *Particle swarm optimization*, Proc. of IEEE International Conference on Neural Networks, Vol. 4, 1995, 1942–1948.
- [14] Kennedy J., Eberhart R., Shi Y., *Swarm Intelligence*, Academic, 2001.
- [15] Kielkowicz K., Grela D., *FLC control for tuning exploration phase in bio-inspired metaheuristic*, Annales Universitatis Mariae Curie-Sklodowska, sectio AI – Informatica, 2017.
- [16] Kielkowicz K., Grela D., *Modified Bat Algorithm for Nonlinear Optimization*, International Journal of Computer Science and Network Security (IJCSNS), 2016, 46–50.
- [17] Melin P., Olivas F., Castillo O., Valdez F., Soria J., Valdez M., *Optimal design of fuzzy classification systems using PSO with dynamic parameter adaptation through fuzzy logic*, Expert Systems with Applications, Vol. 40, Issue 8, 2013, 3196–3206.
- [18] Merwe D., Engelbrecht A., *Data clustering using particle swarm optimization*, Proc. Congr. EVol. Comput, Vol. 1, 215–220.
- [19] Mirjalili S., Mirjalili S. M., Yang Xin-She, *Binary Bat Algorithm*, Neural Computing and Applications, Vol. 25, Issue 3, 2014, 663–681.
- [20] Storn R., Price K., *Differential Evolution – A Simple and Efficient Adaptive Scheme for Global Optimization Over Continuous Spaces*, Technical Report, 1995.
- [21] Xu R., Xu J., Wunsch C., *A Comparison Study of Validity Indices on Swarm-Intelligence-Based Clustering*, IEEE TRANSACTIONS ON SYSTEMS, MAN, AND CYBERNETICS, PART B: CYBERNETICS, Vol. 42, No. 4, 2012
- [22] Yang X. S., *A New Metaheuristic Bat-Inspired Algorithm*, Nature Inspired Cooperative Strategies for Optimization, 2010, 65–74.
- [23] Yang X. S., *Bat Algorithm for Multi-Objective Optimization*, International Journal of Bio-Inspired Computation, Vol. 3, Issue 5, 2011, 267–274
- [24] Rousseeuw P., *Silhouettes: Silhouettes: a Graphical Aid to the Interpretation and Validation of Cluster Analysis*, Computational and Applied Mathematics 20, 53–65.
- [25] Sparck Jones, K., *A statistical interpretation of term specificity and its application in retrieval*, Journal of Documentation, 28, 11–21.
- [26] Sparck Jones, K., *IDF term weighting and IR research lessons*, Journal of Documentation, 60(6), 521–523.

Ryszard Mielnik  orcid.org/0000-0001-7012-4090

rmiel@pk.edu.pl

Institute of Electromechanical Conversion, Department of Electrical and Computer Engineering, Cracow University of Technology

THE INTEGRATION OF AN AUTOMATIC RESERVE SWITCHING CONTROLLER INTO A RAILWAY TRAFFIC CONTROL SYSTEM POWER SUPPLY THROUGH THE USE OF A PETRI NET AND A GRAPHICAL PROGRAMMING LANGUAGE

INTEGRACJA STEROWNIKA ZAŁĄCZENIA REZERWY ZASILANIA URZĄDZEŃ STEROWANIA RUCHEM KOLEJOWYM Z WYKORZYSTANIEM SIECI PETRIEGO I GRAFICZNEGO JĘZYKA PROGRAMOWANIA

Abstract

The requirement for high reliability and safety in the operation of measuring and control systems is particularly relevant in critical applications in which system failure can lead to large material losses and can constitute threat to health and even to life. Railway traffic control systems are one such application. There is a requirement for the use of powerful tools and methods of modelling the function and operation of this system. The purpose of this publication is to present the use of a Petri net in modelling automatic reserve switching device controllers of railway traffic control system power. The publication also shows the practical implementation of such a controller. It was implemented using the hardware platform of the NI CompactRIO family of controllers and an application made in the National LabView graphical programming environment.

Keywords: power supply of railway traffic control systems, Petri nets, graphical programming of industrial controllers

Streszczenie

Wysoka niezawodność i rzetelne działanie systemów pomiarowo-sterujących w zastosowaniach krytycznych w obecnej dobie jest coraz bardziej wymagany. Niewłaściwa praca takich systemów może doprowadzić do dużych strat materialnych, a nawet utraty zdrowia i życia ludzi. Dlatego też uwarunkowania te wymuszają stosowania narzędzi i metod do formalnego modelowania funkcji oraz symulowania pracy powyższych systemów. W artykule zaproponowano wykorzystanie Sieci Petriego w procesie modelowania funkcji sterownika układu automatycznego załączania rezerwy urządzeń zasilania systemów sterowania ruchem kolejowym. W artykule przedstawiono także praktyczną realizację sterownika wspomnianego wcześniej układu. Zrealizowano go na platformie sprzętowej rodziny sterowników NI CompactRIO oraz aplikacji wykonanej w graficznym środowisku programowania LabView firmy National Instruments.

Słowa kluczowe: zasilanie systemów sterowania ruchem kolejowym, Sieci Petriego, programowanie kontrolerów przemysłowych.

1. Introduction

Nowadays, measurement and control digital systems (MCD systems) are commonly used in industrial processes [12]. These systems are constructed using hardware platforms such as PLC's, industrial computers and embedded systems. The functionality of MCD systems depends on implementing software applications. Thus, the quality of the action of this system is influenced not only by a hardware platform, but also by its software. The need to ensure high software reliability and reliability of the entire MCD system is required especially in so-called critical applications. In these applications, malfunction or damage of MCD systems during their operation can lead to abnormal functioning of the monitored process which can result in loss of life and material waste. Ensuring the required quality of the MCD system in its design and prototyping stages requires the use of appropriate tools and methods to formalise its functions and actions. Suitable instruments for this purpose may be Petri nets. These are graphic and formal tools for modelling, formal analysis and the design of discrete event systems. A model represented by such a net allows the analysis of the characteristics of the system's behaviour and allows its evaluation within each phase of the system's life cycle.

The aim of this publication is to present the possibilities of using Petri nets in modelling MCD systems in a critical application [2, 4, 5, 6, 7], specifically, the integrated controller of the automatic reserve switching device of a railway traffic control system power supply. This publication also shows the practical implementation of such a controller [7, 8, 17].

2. Power supply of railway traffic control systems

2.1. Railway traffic control systems

Railway traffic control systems (RTCS) provide the safe, reliable and efficient movement of rolling stock on the railway network [2]. Therefore, RTCSs are classified as critical equipment and systems [5, 6, 7, 8]. The history of RTCSs dates back to the end of the nineteenth century, when the industrial revolution introduced rolling stock for the transport of first goods and then people. Initially, railway traffic safety devices were simple and the main role in the decision making and execution process was fulfilled by a person. Currently, mounted station-based RTCSs are comprised of either a relay and computer systems, or only computer systems without a relay [2, 4]. In relays and computers systems, security is ensured in the relay layer, and the setting functions are performed by a computer control panel [2]. The development of information and computer technology has led to the construction of secure computer systems. For systems of this type, PLCs or computers with '2 of 2' or '2 of 3' voting systems are used to provide the required level of security [2, 4, 8].

The use of relays and computer systems requires the provision of adequate reliability and quality of power [16]. Therefore, new, more suitable power supply systems are being introduced that can meet the increased requirements.

2.2. Power supply systems for RTCS

The current requirements for the design and manufacture of power supply systems for RTCS are presented in Chapter 13 of Management Order No. 1/2014 of PKP Polish Railways. [16]. The general requirements (§ 72) of this chapter are to state that the primary sources of power supply for station-based RTCS are power grids that meet the requirements for [6, 16]:

- ▶ regulations for the construction of power equipment;
- ▶ strategies for protection against overvoltage;
- ▶ strategies for shock protection.

In § 73 of the above chapter on power supply, station-based RTCS have the following requirements [6, 16]:

- ▶ electricity must be supplied from terminals from a non-traction line (LPN); This power supply should be provided by two 3x400/230V power network meshes;
- ▶ power supplies must have a built-in backup (emergency) power supply in the form of a combustion-power unit (chiller), inverters or UPSs;
- ▶ bypass systems for switching equipment and a backup power supply should be provided;
- ▶ voltage fluctuations in the power supply and the backup power supply sources must not exceed $\pm 10\%$ of the nominal value;
- ▶ circuits for powering electronic and computer systems must be protected against overvoltage protection;
- ▶ dedicated AC circuits of stations-based RTCSs and circuits supplying DC relays requiring an uninterrupted power supply should be supplied with power during the changeover from dedicated power sources such as inverters; Inverter batteries must ensure that they sufficiently operate for 1 hour;
- ▶ the power supply system of stations-based RTCSs should have:
 - ▷ equipment for the control and automatic switching of power lines, equipment for controls and automatic (or manual) switching of the power line to a backup source;
 - ▷ components for the distribution of electricity to individual circuits;
 - ▷ equipment for signalling the status of power supply equipment and the table of setting fuses (in the control room).

A general block diagram of the power supply system intended for relays and computer, computers station-based RTCS is shown in Fig. 1 [6, 13, 14, 15].

As shown in the above block diagram, the power supply system is powered by two independent 3x400/230 V power networks. A spare power source (the power generator) is also included in the system. Overvoltage protection elements (OVPs) are installed on the power lines in the power supply cabinet (PSC).

The parameters of the mains power supply and the backup power source (power generator) are measured by MS1, MS2 and MS3 measuring modules. The MS4 measurement modul measures the power supply parameters at the output of the automatic reserve switching device (ARS device). These systems in the current solutions are modules for measuring

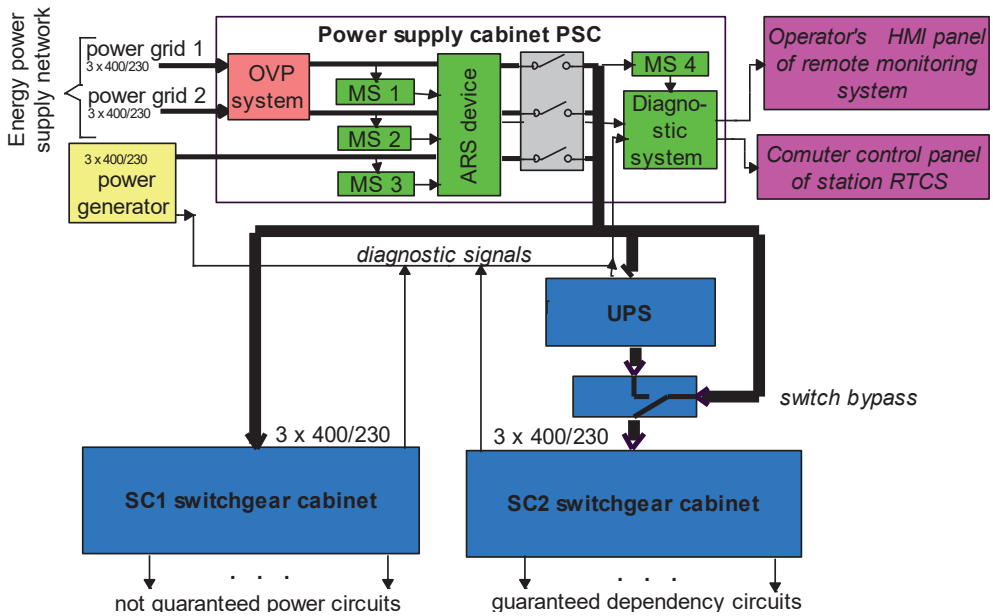


Fig. 1. General structure of the station RTCS's power supply system

power supply parameters. They measure not only the correctness of the power supply voltage but also the frequency, the total harmonic distortion THD and the correct phase sequence. In the case of an incorrect value of any of the measured power parameters, the ARS devices switch the power supply so that the power supply to the station RTCS is uninterrupted. The ARS device, in addition to its control logic, also has a contactor-mechanical coupling that provides power to the device from only one power source, even in the event of an ARS failure.

The voltage of the power supply from the ARS device is divided into two power distribution cabinets. The first (DC1 switchgear cabinet) supplies components of the station-based RTCS; however, this supply is not guaranteed. This means that these components, in the absence of power, will not endanger the safety of railway traffic at the station. The second distribution cabinet (DC 2 switchgear cabinet), powered by an uninterruptible power supply (UPS), supplies the station components of RTCS that must have a guaranteed power supply. These include: light circuits that prohibit track signallers, DC relays, power supplies for computers and computer control panels. The above mentioned cabinets contain appropriate bypass systems, which can be used to manually switch power sources. The block diagram in Fig. 1 also shows a diagnostic system that collects measurement data and status data relating to power components and devices. This information is saved in the recorder of this system and the selected text or graphic information (pictogram) is displayed on the operator panel display. From the diagnostic system the required information is transferred to the computer control panel of the station-based RTCS.

2.3. ARS controller

The development of an integrated ARS controller has been proposed on the basis of an analysis of the requirements and the technical solution of the currently produced power supply systems of the station RTCS (p. 2.2). This controller integrates power components such as MS1, MS2, MS3 and MS4 measuring modules and ARS logic and diagnostics system with data transfer interfaces. The location of this controller in the power supply system is shown in Fig. 2 [6].

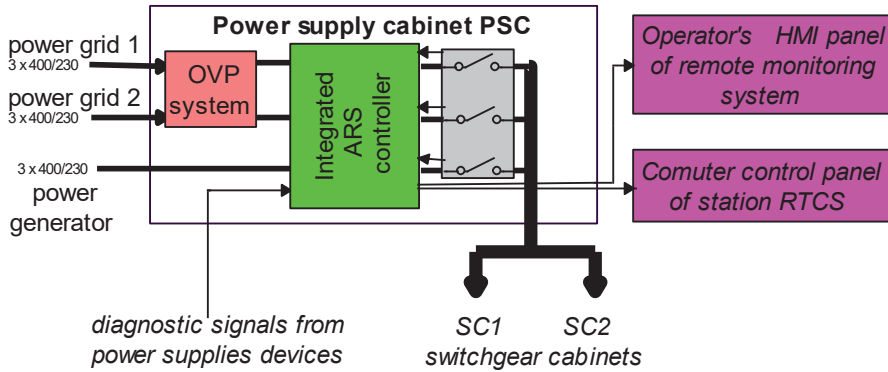


Fig. 2. Structure of the station RTCS power supply system with ARS controller

2.4. Application steps of ARS controller

Controllers for the automation devices are implemented on programmable hardware platforms. They can be classified as being discrete real-time MCD systems. Systems of this type are reactive systems, which implies an immediate (finite) response of the system to events. Designing such systems requires a behavioral approach to modelling functions and system operation. Such modelling enables the effective use of graphing tools such as the Petri nets or state diagrams [1, 3, 6, 8, 10, 18]. An important advantage of these tools is the ability to manipulate state concepts and construct hierarchical structures and concurrent modelling.

Based on the analysis of current solutions [2, 13, 14, 15] and the requirements for power supply systems of station-based RTCSS [16], a functional model of a controller with a Petri net has been developed. Based on the developed net and the use of the National Instruments LabView graphical programming language, software applications have been developed. In parallel with the design and implementation of the software, assumptions are made regarding the hardware platform of the controller. The National Instruments CompactRIO platform as the base platform. The next step of the ARS controller implementation is the integration of the software application developed with the hardware platform. After the integration and positive activation of the controller, functional tests were performed on the basis of a previously developed research program. This enabled the verification of objectives for the ARS controller.

3. Petri net based ARS controller

3.1. Petri nets

In 1962, Carl A Petri developed a tool called a Petri net (PN) which is based on graph theory and is used to model discrete systems [1, 3, 9, 10, 11]. As a result of the long-term development of the theory of these nets, a number of classes of PN emerged for which wide applications have been found [1, 3, 5–8]. As the graphical tool for modelling complex systems, during the development phase Petri nets allow for good and clear communication between designers and customers. As a result of this, a comprehensive requirement specification was created, which does not contain vague rules and formal records that are inconvenient for customers. The resulting graphic model of the system can also be applied in computer graphic simulation environments of PN – this resulted in a virtual prototype of the system being designed [1, 3]. This allows designers fast, interactive and comprehensive testing of the functionality and features at every stage of its life cycle. Petri nets are ideal for the system modelling of discrete events and the analysis of their properties [1, 3, 9–11], such as the synchronisation of processes, asynchronous events, competing tasks, conflict shared resources jams, etc. Petri nets are described by linear algebraic equations or other mathematical formula reflecting the behaviour of the designed system [9–11]. The ability to formally verify the model is quite important in the construction of industrial MCD systems. Petri Net that is extended with a time-domain model can be used to model embedded systems [11], real-time systems [1, 10], and in particular, real-time safety critical systems, which include railway traffic control systems [2, 4–8].

One of the essential characteristics of Petri nets is their relatively simple and intuitive graphical representation. These nets, which are derived from the theory of directed bipartite graphs, allow the use of terms specific to these graphs [9, 10, 11]. These graphs contain two types of vertices called places and transitions. The vertices represent states or activity of the modelled system, respectively. They are connected with each other by arcs in such a way that the arcs connect only vertices of different types. The resulting graphic notation is characterised by a net structure. Graphic representation and structural properties are common features for all classes of nets [9, 11].

To be able to fully model the system, taking its dynamics into account, a definition of PN was extended by net marking. This represents the state of the modelled system. The net status is represented by token changes as a result of pass-time simulation of the net. Therefore, a Marked Petri Net (MPN) is an ordered quadruple [6, 9, 11]:

$$N=(P, T, A, M_0) \quad (1)$$

where:

$N=(P, T, A)$ – is the PN,

$M_0:P \rightarrow \mathbb{Z}_+$ – is a function defined on the set of places called the *initial marking* of the N net.

In this class of net, places have unlimited capacity for tokens, but arcs can carry only one token. Execution of the transition involves the elimination of individual tokens from the input

places and adding the individual tokens to the exit places of this performed transition. In the *generalised Petri net (GPN)* class [6, 9, 11] it is possible to eliminate or add more tokens to one place in the performance of a single transition by assigning appropriate weight arcs. By introducing the function of limiting the capacity of the places for tokens to the GPN, one of the most common net class in literature [9, 11], called *places and transitions Petri net (PTPN)* is obtained [9, 11]. The PNPT can easily replace a GPN which has the same properties. Accordingly, the term PTPN often refers to GPN in the literature [9, 11]. It can be stated that the MPN class is a special case of GPN and PTPN, in which there is unlimited token capacity, and arcs carry only one token (the weight of the arcs is 1).

A Petri net, as a bipartite graph, can have a hierarchical structure [1, 11], greatly facilitating the modelling of complex systems. Constructing the net can be performed in two ways [6, 7, 8, 11]. The first of these, from the specific to the general (*bottom – up*), involves the extration of separate, small sub-systems of the model system and then building simple nets. These simple nets are then deposited in growing parts until a whole net of the modelled system is given. The second way, from the general to the specific (*top – down*), is to build a net for the entire system, without a detailed analysis of the fragments and treating the individual parts of the net in a similar. This procedure is called structural modelling (hierarchical modelling). A net built using one of these methods is called a *hierarchical net* and the net elements of the composite structure are called hierarchical net elements [1, 11]. These elements representing parts of the net are called macroplaces and macrotransitions. The choice of modelling depends largely on the type of a system which is being modelled. If the szstem is completely unknown to the designer of the system, using the second method is more efficient. However, when past experience can be used in modelling the system, the first method becomes more convenient.

3.2. Marked Petri net ARS controller

The marked Petri net based ARS controller (MPN ARS controller) has been developed based on the features of the ARS integrated controller power supply system of station-based RTCS (p. 2.2 and p. 2.3 of this article). This MPN is a special case of a GPN and PTPN class of PN in which the capacity of the places is unlimited and only one token can pass through the arc. The developed MPN ARS controller (Fig. 3) can be characterised by [6]:

- ▶ a production process which generates tokens,
- ▶ a storage process (token buffer),
- ▶ two consumer processes that absorb tokens.

In the production process, tokens are generated corresponding to places and transitions $p7 - t3$, $p8 - t4$, $p9 - t5$ and $p10 - t6$, which represent the voltage signal acquisition by the measurement modules MS1, MS2, MS3 and MS4. Places and transitions $p11 - t7$, $p12 - t8$, $p13 - t9$, $p14 - t10$ are responsible for the analysis of the measured signals, resulting in parameters relating to the quality of the supplied electricity. These parameters are passed to two consumer processes through the storage process (buffer data), place $p15$ and transition $t11$. Consumer process 1 is responsible for the control logic of the ARS controller. In this process, in addition to the supplied power supply parameters (place $p16$), signals from the

binary inputs of the ARS contactors (place p19 and transition t14) are read from the binary inputs. On this basis, the logic of the ARS controller (place p16 and transition t12) generates control signals for the contactor (place p17 and transition t13) via binary outputs. Consumer process 2 is responsible for recording the power quality parameters and the current state of the ARS controller (place p27 and transition t20). The above data is transmitted to the HMI operator terminal (place p22 and transition t17) and to the computer control panel of the station RTCS (place p25 and transition t19).

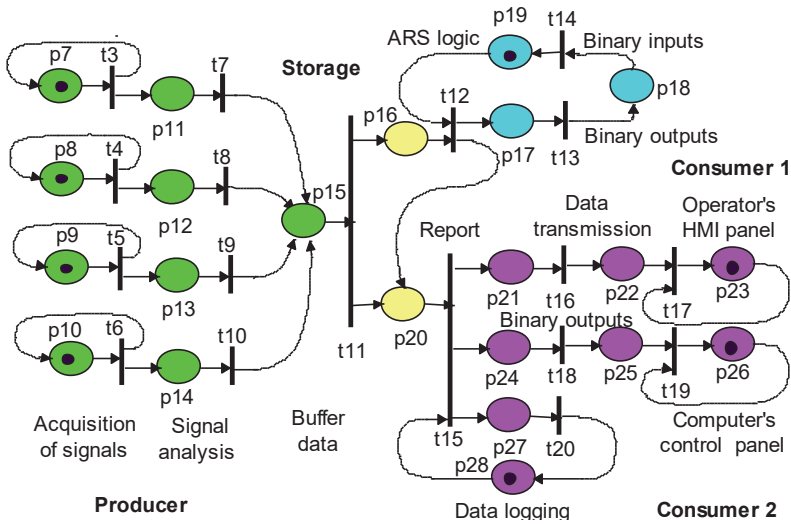


Fig. 3. The marked Petri net based ARS controller

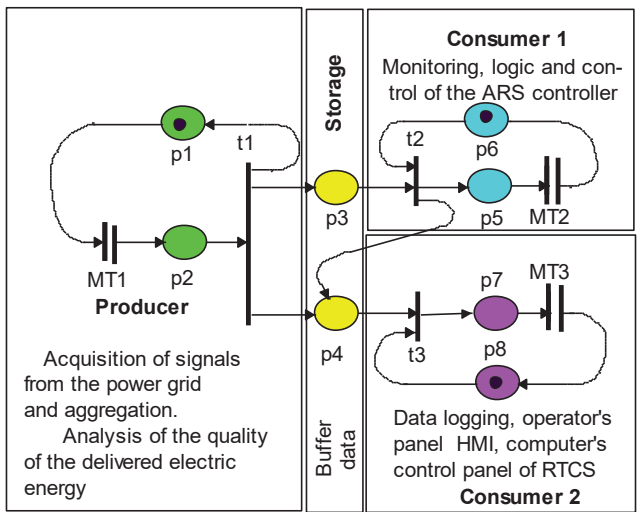


Fig. 4. The hierarchical simplified marked Petri net based ARS controller

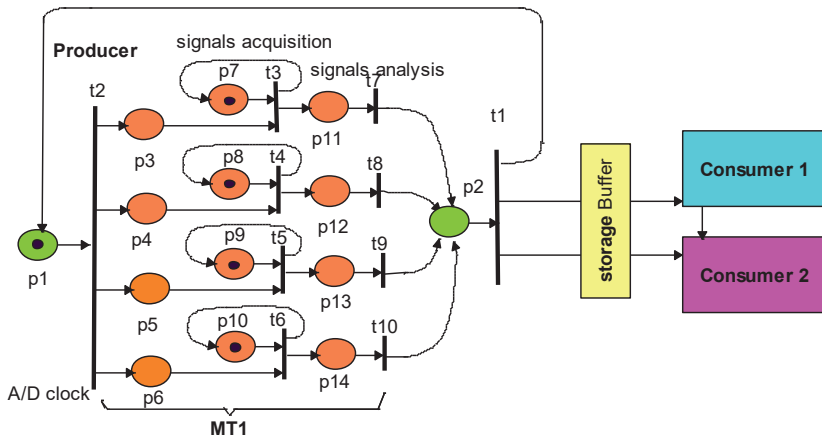


Fig. 5. The ARS controller block' diagram with macro transition MT1

Fig. 4 shows the hierarchical simplified MPN ARS controller. This net was created as a result of the hierarchy of the ARS controller [6] MPN from Fig. 3, using the bottom – up method [11]. The resulting simplified hierarchical MPN is easier to analyse. This net corresponds to the producer – consumer model system. The class of this type of net is well known in literature [11]. One of the important features of this net is its liveness; this means that the net does not become jammed, and every producer's token is consumed by consumer processes [11].

Fig. 5 shows the block-diagram of the ARS controller with the macro transition MT1 from the simplified hierarchical marked Petri net [6]. In this macrotransition, the functions of the AC voltage acquisition sub-system were modelled using a measuring card with parallel analogue-digital processing and digital signal processing.

4. Practical implementation of the ARS controller

4.1. Hardware platform of the ARS controller

The ARS controller hardware platform was configured using National Instruments NI CompactRIO components [5, 17]. This is a real-time platform with modular construction. It meets the stringent requirements of environmental standards approved by the Management of the Polish Railway Lines. This platform consists of [6]:

- ▶ NI cDAQ-9135 cassette with a processor module equipped with: an Atom processor 1.33 GHz, 32 GB RAM, 8 slots, Linux RT real-time operating system, an HMI interface;
- ▶ NI PS power supply module: 24 VDC, 5 A, 100-120 / 200-240 VAC input;
- ▶ 4 analogue input modules NI 9244: 400 Vrms L-N, 24-Bit, 50 kS / s / ch, 3-Ch – these modules are designed to measure the supply voltage of the power system;
- ▶ 2 digital inputs/outputs NI 9375: 16-DI, 16-DO, DI / DO – these modules are designed to control and monitor the state of the ARS contactors and to transmit information to the computer control panel of the station RTCS.

4.2. Software application of the ARS controller

The National Instruments LabView graphical software environment [6, 17] was used to implement the ARS controller software application. This environment has many tools for fast software development. The main advantage of this environment is that the execution of the program is based on the data flow between the nodes of the program. These nodes include simple functions, complex functions, the VI Express function and the SubVI functions made by the user. Execution of the node function will only occur if the node inputs have data. This requirement is similar to the mechanism of triggering transitions in the Petri net. This environment also includes programming structure patterns; one of these being the Statechart module [6, 17, 18].

The Statechart module of the LabView graphic programming environment is a tool for creating state machine diagrams. Among other features, the functions of this module enable defining states and transitions, events, hierarchies and sub-states. As a result of the introduction of the appropriate graphical program code to the created diagram structure after translation and compilation, the program code for the designed ARS controller is obtained.

D. Harel proposed machine state diagrams [10] as a visual formalism tool to describe complex control systems. These diagrams introduce the concept of state and spread the concept of a finite automaton. The graphical representation of the state machine is a diagram of states and transitions. In the basic, parental state diagram, sub-states that assign states to their state diagrams can be defined. The orthogonality of state diagrams enables the ordering of sequential automata which can model concurrent phenomena. In turn, the broadcasting mechanism is realised by generating events that have a detrimental effect on the functioning of the diagram [17, 18].

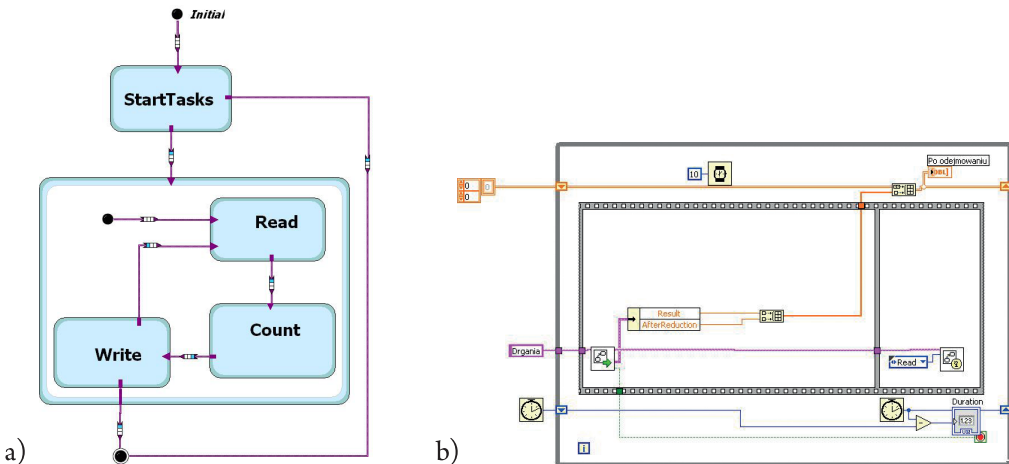


Fig. 6. a – State diagram of ARS controller, b – main loop

The basic state diagram, corresponding to the hierarchical simplified Marked Petri Net ARS in Fig. 4, performs four basic states:

- ▶ wait state,
- ▶ acquisition and analysis of measured voltage state,
- ▶ ASR logic implementation state,
- ▶ data transfer to the control system and remote monitoring state.

The main loop of the LabView application of the ARS controller (Fig. 6b) through the state chart Run starts the diagram of the controller's state machine – Fig. 6a. This loop also calculates the execution time of one loop iteration with an accuracy of 1 ms.

Fig. 7. shows the remote monitoring panel of the ARS controller. The visualisation display enables the user to continuously monitor the state of the power supply system.

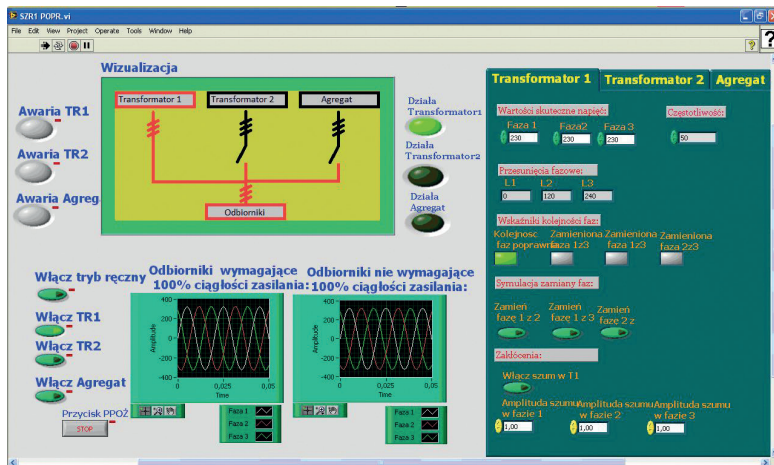


Fig. 7. View of remote control front panel of ARS controller

5. Conclusions

To summarise, functional laboratory tests of the controller were performed after the integration of the hardware platform, the application software and the launch of the ARS controller. These studies were conducted on the basis of a previously prepared research program. After minor modifications to the controller's application software, it can be said that the ARS controller is working properly. This tested controller and documentation was provided by the manufacturer of the power supply system of the station RTCS. The controller is currently undergoing field testing; and once completed, it will be possible to issue an application for use of the integrated ARS controller in station-based RTCSs on Polish railway lines.

The presented research, which was performed under the theme No. E-2/644/2017/DS, was funded by subsidies on science granted by the Polish Ministry of Science and Higher Education.

References

- [1] David R., Alla H., *Continuous and Hybrid Petri Nets*, Discrete, Springer 2005.
- [2] Dąbrowa-Bajon M., *Podstawy sterowania ruchem kolejowym*, Oficyna Wydawnicza Politechniki Warszawskiej, Warszawa 2002.
- [3] Hruz B., Zhou M.C., *Modeling and Control of Discrete-Event Dynamic Systems with Petri Nets and other tool*, Springer, 2007.
- [4] Lewiński A., Perzyński T., *Nowe rozwiązania komputerów sterujących w systemach sterowania ruchem kolejowym na przykładzie SSP*, Materiały konferencyjne „Transport w XXI wieku”, Warszawa 2001.
- [5] Mielnik R., *Petri Net as a tool for modelling a microprocessor measurement-control system using in critical applications*, Proceedings of the IMEKO-TC7 Symposium, Cracow 2002.
- [6] Mielnik R., *Synteza sterownika układu SZR urządzeń zasilania ruchem kolejowym z wykorzystaniem sieci Petriego oraz środowiska Labview*, Materiały XVII Ogólnopolskiej Konferencji Naukowej Trakcja Elektryczna, SEMTRAK, Zakopane 2016.
- [7] Mielnik R., *Synthesis of controller for railway – level crossing devices using Petri Nets and state machine*, Technical Transactions 1-E (2)/2016.
- [8] Mielnik R., Sułowicz M., Ludwinek K., Jaśkiewicz M., *The reliability of critical systems in railway transport based on the track rail circuit*, Lecture Notes in Electrical Engineering, Springer 2018, Vol. 452, pp. 377 – 393.
- [9] Starke Peter H., Żurek J., *Sieci Petriego: podstawy, zastosowania, teoria*, PWN, Warszawa 1987.
- [10] Szmuc T., Szpyrka M., *Metody formalne w inżynierii oprogramowania systemów czasu rzeczywistego*, WNT, Warszawa 2010.
- [11] Szpyrka M., *Sieci Petriego w modelowaniu i analizie systemów współbieżnych*, WNT, Warszawa 2008.
- [12] Winięcki W., *Organizacja komputerowych systemów pomiarowych*, Oficyna Wydawnicza Politechniki Warszawskiej, Warszawa 2006.
- [13] Kornaszewski M., *Systemy zasilania rezerwowego urządzeń sterowania ruchem kolejowym*, Logistyka 10/2013.
- [14] System zasilania urządzeń sterowania typu SZUS – Album urządzeń zasilających, KZA Kraków, 1995.
- [15] System zasilania urządzeń stacyjnych type ELZAS, Dokumentacja Techniczno-Ruchowa, KZA Kraków, 2005.
- [16] Wytyczne techniczne budowy urządzeń sterowania ruchem kolejowym, Ie-4 (WTB-E10), PKP Polskie Linie Kolejowe S.A. Warszawa 2014.
- [17] National Instruments website, www.ni.com (access: 03.07.2017).
- [18] National Instruments website www.ni.com/tutorial/7425/en/ LabVIEW Statechart Module Tutorial (access: 03.07.2017).

Stanisław Kuciel

stask@mech.pk.edu.pl

Karolina Mazur

Institute of Material Engineering, Faculty of Mechanical Engineering, Cracow University of Technology

THE EFFECT OF LONG-TERM STORAGE ON THE MECHANICAL PROPERTIES OF COMPOSITES BASED ON POLYAMIDE 10.10 DERIVED FROM RENEWABLE SOURCES

WPLYW DŁUGOTRWĄŁGO PRZECHOWYWANIA NA WŁAŚCIWOŚCI MECHANICZNE KOMPOZYTÓW NA OSNOWIE POLIAMIDU 10.10 Z SUROWCÓW NATURALNYCH

Abstract

This paper presents an investigation in which bio-based polyamide 10.10 was used as a polymer matrix. Composites were reinforced in three different ways including: 10 wt% and 30 wt% of walnut shell flour as well as 30 wt% of glass fibres. The composites were prepared by injection moulding. Mechanical properties (tensile strength (σ_t), modulus of elasticity (E_t) as well as flexural modulus (E_f) and flexural stress at 3.5% strain (σ_f)) were obtained. The mechanical data of analysis showed that tensile strength and tensile stiffness significantly decreased after four years of storage. Another state was noted for the bending module, where the decrease in value was at a level of 5% compared to results obtained immediately after injection. Additionally, SEM images were taken to assess the distribution of particles and the adhesion of fillers to the matrix.

Keywords: bio-based composite, mechanical properties, injection moulding, Hiprolon 211

Streszczenie

W artykule zostały opisane kompozyty wytworzone na osnowie całkowicie biopochodnego poliamidu 10.10 wzmocnionego zmielonymi lupinami orzecha włoskiego w ilości masowej 10% oraz 30% jak również kompozyty z dodatkiem 30% masowej ilości włókien szklanych. Zbadano właściwości mechaniczne (wytrzymałość na rozciąganie (σ_t), moduł sprężystości (E_t) oraz moduł sprężystości przy zginaniu (E_f) i naprężenie zginające przy naprężeniu 3,5% (σ_f)) wytworzonych kompozytów. Dane analizy mechanicznej wykazały, że wytrzymałość na rozciąganie oraz sztywność kompozytów po czterech latach przechowywania znacznie spadły. Jednakże zaobserwowany został niewielki spadek wartości modułu zginania na poziomie 5% w porównaniu do wyników uzyskanych dla kompozytów bezpośrednio po wtrysku. Dodatkowo w celu oceny rozkładu cząstek i adhezji napelniaczy do matrycy wykonano zdjęcia SEM.

Słowa kluczowe: kompozyty na bazie surowców odnawialnych, właściwości mechaniczne, formowanie wtryskowe, Hiprolon 211

1. Introduction

Over the last decade, the replacement of polymer matrix obtained from crude oil by bio-based matrix has seen a significant increase [1]. Due to the rapid development of the automotive industry, which is the largest consumer of polyamides, the reduction of elements made from petroleum is justified. The use of bio-based matrix is beneficial in many respects because they address the import of non-renewable feedstock sources and end of life recycling [2, 3].

Composites based on polyolefin, such as polypropylene (PP) or polyethylene (PE), which are widely used on an industrial scale, are often reinforced with conventional and heavy glass fibres [4, 5]. Although on the one hand the addition of glass fibres increases the mechanical properties of composites, on the other hand it significantly increases the density of composites, which in the case of products for the automotive component is not recommended. However, the increased usage of natural fillers is clearly observed [6]. The main advantage of bio-based additives is their low density whilst retaining excellent mechanical properties, lower price, high availability and lower abrasion during preparation and manufacturing [6, 7, 8]. In addition, the use of a bio-based matrix in combination with natural additives leads to the manufacturing of fossil- and mineral-resource-free composites which promises an advantageous eco-balance. Nonetheless, fully bio-based composites have a few disadvantages. Firstly, they have poor ability to sustain high deformation without breaking. Furthermore, the addition of natural fillers makes them difficult to manufacture because natural fillers, mainly those containing lignocelluloses, are thermally sensitive components. Additionally, they have the disadvantage of having a highly hydroscopic character in comparison to the hydrophobic polyolefin matrices, which leads to weak fibre matrix interphases [3, 4].

A lot of research has been conducted which supports to the use of polymers with natural fibres such as cellulose, hemp, flax, jute, cotton and many more [9, 10, 11, 12]. The largest problem with the use of natural fillers is their low temperature of the processing. For example, lignocellulose fillers require processing at temperatures below 200 °C [13]. However, it can be find many reports of polyamide which is reinforced with natural fibres [14, 15]. These tests are mainly carried out on bio-based polyamides, such as polyamide 10.10 (PA.10.10) or polyamide 11 (PA11) because they have generally lower melting temperatures than convectional polyamide 6 (PA6) [16].

In the work of Feldman et al., PA 10.10 fully bio-based composites reinforced with 15 wt% and 30 wt % short man-made cellulose were prepared and comparison composites were filled with 30 %wt glass fibres. The researchers evaluated the influence of compounding parameters and temperature settings on the mechanical properties. They observed significant improvements in the properties such as tensile modulus, tensile strength, notched Charpy strength, energy absorption and heat distortion temperature. The obtained results from composites made using a single-step pultrusion process were higher than composites made with the use of a two-step process [16].

In another study, Battezzatore et al. investigated composites based on PA10.10 and PA6.10 reinforcement with 10 and 20 wt% of rice-husk ash (RHA). The mechanical analysis data showed that fillers increased Young's modulus, slightly decreased the tensile strength and high decreased in strain at break. In addition, Battezzatore et al. studies are important because waste which may otherwise have constituted a source of environmental pollution was used as a filler [17].

The aim of this study was to evaluate the influence of four-year storage period on the mechanical properties of neat PA10.10 (with cross-linked additives) and its composites. The mechanical properties (tensile strength (σ_t), modulus of elasticity (E_t) as well as flexural modulus (E_f) and flexural stress at 3.5% strain (σ_f) at -24 °C, +23 °C, +80 °C were obtained. SEM images revealed the distribution of particles and the adhesion of fillers in the matrix.

2. Methodology

A polyamide 10.10 was used as a matrix; which was obtained from raw materials of natural origin, based on castor oil. This polyamide 10.10 has been produced since 2011 by the Chinese company Suzhou Hipro Polymers under the trade name Hiprolon 211.

Hiprolon 211 is a cable type product with cross-linked additives. It is a long-chain polymer characterised by very good dimensional stability, low density and water absorption, high impact resistance and good chemical resistance.

As a fillers the following additives were used:

- ▶ walnut shell flour (REHOFIX UNG 300) supplied by J. Rettenmaier & Söhne in range of particles 40-100 μm . It is natural filler which is “ready-to-use” for extrusion facilities and injection moulding machinery,
- ▶ glass fibres (GF) delivered from Lanxess AG with a diameter of 10 μm and approx length 150 μm .

Using the polyamide 10.10 matrix, composites reinforced with 10% and 30% by mass of walnut shell particles and composites with a fibres glass additive of 30 wt %, were produced. Standard dumb-bell samples in accordance with PN-EN ISO 3167 were used in the tests, which were produced on the Engel ES 200/40 HSL injection moulding machine in Tarnow by Grupa Azoty. The parameters of the injection process were the same for all of the tested materials: injection temperature range of 190-210 °C, a screw-rotation speed of 50 rpm, an injection time of 2 s, a holding pressure time of 4s, a cooling time of 20 s, a mould temperature of 50 °C, a hydraulic back pressure of 80 MPa.

Samples, density and content of renewable sources are shown in Table 1.

Table 1.

Sample	Composition	$\rho(\text{g}/\text{cm}^3)$	Content of renewable sources (%)
PA10.10	Polyamide 10.10	1.0340±0.1	~100
PA10.10/10WSF	Polyamide 10.10 +10 wt% walnut shells flour	1.0644±0.3	~100
PA10.10/30WSF	Polyamide 10.10 +30 wt% walnut shells flour	1.1115±0.1	~100
PA10.10/30GF	Polyamide 10.10 +30 wt% glass fibres	1.2063±0.2	~70

2.1. Mechanical properties

All tests were carried out on samples immediately after the injection process from data obtained from the work of Czarnecka and Kuciel [18] and after four years of storage at 23 °C and 65% HR.

The mechanical properties were estimated by means of a universal MTS Criterion Model 43 testing machine. The tensile test was performed with a constant cross-head speed of 10 mm/min and the elongation was evaluated using an MTS axial extensometer and crosshead displacement. The values were obtained from an average of at least five specimens. The tensile test (tensile strength (σ_t), modulus of elasticity (E_t)) according to the PN-EN ISO 527-1:1998 standard was carried out. Furthermore, tensile test was carried out at temperatures -24 °C and 80 °C by placing specimens in the temperature chamber (Instron). The values of the lowered and elevated temperatures reflected the lowest and the highest temperatures at which bio-based polyamide's composites can be used.

The flexural three-point bending test (flexural modulus (E_f) and flexural stress at 3.5% strain (σ_f)) according to the PN-EN ISO 14125:2001 standard was performed on the neat PA 10.10 and its composites (23 °C and 65%HR) with a constant cross-head speed of 5 mm/min.

The morphology of each fibres type in matrix was studied using scanning electron microscope (JEOL 5510LV low vacuum) with an accelerating voltage of 15 or 20 kV on gold-sputtered tensile-test fracture surfaces specimen.

3. Results and Discussion

Figures 1 and 2 show the tensile strength and tensile modulus of the studied composites at -24 °C, +23 °C, +80 °C after four years of storage. The best results were obtained for all composites at -24 °C and the lowest at +80 °C. The tensile strength was similar for all

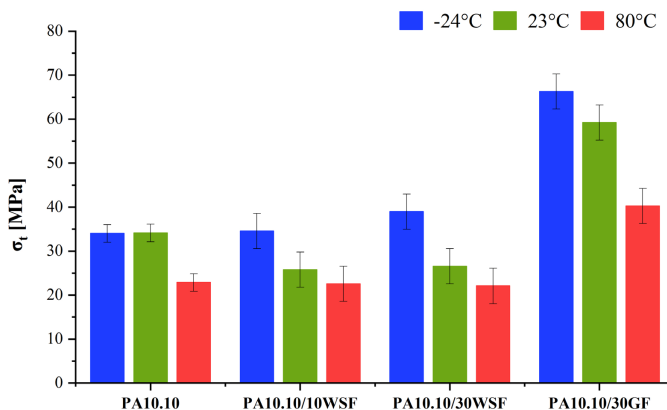


Fig. 1. Comparison of the tensile strength of neat PA10.10 and its composites at various temperatures -24 °C, 23 °C, +80 °C

composites with WSF in the range of 34-39 MPa at -24 °C. The elastic modulus for composites with WSF at -24 °C is almost tripled compared to result obtained at 23 °C and +80 °C.

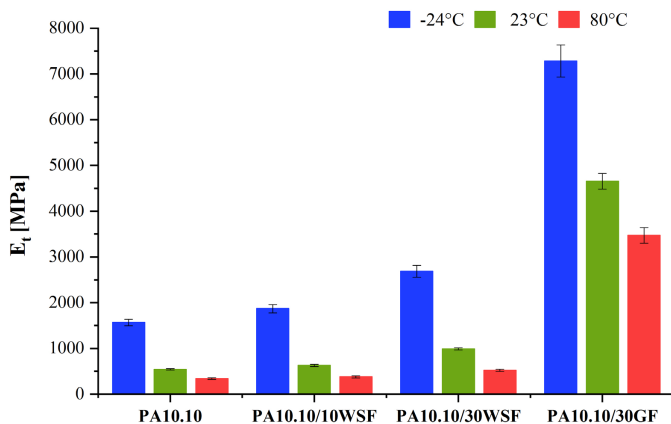


Fig. 2. Comparison of the elastic modulus of neat PA10.10 and its composites at various temperatures -24 °C, 23 °C, +80 °C

The obvious fact is that the best results were obtained for glass fibres reinforced composites. The composites have almost four-fold increase in mechanical properties compared to neat PA10.10.

Table 2. Mechanical properties of neat PA10.10 and its composites immediately after injection and after four years of storage

Temperature	Symbol	σ_t [MPa]		E_t [MPa]	
		after injection	after four years	after injection	after four years
-24 °C	PA10.10	42.1±0.4	34.00±0.3	2,131±62	1,567±54
	PA10.10/10WSF	42.9±0.4	34.55±0.4	2,599±85	1,870±103
	PA10.10/30WSF	44.1±0.3	38.95±0.4	2,599±96	2,686±93
	PA10.10/30GF	105.5±0.9	66.26±1.3	9,266±125	7,283±194
23 °C	PA10.10	29.4±0.1	34.11±0.1	658±32	541±13
	PA10.10/10WSF	26.63±0.1	25.78±0.1	800±56	627±57
	PA10.10/30WSF	28.17±0.2	26.54±0.2	1,314±78	990±67
	PA10.10/30GF	45.53±0.5	59.23±1.9	5,174±94	4,655±102
+80 °C	PA10.10	22.7±0.1	22.85±0.1	385±21	339±18
	PA10.10/10WSF	21.8±0.1	22.57±0.1	460±31	378±22
	PA10.10/30WSF	21.05±0.1	22.06±0.3	764±25	522±15
	PA10.10/30GF	39.5±0.7	40.25±1.2	4,419±31	3,471±16

A comparison of the mechanical properties of composites immediately after the injection process with composites after four years of storage is shown in Table 2. The addition of a natural filler such as WSF resulted in a significant increase in the modulus of elasticity and a slight reduction in tensile strength with increasing fibre content at all temperatures. Research conducted by Feldman and Bledzki and the results of Battegazzore et al. mentioned above show similar relationships. The authors argue that the cause of this is a higher ability to transfer stresses by particles [16, 17]. The obtained results are characteristic for composites with the addition of lignocellulosic particles [19, 20]. For composites filled with WSF, both strength and modulus values decreased after four years of storage for all temperatures. This is most probably associated with the breakdown of lignocellulosic particles.

Not surprisingly, the best results for both the elasticity modulus and strength were obtained for the composites reinforced with GF at all temperatures. This is due to the excellent mechanical properties of these fibres and the additional special fibre treatment that results in better adhesion to the matrix [21].

A surprising phenomenon is that there may only be a slight decrease in the strength properties of the composites immediately after injection at 80 °C, which is due to the partial activation of the cross-linking agent after an hour of heating in the thermal chamber. The long-term storage for four years resulted in a very similar effect of activation of the cross-linking agent. This resulted in a slight increase in tensile strength after four years with a significant 20% reduction in the modulus of elasticity. At room temperature, the cross-linking agent in time increased the strength of the composites, and the second ageing process probably caused the disintegration of the long-chain polyamide and the lowering of its stiffness.

Table 3. Bending properties of the neat PA10.10 and its composites after injection and after 4 years of storage

Symbol	σ_f [MPa]		E _f [MPa]	
	after injection	after four years	after injection	after four years
PA10.10	29±0.1	23±0.1	482±22	480±21
PA10.10/10WSF	59±0.2	27±0.1	581±28	581±25
PA10.10/30WSF	76±0.4	35±0.3	921±56	910±55
PA10.10/30GF	163±1.2	94±0.8	4,151±120	4,252±131

In table 2 was shown a comparison of the mechanical properties of the bending test immediately after injection and after four years of storage. For the neat PA10.10, an insignificant decrease in bending strength was obtained. However, for all composites over two-fold decrease was observed. With regard to the modulus of elasticity, the decrease in value was at a level of 5% compared to the results obtained immediately after injection.

Composite materials require strong adhesion between phases and uniform distribution of all components in the matrix to obtain composites with satisfactory mechanical properties. SEM images were used to characterize the morphology of individual fillers of composites and to assess their dispersion in the matrix as well as interfacial interactions between matrix and fillers. Figure 3 a–d shows SEM images of the tensile fracture specimens.

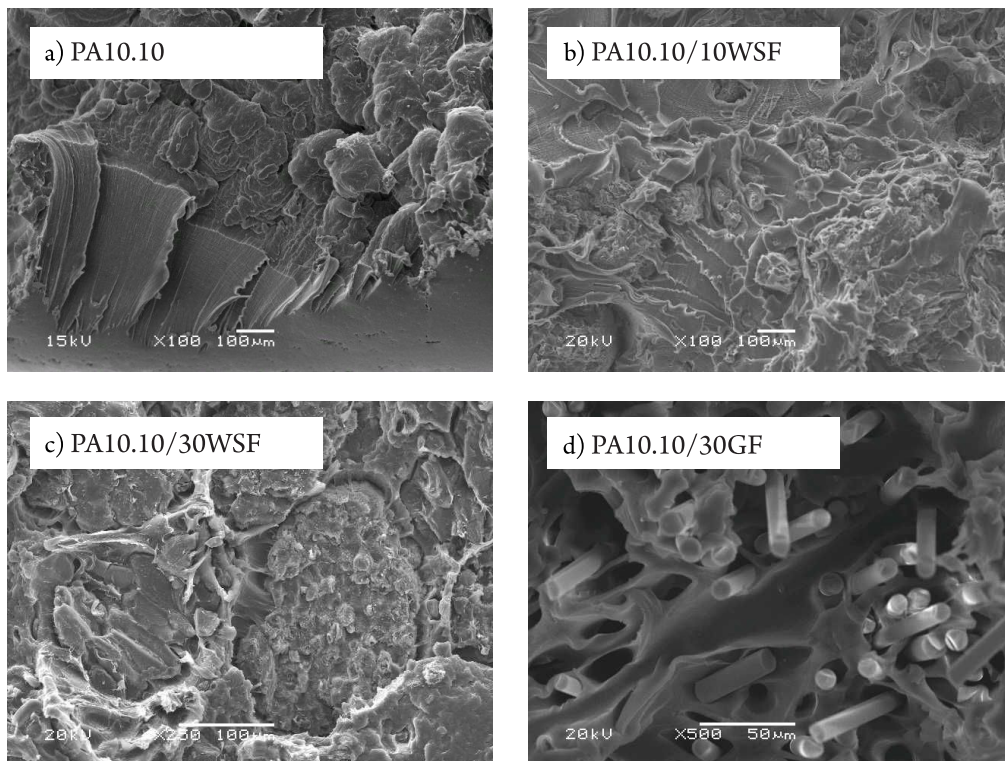


Fig. 3. SEM images of microstructure of PA10.10 composites a) neat, b) with 10 %wt of walnut shell flour, c) with 30 %wt of walnut shells flour, d) with 30 %wt of glass fibres

As can be seen in Figure 3a, neat PA10.10 is characterized by high plasticity of the breakthrough. In the Figure 3b, can be observed very well dispersed walnut shell particles in the polyamide matrix. In Figure 3c, it can be observed numerous and very regularly dispersed walnut particles in the polymer matrix, the breakthrough after fracture is characterized by brittleness. Clearly, empty places with a very small cross-section testify to the small adhesion of the nut shell particles to the resin. Figure 3d shows a fragment of a plastic fracture after fracturing with clearly cracked glass fibres partially embedded in the polymer matrix.

4. Conclusion

As a result of the tests, it was found that the properties of the cross-linking agent contained in Hiprolon 211 are much lower or no longer active after long-term storage. For all temperatures (-24 °C, 23 °C and 80 °C), the strength and the Young's modulus decreased. It can be concluded that materials of this type cannot be used for responsible parts of finished products but only for less-responsible parts with a short period of use, such as sports shoes or household appliances. The use of this type of material is possible using, for example, hybrid materials, such as combinations of biocomponents with conventional materials. Hiprolon

211 has been used in the last few years for the production of cable shields for the automotive industry, although it has currently been replaced by another product from the 10.10 polyamide group which is also manufactured from renewable raw materials.

References

- [1] european-bioplastics.org/market (access: 24.05.2018).
- [2] Vold J.L., Ulven C.A., Chisholm B.J., *Torrefied biomass filled polyamide biocomposites: mechanical and physical property analysis*, Journal of Materials Science, 2015, 725–732.
- [3] Espinach F.X., Delgado-Aguilar M., Puig J., Julian F., Boufi S., Mutjé P., *Flexural properties of fully biodegradable alpha-grass fibers reinforced starch-based thermoplastics*, Composites Part B: Engineering, 2015, 98–106.
- [4] Oliver-Ortega H., Granda L.A., Espinach F.X., Delgado-Aguilar M., Duran J., Mutjé P., *Stiffness of bio-based polyamide 11 reinforced with softwood stone ground-wood fibres as an alternative to polypropylene-glass fibre composites*, European Polymer Journal, 2016, 481–489.
- [5] Alves C., Ferrão P.M.C., Silva A.J., Reis L.G., Freitas M., Rodrigues L.B., Alves D.E., *Ecodesign of automotive components making use of natural jute fiber composites*, Journal of Cleaner Production, 2010, 313–327.
- [6] Heitzmann M.T., Veidt M., Ng C.T., Lindenberger B., Hou M., Truss R., Liew C. K., *Single-Plant Biocomposite from Ricinus Communis: Preparation, Properties and Environmental Performance*, Journal of Polymers and the Environment, 2013, 366–374.
- [7] Bledzki A.K., Reihmane S., Gassan J., *Thermoplastics reinforced with wood fillers: a literature review*, Polymer Plastic Technology Engineering, 1998, 451–468.
- [8] Velthoven J.L.J., Gootjes L., Noordover B.A.J., Meuldijk J., *Bio-based, amorphous polyamides with tunable thermal properties*, European Polymer Journal, 2015, 57–66.
- [9] McHenry E., Stachurski Z.H., *Composite materials based on wood and nylon fibre*, Composites Part A: Applied Science and Manufacturing, 2003, 171–181.
- [10] Sui G., Fuqua M.A., Ulven C.A., Zhong W.H., *A plant fiber reinforced polymer composite prepared by a twin-screw extruder*, Bioresources Technology, 2009, 1246–1251.
- [11] Orue A., Eceiza A., Arbelaiz A., *Preparation and characterization of poly(lactic acid) plasticized with vegetable oils and reinforced with sisal fibres*, Industrial Crops and Products, 2018, 170–180.
- [12] Awal A., Rana M., Sain M., *Thermorheological and mechanical properties of cellulose reinforced PLA bio-composites*, Mechanics of Materials, 2015, 87–95.
- [13] Nguyen T., Zavarin E., Barral II E.M., *Thermal analysis of lignocellulosic materials. Part I. Unmodified materials*, Journal of Macromolecular Science Part C Polymer Reviews, 1981, 1–65.
- [14] Zierdt P., Theumer T., Kulkarni G., Däumlich V., Klehm J., Hirsch U., Weber A., *Sustainable wood-plastic composites from bio-based polyamide 11 and chemically modified beech fibers*, Sustainable Materials and Technologies, 2015, 6–14.

- [15] Duigou L., Bourmaud A., Gourier C., Baley C., *Multi-scale shear properties of flax fibre reinforced polyamide 11 biocomposites*, Composites: Part A, 2016, 123–129.
- [16] Feldmann M., Bledzki A.K., *Bio-based polyamides reinforced with cellulosic fibres – Processing and properties*, Composites Science and Technology, 2014, 113–120.
- [17] Battagazzore D., Salvetti O., Frache A., Peduto N., De Sio A., Marino F., *Thermo-mechanical properties enhancement of bio-polyamides (PA10.10 and PA6.10) by using rice husk ash and nanoclay*, Composites: Part A, 2016, 193–201.
- [18] Czarnecka S., Kuciel S., *Polyamides composites with nanosilver particles for medical application*, Bachelor's thesis, Cracow University of Technology, 2014.
- [19] Gordobil O., Delucis R., Egüés I., Labidi J., *Kraft lignin as filler in PLA to improve ductility and thermal properties*, Industrial Crops and Products, 2015, 46–53.
- [20] Elanchezhian C., Ramnath B.V., Ramakrishnan G., Rajendrakumar M., Naveenkumar V., Saravanakumar M.K., *Review on mechanical properties of natural fiber composites Materials Today: Proceedings*, 2018, 1785–1790.
- [21] Sanjay M.R., Arpitha G.R., Yogesha B., *Study on Mechanical Properties of Natural - Glass Fibre Reinforced Polymer Hybrid Composites: A Review*, Materials Today: Proceedings, 2015, 2959–2967.

Łukasz Ślusarczyk  orcid.org/0000-0002-3565-7868

slusarczyk@mech.pk.edu.pl

Emilia Franczyk

Institute of Production Engineering, Faculty of Mechanical Engineering, Cracow
University of Technology

EXPERIMENTAL DETERMINATION OF FORCES IN A CUTTING ZONE DURGING TURNING A STAINLESS STEEL SHAFT

EKSPERYMENTALNE WYZNACZANIE SIŁ W STREFIE SKRAWANIA PODCZAS TOCZENIU WAŁKA ZE STALI NIERDZEWNEJ

Abstract

The article presents the results of laboratory tests, the aim of which was to measure cutting forces during parallel turning of an AMS 5643 steel bar. The cutting trials were registered with a 3-axis Kistler 9257B piezoelectric dynamometer, and the DynoWare computer program was used to archive and analyse the results. The experimental test plan for variable cutting parameters (v_c, a_p, f) was created according to the Taguchi method and the statistical analysis of the results was performed using ANOVA. The work involved carrying out 9 tests with the use of an uncoated carbide cutting insert. The obtained test results will be used to specify a simulation model of the cutting process.

Keywords: stainless steel, cutting forces, ANOVA

Streszczenie

Artykuł prezentuje wyniki badań laboratoryjnych pomiaru sił skrawania podczas toczenia wzdłużnego wałka ze stali AMS 5643. Próby skrawne rejestrowano 3-osiowym siłomierzem piezoelektrycznym Kistler 9257B, do archiwizacji i analizy wyników pomiarów zastosowano program komputerowy DynoWare. Eksperymentalny plan badań dla zmiennych parametrów skrawania (v_c, a_p, f) stworzono według metody Taguchi, a statystyczne opracowanie wyników wykonano za pomocą analizy ANOVA. W ramach prac zostało przeprowadzone 9 testów z zastosowaniem płytki skrawającej węglkowej niepokrywanej. Uzyskane wyniki badań będą wykorzystane do uściślenia modelu symulacyjnego procesu skrawania.

Słowa kluczowe: stal nierdzewna, siły skrawania, ANOVA

1. Introduction

Chip machining is one of the most common ways of shaping parts of machines and devices. The use of modern tools and numerically controlled machines enables obtaining objects of high technological quality [5]. The dynamic development of the aviation and automotive industries forces the use of machining in the production of complex components, often made from special, difficult-to-cut materials. At the stage of production planning, the correct selection of cutting parameters is very important for the issue [2, 3]. For this purpose, simulation methods are used, and laboratory tests are carried out. There are many computer programs available on the market that allow simulations of the phenomena that occur during the cutting process, including the determination of cutting forces or temperature values in the cutting zone. Simulation results should be verified with the results of laboratory tests. This is important when calibrating the simulation models of the cutting process [7, 8]. In the literature, a lot of space concerns improving the efficiency of the cutting process, while maintaining a minimal wear of the cutting tools [1, 4]. One of the practical ways to accomplish this task is to monitor and reduce cutting forces [6]. During rough machining, process efficiency is more important than a reduction of the cutting forces, and therefore great cutting depths, high feed rates and relatively low cutting speeds are assumed. When finishing, the cutting forces affecting the accuracy of the workpiece should be as low as possible. In this case, small cutting depths and feeds as well as higher cutting speeds are used. Many different conditions affect the cutting forces. These include, among other things, the geometry of the cutting tool's edge as well as the type and properties of the material being processed.

2. Conducted research

The laboratory stand was equipped with a set of measuring instruments to record the cutting forces of components. The arrangement of measuring instruments is shown in Fig. 1.



Fig. 1. The arrangement of measuring instruments to record the cutting forces of components:

1. KISTLER 9257B 3 axis piezoelectric dynamometer,
2. KISTLER type 5070A charge amplifier,
3. PC with DynoWare software.

The cutting force recording frequency was 1000 Hz. The combined measuring path enabled measurements of the components of the total cutting force with inaccuracy F_x – feed force

and F_y – radial force: $\pm 0,25$ N, F_z – tangential force: ± 1 N. Fig. 2 presents the dynamometer mounted on the lathe slide and the tool in the holder. 1 – piezoelectric dynamometer, 2 – single-position tool holder with insert installed, 3 – workpiece: AMS 5643 steel shaft.

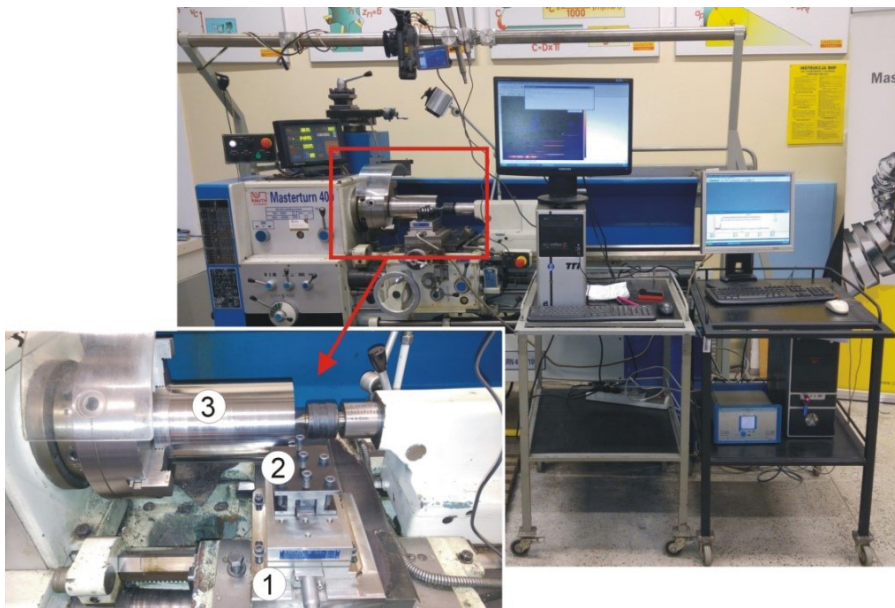


Fig. 2. The dynamometer mounted on the lathe slide and the tool in the holder

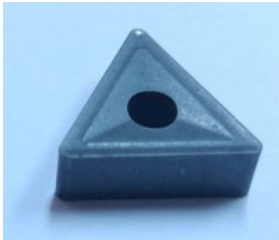
The machined material was an AMS 5643 stainless steel bar. This material belongs to the group of low-carbon, precipitation-hardened stainless steels. It is characterised by high static and fatigue strength, resistance to corrosion and high operating temperatures. The chemical composition of the steel according to the standards [10] is presented in Table 1.

Table 1. Chemical composition of AMS 5643 steel [9]

	Min. [%]	Max. [%]
C	-	0.07
Si	-	0.07
Mn	-	1.50
P	-	0.04
S	-	0.015
Cr	15.00	17.00
Mo	-	0.60
Ni	3.00	5.00
Cu	3.00	5.00

A triangular insert, without a protective coating, made of S20 sintered carbide was used for parallel turning test runs. The insert was mounted in the holder, and the wedge angle was -6° . The geometrical parameters of the cutting insert used are presented in Table 2.

Table 2. Geometrical parameters of the cutting insert used

Name	Picture	Holder	Insert geometry in the tool coordinate system
Uncoated plate with chip flute		PTGNR 2020K16	$\alpha = 5^\circ$ $\gamma = 9^\circ$ $\kappa = 90^\circ$

3. Findings

The test plan for the influence of three independent factors (v_c , f and a_p) on the total cutting force value was developed in accordance with the experimental design guidelines (DOE). A research plan was generated using the Taguchi method. Parameters v_c , f and a_p were assumed respectively as independent variables A, B and C. Ranges of the variation of cutting parameters were determined on the basis of catalogue data. Table 3 presents assumed values of the cutting parameters.

Table 3. Values of cutting parameters

Symbol	Cutting parameters	Parameter values		
A	v_c [m/min]	90	120	150
B	f [mm/rev]	0.105	0.153	0.211
C	a_p [mm]	0.5	1	1.5

A research plan generated according to the Taguchi method is shown in Table 4. The research plan was compiled in the form of an orthogonal table L9, which describes the individual trials for three factors at their different values (levels).

Table 4. Research plan by the Taguchi method

Sample number	Parameters			Parameter values		
	A	B	C	v_c [m/min]	f [mm/rev]	a_p [mm]
1	1	1	1	90	0.105	0.5
2	1	2	2	90	0.153	1.0
3	1	3	3	90	0.211	1.5
4	2	1	2	120	0.105	1.0

Sample number	Parameters			Parameter values		
	A	B	C	v_c [m/min]	f [mm/rev]	a_p [mm]
5	2	2	3	120	0.153	1.5
6	2	3	1	120	0.211	0.5
7	3	1	3	150	0.105	1.5
8	3	2	1	150	0.153	0.5
9	3	3	2	150	0.211	1.0

At the stage of statistical analysis of the results, the S/N ratio was determined; the smaller the better criterion was adopted. According to Taguchi, this type of coefficient is used when it is appropriate to minimise some of the undesirable features of the product.

The S/N ratio was calculated from the formula:

$$\frac{S}{N} = -10 \cdot \log \left(\frac{1}{n} \sum_{i=1}^n y_i^2 \right) \quad (1)$$

On the basis of the conducted research, it was found that it is possible to determine the order of influence of particular factors (v_c , f and a_p) on the studied phenomenon. Table 5 presents the results of the analysis of the order of impact of parameters on the value of the total cutting force.

Table 5. Analysis of the order of factors influence on the value of the total cutting force

Level	$F = f(v_c)$	Level	$F = f(f)$	Level	$F = f(a_p)$
1	593.2	1	4456	1	343.9
2	545.9	2	560.6	2	575.7
3	555.2	3	688.1	3	774.7
Delta	47.3		242.6		430.7
Rank	III		II		I

By analysing the results from table 5, it can be concluded that the cutting force a_p has the greatest influence on the cutting force value, followed by the feed f , and the cutting speed v_c .

An exemplary cutting force value waveform for run no. 5 is presented in Fig. 3.

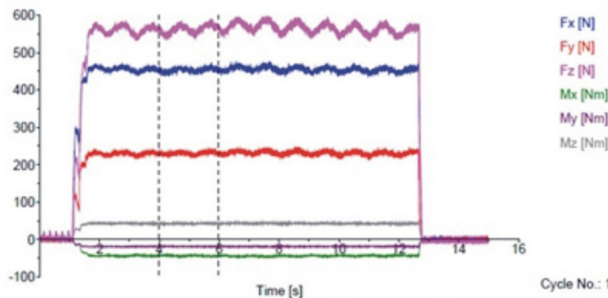


Fig. 3. An exemplary cutting force value waveform for run no. 5

The components of the cutting force: the feed force, the radial force and the tangential cutting force from Fig. 3 are marked respectively as F_x , F_y , F_z . For further analysis based on the stabilised waveforms, the mean values of the cutting force components were measured, and the value of the total cutting force was determined. In addition, as part of the work, an ANOVA was carried out, on the basis of which a regression equation was obtained for the calculation of the total cutting force F_{calc} .

$$F_{calc}(v_c, f, a_p) = 548,8 - 8,10 \cdot v_c - 3961,0 \cdot f + 884,90 \cdot a_p + 0,03 \cdot v_c^2 + 9200,0 \cdot f^2 + 16,0 \cdot a_p^2 + 23,42 \cdot v_c \cdot f - 3,75 \cdot v_c \cdot a_p$$

The value of the correlation coefficient for the obtained equation is: R-Sq = 92.24%, R-Sq(adj) = 84.24 %. The dependence of the calculated total cutting force on the cutting speed, feed rate and depth of cut is shown in the Fig. 4.

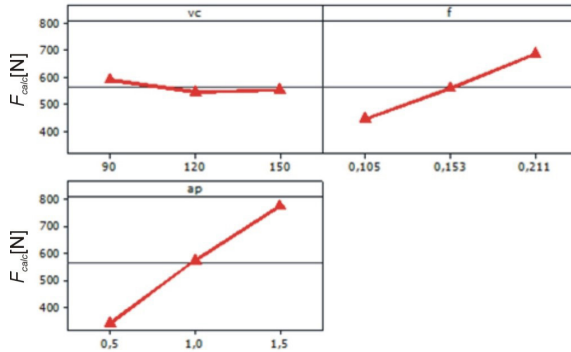


Fig. 4. The dependence of the calculate total cutting force on the cutting speed, feed rate and depth of cut

The measured values of the cutting force components F_x , F_y , F_z , the total cutting force value F , S/N ratio and the total cutting force value, calculated from the obtained regression equation F_{calc} , are shown in Table 6.

Table 6. Experimental and calculated values of forces and S / N ratio

Run number	F_x [N]	F_y [N]	F_z [N]	F [N]	S/N [dB]	F_{calc} [N]
1	123.25	146.94	174.46	259.26	-48.27	247.34
2	324.93	218.74	414.01	569.94	-55.12	558.02
3	511.32	275.00	752.44	950.39	-59.56	938.47
4	286.33	183.46	312.01	461.51	-53.28	440.32
5	452.84	230.38	562.05	757.65	-57.59	736.47
6	178.45	254.13	280.43	418.41	-52.43	397.07
7	398.93	192.95	427.76	615.92	-55.79	582.79
8	168.78	215.88	224.34	354.15	-50.98	320.82
9	371.48	280.61	516.81	696.58	-56.85	662.27

Exemplary characteristics of the impact of individual cutting parameter on the total cutting force values are shown in the following graphs. Fig. 4a, 4b, 4c present the influence of the cutting speed on the total cutting force value (at fixed a feed rate and depth of cut).

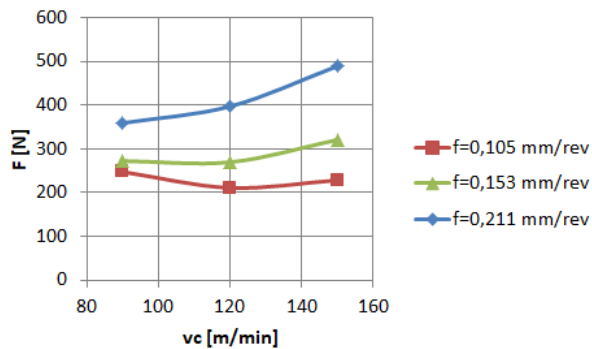


Fig. 4a. The influence of the cutting speed on the total cutting force, $a_p = 0.5$ mm

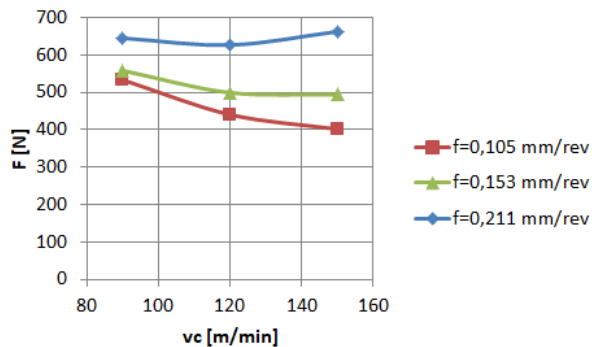


Fig. 4b. The influence of the cutting speed on the total cutting force, $a_p = 1.0$ mm

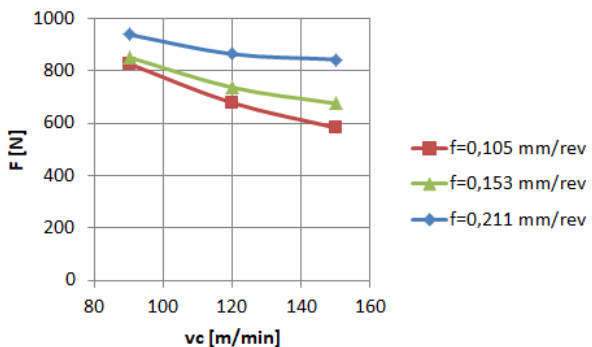


Fig. 4c. The influence of the cutting speed on the total cutting force, $a_p = 1.5$ mm

Fig. 5a, 5b, 5c present the influence of the feed rate on the total cutting force value (at a constant cutting speed and depth of cut).

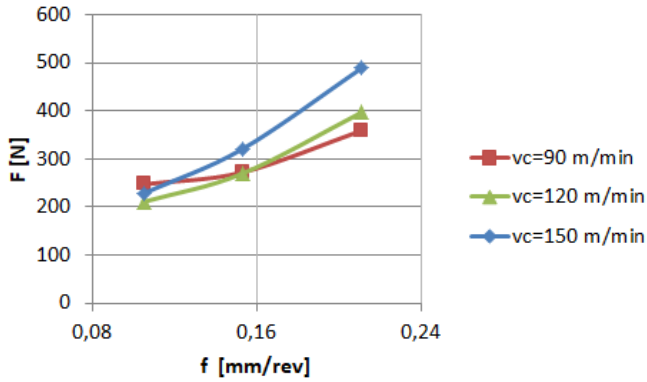


Fig. 5a. The influence of the feed rate on the total cutting force, $a_p = 0.5$ mm

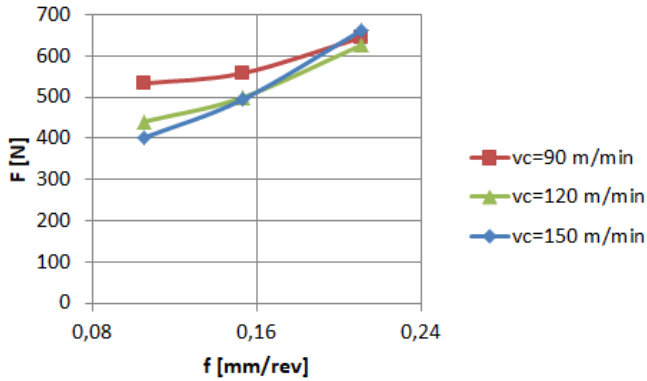


Fig. 5b. The influence of the feed rate on the total cutting force, $a_p = 1,0$ mm

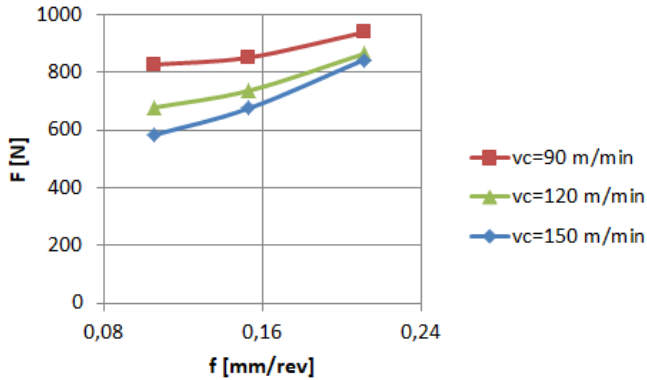


Fig. 5c. The influence of the feed rate on the total cutting force, $a_p = 1.5$ mm

Fig. 6a, 6b, 6c present the influence of the depth of cut on the total cutting force value (at a constant cutting speed and feed rate).

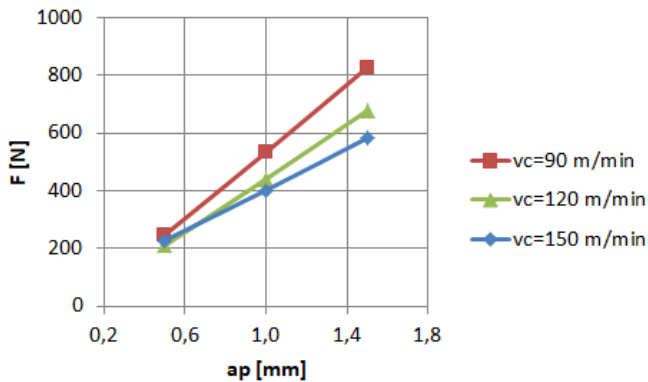


Fig. 6a. The influence of the depth of cut on the total cutting force, $f = 0.105$ mm/rev

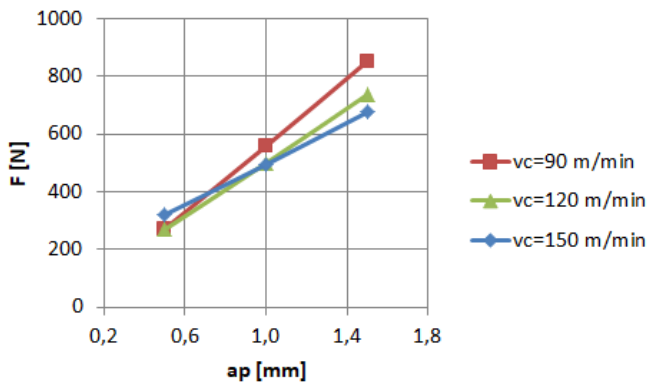


Fig. 6b. The influence of the depth of cut on the total cutting force, $f = 0.153$ mm/rev

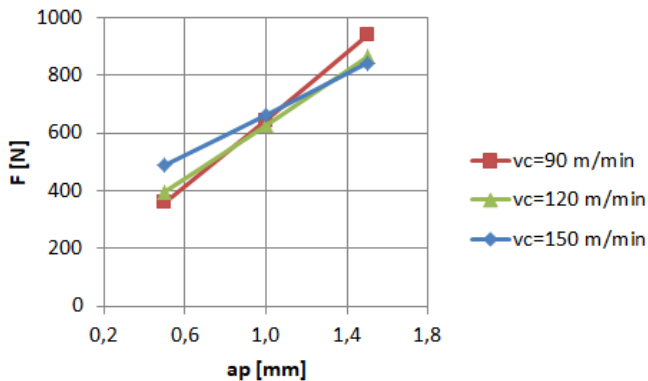


Fig. 6c. The influence of the depth of cut on the total cutting force, $f = 0.211$ mm/rev

Below are 3D graphs presenting the relationship between the cutting speed, feed rate and the total cutting force, for different depths of cut (Fig. 7) and the relationship between the cutting speed, depth of cut and the total cutting force for different feed rates (Fig. 8).

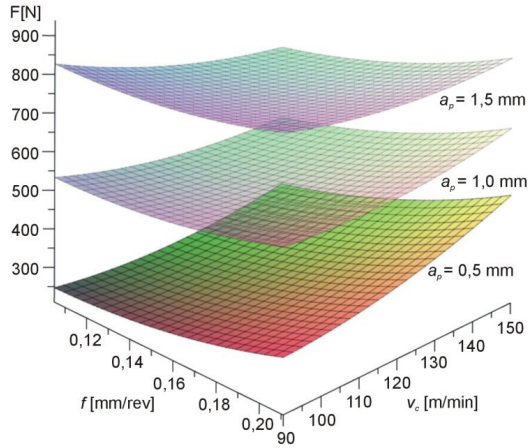


Fig. 7. The relationship between the cutting speed, feed rate and the total cutting force for different depths of cut

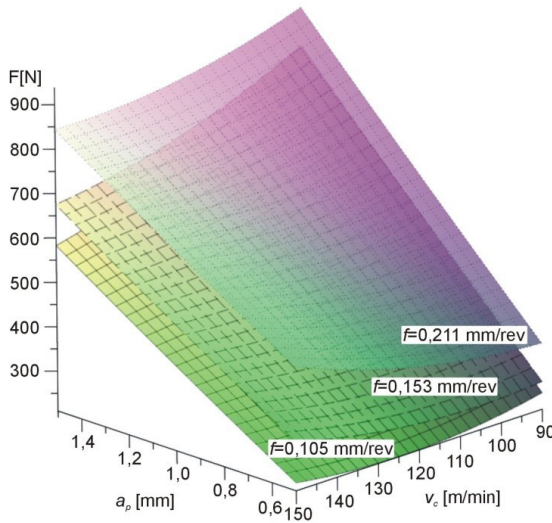


Fig. 8. The relationship between the cutting speed, depth of cut and the total cutting force for different feed rates

4. Conclusions

The paper presents the results of parallel turning of the AMS5643 steel shaft using a non-coated S20 carbide insert. During the research, the main focus was concentrated on the values of components of the total cutting force (F_x – feed force, F_y – radial force, F_z – tangential force), which were recorded using a piezoelectric dynamometer. The research plan was made according to the Taguchi method, based on the L9 orthogonal table, which describes the research plan for three independent factors, with three different values of each. The independent factors in the presented tests were: v_c – cutting speed, f – feed, and a_p – depth of cut. At each test, the highest value of force was recorded for the tangential component, followed by the feed, and the lowest for the radial thrust force.

Based on the ANOVA analysis of variances, the impact of individual cutting parameters on the value of the total cutting force was determined. It was found that the a_p , followed by f , has the greatest influence on the increase of the total cutting force value. A decrease in the total cutting force caused by the increase of v_c in the considered range of variability is not significant. In future tests, the influence of the corner radius of the cutting insert on the cutting force value should be taken into account.

References

- [1] Chomsamutr K., Jongprasithporn S., *Optimization Parameters of tool life Model Using the Taguchi Approach and Response Surface Methodology*, IJCSI International Journal of Computer Science Issues, 9, 1/3, 2012, 120–125.
- [2] Ezugwu E.O., Bonney J., Yamane Y., *An overview of the machinability of aeroengine alloys*, Journal of Materials Processing Technology, 134, 2003, 233–253.
- [3] Gawlik J., Zębala W., *Kształtowanie jakości wyrobów w obróbce precyzyjnej*. Mechanik, 2005, 12/2011.
- [4] Kruszczyński B., Stachurski W., Zgórniak P., *Wpływ warunków obróbki podczas toczenia ostrzami typu Wiper na jakość powierzchni obrabianej i siły skrawania*, Inżynieria Maszyn, 15/4, 2010, 7–20.
- [5] Słodki, B., Zębala, W., Struzikiewicz, G., *Correlation between cutting data selection and chip form in stainless steel turning*, Machining Science and Technology, Vol. 19, Issue 2, 2015, 217–235.
- [6] Ślusarczyk, Ł., Franczyk, E., *Development and verification of a measuring stand for recording the physical phenomena during turning*, Photonics Applications in Astronomy Communications Industry and High-Energy Physics Experiments Book Series: Proceedings of SPIE 10445, 104456G, 2017.
- [7] Ślusarczyk, Ł., *The construction of the milling process simulation models*, Photonics Applications in Astronomy Communications Industry and High-Energy Physics Experiments Book Series: Proceedings of SPIE 10031, 100310C, 2016.

- [8] Zebala W., *Modelowanie procesu toczenia materiałów trudnoskrawalnych*, Czasopismo Techniczne, 5-M/2011.
- [9] www.tachart.com/material/ams-5643 (access: 13.07.2018).
- [10] PN/EN 10088-1:2005 Stale odporne na korozję. Część 1: Wykaz stali odpornych na korozję

Łukasz Ślusarczyk  orcid.org/0000-0002-3565-7868

slusarczyk@mech.pk.edu.pl

Emilia Franczyk

Institute of Production Engineering, Faculty of Mechanical Engineering, Cracow
University of Technology

EXPERIMENTAL DETERMINATION OF THE TEMPERATURE IN THE CUTTING ZONE DURING TURNING OF TITANIUM ALLOY GRADE 2

EKSPERYMENTALNE WYZNACZENIE TEMPERATURY W STREFIE SKRAWANIA PODCZASTOCZENIA STOPU TYTANU GRADE 2

Abstract

The paper presents the laboratory measurements results of temperature distribution in the cutting zone during orthogonal turning of a GRDE 2 titanium tube. The cutting tool used during the tests was a bimetallic cut-off tool with an uncoated insert made of P10 sintered carbide. The test plan was developed using the MiniTab16 computer application and the Taguchi method. The tests were performed in accordance with orthogonal table L9, which describes nine cutting trials for two independent factors, cutting speed v_c [m/min] and feed rate f [mm/rev], at three different values. The temperature distribution in the cutting zone was measured by means of a FLIR SC 620 thermal imaging camera. The archiving and processing of measurement results was performed with the ThermoCamResearcher Pro 2.9 computer application. The obtained results were used to determine the average temperature for each of the nine trials; then, a statistical analysis of the results was performed.

Keywords: GRADE 2, temperature, thermovision camera

Streszczenie

Artykuł prezentuje wyniki badań laboratoryjnych pomiaru rozkładu temperatury w strefie skrawania podczas toczenia ortogonalnego rury ze stopu tytanu GRDE 2. Narzędziem skrawającym wykorzystanym podczas badań był przecinak bimetaliczny z niepokrywaną płytką z węglika spiekanego P10. Plan badań zbudowano przy pomocy aplikacji komputerowej MiniTab16, z wykorzystaniem metody Taguchi. Badania realizowano zgodnie z wyznaczoną tablicą ortogonalną L9, która opisuje wykonanie dziewięciu prób skrawnych dla dwóch niezależnych czynników, prędkości skrawania v_c [m/min] oraz posuwu f [mm/obr], przy ich trzech różnych wartościach. Rozkład temperatury w strefie skrawania był mierzony z wykorzystaniem kamery termowizyjnej FLIR SC 620. Archiwizację i opracowanie wyników pomiarów zrealizowano z wykorzystaniem aplikacji komputerowej ThermoCamResearcher Pro 2.9. Na podstawie uzyskanych wyników wyznaczono wartość średniej temperatury w strefie skrawania dla każdej z dziewięciu prób, następnie dokonano statystycznej analizy wyników.

Słowa kluczowe: GRADE 2, temperatura, kamera termowizyjna

1. Introduction

CNC machine tools are now widely used in mass production. A huge emphasis is placed on the reduction of manufacturing costs. In machining, one of the factors that allows for a cost reduction is minimising the cutting tool wear [1, 10]. The key issue in this regard is a correct choice of cutting parameters, which is particularly difficult in case of machining of titanium alloys, as these alloys have a low thermal conductivity coefficient and, in addition, they are cold-work hardened during the machining. These factors expose a cutting tool to an intensive wear [2, 3]. One of the methods to extend the tool life is the optimisation of the cutting process: cutting speed, feed rate and cutting depth. This can be implemented through an experimental determination of the impact of individual cutting parameters on the wear intensity of the tool blade. The other method is the measurement of physical magnitudes during the machining, such as cutting force or temperature in the cutting zone [5, 7, 9]. A lot of attention is given in the literature to the contact and contactless temperature measurement in the cutting zone [4, 6, 8]. The contact methods use thermocouples installed in the vicinity of the cutting edge. These methods are relatively difficult to implement, or even impossible to use in industrial practice. The other method to measure the temperature in the cutting zone is the use of devices measuring the infrared radiation, pyrometers, and thermal imaging cameras. These methods are much easier to implement than the contact methods, and the obtained temperature values and distributions in the cutting zone allow for a verification of the correctness of the applied cutting parameters and machining process [3].

2. Conducted research

The laboratory tests were conducted on a stand, which, in addition to the cutting zone temperature measurement, also allows for the measurement of cutting forces and a recording of fast-changing images during the chip formation process. The test stand, where the temperature in the cutting zone was recorded, is shown in Fig. 1.

The workpiece was a tube made of titanium alloy GRADE 2, diameter $D = 60$ mm.

The chemical composition of the titanium alloy GRADE 2, according to the EN 10204-3.1 standards, is presented in Table 1.

Table 1. The percentage chemical composition of the titanium alloy GRADE 2

	Fe	C	N	O	H	Ti
GRADE 2 max.	0.30	0.08	0.03	0.25	0.015	Bal.

Some properties of the titanium alloy GRADE 2 are presented in Table 2.

The thermographic camera was placed in front of the machining zone. Table 3 presents the configuration parameters of the FILR SC 620 thermovision camera.

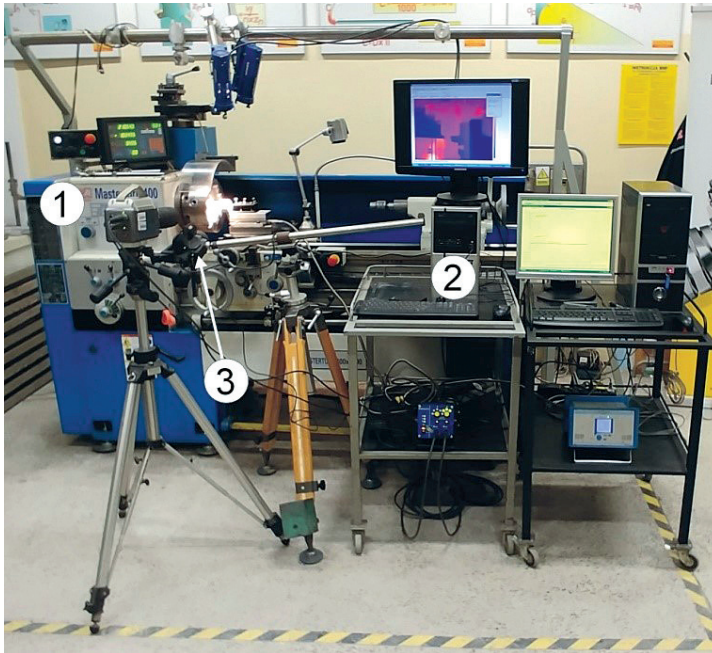


Fig. 1. The test stand where the temperature in the cutting zone was recorded. The compared measurement path consisted of:

1. a conventional turning machine Knuth Masterturn 400,
2. computer PC with ThermoCam Researcher 2.9 software,
3. thermovision camera FLIR SC 620.

Table 2. The properties of the titanium alloy GRADE 2

Melting Point	ca.1660 [°C]
Density	4510 [kg*m ⁻³]
Modulus of Elasticity	105 [GPa]
Specific Heat Capacity	526 [J*kg ⁻¹ *K ⁻¹]
Thermal Conductivity	16.4 [W*m ⁻¹ *K ⁻¹]

Table 3. The configuration parameters of the FILR SC 620 thermovision camera

	ambient temperature	22 °C
	emissivity	0.4
	relative humidity	37 %
	distance measurement	1 m
	Image frequency	30 frame/s
	focal lens	36 mm

The cutting tool used during the tests was a bimetallic cut-off tool with a 5mm-wide uncoated insert made of P10 sintered carbide. The cutting insert had a flat face. In the tool coordinate system, the rake angle was $\gamma = 10^\circ$, and the clearance angle was $\alpha = 8^\circ$. The machining involved straight turning along the tube wall. Fig. 2 presents the tool position relative to the workpiece.

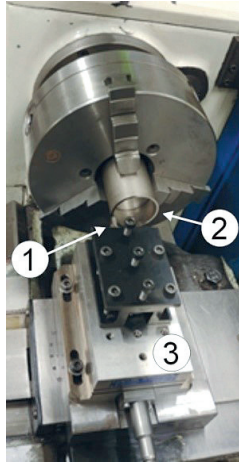


Fig. 2. The tool position relative to the workpiece, where:
 1. single-position tool holder with insert installed,
 2. a tube made of titanium alloy GRADE 2, diameter $D = 60$ mm,
 3. a dynamometer mounted on the lathe slide.

The cutting parameters (speed and feed rate) were chosen according to the recommended datasheet values. The test plan, developed on the basis of the Taguchi method, involved nine trials. The cutting speed v_c and feed rate f , were independent variables. The parameter values for the individual trials are given in the table below (Table 4). The cutting depth was identical to the tube wall thickness and it was the same in each trial - equal to $a_p = 2.77$ mm.

Table 4. The parameter values for individual trials

Test no.	A	B	v_c [m/min]	f [mm/rev]	a_p [mm]
1	1	1	60	0.048	2.77
2	1	2	60	0.153	2.77
3	1	3	60	0.249	2.77
4	2	1	100	0.048	2.77
5	2	2	100	0.153	2.77
6	2	3	100	0.249	2.77
7	3	1	140	0.048	2.77
8	3	2	140	0.153	2.77
9	3	3	140	0.249	2.77

The maximum temperatures in the cutting zone during straight turning in each of the 9 trials were recorded by a thermovision camera and connected to a computer with the ThermaCAM Researcher 2.9 software installed. Exemplary frames with maximum temperature in the no. 1 and 2 trials are shown below (Fig. 3–4).

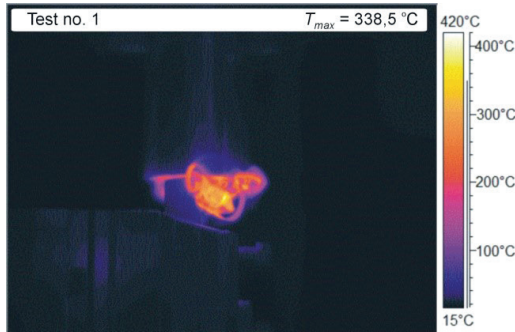


Fig. 3. Thermogram with maximum temperature during test no. 1

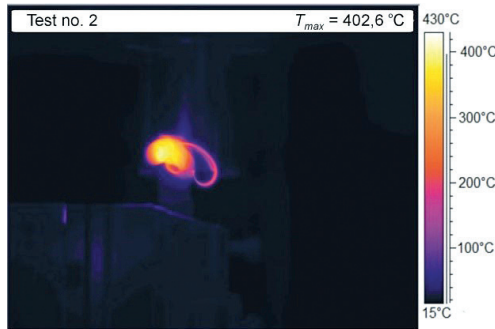


Fig. 4. Thermogram with maximum temperature during test no. 2

The data received from the software were also used to obtain the stabilised temperature values. Fragments of temperature curves (typical figures below Fig. 5 a) b)) were selected based on the stabilised maximum temperature curves for each trial in order to determine the average maximum temperature values.

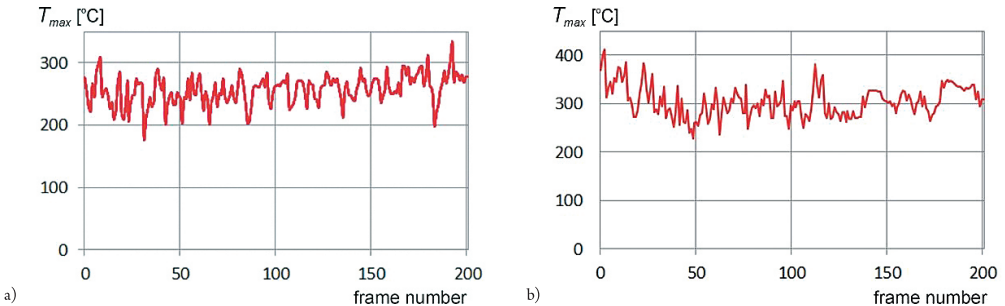


Fig. 5. The maximum temperature during the turning
a) test no. 1, b) test no. 2

3. Findings

On the basis of the performed analysis, the average values of the maximum temperature were determined for each of the 9 tests (Fig. 6). Due to the variable values of cutting parameters (v_c, f), the stabilised temperature waveforms were characterised by different amplitudes.

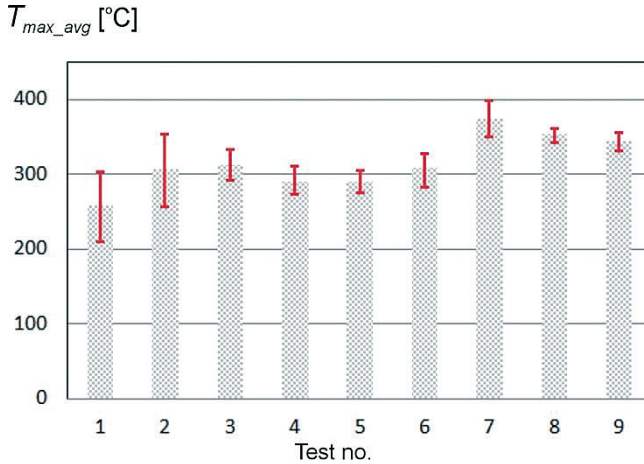


Fig. 6. Average values of the maximum temperature for each of the 9 tests

Table 5 below includes the average maximum temperature values.

Table 5. The average maximum temperature values

A	B	v_c [m/min]	f [mm/rev]	T_{max_1} [°C]	T_{max_2} [°C]	T_{max_3} [°C]	T_{max_avg} [°C]
1	1	60	0.048	210.3	257.2	303.6	257.0
1	2	60	0.153	256.5	309.9	353.3	306.7
1	3	60	0.249	291.6	308.6	332.1	310.8
2	1	100	0.048	272.4	286.4	309.9	289.6
2	2	100	0.153	274.9	286.5	305.0	288.9
2	3	100	0.249	283.4	311.2	327.2	307.3
3	1	140	0.048	350.0	371.0	399.1	373.3
3	2	140	0.153	342.0	357.4	361.1	353.5
3	3	140	0.249	330.4	343.3	356.0	343.2

Then, the signal-to-noise ratio was determined using the ANOVA statistical result analysis. The applied criterion was - the less, the better. The S/N ratio was calculated using the formula:

$$\frac{S}{N} = -10 \cdot \log \left(\frac{1}{n} \sum_{i=1}^n y_i^2 \right) \quad (1)$$

The quadratic equation was formulated to describe the average maximum temperature:

$$T_{max_avg_calc} = 0.0180174*v_c^2 - 245.926*f^2 - 1.998*v_c + 668.014*f - 5.26*f*v_c + 300 \text{ [}^\circ\text{C]} \quad (2)$$

Table 6 includes the values of the S/N ratio, the average maximum temperature (T_{max_avg}) and the calculated average maximum temperature ($T_{max_avg_calc}$) determined using the formula (2).

Table 6. The values of the S/N ratio, T_{max_avg} and $T_{max_avg_calc}$

Test no.	v_c [m/min]	f [mm/rev]	a_p [mm]	T_{max_avg} [°C]	S/N [dB]	$T_{max_avg_calc}$ [°C]
1	60	0.048	2.77	257.0	-48.1978	261.3
2	60	0.153	2.77	306.7	-49.7308	293.1
3	60	0.249	2.77	310.8	-49.8488	317.5
4	100	0.048	2.77	289.6	-49.2353	286.6
5	100	0.153	2.77	288.9	-49.2121	296.3
6	100	0.249	2.77	307.3	-49.7508	300.5
7	140	0.048	2.77	373.3	-51.4405	369.6
8	140	0.153	2.77	353.5	-50.9681	357.2
9	140	0.249	2.77	343.2	-50.7125	341.1

The correlation coefficient value is $R-Sq = 93.21\%$, $R-Sq(adj) = 72.54\%$.

The impact of the feed rate and cutting speed on the $T_{max_avg_calc}$ was determined based on the statistical analysis (Fig.7).

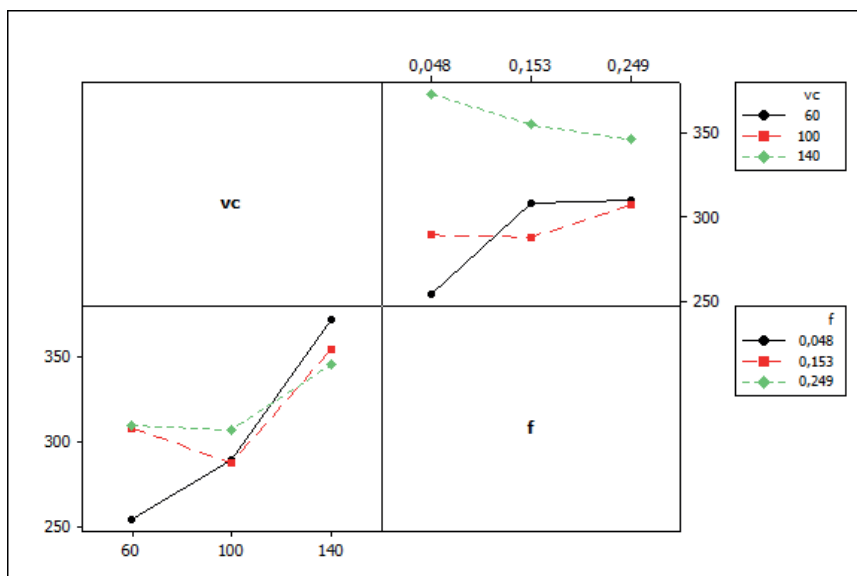


Fig. 7. The impact of the feed rate and cutting speed on the $T_{max_avg_calc}$

Below (Fig. 8) is a 3D graph presenting the relationship between the cutting speed, feed rate and the calculated average maximum temperature.

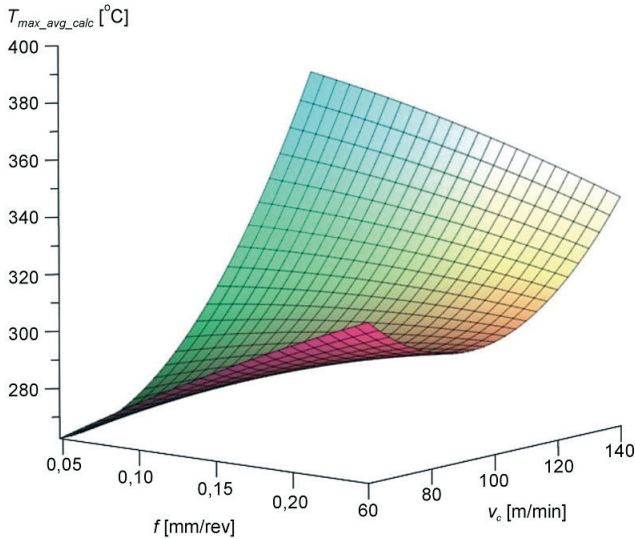


Fig. 8. The relationship between the cutting speed, feed rate and the calculated average maximum temperature

4. Conclusions

The graphs obtained based on the regression function $T_{max_avg_calc}$ allow for a determination of the impact of machining parameters (v_c and f) on the cutting zone temperature. The cutting zone temperature grew as the cutting speed increased for all three feed rate values. The lowest temperature (about 261 °C) was recorded for $v_c = 60$ m/min and feed rate $f = 0.048$ mm/rev. Higher temperatures are observed for faster feed rates $f = 0.153$ and $f = 0.249$. The obtained trend indicates a temperature increase along with the cutting speed increase. The maximum temperature values of about 340–370 °C were obtained for $v_c = 140$ m/min, for three feed rate values. The situation in the case of increasing the feed rate at three cutting speed values is somewhat different. In case of two lower cutting speeds, the temperature grew as the feed rate is increased, although larger differences occur for $v_c = 60$ m/min. In case of the highest cutting speed, the feed rate increase caused a drop of the recorded average maximum temperature by about 25°C. A thermal balance model for orthogonal turning can be used to explain the obtained trends describing the temperature value. For a feed rate increase, it can be said that the thermal energy generated in the cutting zone in the form of heat fluxes penetrates between the tool, the chip and the workpiece. In orthogonal turning, the feed rate value is identical with the cut layer thickness. The chip cross section increases, and the energy dissipation is larger. The cutting speed increases results in the higher chip flow speed along the tool face, and this in turn causes a destruction of heat fluxes penetrating between the chip and the tool.

References

- [1] Chauvy P.F., Madore C., Landolt D., *Variable length scale analysis of surface topography: characterization of titanium surfaces for biomedical applications*, Surface and Coatings Technology, 1998, 110, 48–56.
- [2] Che-Haron C.H., *Tool life and surface integrity in turning titanium alloy*, Journal of Materials Processing Technology, 2001, 118, 231–237.
- [3] Grzesik W., *A survey of current knowledge on machining titanium and its alloys*, The 5th International Scientific Conference Development of Metal Cutting, 21–26.
- [4] Jaspers, S.P.F.C., Dautzenberg, J. H., Taminiau, D. A., *Temperature Measurement in Orthogonal Metal Cutting*, Int. J Advanced Manufacturing Technology, 14, 1998, 7–12.
- [5] Kolahani F., Manoochehri M., Hosseini A., 2011, *Application of Taguchi Method and ANOVA Analysis for Simultaneous Optimization of Machining Parameters and Tool Geometry in Turning*, World Academy of Science, Engineering and Technology, 74, 82–85.
- [6] Siwiec, J., *Obróbka materiałów w stanie utwardzonym*, Czasopismo Techniczne, 5-M/2011.
- [7] Struzikiewicz, G., Zębala, W., Rumian, K., *Application of Taguchi method to optimization of cutting force and temperature during turning of difficult to cut materials*, Key Engineering Materials 686, 2016, 114–118.
- [8] Ślusarczyk, Ł., *The implementation of a thermal imaging camera for testing the temperature of the cutting zone in turning*. Proceedings of 10031, 2016, 100310L1-100310L7.
- [9] Ślusarczyk, Ł., Franczyk, E., *Development and verification of a measuring stand for recording the physical phenomena during turning*, Photonics Applications in Astronomy Communications Industry and High-Energy Physics Experiments Book Series: Proceedings of SPIE 10445, 2017, 104456G.
- [10] Zębala, W., Gawlik, J., Matras, A., Struzikiewicz, G., Ślusarczyk, Ł., *Research of surface finish during titanium alloy turning*, Key Engineering Materials, 581, 2014, 409–414.

Krzysztof Wach

krzysztof.wach@mech.pk.edu.pl

Institute of Automobiles and Internal Combustion Engines, Faculty
of Mechanical Engineering, Cracow University of Technology

THE INFLUENCE OF VEHICLE PREPARATION ON THE RESULTS
OF SUSPENSION KINEMATICS MEASUREMENT

WPLYW PRZYGOTOWANIA POJAZDU NA WYNIKI
POMIARU KINEMATYKI ZAWIESZENIA

Abstract

This paper concerns the assessment of the impact of tyre pressure and additional vehicle loading which is inconsistent with the manufacturer's requirements on the results of wheel alignment measurement. A sample of results from tests performed on a second generation Toyota Prius and a fifth generation Volkswagen Passat are presented. The tested vehicles differed in the types of front axle wheel suspension. An analysis of the obtained results was conducted. The analysis revealed differences between the results of reference tests performed in accordance with the requirements of vehicle manufacturers and those conducted for incorrectly prepared vehicles. The values of these differences depended, inter alia, on the type of suspension.

Keywords: car, suspension, wheel alignment, measurement, road safety

Streszczenie

Praca dotyczy oceny wpływu ciśnienia w ogumieniu oraz obciążenia pojazdu niezgodnego z wymaganiami producenta, na wyniki pomiaru geometrii zawieszenia. Przedstawione zostały przykładowe wyniki prób przeprowadzonych na samochodach Toyota Prius II generacji oraz Volkswagen Passat generacji piątej. Pojazdy różniły się rodzajami zawieszenia kół osi przedniej. Wykonana została analiza uzyskanych wyników, która wskazała różnice pomiędzy wynikami prób referencyjnych – przeprowadzonych zgodnie z wymaganiami producentów – a próbami dla pojazdów niewłaściwie obciążonych bądź z niewłaściwym ciśnieniem w ogumieniu. Wartości tych różnic uzależnione były między innymi od rodzaju zawieszenia.

Słowa kluczowe: samochód, zawieszenie, geometria zawieszenia, pomiar, bezpieczeństwo ruchu drogowego

1. Introduction

The suspension system is a significant part of a car which is responsible for transferring forces between the wheels and the body, as well as damping and reducing the dynamic forces acting on the wheels and the entire vehicle [14]. The front-wheel suspension systems of modern cars are usually independent systems; one of the most popular is the MacPherson strut, while the most complicated is multi-link suspension. Rear wheels are usually guided by a twist-beam or by independent suspension systems. Due to the significant impact of the suspension on vehicle handling and driving safety [1, 9, 15], a number of pieces of research and scientific works, including numerical simulations [16–20], have been conducted in order to improve and develop their construction and capabilities [4, 5, 7–10, 12, 14, 15]. As a result of appropriate suspension characteristics, it is possible to ensure adequate stability and steerability, which are the features that ensure the car's resistance to forces interfering with its movement [6, 11].

Regardless of the design and type of suspension, its proper maintenance is very important. Wheel alignment inspection and, if necessary, adjustment should be performed regularly [3]. Correct wheel geometry is very important in the context of road traffic safety; moreover, inaccurate alignment causes excessive tyre wear and has an influence upon fuel consumption [3]. To properly conduct measurements of wheel alignment, the vehicle should be in working order, any backlashes in suspension and steering systems should be removed and the tyre pressure should be correct. Additionally, measurement conditions such as proper vehicle load specified by the manufacturer must be provided.

2. Tested cars

Two cars with different types of suspension were used in the measurements of wheel alignment: a second generation Toyota Prius (XW20) and a fifth generation Volkswagen Passat Variant (B5). The Toyota was equipped with an independent MacPherson front wheel suspension system; the Volkswagen's front wheels were guided with a multi-link independent suspension system. The rear axles of both cars were equipped with semi-independent twist-beam suspensions. The basic parameters of the tested cars are presented in Table 1.

Table 1. The basic technical data of the tested cars

	Toyota Prius XW20	VW Passat Variant B5
Engine	1.5	1.9 TDi
Drive wheels	front	front
Front suspension	MacPherson	Multi-link
Rear suspension	twist-beam	twist-beam
Length [mm]	4450	4675
Wheelbase [mm]	2700	2705
Track front/rear [mm]	1505/1480	1515/1515
Curb weight [kg]	1317	1445
GVM* [kg]	1725	2010
* GVM – gross vehicle mass		

Figure 1 shows overviews of the examined vehicles on the test bench.

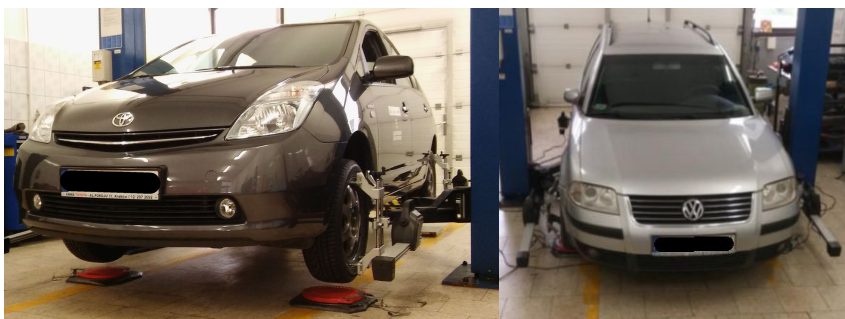


Fig. 1. Tested cars on the test bench: Toyota Prius (left); Volkswagen Passat (right)

Table 2 presents wheel alignment specification of tested vehicles.

Table 2. Wheel alignment specification of the tested cars

	Toyota Prius XW20	VW Passat Variant B5
Front wheels		
Caster angle	$+ 3^{\circ}10' \pm 45'$	n/n
Camber angle	$- 0^{\circ}35' \pm 45'$	$- 0^{\circ}35' \pm 25'$
Total toe	$0^{\circ}00' \pm 12'$	$0^{\circ}20' \pm 4'$
FL/FR* toe	$0^{\circ}00' \pm 6'$	$0^{\circ}10' \pm 2'$
SAI**	$+ 12^{\circ}35' \pm 45'$	n/n
Rear wheels		
Camber angle	$- 1^{\circ}30' \pm 30'$	$- 1^{\circ}30' \pm 20'$
Total toe	$+ 0^{\circ}18' \pm 15'$	$+ 0^{\circ}22' \pm 13'$
RL/RR*** toe	$+ 0^{\circ}09' \pm 7'$	$+ 0^{\circ}11' \pm 6'$
* FL/FR – front left/front right ** SAI – steering angle inclination *** RL/RR – rear left/rear right		

3. Used equipment

The measurements were conducted using a CUSTOR HWA G58 wheel alignment device [2]. The device is equipped with four heads with CCD cameras attached to the wheels using rim clamps.

Figure 2 shows an overview of a wheel alignment device used in the measurements and one of its heads fitted with CCD cameras; the basic technical specification of the device is presented in Table 3.



Fig. 2. An overview of the CUSTOR HWA G58 wheel alignment device and a close-up of a front left head attached to the wheel

Table 3. The basic technical specification of the CUSTOR HWA G58 wheel alignment device

	Parameter	Range	Accuracy
Front axle	Toe	$\pm 24^\circ$	$\pm 1'$
	Camber	$\pm 10^\circ$	$\pm 1'$
	Caster	$\pm 20^\circ$	$\pm 2'$
	SAI*	$\pm 20^\circ$	$\pm 2'$
	Setback	$\pm 10^\circ$	$\pm 1'$
Rear axle	Toe	$\pm 24^\circ$	$\pm 1'$
	Camber	$\pm 10^\circ$	$\pm 1'$
	Setback	$\pm 10^\circ$	$\pm 1'$
	Thrust angle	$\pm 10^\circ$	$\pm 1'$
* SAI – steering angle inclination			

4. Measurements and their results

The aim of this study was the analysis of the influence of improper preparation of a car on results of wheel alignment measurement. A correctly prepared car must be free of defects or damage to suspension and steering systems; it should be loaded in accordance with the manufacturer's specifications and the tyre pressure should be correct. The presented work consists of multiple measurements of the wheel geometry of two cars: a second generation Toyota Prius and a fifth generation Volkswagen Passat Variant, with different loading of the tested cars which are noncompliant with the manufacturer's requirements. In the case of the Toyota Prius, the influence of tyre pressure was also taken into account. Before each measurement, a rims runout compensation was performed.

4.1. Impact of vehicle load

In accordance with the requirements of the manufacturers of both tested cars, the measurements should be performed without any additional load. However, in accordance with the aim of this study, vehicles were additionally loaded during the measurements. In the case of the Toyota Prius, the tests were conducted for 1, 2 and 3.5 kN of extra load placed in the boot; in the case of the Volkswagen, the extra load was 1, 2, 3.5 and 5 kN. The load was placed symmetrically in relation to the longitudinal axis. In addition to these measurements, the vehicles were also tested with only the curb weight in order to provide a control reference.

Figures 3 to 8 show sample results of the conducted measurements.

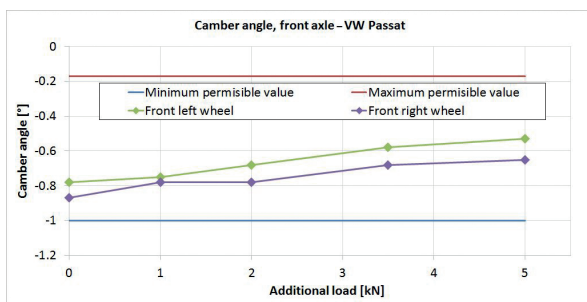


Fig. 3. Impact of additional vehicle load on front wheel camber angle value for VW Passat

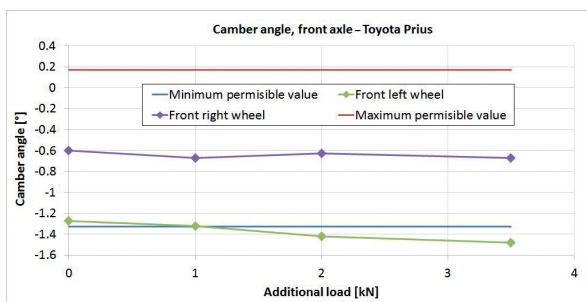


Fig. 4. Impact of additional vehicle load on front wheel camber angle value for Toyota Prius

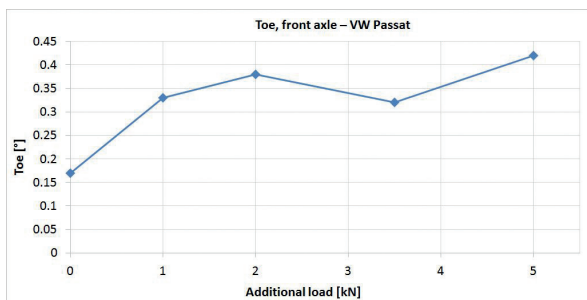


Fig. 5. Impact of additional vehicle load on front wheel toe value for VW Passat

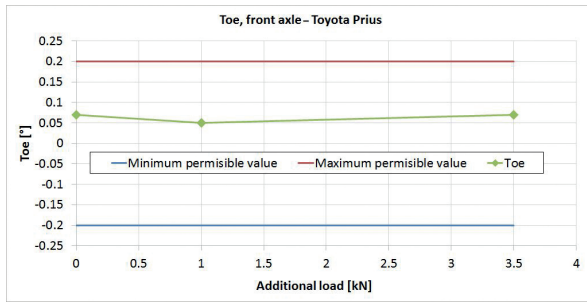


Fig. 6. Impact of additional vehicle load on front wheel toe value for Toyota Prius

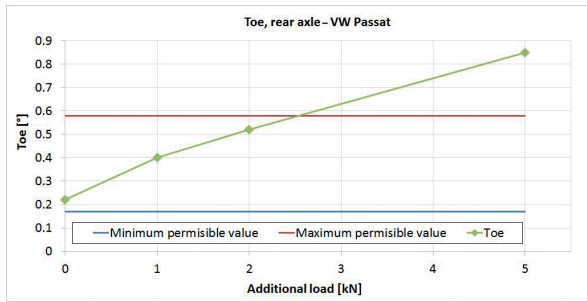


Fig. 7. Impact of additional vehicle load on rear wheel toe value for VW Passat

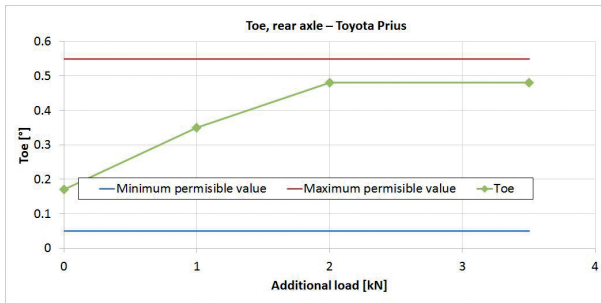


Fig. 8. Impact of additional vehicle load on rear wheel toe value for Toyota Prius

The obtained results of the measurements of the sample wheel alignment parameters are presented in Tables 4 to 7. The differences between the values obtained during the correct (referential) measurement and those obtained for the conditions with additional loading were calculated using Formula 1.

$$Difference = \left| \frac{A - B}{A} \right| \cdot 100\% \quad (1)$$

where

- A – the value obtained during correct measurement
- B – the value obtained for the car with additionally loading

Table 4. The results of the front wheel camber angle measurement for the VW Passat

Additional load [kN]	Camber front left [°]	Difference front left [%]	Camber front right [°]	Difference front right [%]
0	-0.78	—	-0.87	—
1	-0.75	4	-0.78	10
2	-0.68	13	-0.78	10
3.5	-0.58	26	-0.68	22
5	-0.53	32	-0.65	25

Table 5. The results of the front wheels camber angle measurement for the Toyota Prius

Additional load [kN]	Camber front left [°]	Difference front left [%]	Camber front right [°]	Difference front right [%]
0	-1.27	—	-0.6	—
1	-1.32	4	-0.67	12
2	-1.42	12	-0.63	5
3.5	-1.48	17	-0.67	12

Table 6. The results of the toe measurement for the VW Passat

Additional load [kN]	Toe front [°]	Difference [%]	Toe rear [°]	Difference [%]
0	0.17	—	0.22	—
1	0.33	94	0.4	82
2	0.38	124	0.52	136
3.5	0.32	88	—	—
5	0.42	147	0.85	286

Table 7. The results of the toe measurement for the Toyota Prius

Additional load [kN]	Toe front [°]	Difference [%]	Toe rear [°]	Difference [%]
0	0.07	—	0.17	—
1	0.05	29	0.35	106
2	—	—	0.48	182
3.5	0.07	0	0.48	182

4.2. Impact of tyre pressure

An additional area of interest was the impact of tyre pressure on the measurement results; this was tested for the Toyota Prius. Aside from the correct (referential) measurement with the correct tyre pressure of 0.2 MPa, two cases were considered: reduced front wheel tyre pressure to 0.14 MPa with normal rear wheel pressure and reduced pressure to 0.14 MPa in all four wheels.

Example results of conducted measurements are presented in Figs. 9 and 10.

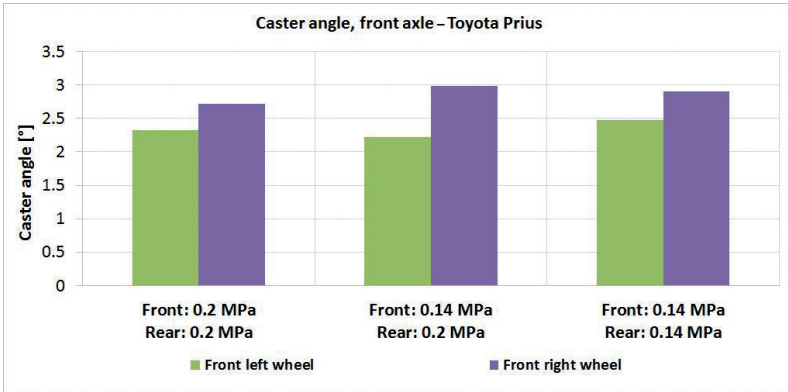


Fig. 9. Impact of tyre pressure on front wheel camber angle values for the Toyota Prius

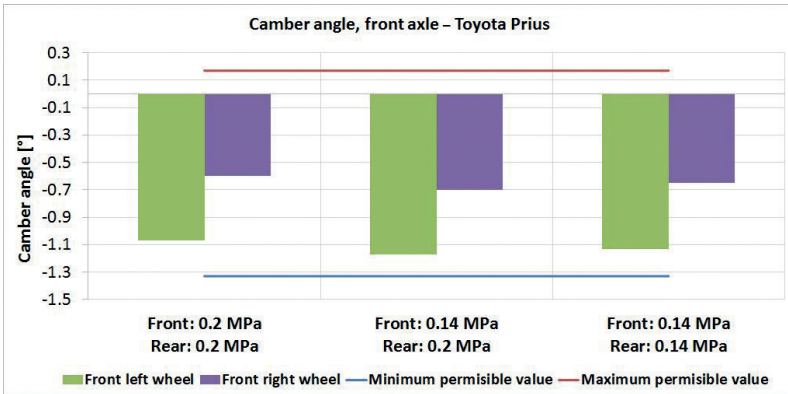


Fig. 10. Impact of tyre pressure on camber angle values for the Toyota Prius

Tables 8 and 9 show sample measurement results and differences between the correct measurement and the measurements performed for incorrect tyre pressures. The differences were calculated using Formula 1.

Table 8. The results of the camber angle measurement for the Toyota Prius

Tyre pressure [MPa]	Camber front left [°]	Difference front left [%]	Camber front right [°]	Difference front right [%]
front/rear: 0.2	-1.07	—	-0.60	—
front/rear: 0.14/0.2	-1.17	9	-0.70	17
front/rear: 0.14	-1.13	6	-0.65	8

Table 9. The results of the caster measurement for the Toyota Prius

Tyre pressure [MPa]	Caster front left [°]	Difference front left [%]	Caster front right [°]	Difference front right [%]
front/rear: 0.2	2.33	—	2.72	—
front/rear: 0.14/0.2	2.22	5	2.98	1
front/rear: 0.14	2.47	6	2.9	7

5. Summary

Analysis of the presented results shows that the preparation of the vehicle has an influence on the obtained values of the measured parameters. The incorrect tyre pressure and vehicle load resulted in changes to the results of the measurement compared to those conducted on properly prepared cars. These changes were dependent on the type of suspension, but in most cases, the obtained values were within the tolerance limits given by the manufacturer. The differences between the measured values and the result of the reference measurements ranged from a few to a dozen or so per cent, although in some cases, they exceeded one hundred per cent.

The measured values of camber angle changed with the additional load, the changes were different for the MacPherson and multi-link suspension systems. In the case of Volkswagen, the additional load placed in the boot caused an increase in the measured value. In the case of the Toyota Prius, the camber angle slightly decreased with increases to the additional load (see Figs. 3 and 4).

Figures 5 and 6 present the impact of the additional load on the front axle toe measurements. The value of toe for the Volkswagen Passat increased by 147 % for 5 kN additional load; for the Toyota it did not significantly change.

Both cars were equipped with twist beam rear suspension; in both cases, the additional load caused growth of the measured values of the rear toe (see Figs. 7 and 8).

The influence of tyre pressure on wheel alignment measurement results was also analysed. The 30% reduction of tyre pressure caused a change in the values of the measured parameters by a few per cent.

The results obtained show that the correct preparation of a car for a wheel alignment measurement is crucial and must not be overlooked. This is especially true in the case of additional loading of a vehicle as this may distort the measurement and can lead to improper wheel alignment adjustment. In some cases, the additional load caused significant changes to the values of the measured parameters; however, these values exceeded the acceptable limits only for a load greater than 2 kN.

References

- [1] Cho Y.G., *Steering pull and drift considering road wheel alignment tolerance during high-speed driving*, International Journal of Vehicle Design, Vol. 54(1)/2010.
- [2] CUSTOR HWA-G58 User manual, Sulejówek, Poland 2011.
- [3] Gajek A., Strzępek P., *The analysis of the accuracy of the wheel alignment inspection method on the side-slip plate stand*, IOP Conference Series: Materials Science and Engineering IOP, Vol. 148(1)/2016.
- [4] Gobbi M., Mastinu G., Doniselli C., *Optimising a Car Chassis*, Vehicle System Dynamics, Vol. 32(2-3)/1999, 149–170.
- [5] Grzyb A., Struski J., *Metody wyznaczania kinematyki wielowahaczowych zawiesznień kół ogumionych*, Teka Komisji Naukowo-Problemovej Motoryzacji, Vol. 16/1998, 9–17.
- [6] Janczur R., *Analityczno-eksperymentalna metoda badań sterowności samochodu*, Politechnika Krakowska, Rozprawa doktorska (PhD thesis), Kraków 2002
- [7] Jonsson J. , *Simulation of Dynamical Behaviour of a Front Wheel Suspension*, Vehicle System Dynamics, Vol. 20(5)/1991, 269–281.
- [8] Klaps J., Day A.J., *Steering drift and wheel movement during braking: Parameter sensitivity studies*, Journal of Automobile Engineering, Vol. 217(D2)/2005.
- [9] Klaps J., Day A.J., *Steering drift and wheel movement during braking: Static and dynamic measurements*, Journal of Automobile Engineering, Vol. 219(D1)/2005.
- [10] Lee J.H., Lee J.W., Sung I.C., *Road crown, tire, and suspension effects on vehicle straight-ahead motion*, International Journal of Automotive Technology, Vol. 6(2)/2005, 183–190.
- [11] Lozia Z., *An analysis of vehicle behaviour during lane-change manoeuvre on an uneven ROAD surface*, Vehicle System Dynamics, Vol. 20(sup1)/1992, 417–431.
- [12] Mántaras D.A., Luque P., *Virtual test rig to improve the design and optimisation process of the vehicle steering and suspension systems*, Vehicle System Dynamics, Vol. 50(50)/2012, 1563–1584.
- [13] Reimpell J., Betzler W., *Podwozia samochodów. Podstawy konstrukcji*, WKŁ, Warszawa 2002.
- [14] Shim T., Velusamy P.C., *Improvement of vehicle roll stability by varying suspension properties*, Vehicle System Dynamics, Vol. 49(1-2)/2011, 129–152.
- [15] Sohn H.S., Park T.W., *Improvement of vehicle roll stability by varying suspension properties. The process control and robust design for the reduction of vehicle drift and brake pulling*, International Journal of Vehicle Design, Vol. 32(2)/2004.
- [16] Struski J., *Quasi-statyczne modelowanie sterowności samochodu*, Wydawnictwo Politechniki Krakowskiej, Monografia 144, Kraków 1993.
- [17] Struski J., Kowalski M., *Podstawy teoretyczne uogólnionych zagadnień z zakresu parametryzacji układów prowadzenia kół względem nadwozia*, Technical Transactions, 6-M/2008, 119–129.
- [18] Struski J., Wach K., *Analiza mechanizmu przyrządu pomiarowego do wyznaczania translacji i rotacji zwrotnicy z kołem kierowanym*, Technical Transactions, 3-M/2012, 87–100.

- [19] Struski J., Wach K., *Teoretyczne podstawy wyznaczania przemieszczeń liniowych oraz kątowych koła kierowanego*, Czasopismo Logistyka-Nauka [Electronic document], Optical Disc CD, Vol. 4/2015, 5840–5849.
- [20] Wach K., *The theoretical analysis of an instrument for linear and angular displacements of the steered wheel measuring*, IOP Conference Series: Materials Science and Engineering IOP, Vol. 148(1)/2016.

